

Report No. K-TRAN: KU-99-2  
FINAL REPORT

## **FATIGUE PRONE STEEL BRIDGE DETAILS: INVESTIGATION AND RECOMMENDED REPAIRS**

Yuan Zhao  
W. M. Kim Roddis

University of Kansas  
Lawrence, Kansas



MAY 2004

**K-TRAN**

A COOPERATIVE TRANSPORTATION RESEARCH PROGRAM BETWEEN:  
KANSAS DEPARTMENT OF TRANSPORTATION  
KANSAS STATE UNIVERSITY  
THE UNIVERSITY OF KANSAS

<b>1 Report No.</b> K-TRAN: KU-99-2	<b>2 Government Accession No.</b>	<b>3 Recipient Catalog No.</b>	
<b>4 Title and Subtitle</b> FATIGUE PRONE STEEL BRIDGE DETAILS: INVESTIGATION AND RECOMMENDED REPAIRS		<b>5 Report Date</b> May 2004	<b>6 Performing Organization Code</b>
		<b>8 Performing Organization Report No.</b>	
<b>7 Author(s)</b> Yuan Zhao and W. M. Kim Roddis		<b>10 Work Unit No. (TRAIS)</b>	
<b>9 Performing Organization Name and Address</b> University of Kansas 127 Broadcasting Lawrence, Kansas 66045		<b>11 Contract or Grant No.</b> C1114	
		<b>13 Type of Report and Period Covered</b> Final Report January 1999 – June 2003	
<b>12 Sponsoring Agency Name and Address</b> Kansas Department of Transportation Bureau of Materials and Research, Research Unit 2300 Southwest Van Buren Street Topeka, Kansas 66611-1195		<b>14 Sponsoring Agency Code</b> RE-0177-01	
		<b>15 Supplementary Notes</b> For more information write to address in block 9.	
<b>16 Abstract</b> <p>Development of fatigue cracking has led to severe structural deficiency in many of the Kansas Department of Transportation's (KDOT) welded steel bridges. In most circumstances, cracks were found to have developed at the connections of transverse structural members and longitudinal girders due to out-of-plane distortion. Procedures for determination of secondary stresses are not addressed by the current bridge design or rating specifications, since the details subjected to distortion-induced fatigue are often confined to highly localized regions and their corresponding stress fields are difficult to predict using conventional design or analysis approaches.</p> <p>This study presents the application of finite element methods for evaluation of out-of-plane fatigue behavior and recommendation of appropriate retrofit. Through proper modeling of the interaction between longitudinal girders and transverse structural members, causes of distortion-induced cracking were determined and different repair options were assessed. The central focus of the research is the case studies of five KDOT bridges with typical superstructure types and cracking scenarios. To link the global structural behavior under truck loading to the local stress concentration of crack prone details, a two-level finite element modeling approach was employed during the investigations. Both modeling procedures successfully determined the stress magnitude and distribution caused by out-of-plane distortion, and at the same time minimized the computation effort as well.</p> <p>Results obtained from the case studies verified crack severity observed in the field, helped identify potential crack locations, and suggested repair solutions to extend the bridges' life. The overall repair method proposed for these four bridges is to stiffen the web gaps by welding or bolting the connection plates to girder flanges. The web gap regions should be able to withstand unlimited number of load cycles once the repair is carried out. The repair method proposed for the fifth bridge is to partially cut short the connection plate and reweld the crack. This repair is expected to provide a minimum remaining service life of fifteen years.</p> <p>The finite element modeling procedures used in this research effectively interpreted the out-of-plane fatigue behavior and crack growth characteristics, and provided guidance for future retrofit and field test implementations. The same analytical procedures can be extended to the study of other bridges as an alternative to experimental testing. It is recommended that this approach be included in the future update of AASHTO <i>Guide Specifications for Fatigue Evaluation of Existing Steel Bridges</i> as a method for evaluation of distortion-induced fatigue.</p>			
<b>17 Key Words</b> Bridge, Cracking, Fatigue, Finite Element, Girders, Service Life and Repair		<b>18 Distribution Statement</b> No restrictions. This document is available to the public through the National Technical Information Service, Springfield, Virginia 22161	
<b>19 Security Classification (of this report)</b> Unclassified	<b>20 Security Classification (of this page)</b> Unclassified	<b>21 No. of pages</b> 427	<b>22 Price</b>

# **FATIGUE PRONE STEEL BRIDGE DETAILS: INVESTIGATION AND RECOMMENDED REPAIRS**

Final Report

Prepared by

Yuan Zhao

and

W. M. Kim Roddis

University of Kansas

A Report on Research Sponsored By

**THE KANSAS DEPARTMENT OF TRANSPORTATION  
TOPEKA, KANSAS**

**UNIVERSITY OF KANSAS  
LAWRENCE, KANSAS**

May 2004

## **PREFACE**

The Kansas Department of Transportation's (KDOT) Kansas Transportation Research and New-Developments (K-TRAN) Research Program funded this research project. It is an ongoing, cooperative and comprehensive research program addressing transportation needs of the state of Kansas utilizing academic and research resources from KDOT, Kansas State University and the University of Kansas. Transportation professionals in KDOT and the universities jointly develop the projects included in the research program.

## **NOTICE**

The authors and the state of Kansas do not endorse products or manufacturers. Trade and manufacturers names appear herein solely because they are considered essential to the object of this report.

This information is available in alternative accessible formats. To obtain an alternative format, contact the Office of Transportation Information, Kansas Department of Transportation, 915 SW Harrison Street, Room 754, Topeka, Kansas 66612-1568 or phone (785) 296-3585 (Voice) (TDD).

## **DISCLAIMER**

The contents of this report reflect the views of the authors who are responsible for the facts and accuracy of the data presented herein. The contents do not necessarily reflect the views or the policies of the state of Kansas. This report does not constitute a standard, specification or regulation.

## ABSTRACT

Development of fatigue cracking has led to severe structural deficiency in many of the Kansas Department of Transportation's (KDOT) welded steel bridges. In most circumstances, cracks were found to have developed at the connections of transverse structural members and longitudinal girders due to out-of-plane distortion. Procedures for determination of secondary stresses are not addressed by the current bridge design or rating specifications, since the details subjected to distortion-induced fatigue are often confined to highly localized regions and their corresponding stress fields are difficult to predict using conventional design or analysis approaches.

This study presents the application of finite element methods for evaluation of out-of-plane fatigue behavior and recommendation of appropriate retrofit. Through proper modeling of the interaction between longitudinal girders and transverse structural members, causes of distortion-induced cracking were determined and different repair options were assessed. The central focus of the research is the case studies of five KDOT bridges with typical superstructure types and cracking scenarios. The Arkansas River Bridge developed fatigue cracks at the coped floor-beam flange to connection plate fillet welds, while the Westgate Bridge, the Winfield Bridge, the Hump Yard Bridge, and the Tuttle Creek Bridge developed fatigue cracks at the unstiffened web gaps where the transverse connection plates were not rigidly attached to girder flanges. To link the global structural behavior under truck loading to the local stress concentration of crack prone details, a two-level finite element modeling approach was employed during the investigations. Stick frame to finite element modeling was used for the analysis of the Westgate Bridge, and direct finite element coarse-to-fine submodeling was used

for the analyses of the other four bridges. Both modeling procedures successfully determined the stress magnitude and distribution caused by out-of-plane distortion, and at the same time minimized the computation effort as well.

Results obtained from the case studies verified crack severity observed in the field, helped identify potential crack locations, and suggested repair solutions to extend the bridges' life. For the four bridges that experienced web gap cracking, the maximum distortion-induced stresses were found close to or above yielding with corresponding out-of-plane movements of only a few thousandths of an inch. Both the web gap stresses and displacements obtained in this research using finite element methods indicated a good agreement with the experimental results of other field or laboratory studies. Based on the analytical solutions, a linear out-of-plane stress-displacement relationship was established for each of the bridges under investigation. The overall repair method proposed for these four bridges is to stiffen the web gaps by welding or bolting the connection plates to girder flanges. The web gap regions should be able to withstand unlimited number of load cycles once the repair is carried out. The repair method proposed for the fifth bridge is to partially cut short the connection plate and reweld the crack. This repair is expected to provide a minimum remaining service life of fifteen years.

The finite element modeling procedures used in this research effectively interpreted the out-of-plane fatigue behavior and crack growth characteristics, and provided guidance for future retrofit and field test implementations. The same analytical procedures can be extended to the study of other bridges as an alternative to experimental testing. It is recommended that this approach be included in the future update of AASHTO *Guide Specifications for Fatigue Evaluation of Existing Steel Bridges* as a method for evaluation of distortion-induced fatigue.

# TABLE OF CONTENTS

ABSTRACT.....	i
TABLE OF CONTENTS .....	iii
LIST OF TABLES .....	ix
LIST OF FIGURES .....	xi
CHAPTER 1 Introduction	
1.1 Highway Bridge Repair and Rehabilitation.....	1
1.2 Fatigue Prone Steel Bridge Details .....	3
1.3 Research Background and Scope of Work .....	6
1.4 Fatigue Cracking Experienced by the KDOT Bridges .....	9
1.5 Research Objectives.....	13
1.6 Report Organization.....	14
CHAPTER 2 Out-of-Plane Fatigue Cracking in Welded Steel Bridges	
2.1 Out-of-Plane Distortion .....	16
2.2 Evolution of AASHTO Specifications for the Connection Plate Design .....	20
2.3 Current Connection Plate Design Details .....	22
2.3.1 <i>Welded Connection Plate Detail</i> .....	22
2.3.2 <i>Bolted Connection Plate Detail</i> .....	24
2.3.3 <i>All Bolted Connection Angle Detail</i> .....	26
2.3.4 <i>Directly Bolted Connection Angle Detail</i> .....	26
2.4 Retrofitting Distortion-Induced Fatigue .....	29
2.4.1 <i>Hole Drilling</i> .....	29
2.4.2 <i>Cold Expansion</i> .....	30
2.4.3 <i>Filling Drilled Holes with Pretensioned Bolts</i> .....	32
2.4.4 <i>Stiffening the Web Gap</i> .....	32
2.4.5 <i>Bolted Splices</i> .....	34
2.4.6 <i>Cutting the Connection Plate Short</i> .....	34
2.4.7 <i>Diaphragm Removal</i> .....	35
2.4.8 <i>Bolt Loosening</i> .....	36
2.4.9 <i>Diaphragm Repositioning</i> .....	36

2.4.10	<i>Rewelding</i> .....	37
2.4.11	<i>Peening</i> .....	37
2.4.12	<i>Gas Tungsten Arc Remelting</i> .....	38
2.4.13	<i>Ultrasonic Impact Treatment</i> .....	39
2.4.14	<i>Using Composite Materials</i> .....	40
2.5	Stay Alert to Unforeseen Cracking and Repair Failure .....	40
2.5.1	Bridges over I-10, Phoenix, Arizona .....	41
2.5.2	Bridges in Birmingham, Alabama .....	42
CHAPTER 3 Fatigue Performance Evaluation		
3.1	Loading .....	44
3.2	Crack Growth Characteristics Defined by Fracture Mechanics .....	45
3.2.1	<i>Stress Intensity Factor <math>K_I</math></i> .....	45
3.2.2	<i>Fatigue Crack Propagation</i> .....	48
3.2.3	<i>Fatigue Life Evaluation</i> .....	50
3.3	AASHTO LRFD Fatigue Design Provisions .....	51
3.3.1	<i>AASHTO Fatigue Detail Categories</i> .....	51
3.3.2	<i>Applicability to Repair Evaluation</i> .....	52
3.3.3	<i>Infinite Life Fatigue Limit</i> .....	57
CHAPTER 4 Applied Finite Element Procedures		
4.1	Related Work .....	61
4.2	Submodeling .....	71
4.3	Modeling Noncomposite Action.....	74
4.3.1	<i>Example 4.1</i> .....	77
4.3.2	<i>Example 4.2</i> .....	79
4.3.3	<i>Example 4.3</i> .....	81
4.3.4	<i>Example 4.4</i> .....	84
4.4	Other Considerations for Model Validation .....	86
CHAPTER 5 Case Study 1 The Arkansas River Bridge		
5.1	Description of the Bridge Structure .....	89
5.2	Fatigue Crack Observation .....	91
5.2.1	<i>Crack Type 1 <math>\frac{3}{4}</math> Broken Welds at the</i>	

<i>Stringer to Floor-beam Connections</i> .....	94
5.2.2 <i>Crack Type 2 <math>\frac{3}{4}</math> Fatigue Cracks at the Expansion Joints</i> .....	94
5.2.3 <i>Crack Type 3 <math>\frac{3}{4}</math> Out-of-Plane Fatigue Cracks at     the Floor-beam to Exterior Girder Connections</i> .....	96
5.2.4 <i>Other Crack Type <math>\frac{3}{4}</math> Vertical Crack at the     Floor-beam to Interior Girder Connection</i> .....	97
5.3 <i>Finite Element Stress Analysis for Type 3 Cracks</i> .....	98
5.3.1 <i>Coarse Model</i> .....	99
5.3.2 <i>Submodel</i> .....	107
5.3.3 <i>Unzipping fatigue cracks</i> .....	113
5.4 <i>Fatigue Life Evaluation</i> .....	119
5.4.1 <i>Fatigue Life Calculated by Using Conventional <math>K_I</math> Formula</i> .....	120
5.4.2 <i>Fatigue Life Calculated by Using ANSYS <math>K_I</math> Results</i> .....	125
5.4.3 <i>Evaluation of the Different Approaches for Fatigue Life Estimation</i> .....	128
5.5 <i>Retrofit Study for Type 3 Out-of-Plane Fatigue Cracking</i> .....	132
5.5.1 <i>Repair Guidelines</i> .....	132
5.5.2 <i>Finite Element Repair Analysis</i> .....	133
5.5.2.1 <i>Repair Plan 1 — Add Backup Plate to the Stiffener</i> .....	133
5.5.2.2 <i>Repair Plan 2 — Cut Short Stiffener Completely</i> .....	137
5.5.2.3 <i>Repair Plan 3 — Cut Short Stiffener Partially and Drill Holes</i> .....	140
5.5.2.4 <i>Repair Plan 4 — Cut Short Stiffener             Partially and Reweld the Crack</i> .....	141
5.5.3 <i>Repair Recommendations</i> .....	144
5.5.4 <i>Remaining Service Life</i> .....	146
5.6 <i>Summary</i> .....	148
<b>CHAPTER 6 Case Study 2: The Westgate Bridge</b>	
6.1 <i>Bridge Structure and Crack Observation</i> .....	149
6.2 <i>Repair Methods Used by KDOT</i> .....	153
6.3 <i>Modeling Procedures</i> .....	155
6.4 <i>Connections at the Positive Moment Regions</i> .....	161
6.4.1 <i>Exploring Web Gap Stresses (Model FM1)</i> .....	161

6.4.2	<i>Repair Analysis</i> .....	172
6.4.2.1	Welding Connection Stiffener to Top Flange (Model FM1-w).....	173
6.4.2.2	Removing Upper Truss Chord (Model FM1-r) .....	175
6.4.2.3	Adding Connection Welds and Removing Truss Members (Model FM1-wr) .....	176
6.4.3	<i>Evaluation of FM1 Model Series</i> .....	176
6.5	Connections at the Negative Moment Regions .....	179
6.5.1	<i>Exploring Web Gap Stresses (Model FM3)</i> .....	179
6.5.2	<i>Repair Analysis</i> .....	184
6.5.2.1	Adding New Stiffener Plate on the Other Side of the Girder Web (Model FM3-p).....	185
6.5.2.2	Removing Upper Truss Chord (Model FM3-r) .....	187
6.5.2.3	Adding New Stiffener Plate and Removing Truss Members (Model FM3-pr) .....	188
6.5.3	<i>Evaluation of FM3 Model Series</i> .....	190
6.6	Out-of-plane Displacement.....	193
6.6.1	<i>Definition</i> .....	193
6.6.2	<i>Fisher's <math>s - D</math> Expression</i> .....	195
6.7	Summary.....	197
CHAPTER 7 Case Study 3: The Winfield Bridge		
7.1	Bridge Structure and Fatigue Cracking .....	199
7.2	Evaluation of KDOT Repair Approach.....	203
7.3	Finite Element Investigation.....	204
7.3.1	<i>Coarse Model Analysis</i> .....	204
7.3.2	<i>Submodel Analysis</i> .....	211
7.3.2.1	Details of Interest.....	211
7.3.2.2	Comparison of Web Gap Stresses Developed at Mid-Span Diaphragm-Girder Connections of the Four Main Girders .....	214
7.3.2.3	Submodel Analysis for Girder G3 Diaphragm-Girder Connections with Unstiffened Web Gaps at the Bottom Flange .....	218

7.3.2.4	Submodel Analysis for Girder G3 Diaphragm-Girder Connections with Unstiffened Web Gaps at the Top Flange .....	229
7.3.3	<i>Importance of the Diaphragm-Girder Connections in Span No. 3</i> .....	241
7.4	Repair Analysis.....	243
7.4.1	<i>KDOT Repair for Cracked Connections</i> .....	243
7.4.2	<i>Repair Analysis for Uncracked Connections</i> .....	247
7.4.2.1	Repair Analysis for Connection 3f .....	247
7.4.2.2	Repair Analysis for Connection 3h.....	250
7.4.2.3	Repair Analysis for Connection 3k.....	253
7.4.3	<i>Repair Recommendations</i> .....	260
7.5	Fisher's $\sigma - \Delta$ Expression.....	261
7.6	Summary.....	236
CHAPTER 8 Case Study 4: The Humpyard Bridge		
8.1	Description of the Bridge .....	263
8.2	Crack Scenario and KDOT Repair Plan.....	264
8.3	Finite Element Study .....	271
8.3.1	<i>Coarse Model Analysis</i> .....	272
8.3.1.1	Assumptions and Simplifications .....	272
8.3.1.2	Numbering and Designation.....	276
8.3.1.3	Coarse Model Structure .....	278
8.3.1.4	Cross-frame and Bracing Member Forces .....	281
8.3.2	<i>Submodel Analysis</i> .....	289
8.3.2.1	Submodel Structure .....	289
8.3.2.2	Bottom Flange Submodels.....	291
8.3.2.3	Top Flange Submodels .....	302
8.4	Repair Analysis.....	310
8.5	<i>Brace Removal</i> .....	310
8.5.1	<i>Welded Repair</i> .....	319
8.5.2	<i>Repair Recommendations</i> .....	323
8.6	Fisher's $\sigma - \Delta$ Expression.....	327

8.7 Summary.....	327
CHAPTER 9 Case Study 5: The Tuttle Creek Bridge	
9.1 Bridge Structure .....	329
9.2 Crack Observation and KDOT Repair Recommendations .....	332
9.3 Similar Cases .....	336
9.4 Finite Element Study .....	337
9.4.1 <i>The Coarse Model</i> .....	337
9.4.2 <i>The Submodels</i> .....	338
9.4.2.1 Mid-Span Connections .....	342
9.4.2.2 Girder B Top Flange Submodels .....	347
9.4.2.3 Girder A Bottom Flange Submodels .....	352
9.5 Repair Analysis.....	358
9.5.1 <i>4.5 in. Slot Repair</i> .....	359
9.5.2 <i>12.5 in. Slot Repair</i> .....	364
9.5.3 <i>Broken First Intermittent Welds</i> .....	367
9.5.4 <i>Welded Repair</i> .....	370
9.5.5 <i>Repair Recommendations</i> .....	373
9.6 Fisher’s $\sigma - \Delta$ Expression.....	374
9.7 Summary.....	376
CHAPTER 10 Conclusions and Recommendations	
10.1 Effectiveness and Advantage of Finite Element Modeling .....	378
10.2 Correlation between Out-of-Plane Stresses and Displacements.....	384
10.3 Conclusions and Recommendations .....	392
10.4 Future Work.....	394
10.5 Implementation Plan.....	394
REFERENCES .....	396

## LIST OF TABLES

Table 1-1	Bridges selected for case studies.....	12
Table 2-1	Cost comparison of different connection plate to girder flange connections .....	29
Table 3-1	Detail category constant A and fatigue thresholds ( $DF$ ) <sub>TH</sub> .....	55
Table 3-2	Cycles per truck passage, $n$ .....	56
Table 5-1	Fatigue crack characteristics of the Arkansas River Bridge .....	94
Table 5-2	Comparison of noncomposite and composite analysis results for Floor-beam 12-1 to Girder D connection at load case 3 based on coarse model study.....	107
Table 5-3	Y direction stresses obtained from the submodel analysis .....	110
Table 5-4	ANSYS load case 3 solutions for submodels of different crack sizes .....	123
Table 5-6	Ranges of tested properties documented by mill reports .....	124
Table 5-7	Standard properties specified for ASTM A373 steel.....	124
Table 5-8	Fatigue crack growth calculation assuming single edge crack .....	126
Table 5-9	Fatigue crack growth calculation using ANSYS $K_I$ factors .....	127
Table 5-10	Fatigue life estimated by using different approaches.....	131
Table 5-11	Remaining service life using repair plan 1 .....	135
Table 5-12	Remaining service life using repair plan 2.....	138
Table 5-13	Remaining service life using repair plan 3.....	140
Table 5-14	Remaining service life using repair plan 4.....	144
Table 5-15	Traffic prediction for the Arkansas River Bridge .....	147
Table 6-1	Plate and weld dimensions for finite element modeling .....	158
Table 6-2	Critical crack opening stresses in model FM1 at Load Case No. 7 .....	171
Table 6-3	Web gap stresses for FM1 model series .....	179
Table 6-4	Critical crack opening stresses in model FM3 at Load Case No. 7 .....	181
Table 6-5	Web gap stresses for FM3 model series .....	191
Table 6-6	Web gap stress comparison for Load Case No. 7 .....	196
Table 7-1	Girder-diaphragm connections selected for submodel study.....	212
Table 7-2	Maximum web gap stresses for mid-span girder connections .....	215
Table 7-3	Maximum web gap stresses of Girder G3 bottom flange submodels .....	224

Table 7-4	Significant web gap stresses of Girder G3 top flange submodels .....	220
Table 7-5	Stresses of potential crack locations in connection 3g after the repair .....	225
Table 7-6	Comparison of connection 3f web gap stresses before and after the repair .....	227
Table 7-7	Stresses of potential crack locations in connection 3f after the repair .....	228
Table 7-8	Comparison of connection 3h web gap stresses before and after the repair .....	229
Table 7-9	Stresses of potential crack locations in connection 3h after the repair .....	229
Table 7-10	Comparison of connection 3k web gap stresses before and after the repair .....	230
Table 7-11	Stresses of potential crack locations in connection 3k after the repair .....	231
Table 7-12	Repair recommendations for the Winfield Bridge .....	234
Table 7-13	Web gap stresses obtained from Fisher's formula and ANSYS analysis .....	235
Table 8-1	Summary of cross-frame and bracing member forces .....	288
Table 8-2	Maximum web gap stresses of the bottom flange submodels .....	301
Table 8-3	Maximum web gap stresses of the top flange submodels .....	309
Table 8-4	Comparison of the maximum web gap stresses before and after brace removal for the bottom flange submodels .....	324
Table 8-5	Comparison of the maximum web gap stresses before and after welded repair for the bottom flange submodels .....	325
Table 8-6	Comparison of the maximum web gap stresses before and after welded repair for the top flange submodels .....	326
Table 8-7	Web gap stresses obtained from Fisher's formula and ANSYS analysis .....	327
Table 9-1	Cross-frames and diagonal bracings .....	330
Table 9-2	Maximum web gap stresses of mid-span girder connections .....	346
Table 9-3	Maximum web gap stresses of Girder B top flange submodels .....	353
Table 9-4	Maximum web gap stresses of Girder A bottom flange submodels .....	354
Table 9-5	Stress changes of connection B2W due to four different repair schemes .....	361
Table 9-6	Comparison of web gap stresses obtained from Fisher's formula and ANSYS analysis .....	375
Table 10-1	Summary of web gap stresses and .....	383
Table 10-2	Out-of-plane stress-displacement correlation .....	387

## LIST OF FIGURES

Figure 1-1	Bridges built in the US during the 20 <sup>th</sup> century .....	2
Figure 1-2	Bridge deficiency trends .....	3
Figure 1-3	Bridges built in Kansas during the 20 <sup>th</sup> century.....	7
Figure 1-4	Condition of bridge deficiency in Kansas.....	8
Figure 1-5	Typical out-of-plane crack details observed in KDOT bridges .....	11
Figure 2-1	Out-of-plane distortion in small web gap at connection plate end .....	17
Figure 2-2	Development of horizontal and horseshoe cracks due to out-of-plane distortion .....	17
Figure 2-3	Cracking and repair condition on each side of a connection plate in the Fancy Creek Bridge .....	19
Figure 2-4	Connection plate welded to both girder flanges .....	24
Figure 2-5	Connection plate bolted to tension flange .....	25
Figure 2-6	Connection angle bolted to both girder web and flanges.....	26
Figure 2-7	Diaphragm bolted directly to girder web .....	28
Figure 2-8	Stop holes drilled at crack ends.....	30
Figure 2-9	Cold expansion used to improve fatigue resistance of drilled holes.....	31
Figure 2-10	Stiffening web gap by welding connection plate to girder flange .....	33
Figure 2-11	Stiffening web gap by bolting connection plate to girder flange .....	33
Figure 2-12	Reinforcing splices used for restoring girder section properties .....	34
Figure 2-13	Releasing web gap stresses by cutting the connection plate short.....	35
Figure 2-14	Diaphragm repositioning.....	37
Figure 2-15	Peening applied in addition to the welded retrofit .....	38
Figure 2-16	Connection plate detail used by bridges over I-10 in Phoenix, Arizona .....	42
Figure 2-17	Connection angle used for web gap crack repair in the Alabama DOT bridges .....	43
Figure 3-1	$K_I$ values for three basic crack geometries.....	46
Figure 3-2	Distribution of $\sigma_y$ stress component at the crack tip region.....	47
Figure 3-3	$K$ -field outside of the plastic zone .....	47

Figure 3-4	Schematic relation among stress, flaw size, and material toughness.....	48
Figure 3-5	Fatigue crack growth of typical structural steels .....	49
Figure 3-6	<i>S-N</i> curves for AASHTO fatigue detail categories .....	52
Figure 3-7	Relationship between the spectrum of applied stress ranges and the <i>S-N</i> curve.....	59
Figure 4-1	Finite element models for the web-gusset-stiffener connection .....	63
Figure 4-2	Finite element of web, gusset plate, and lateral braces .....	64
Figure 4-3	Fatigue study for coped diaphragm to girder connection .....	65
Figure 4-4	Investigation of design load for cross-frame members .....	67
Figure 4-5	Finite element analysis for girder-diaphragm interaction.....	68
Figure 4-6	Crack and repair analysis at stringer to floor-beam connection.....	70
Figure 4-7	Finite element analyses for drilled holes and flame cut holes .....	71
Figure 4-8	Coarse model vs. submodel .....	73
Figure 4-9	Schematic of coupled DOF sets used for modeling bridge noncomposite action.....	77
Figure 4-10	Simply supported rectangular beams .....	79
Figure 4-11	Two-span rectangular beams .....	81
Figure 4-12	Simply supported noncomposite bridge section .....	83
Figure 4-13	Two-span noncomposite bridge section.....	85
Figure 5-1	Frame plan and crack distribution of the Arkansas River Bridge .....	90
Figure 5-2	Cross section of the Arkansas River Bridge .....	90
Figure 5-3	Type 1 fatigue cracking.....	92
Figure 5-4	Type 2 fatigue cracking.....	92
Figure 5-5	Type 3 fatigue cracking.....	93
Figure 5-6	Other type of fatigue cracking .....	98
Figure 5-7	Coarse model of the Arkansas River Bridge superstructure from Pier No. 10 to 12.....	101
Figure 5-8	Element combination at a typical girder section for the coarse model.....	102
Figure 5-9	Truck location for load cases 3 and 15 .....	103
Figure 5-10	Deflection of steel members .....	104

Figure 5-11	Stress concentration occurring at Floor-beam 12-1 to Girder D connection at load case 3 .....	106
Figure 5-12	Submodeling of the crack region.....	108
Figure 5-13	Out-of-plane stress variation at Floor-beam 12-1 to Girder D connection.....	109
Figure 5-14	Submodel element solution for Y direction stress at load case 3 .....	112
Figure 5-15	Load case 3 Y-stress contour of the submodel with 1 in. crack .....	115
Figure 5-16	Schematic showing locations for normal stress and CMOD measurement .....	115
Figure 5-17	ANSYS typical path definition for a full crack model .....	116
Figure 5-18	Correlation of normal stress and CMOD with crack growth.....	117
Figure 5-19	ANSYS stress intensity factor results for three basic crack modes .....	118
Figure 5-20	Single edge notched plate .....	120
Figure 5-21	Location of the maximum normal stress range used for fatigue life calculation.....	121
Figure 5-22	Change of geometry factors vs. $a/b$ ratio for different $F$ formulas.....	122
Figure 5-23	Fatigue crack growth curves obtained by using different $K_I$ approaches .....	128
Figure 5-24	Repair plan 1 — add backup plate to the stiffener.....	134
Figure 5-25	Maximum stress range locations for repair plan 1 .....	135
Figure 5-26	Repair plan 2 — cut short stiffener completely .....	137
Figure 5-27	Repair plan 3 — cut short stiffener partially and drill holes.....	141
Figure 5-28	ANSYS load case 3, 1 <sup>st</sup> principal stress solution for repair plan 3 .....	142
Figure 5-29	Repair plan 4 — cut short stiffener partially and reweld the crack .....	143
Figure 6-1	Framing plan and retrofit locations of the Westgate Bridge .....	150
Figure 6-2	Cross section of the Westgate Bridge .....	150
Figure 6-3	Crack growth near the girder top flange connection.....	151
Figure 6-4	Inspection pictures showing web gap cracks in the Westgate Bridge .....	152
Figure 6-5	Repair approaches used in the Westgate Bridge .....	154
Figure 6-6	Girder elevation for Span No. 10.....	156
Figure 6-7	Boundary conditions for the finite element model .....	156
Figure 6-8	Framing plan for diagonal bracings in Span No. 10 .....	157
Figure 6-9	Stick frame models for load path calculation.....	158
Figure 6-10	Schematic of loads imposed on the finite element model.....	160

Figure 6-11	Nodes in the web gap specified for stress analysis .....	162
Figure 6-12	Model FM1 deformation and $\sigma_y$ contour at Load Case No. 7 .....	164
Figure 6-13	Model FM1 web gap stress contours for Load Case No. 7 (flange elements are hidden) .....	165
Figure 6-14	Crack formation subject to different axial stresses at the stiffener end .....	165
Figure 6-15	Model FM1 $\sigma_y$ contour of Load Case No. 7 on the exterior girder face.....	166
Figure 6-16	Model FM1 web gap stress gradient at Load Case No.7 .....	167
Figure 6-17	Model FM1 $\sigma_y$ distribution along the flange-to-web weld toe at Load Case No.7.....	168
Figure 6-18	Comparison of web gap details required by KDOT in the earlier and current design .....	169
Figure 6-19	Model FM1 out-of-plane displacement .....	171
Figure 6-20	Model FM1 web gap stress variation for nodes on the interior web side .....	171
Figure 6-21	Model FM1 web gap stress variation for nodes on the exterior web side .....	172
Figure 6-22	Model FM1 maximum $\sigma_x$ and $\sigma_z$ stress variation.....	172
Figure 6-23	FM1 model series.....	173
Figure 6-24	Stress distribution along the repair welds .....	174
Figure 6-25	ANSYS $\sigma_y$ stress contour for Model FM1-w at Load Case No. 6.....	175
Figure 6-26	Load Case No. 7 web gap stress gradient of FM1 model series on interior web side.....	177
Figure 6-27	Load Case No. 7 web gap stress gradient of FM1 model series on exterior web side.....	178
Figure 6-28	Schematic of floor-beam lateral support without upper truss chords .....	178
Figure 6-29	Model FM3 deformation and $\sigma_y$ contour at Load Case No. 7 .....	180
Figure 6-30	Model FM3 web gap stress contours for Load Case No. 7 (flange elements are hidden) .....	182
Figure 6-31	Model FM3 web gap stress gradient at Load Case No.7 .....	182
Figure 6-32	Model FM3 $\sigma_y$ distribution along the flange-to-web weld toe at Load Case No.7.....	183
Figure 6-33	Model FM3 web gap stress variation for nodes on the interior web side .....	183
Figure 6-34	Model FM3 web gap stress variation for nodes on the exterior web side .....	184

Figure 6-35	Model FM3 maximum $\sigma_x$ and $\sigma_z$ stress variation.....	184
Figure 6-36	FM3 model series.....	185
Figure 6-37	Schematic showing penetration of the newly added stiffener plate.....	188
Figure 6-38	Coupled sets used in Model FM3-p.....	188
Figure 6-39	Model FM3-p overall deformation and $\sigma_y$ stress distribution for Load Case No. 6.....	189
Figure 6-40	Model FM3-p web gap stress contour on the existing connection stiffener side for Load Case No. 6.....	190
Figure 6-41	Model FM3-p web gap stress contour on the newly installed stiffener side for Load Case No. 6.....	190
Figure 6-42	Variation of out-of-plane displacements for FM3 model series .....	192
Figure 6-43	Node A $\sigma_y$ stress variation for FM3 model series.....	192
Figure 6-44	Load Case No. 7 web gap stress gradient of FM3 model series on the existing connection stiffener side.....	192
Figure 6-45	Load Case No. 7 web gap stress gradient of FM3 model series on the newly installed stiffener side .....	193
Figure 6-46	Dimensions used for measurement of out-of-plane displacement and web gap length.....	193
Figure 7-1	Elevation of the Winfield Bridge .....	200
Figure 7-2	Span No. 3 framing plan and crack locations of the northbound Winfield Bridge.....	201
Figure 7-3	Inspection pictures of Crack Location No. 1 .....	201
Figure 7-4	Crack shape and size observed at Location No. 1.....	202
Figure 7-5	Cross section of the northbound Winfield Bridge (looking north) .....	202
Figure 7-6	Crack repair details of the Winfield Bridge .....	204
Figure 7-7	Coarse model for Span No. 3 of the northbound Winfield Bridge .....	207
Figure 7-8	Typical girder section of the coarse model.....	208
Figure 7-9	Half span girder plan and elevation.....	208
Figure 7-10	Intermediate diaphragm detail .....	209
Figure 7-11	Intermediate stiffener detail .....	209
Figure 7-12	Truck position of Load Case No. 1 and girder section A, B, and C .....	210

Figure 7-13	Coarse model deformation.....	210
Figure 7-14	Submodel with web gap geometry.....	211
Figure 7-15	Grid points specified for web gap stress evaluation .....	215
Figure 7-16	Point E' $\sigma_y$ stress for mid-span diaphragm-girder connections .....	216
Figure 7-17	Point A $\sigma_y$ stress for mid-span diaphragm-girder connections .....	216
Figure 7-18	Point A $\sigma_x$ stress for mid-span diaphragm-girder connections .....	216
Figure 7-19	Point A $\sigma_z$ stress for mid-span diaphragm-girder connections .....	217
Figure 7-20	Point E' $\sigma_y$ stress variation for Girder G3 bottom flange submodels .....	219
Figure 7-21	Point A $\sigma_x$ stress variation for Girder G3 bottom flange submodels.....	220
Figure 7-22	Point A $\sigma_z$ stress variation for Girder G3 bottom flange submodels .....	220
Figure 7-23	Variation of out-of-plane displacement for Girder G3 bottom flange submodels.....	221
Figure 7-24	Web gap stress gradient for bottom flange submodels of Girder G3 positive moment region connections .....	222
Figure 7-25	Web gap stress gradient for bottom flange submodels of Girder G3 transition region connections .....	223
Figure 7-26	Load Case No. 9 $\sigma_y$ stress contour of submodel 3g on the stiffener side .....	226
Figure 7-27	Load Case No. 9 $\sigma_y$ stress contour of submodel 3g on the no-stiffener side ....	227
Figure 7-28	Load Case No. 9 web gap $\sigma_x$ stress contour of submodel 3g.....	228
Figure 7-29	Load Case No. 9 web gap $\sigma_z$ stress contour of submodel 3g.....	228
Figure 7-30	Load Case No. 9 $\sigma_y$ stress distribution of submodel 3g along the flange-to-web welds .....	229
Figure 7-31	Schematic of different web gap distortion curvature .....	231
Figure 7-32	Web gap $\sigma_y$ stress variation for Girder G3 top flange submodels .....	231
Figure 7-33	Point A $\sigma_x$ stress variation for Girder G3 top flange submodels .....	232
Figure 7-34	Point A $\sigma_z$ stress variation for Girder G3 top flange submodels .....	232
Figure 7-35	Variation of out-of-plane displacement for Girder G3 top flange submodels.....	232
Figure 7-36	Web gap stress gradient for top flange submodels of Girder G3 negative moment region connections .....	234

Figure 7-37	Web gap stress gradient for top flange submodels of Girder G3 transition region connections .....	235
Figure 7-38	Load Case No. 12 $\sigma_y$ stress contour of submodel 3j on the stiffener side .....	237
Figure 7-39	Load Case No. 12 $\sigma_x$ stress contour of submodel 3j .....	238
Figure 7-40	Load Case No. 12 $\sigma_z$ stress contour of submodel 3j .....	238
Figure 7-41	Load Case No. 12 $\sigma_y$ stress contour of submodel 3k on the stiffener side .....	239
Figure 7-42	Load Case No. 12 $\sigma_x$ stress contour of submodel 3k .....	240
Figure 7-43	Load Case No. 12 $\sigma_z$ stress contour of submodel 3k .....	240
Figure 7-44	Load Case No. 12 $\sigma_y$ stress distribution of submodel 3j along the flange-to-web welds on the no-stiffener side of the girder web .....	241
Figure 7-45	Load Case No. 12 $\sigma_y$ stress distribution of submodel 3k along the flange-to-web welds on the stiffener side of the girder web.....	241
Figure 7-46	Connection 3g web gap stress gradient before and after the repair .....	244
Figure 7-47	Locations of maximum $\sigma_x$ and $\sigma_y$ stresses using KDOT repair.....	244
Figure 7-48	Post retrofit $\sigma_x$ stress contour of connection 3g at Load Case No. 9 .....	245
Figure 7-49	Post retrofit $\sigma_y$ stress contour of connection 3g at Load Case No. 9 .....	245
Figure 7-50	Connection 3f web gap stress gradient before and after the repair .....	249
Figure 7-51	Areas of interest in the connection 3f repair model.....	250
Figure 7-52	Connection 3h web gap stress gradient before and after the repair .....	252
Figure 7-53	Areas of interest in the connection 3h repair model .....	252
Figure 7-54	Connection 3k web gap stress gradient before and after the repair .....	255
Figure 7-55	Areas of interest in the connection 3k repair model .....	255
Figure 7-56	Post retrofit $\sigma_x$ stress contour of connection 3k at Load Case No. 12 .....	256
Figure 7-57	Post retrofit $\sigma_y$ stress contour of connection 3k at Load Case No. 12 .....	257
Figure 7-58	Bolted repair used for the positive moment region connections .....	259
Figure 7-59	Welded repair used for the transition and negative moment region connections .....	260
Figure 8-1	Steel framing plan and crack locations of the Hump Yard Bridge Span No. 8.....	265
Figure 8-2	Bridge plan showing traffic lanes between Pier No. 5 and No. 7 .....	266

Figure 8-3	Inspection pictures showing bottom flange web gap cracks in Span No. 8.....	267
Figure 8-4	Crack locations in Span No. 20 and No. 33 .....	269
Figure 8-5	Top flange web gap cracks developed in Span No. 33 .....	269
Figure 8-6	Type A repair for web gap cracks .....	270
Figure 8-7	Type B crack locations at Abutment No. 2.....	270
Figure 8-8	Type B repair for cracks in bearing stiffener plate .....	270
Figure 8-9	Intermediate cross-frame details of the west Hump Yard Bridge Span No. 8.....	274
Figure 8-10	Lateral bracing details of the west Hump Yard Bridge Span No. 8 .....	275
Figure 8-11	Girder 2-4W details of the Hump Yard Bridge .....	276
Figure 8-12	Revised bridge plan of Span No. 8 for coarse model construction.....	277
Figure 8-13	Revised bridge cross section and fatigue truck location for coarse model investigation.....	277
Figure 8-14	Designation of cross-frame members .....	278
Figure 8-15	Coarse model of the Hump Yard Bridge Span No. 8 .....	279
Figure 8-16	Typical girder section of the coarse model showing element combination.....	280
Figure 8-17	Coarse model contour showing vertical deflection at load case No. 13 .....	281
Figure 8-18	Cross-frame member forces of CF20 and CF16 .....	282
Figure 8-19	Cross-frame member forces of CF19 and CF15 .....	282
Figure 8-20	Cross-frame member forces of CF2E and CF2C .....	283
Figure 8-21	Cross-frame member forces of CF1E and CF1C .....	283
Figure 8-22	Cross-frame member forces of sections C-C and E-E at Load Case No. 21 ....	285
Figure 8-23	Bracing member forces .....	285
Figure 8-24	Load Case No. 21 bottom flange details of connections 8e and 8c .....	286
Figure 8-25	Load Case No. 21 top flange details of connections 8c and 5c .....	287
Figure 8-26	Schematic relationship between coarse model and submodel .....	289
Figure 8-27	ANSYS screen capture showing the cut boundary DOFs and the bottom chord and brace forces applied to submodel 8e .....	290
Figure 8-28	Area of interest for the web gap stress evaluation.....	293
Figure 8-29	Maximum web gap $\sigma_y$ stress variation of the bottom flange submodels .....	294

Figure 8-30	Bottom flange web gap stress gradient of the connections at cross section E-E .....	295
Figure 8-31	Load Case No. 21 $\sigma_y$ stress contour of submodel 8e on the stiffener side.....	297
Figure 8-32	Load Case No. 21 $\sigma_y$ stress contour of submodel 8e on the no-stiffener side .....	298
Figure 8-33	Load Case No. 21 $\sigma_x$ stress contour of submodel 8e .....	299
Figure 8-34	Load Case No. 21 $\sigma_z$ stress contour of submodel 8e .....	299
Figure 8-35	Load Case No. 21 $\sigma_y$ stress distribution of submodel 8e along flange-to-web welds .....	299
Figure 8-36	Connections subjected to different curvatures of out-of-plane distortion .....	300
Figure 8-37	Variation of out-of-plane displacement for the top flange submodels .....	302
Figure 8-38	Point E' web gap $\sigma_y$ stress variation of the top flange submodels.....	303
Figure 8-39	Top flange web gap stress gradient.....	304
Figure 8-40	Load Case No. 18 $\sigma_y$ stress contour of submodel 8c on the stiffener side.....	306
Figure 8-41	Load Case No. 18 $\sigma_y$ stress contour of submodel 8c on the no-stiffener side .....	307
Figure 8-42	Load Case No. 18 $\sigma_x$ stress contour of submodel 8c .....	308
Figure 8-43	Load Case No. 18 $\sigma_z$ stress contour of submodel 8c .....	308
Figure 8-44	Load Case No. 18 $\sigma_y$ stress distribution of submodel 8c along flange-to-web welds .....	309
Figure 8-45	Load Case No. 21 section E-E cross-frame member forces .....	311
Figure 8-46	CF20 cross-frame member forces before and after brace removal.....	312
Figure 8-47	CF19 cross-frame member forces before and after brace removal.....	313
Figure 8-48	CF2E cross-frame member forces before and after brace removal .....	314
Figure 8-49	CF1E cross-frame member forces before and after brace removal .....	315
Figure 8-50	Bottom flange maximum web gap $\sigma_y$ stress variation before and after brace removal.....	317
Figure 8-51	Bottom flange maximum web gap $\sigma_y$ stress gradient before and after brace removal.....	318

Figure 8-52	Bottom flange maximum web gap $\sigma_y$ stress variation before and after welded repair .....	320
Figure 8-53	Bottom flange maximum web gap $\sigma_y$ stress gradient before and after welded repair .....	320
Figure 8-54	Top flange maximum web gap $\sigma_y$ stress variation before and after welded repair .....	321
Figure 8-55	Top flange maximum web gap $\sigma_y$ stress gradient before and after welded repair .....	322
Figure 9-1	Cross section of the Tuttle Creek Bridge .....	330
Figure 9-2	Intermediate and connection stiffener details .....	331
Figure 9-3	Framing plan of typical end and intermediate spans of the bridge .....	331
Figure 9-4	Girder details of typical intermediate spans .....	332
Figure 9-5	Crack repair detail used in 1986 bridge retrofit .....	333
Figure 9-6	Crack growth along the vertical stiffener-to-web welds .....	333
Figure 9-7	Crack growth along the horizontal flange-to-web welds .....	334
Figure 9-8	The coarse model .....	339
Figure 9-9	Coarse model truck moving direction .....	340
Figure 9-10	Coarse Model vs. Submodel .....	340
Figure 9-11	Web gap grid points specified for submodel stress evaluation .....	341
Figure 9-12	Top flange web gap $\sigma_y$ stress variation of mid-span connections .....	343
Figure 9-13	Bottom flange web gap $\sigma_y$ stress variation of mid-span connections .....	343
Figure 9-14	Web gap $\sigma_y$ stress gradient of the mid-span cross-flange/girder connections .....	344
Figure 9-15	Web gap $\sigma_y$ stress variation of Girder B top flange submodels .....	345
Figure 9-16	Load Case No. 21 web gap $\sigma_y$ stress contour of top flange submodel B2W ....	348
Figure 9-17	Load Case No. 21 web gap $\sigma_x$ stress contour of top flange submodel B2W ....	349
Figure 9-18	Load Case No. 21 web gap $\sigma_z$ stress contour of top flange submodel B2W ....	349
Figure 9-19	Top flange web gap $\sigma_y$ stress gradient of the east half span Girder B connections .....	350

Figure 9-20	Top flange web gap $\sigma_y$ stress gradient of the west half span Girder B connections .....	351
Figure 9-21	Load Case No. 21 $\sigma_y$ stress distribution of connection B2W along the top-flange-to-web welds .....	352
Figure 9-22	Web gap $\sigma_y$ stress variation of the west half span Girder A bottom flange submodels .....	354
Figure 9-23	Load Case No. 22 web gap $\sigma_y$ stress contour of bottom flange submodel A2W .....	355
Figure 9-24	Load Case No. 22 web gap $\sigma_x$ stress contour of bottom flange submodel A2W .....	356
Figure 9-25	Load Case No. 22 web gap $\sigma_z$ stress contour of bottom flange submodel A2W .....	356
Figure 9-26	Bottom flange web gap $\sigma_y$ stress gradient of the west half span Girder A connections .....	357
Figure 9-27	Load Case No. 22 $\sigma_y$ stress distribution of connection A2W along the bottom-flange-to-web welds .....	358
Figure 9-28	Repair schemes investigated using finite element methods.....	360
Figure 9-29	Load Case No. 21 web gap $\sigma_x$ stress contour of the 4.5 inch slot repair .....	362
Figure 9-30	Load Case No. 21 web gap $\sigma_y$ stress contour of the 4.5 inch slot repair .....	362
Figure 9-31	Load Case No. 21 web gap $\sigma_z$ stress contour of the 4.5 inch slot repair .....	363
Figure 9-32	Comparison of web gap $\sigma_y$ stress gradient before and after the 4.5 inch slot repair .....	363
Figure 9-33	Load Case No. 21 web gap $\sigma_x$ stress contour of the 12.5 inch slot repair .....	365
Figure 9-34	Load Case No. 21 web gap $\sigma_y$ stress contour of the 12.5 inch slot repair .....	365
Figure 9-35	Load Case No. 21 web gap $\sigma_z$ stress contour of the 12.5 inch slot repair .....	366
Figure 9-36	Comparison of web gap $\sigma_y$ stress gradient before and after the 12.5 inch slot repair .....	366
Figure 9-37	Load Case No. 21 web gap $\sigma_x$ stress contour due to broken 1 <sup>st</sup> intermittent welds .....	368

Figure 9-38 Load Case No. 21 web gap $\sigma_y$ stress contour due to broken 1 <sup>st</sup> intermittent welds .....	368
Figure 9-39 Load Case No. 21 web gap $\sigma_z$ stress contour due to broken 1 <sup>st</sup> intermittent welds .....	369
Figure 9-40 Change of web gap $\sigma_y$ stress gradient due to broken 1 <sup>st</sup> intermittent welds .....	369
Figure 9-41 Load Case No. 21 web gap $\sigma_y$ stress contour due to welded repair.....	371
Figure 9-42 Load Case No. 19 web gap $\sigma_x$ stress contour due to welded repair.....	372
Figure 9-43 Load Case No. 21 web gap $\sigma_z$ stress contour due to welded repair .....	372
Figure 9-44 Change of web gap $\sigma_y$ stress gradient due to welded repair .....	373
Figure 10-1 The Westgate Bridge web gap stress-displacement relationship .....	388
Figure 10-2 The Winfield Bridge web gap stress-displacement relationship .....	389
Figure 10-3 The Hump Yard Bridge web gap stress-displacement relationship .....	390
Figure 10-4 The Tuttle Creek Bridge web gap stress-displacement relationship.....	391

# Chapter 1

## Introduction

### 1.1 Highway Bridge Repair and Rehabilitation

One of the missions undertaken by today's bridge engineering community is the repair and rehabilitation of existing structures. Since the 1967 Point Pleasant Bridge collapse, increasing effort has been dedicated to bridge maintenance and preservation. An efficient nationwide highway bridge network has been established during the past 30 years through the cooperation between state departments of transportation (DOTs) and the Federal Highway Administration (FHWA). The National Bridge Inspection Standards issued in 1971 provided standardized procedures for bridge inspection, maintenance, and evaluation. Information submitted by the states to FHWA is maintained in the National Bridge Inventory (NBI) database, upon which the federal funding for the Highway Bridge Repair and Rehabilitation Program is determined. While the overall condition of the bridges in the United States is satisfactory, continuous effort is required to ensure safety and to minimize deficiency of the bridges.

A great number of bridges that need repair and rehabilitation are those built during the Interstate construction boom from the late 1950s through the 1970s. Figure 1-1 shows the distribution of bridges constructed in the United States between 1900 and 2000, based on the latest NBI information. Of the approximately 585,000 bridges archived in the current NBI database, more than one-third were constructed during the 20-year period of peak Interstate development. Many are now 30 to 50 years old, and are approaching the end of their design service life. Frequent inspection and maintenance are thus crucial to these bridges, and repair and replacement should be carried out, if necessary, to help extend useful life and to prevent further deterioration of the structures. Figure 1-2 indicates the condition of highway bridge

health and performance over the past 20 years. Although the overall deficiency trend is decreasing, the total of structural deficiency and functional obsolescence remains about 30% of the NBI inventory. As the large bridge population constructed during the Interstate era continues to age, a more challenging and demanding course of repair and rehabilitation will be facing bridge engineers in the near future.

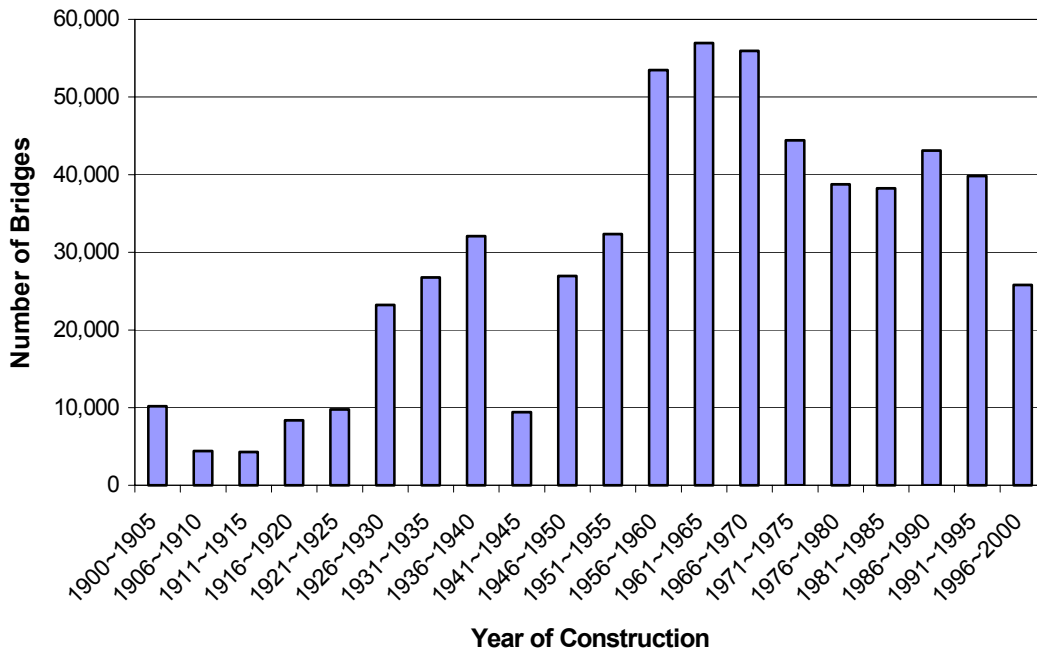


**FIGURE 1-1: Bridges Built in the United States During the 20<sup>th</sup> Century (5-Year Increments)**  
[\[http://www.fhwa.dot.gov/bridge/britab.htm\]](http://www.fhwa.dot.gov/bridge/britab.htm)

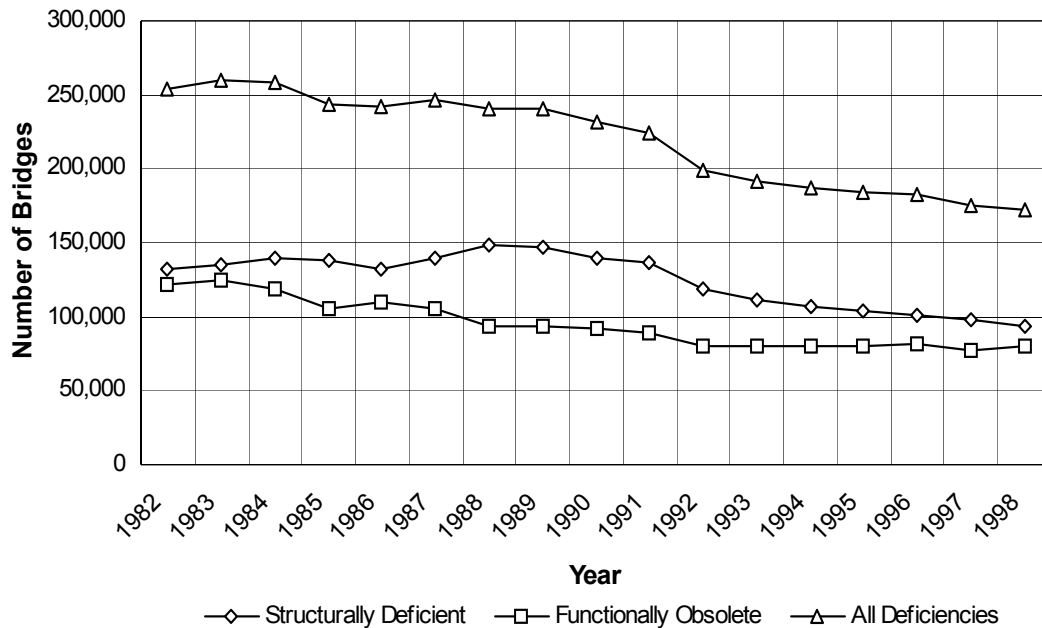


**FIGURE 1-2: Bridge Deficiency Trends**  
 [Small & Cooper, 1998; <http://www.fhwa.dot.gov/bridge/britab.htm>]

## 1.2 Fatigue Prone Steel Bridge Details

Fatigue is one of the most important factors that can contribute to steel bridge structural deficiency. Cracks developed at localized regions decrease the load-carrying capacity of the structural members, and brittle fracture might occur if the cracks continue to grow and the remaining cross sections are not sufficient enough to carry the traffic. Since the 1950s and 1960s, welded construction has been widely accepted in the design of highway and railway bridges in the United States. However, the vulnerability of welded details to fatigue cracking was not widely recognized by the bridge engineering community at that time. The fatigue design specifications used in that era were based on limited test data obtained from small-scale specimens. These provisions were later found to be inadequate and overly optimistic [Fisher 1997]. Beginning from 1960, fatigue cracks were first identified in cover-plate end welds. With the discovery of more cracking conditions at welded attachments such as gussets, stiffeners,

splices, etc., the number of different crack types and crack details grew increasingly through the 1970s and 1980s. The greatest impact came in the 1970s when a large number of cracks were found to have developed at girder web gap areas due to out-of-plane distortion. Note that the time when welded bridges were introduced coincides with the Interstate construction era. Recent statistics given by Fisher [1997] showed that there are about 123,000 steel highway, railway, and mass transit bridges with welded details in the United States; approximately 50,000 of these bridges were built between 1955 and 1975; between 5 and 10 percent of them are estimated to have details that may develop fatigue cracks.

Fatigue control criterion used by early design specifications was to limit the maximum stress below the allowable fatigue stress. The stress range based design concept was not adopted by AASHTO (American Association of State Highway and Transportation Officials) until 1974. Beginning in 1967 a series of NCHRP (National Cooperative Highway Research Program) supported laboratory studies were carried out at Lehigh University in order to develop a sound knowledge base for steel bridge fatigue. Full-size experiments were conducted and various parameters such as stress history, design detail, fabrication quality, steel type, etc. were evaluated to determine their corresponding influences on fatigue behavior. Investigations showed that stress range, connection detail, and frequency of cyclic loading are the three major factors that lead to fatigue cracking, and stress range alone is of the most importance for the fatigue life of bridge details [Fisher, 1997]. Data obtained from these studies formed the basis for the fatigue design provisions currently in use for AASHTO, AREA (American Railway Engineering Association), AISC (American Institute of Steel Construction), and AWS (American Welding Society). In addition, the fracture toughness provisions were also adopted by AASHTO in 1974, which ensure satisfactory material performance even when fatigue cracking is not a concern. As

a result, the general fatigue performance of welded steel bridges built after the mid 1970s is satisfactory, and the focus of crack repair and retrofit is placed mostly on those bridges designed before the current provisions were used.

Often, welded bridge details are more susceptible to fatigue cracking than bolted or riveted ones. Discontinuities in the welds form crack initiation sites at imperfections such as entrapped porosity, lack of fusion or penetration, or incomplete removal of slag. Fractures can also initiate from geometrical stress risers, such as fillet weld toes. Subsequent crack propagation would occur if the surrounding neighborhood is exposed to a cyclic tensile stress field. Unfavorable residual stresses, if occurring simultaneously, could exacerbate the already severe condition of stress concentration and accelerate the process of fatigue crack propagation at these localized regions. Since attached plates are fused together by welding, a continuous path is provided for crack growth from one plate to another.

Most fatigue cracks observed in welded steel bridges were caused by the use of details: 1) with low fatigue resistance; 2) with large initial defects; 3) subjected to out-of-plane distortion; and/or 4) at end restraints, copes, and flange terminations [Fisher & Menzemer, 1990]. Among the four categories, out-of-plane distortion is the largest source of fatigue cracking and has required most of the retrofitting efforts since its advent. Details subjected to this type of cracking were usually exposed to high-frequency and high-magnitude stress variations caused by unequal girder deflection and floor-beam or diaphragm end rotation. Cracks often formed at girder web gap areas where positive attachment between connection stiffeners and girder flanges was not provided. Out-of-plane fatigue cracking takes much fewer stress cycles to develop than other crack categories, thus it is important that correct retrofit actions be taken in an early stage so that severe damage to major girder members can be prevented.

Compared to load-induced fatigue, distortion-induced fatigue is more of a detailing issue and was not observed in bridges until the 1970s. Correspondingly, the appropriate detailing scheme that can prevent cracks from occurring under out-of-plane distortion was not specified by AASHTO until 1985. From the mid 1980s through the 1990s, the research interest for bridge fatigue cracking has shifted from load-induced to distortion-induced fatigue. Considerable experimental studies, including both field and laboratory testings, have been performed with an emphasis on the evaluation of various retrofit techniques. Computational analysis by using finite element methods was also carried out occasionally, but all on a small scale, due to the limited computer resources at that time. Since the secondary stresses are difficult to predict by normal design or analysis procedures, the current design specifications require use of rigid connections between flanges and connection plates to resist out-of-plane distortion.

This limitation was overcome in recent years with the fast development of computer technology. In particular, the ability of accessing large data storage space and high executing speed makes it possible for rigorous finite element investigation of bridge components or even entire bridge structures. The bridge details prone to distortion-induced fatigue are usually subjected to highly localized three-dimensional stress fields. Application of finite element procedures could accurately predict the stress distribution around concentration areas and provide proper retrofit recommendations before field work is carried out. The approach is therefore employed in this study for in-depth modeling of bridge fatigue behavior under out-of-plane distortion.

### **1.3 Research Background and Scope of Work**

Bridge repair and rehabilitation is being addressed by the Kansas Department of Transportation (KDOT). The state of Kansas has the third largest number of bridges in the United States

[<http://www.fhwa.dot.gov/bridge/britab.htm>]. Of the total 25,720 bridges reported to the NBI database, 8,249 are steel structures. Figure 1-3 shows the number of bridges built in Kansas from 1900 to 2000 in 5-year increments. The same construction peak period between 1955 and 1975 appears as was seen nationwide in Figure 1-1. Figure 1-4 shows the condition of bridge deficiency in Kansas for recent years. The total percentage of deficiency (including both structurally deficient and functionally obsolete) has decreased from 35% in 1992 to 26% in 2000.

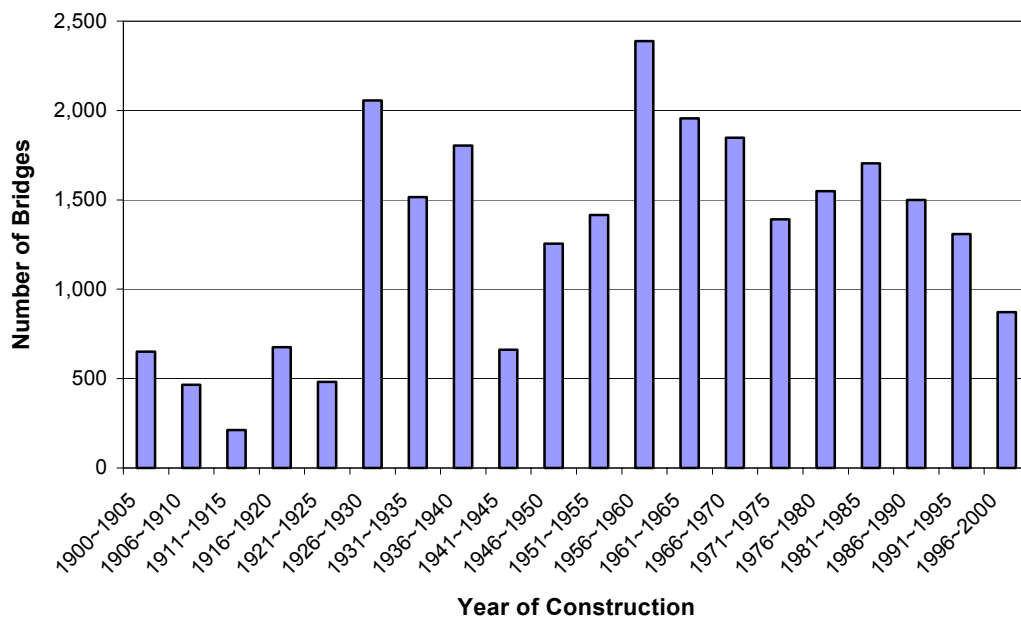


**FIGURE 1-3: Bridges Built in Kansas During the 20<sup>th</sup> Century (5-year increments)**  
[\[http://www.fhwa.dot.gov/bridge/britab.htm\]](http://www.fhwa.dot.gov/bridge/britab.htm)

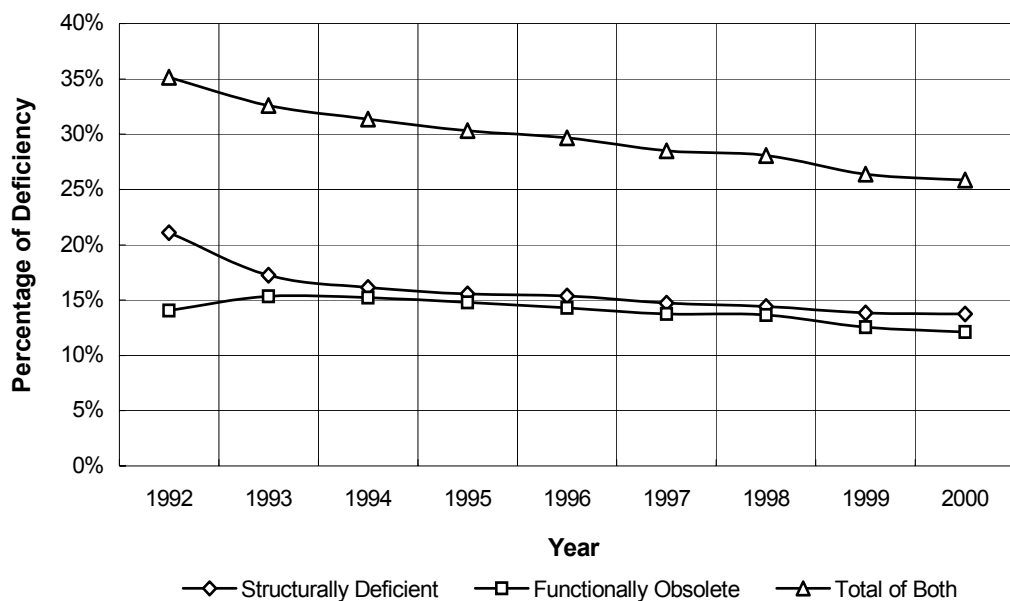


**FIGURE 1-4: Condition of Bridge Deficiency in Kansas**  
[\[http://www.fhwa.dot.gov/bridge/britab.htm\]](http://www.fhwa.dot.gov/bridge/britab.htm)

As numerous cracks were found by the KDOT Special Inspection Team in bridges along major highway systems, The University of Kansas was consulted to provide repair recommendations and to conduct intensive investigations for general fatigue cracking problem of KDOT steel bridges. Bridges kept in KDOT database are those belonging to the state system, including any bridge that carries or crosses a state highway. Currently there are 5150 bridges in the KDOT bridge database, of which 891 are steel structures. Since KDOT experiences fatigue cracking problems mostly in welded plate girder bridges, rolled beam bridges are not the main focus of this research. There are presently 488 plate girder structures in the database record, with 471 of them being welded and the remaining 17 of them being riveted. Based on the knowledge and experience of the KDOT Special Inspection Team, approximately 80% (380) of these welded plate girder bridges are estimated to have developed fatigue cracks of some type, with a great number of these cracks caused by out-of-plane distortion.

To thoroughly investigate the fatigue problem of KDOT welded steel bridges, the following five bridges were chosen for case studies during the research, representing different structural types and cracking conditions:

- The Arkansas River Bridge
- The Westgate Bridge
- The Winfield Bridge
- The Hump Yard Bridge
- The Tuttle Creek Bridge

Though all driven by out-of-plane distortion, the cracks in the Arkansas River Bridge occurred at the coped floor-beam flange to connection plate welds, while those in the other four bridges were found at the unstiffened web gap regions. Studies performed for these five bridges covered the general fatigue scenarios seen in the KDOT bridges and provided valuable insights into the crack evaluation and retrofit methodology.

#### **1.4 Fatigue Cracking Experienced by the KDOT Bridges**

In terms of crack location, the following three out-of-plane crack details are observed in KDOT bridges and are the main focuses of this research:

1. **Web Gap Cracking at Top Flange Connections**: This type of crack has been observed in many of the KDOT existing welded plate girder bridges. As shown in Figure 1-5(a), the connection plate is not rigidly attached to the top flange and there is no additional stiffener placed on the other side of the girder web, such as would be done for bearing purposes. A bridge designed with this detail is often identified with large crack numbers but slow crack growth, as compared with the cracks seen in the bottom flange. In particular, the top flange web gap fatigue cracking occurs more often at a positive moment region, i.e., in a zone of compressive stress, so it appears to be largely self-stabilizing as long as the stress remains in compression.

2. **Web Gap Cracking at Bottom Flange Connections:** This crack detail was found only in the Winfield Bridge and the Hump Yard Bridge. Both of them were skewed bridges with transverse structural members not placed continuously across the bridge width. As shown in Figure 1-5(b), the connection plate is not welded or bolted to the bottom flange and there is no stiffener on the other side of the girder web to help resist out-of-plane distortion, due to the intermittent diaphragm or cross-frame arrangement. In particular, the bottom flange web gap cracks developed in the Winfield Bridge were found in a positive moment region, i.e., in a zone of tensile stress. This crack condition is more severe than that observed in the compression zone. If not arrested promptly, the crack could continue to grow and cause significant damage to primary structural components.
3. **Horizontal Cracking at Coped Floor-Beam Flange to Connection Plate Fillet Welds:** This type of cracking was only identified in the Arkansas River Bridge due to the special means used for the floor-beam to girder connections of this bridge. As shown in Figure 1-5(c), the floor-beam is coped at both the top and bottom flanges, and then attached to the connection plate by horizontal and vertical fillet welds. Cracks initiated from the outer edge of the connection plate and then propagated along the horizontal welds towards the girder web. Cracks occurred only at the intermediate floor-beam to exterior girder connections close to girder positive moment regions. This type of connection requires field welding and is no longer used in current bridge design. The girder sections are rolled beams, so cracks were not observed in the small web gaps.

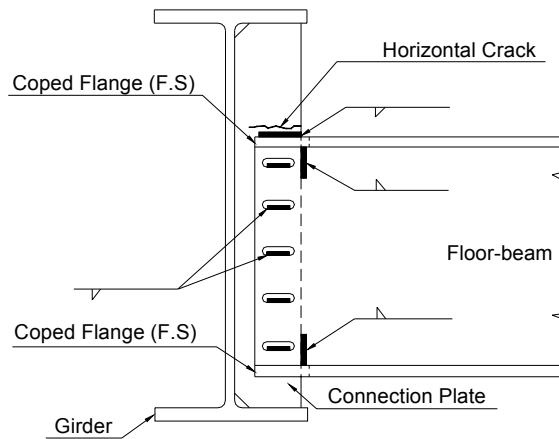
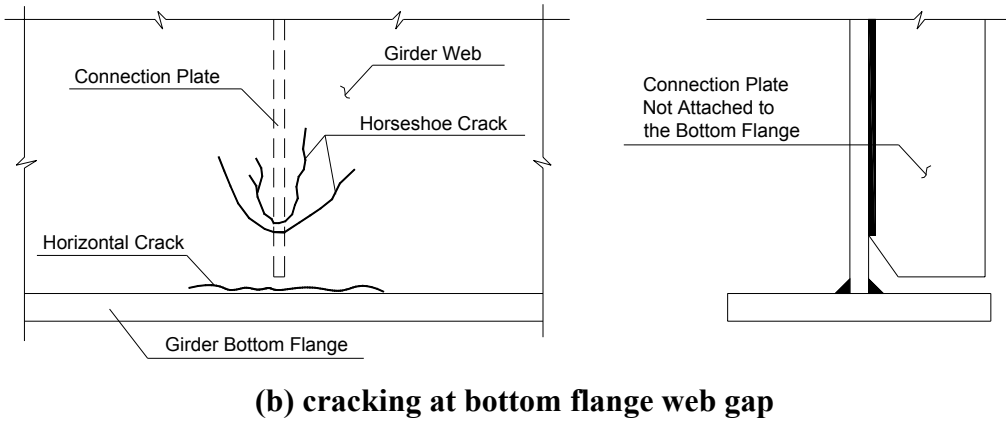
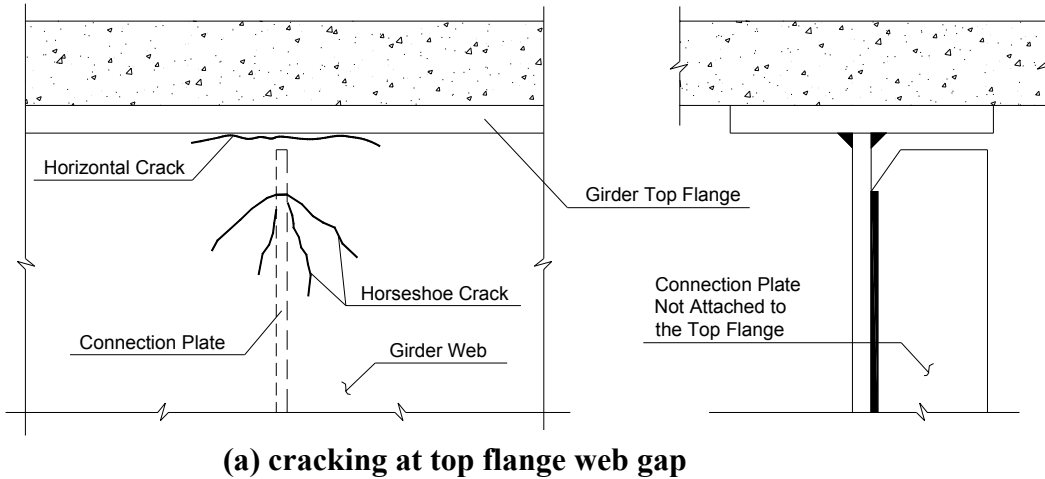


**FIGURE 1-5: Typical Out-of-Plane Crack Details Observed in KDOT Bridges**

**TABLE 1-1: Bridges Selected for Case Studies**

<b>Bridge Name</b>	<b>Superstructure Type</b>	<b>Crack Style</b>	<b>Crack Location</b>	<b>Repair Status</b>
<b>Arkansas River Bridge</b>	Four-girder / floor-beam / stringer	Coped floor-beam flange to connection plate weld crack	-positive moment region	Not yet
<b>Westgate Bridge</b>	Two-girder / floor-truss / stringer	Web gab crack	-top flange -both positive and negative moment regions	Repaired
<b>Winfield Bridge</b>	Skewed four-girder / staggered diaphragm	Web gab crack	-bottom tension flange -positive moment region	Repaired
<b>Hump Yard Bridge</b>	Skewed multi-girder / intermittent cross-frame	Web gab crack	-top and bottom flanges -negative moment regions	Not yet
<b>Tuttle Creek Bridge</b>	Two-girder / cross-frame	Web gab crack	-top flange -both positive and negative moment regions	Repaired, but re-initiated

In summary, top flange web gap cracking is the most frequently occurring fatigue problem found in the KDOT bridges. Two representative bridges, the Westgate Bridge and the Tuttle Creek Bridge, were thus chosen for the study of this type of cracking. Bottom flange web gap cracking was only identified in the Winfield Bridge and the Hump Yard Bridge, so both bridges were modeled and analyzed in detail during the investigation. The horizontal cracking in coped floor-beam flange to connection plate welds was observed only in the Arkansas River Bridge. Mention of this type of out-of-plane cracking has not been found in the literature or other KDOT inspections, therefore a comprehensive study for the fatigue behavior and repair solution of this bridge was performed. General information about the five bridges selected for in-depth study is summarized in Table 1-1.

### **1.5 Research Objectives**

This research is aimed at studying the highway bridge fatigue problem and the corresponding repair methods through finite element analysis. Cracking due to out-of-plane distortion is the major concern of the research as it is experienced most often in KDOT bridges. All five aforementioned bridges were modeled and analyzed using the finite element software package ANSYS 5.6 [2000]. The following are the objectives of this study:

1. To investigate the nature of distortion-induced fatigue and to review the common retrofit strategies for different cracking conditions.
2. To develop proper modeling procedures to effectively simulate the bridge behavior under traffic loading.
3. To identify the fatigue behavior and crack growth characteristics at details subjected to out-of-plane distortion.
4. To determine the stress distribution at the concentration areas, and to quantify and locate the secondary stresses that lead to crack initiation.
5. To evaluate different repair methods and to determine the most applicable retrofit plans to extend the bridges' lives.

6. To estimate the service lives of the crack details both before and after the repair.
7. To recommend fielding testing procedures based on the analytical results.
8. To provide useful information and valuable experience for the investigation of fatigue performance of other KDOT bridges.

## **1.6 Report Organization**

The remaining part of the report is organized as follows:

Chapter 2 introduces the nature of out-of-plane fatigue cracking. To track the origin of distortion-induced fatigue, earlier editions of the AASHTO provisions regarding connection plate details are reviewed. Also included in this chapter are a discussion of the floor-beam/diaphragm/cross-frame to girder connection details used for the current bridge design, and an introduction of the many repair options that can be applied for crack retrofit.

Chapter 3 describes the theory background of the procedures used in this study for fatigue evaluation. The fundamentals of fracture mechanics are reviewed to introduce the general crack growth behavior under cyclic loading. The corresponding fatigue provisions of the AASHTO guide and design specifications are discussed to justify the criteria and procedures used for evaluation of distortion-induced fatigue.

Chapter 4 presents the modeling schemes used during the finite element investigation. A review of the previous studies indicates the necessity of using multi-level modeling procedures for proper access of local stress concentration effect at the crack prone details. The major modeling approaches used in the study, such as submodeling and nodal coupling techniques, are addressed.

Chapters 5 to 9 are the individual case studies carried out for the Arkansas River Bridge, the Westgate Bridge, the Winfield Bridge, the Hump Yard Bridge, and the Tuttle Creek Bridge.

The investigations performed for these five bridges covered a broad range of superstructure configurations and out-of-plane cracking phenomena of the KDOT welded steel bridges. Each chapter includes a description of the bridge structure and crack history, the detailed modeling approaches adopted for fatigue stress analysis, the performance evaluation of the different repairs, and a summary of the findings based on the analytical results.

Chapter 10 concludes the project outlining the general contributions of this research and pointing towards future extension.

## Chapter 2

### Out-of-Plane Fatigue Cracking in Welded Steel Bridges

This chapter reviews the characteristics of out-of-plane distortion-induced fatigue cracking: why it happened and how it can be repaired. To collect information regarding the connection plate details used in the present bridge construction, as well as the crack repair options used in the existing bridge retrofit, the author conducted two surveys among different DOTs and others with an interest in steel bridges. The first survey was carried out in 1999 within the North Central States and FHWA Region 3, including states of Illinois, Michigan, South Dakota, Texas, Missouri, Nebraska, Iowa, Wisconsin, Kansas, Virginia, Pennsylvania, West Virginia, and New York. The second survey was performed in 2000 through the AASHTO/NSBA (National Steel Bridge Alliance) Steel Bridge Collaboration e-mail list ([thelist@steelbridge.org](mailto:thelist@steelbridge.org)). Survey results are presented in sections 2.3 through 2.5.

#### 2.1 Out-of-Plane Distortion

As shown in Figure 2-1, out-of-plane fatigue cracking occurs mostly at locations where transverse structural components such as floor-beams, diaphragms, or cross-frames are framed into longitudinal girders through connection plates. Before and during the early 1980s, the connection plate detail was designed by following the previously established European practice of not welding to the girder tension flange for the purpose of preventing in-plane fatigue. Sometimes the connection plate was not attached to the compression flange either. Therefore a small web gap was left unstiffened during service. When the adjacent girders deflect unequally under traffic loading, the end of the transverse structural member is forced to rotate, pulling the unstiffened portion of the girder web out-of-plane, creating high secondary stresses at the

connection plate end, and leading to fatigue cracking. Cracks developed at both the web-to-flange and web-to-connection-plate fillet welds, typically as horizontal or horseshoe cracks, as indicated in Figure 2-2.

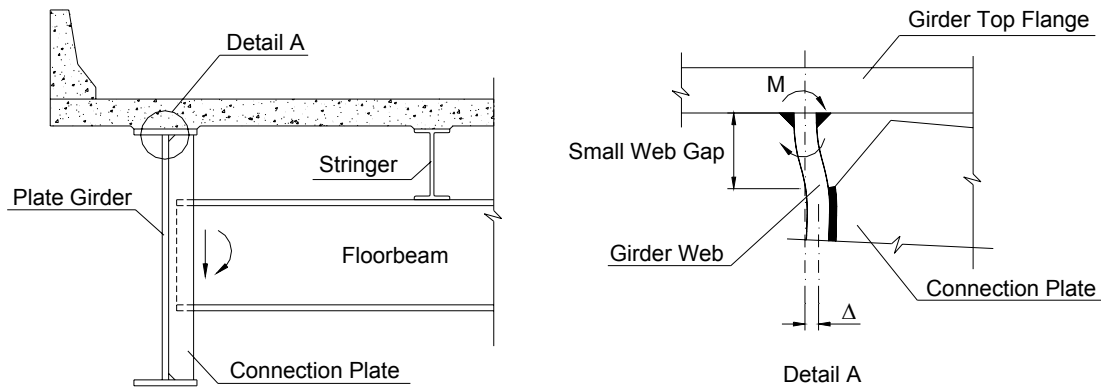


**FIGURE 2-1: Out-of-Plane Distortion in Small Web Gap at Connection Plate End**  
[NCHRP 336, 1990]

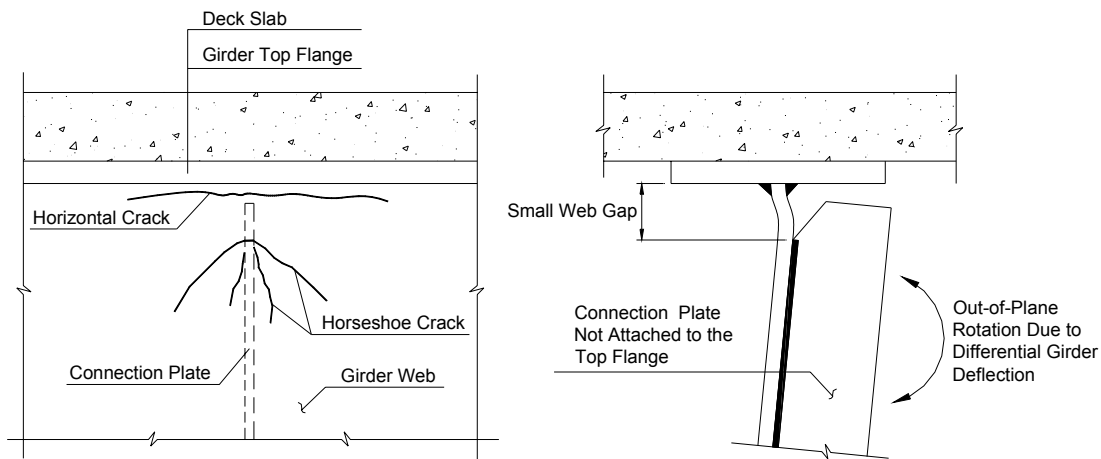


**FIGURE 2-2: Development of Horizontal and Horseshoe Cracks Due to Out-of-Plane Distortion**

The overall characteristics of the cracking phenomena observed in KDOT bridges are:

- 1) Cracks are mostly located in positive moment regions, because large differential girder deflections usually occur at bridge mid spans. Cracks are seldom observed at negative moment

regions, because no girder deflections could occur at bridge piers. 2) Cracks are more easily developed at girder top flanges. This is because the top flange is rigidly embedded into the concrete deck, which restricts it from moving laterally together with the unstiffened small web gap when out-of-plane distortion occurs. The girder bottom flanges are much less constrained compared with the top flanges, and are therefore less susceptible to the distortion-induced fatigue cracking. The photographs in Figure 2-3 illustrate the development of typical horizontal and horseshoe cracks in a KDOT bridge. Crack ends are marked with arrows. The increase in crack length over time can be seen in the difference in location of the light (earlier inspection mark) and dark (later inspection mark) arrow tips.



(a) North Side of Connection Plate



(b) South Side of Connection Plate

**FIGURE 2-3: Cracking and Repair Condition on Each Side of a Connection Plate in the Fancy Creek Bridge**

## 2.2 Evolution of AASHTO Specifications for the Connection Plate Design

To help understand the history of distortion-induced fatigue, a retrospective follows of connection plate provisions from different editions and interims of the AASHTO bridge design specifications published in the past twenty years.

Generally speaking, the detailing of connection plates has never been specified independently as an individual section in the AASHTO *Standard Specifications for Highway Bridges*. From its initial mention in the 1982 Interim, design of connection plates has been included in either the section covering transverse intermediate stiffeners or the section covering diaphragms and cross-frames. It was not until the issuance of the first AASHTO LRFD edition in 1994 that the rationale of distortion-induced fatigue was fully explained and the connection plate design detail was clearly and correctly specified in a separate section.

The story of the connection plate detail should date back to the 1981 Interim, which stated that “*Intermediate stiffeners...may be in pairs...with a tight fit at the compression flange... When stiffeners are used on one side only of the web plate, they shall be fastened to the compression flange*” and “*Transverse intermediate stiffeners need not be in bearing with the tension flange.*” Strictly speaking, stiffeners and connection plates are different components in terms of their structural purposes. However, the same plate can fulfill both functions. Since distortion-induced fatigue was not a widely recognized problem at that time, the specifications were normally interpreted as having the stiffener details requirements also applying to connection plate details. In other words, the connection plate function was seen as subordinate to the intermediate stiffener function.

The 1982 Interim mentioned connection plate details explicitly for the first time in AASHTO. The aforementioned statement for the stiffener-to-compression-flange connection

was revised to “*Stiffeners provided on only one side of the web must be in bearing against but need not be attached to the compression flange for the stiffener to be effective; however, consideration shall be given to the need for this attachment if the location of the stiffener or its use as a connector plate for a diaphragm or cross-frame will produce out-of-plane movements in a welded web to flange connection.*” The author understands this statement to mean that the connection plate was allowed, but was not required, to be attached to the compression flange. The connection plate to tension flange detail was still not explicitly addressed. By default, the relationship between a stiffener and the tension flange would be applied, implying that no welded or bolted connection was needed.

In 1983, the 13<sup>th</sup> AASHTO edition changed to the now current format. The former 1982 Interim provision of the stiffener-to-compression-flange connection was now included in section 10.34.4.6, and that of the stiffener-to-tension-flange connection was now included in section 10.34.4.9. The contents of these two sections were the same as in the 1982 Interim and were kept unchanged until 1995. Design of diaphragms and cross-frames was now specified in section 10.20. No information about connection plate details was mentioned in this section.

The 1985 Interim added to section 10.20.1 an important statement “*Vertical connection plates such as transverse stiffeners which connect diaphragms or cross-frames to the beam or girder shall be rigidly connected to both top and bottom flanges.*” This is the first time AASHTO required that connection plates be attached to both girder flanges. However, those related provisions previously covered in section 10.34.4 for transverse intermediate stiffeners remained the same, which made the specifications very unclear. Unwillingness to change the old design habit, in addition to the ambiguity of the specifications, delayed the process of preventing or eliminating out-of-plane fatigue cracking in newly built bridges. For example, KDOT started

welding or bolting connection plates to both girder top and bottom flanges in early 1989. Fatigue cracking has not been observed to date in bridges designed since this practice was adopted. However, almost all those welded plate girder bridges built with the pre-1989 detail were found to have fatigue cracks in the web gap area.

Finally, in the 1995 Interim, the connection plate detail was made clear and the following revised statement was repeated both in section 10.34.4.6 for the compression flange connection and in section 10.34.4.9 for the tension flange connection. “... *However, transverse stiffeners which connect diaphragms or cross-frames to the beam or girder shall be rigidly connected to both the top and bottom flanges.*”

The AASHTO *LRFD Bridge Design Specifications*, available since 1994, clearly specify that “*Connection plates shall be welded or bolted to both the compression and tension flanges of the cross-section.*” Explanation of distortion-induced fatigue is given in section 6.6.1.3 and its corresponding commentary, and the requirement of rigid attachment between connection plates and girder flanges is addressed in section 6.6.1.3.1 for transverse connection plates, section 6.7.4.1 for diaphragms and cross-frames, and section 6.10.8.1.1 for transverse intermediate stiffeners.

### **2.3 Current Connection Plate Design Details**

Four transverse member to girder connection details are found to be employed during current DOTs’ bridge design procedure: 1) welded connection plate detail; 2) bolted connection plate detail; 3) all bolted connection angle detail; 4) directly bolted connection angle detail. The design intent of these details is to avoid the development of web gap cracking.

#### **2.3.1 Welded Connection Plate Detail**

As previously mentioned, welding of the connection plate to the tension flange was

purposely avoided in the past to prevent fatigue cracking or brittle fracture of the tension flange. This practice then unexpectedly led to distortion-induced fatigue cracking at the small web gap region. The concern of inadequate fracture toughness, however, is no longer a problem to medium bridge steel [Fisher, 1997], and the stiffener-to-flange weld detail has proved to have no less fatigue resistance than the stiffener-to-web weld detail [NCHRP 336, 1990]. Therefore, the current AASHTO design provisions not only allow, but recommend a welded connection-plate-to-flange attachment to preclude distortion-induced fatigue.

As shown in Figure 2-4, connection plates for diaphragms or cross frames shall be welded to both girder flanges with fillet welds on both sides of the connection plates. The distance between the end of the web-to-connection-plate weld and the near edge of the web-to-flange fillet weld shall not be less than  $4t_w$  or more than  $6t_w$  [AASHTO LRFD 6.10.8.1.1, 1998; or AASHTO Standard Specifications 10.34.4.9, 1996]. The connection plate to girder flange fillet weld is an AASHTO fatigue Category C' detail [AASHTO LRFD, 1998]. As long as the girder tension flange stress ranges at these locations are less than Category C' fatigue resistance, this fully welded connection plate detail is preferred because it is the easiest for fabrication. Notice that the horizontal and vertical fillet welds must be terminated at the lengths of X and Y, respectively, from the clipped ends to avoid fatigue problems at the connection plate. Different DOTs may specify the X and Y dimensions differently. KDOT requires 6 mm ( $\frac{1}{4}$  in.) for X and 12 mm ( $\frac{1}{2}$  in.) for Y short of the clip ends [KDOT Design Manual, 2001].

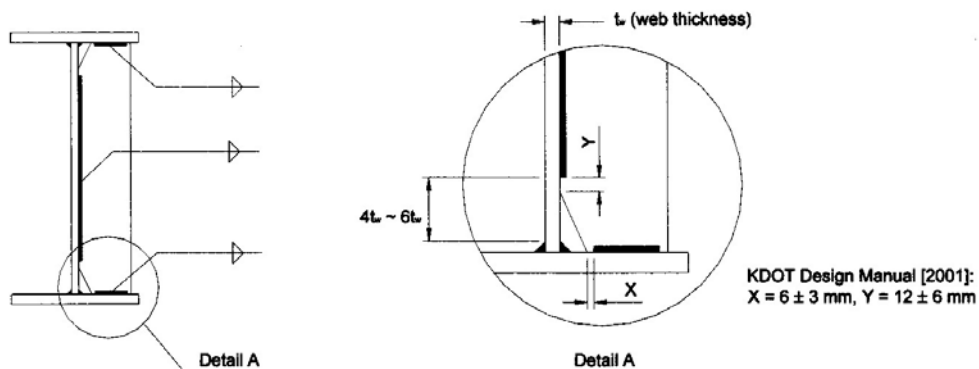


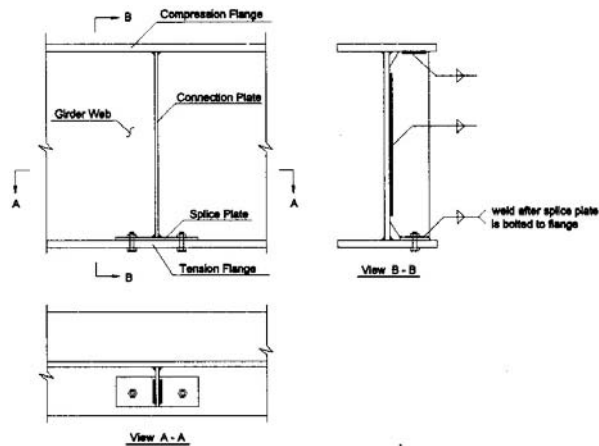
**FIGURE 2-4: Connection Plate Welded to Both Girder Flanges**

The welded attachments of transverse stiffener or connection plate to girder flange and web were grouped to fatigue Category C in the AASHTO Standard Specifications [1996], although these two details have a higher allowable fatigue stress range for over  $2 \times 10^6$  cycles (equivalent to the constant amplitude fatigue threshold in the AASHTO LRFD Specifications) than the rest of the other Category C details. To make things clear, the code writers of the LRFD Specifications created a new fatigue Category C' for these two exceptions. As the bridge design guidance just started switching from the Standard Specifications to the LRFD Specifications, the stiffener-to-flange and the stiffener-to-web fillet welds are still referred to as Category C details during routine design practice and even in most literature. The author prefers to follow the LRFD designation in this report for clarification purposes, as other Category C details are encountered occasionally in this document.

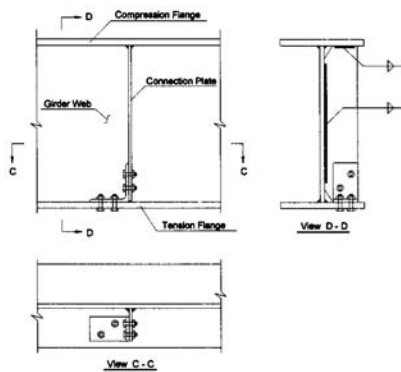
### **2.3.2 Bolted Connection Plate Detail**

If the design stress range at the girder flange exceeds the fatigue resistance of Category C', one of the bolted details from Figure 2-5 may be used to improve fatigue resistance of the

connection to a Category B detail. Option 1 [Figure 2-5(a)] is to bolt a splice plate to the flange and then weld the connection plate to this splice plate. Option 2 [Figure 2-5(b)] is to use a structural angle and bolt one leg to the flange and the other to the connection plate. Notice that only the tension flange needs to be changed to a bolted connection. However, if the other flange also experiences high stress reversal, both should be considered for bolting.



(a) option 1 using splice plate



(b) option 2 using connection angle

**FIGURE 2-5: Connection Plate Bolted to Tension Flange**

### **2.3.3 All Bolted Connection Angle Detail**

If only the plate to girder flange connection is bolted, the plate to girder web fillet weld is still a Category C' detail. Normally this is sufficient because the web is closer to the neutral axis and the stresses developed at the girder web are less than at the flanges. Figure 2-6 shows an all bolted connection angle detail proposed by Nebraska Department of Roads to achieve fatigue Category B for both girder web and flanges. The splice plate bolted to the flange has to be very thick to clear the web-to-flange fillet weld for a plate girder or the transition radius for a rolled beam. The angle has to be coped on one leg, bolted to the girder web, and then welded to the splice plates. This detail is not only expensive, but also complicated to fabricate. It should be used only when a Category B connection is required by design. Otherwise, it is more economical to use other methods such as increasing the web thickness, so that the stress range at the girder web is reduced and the details of Figure 2-5 can still be used.

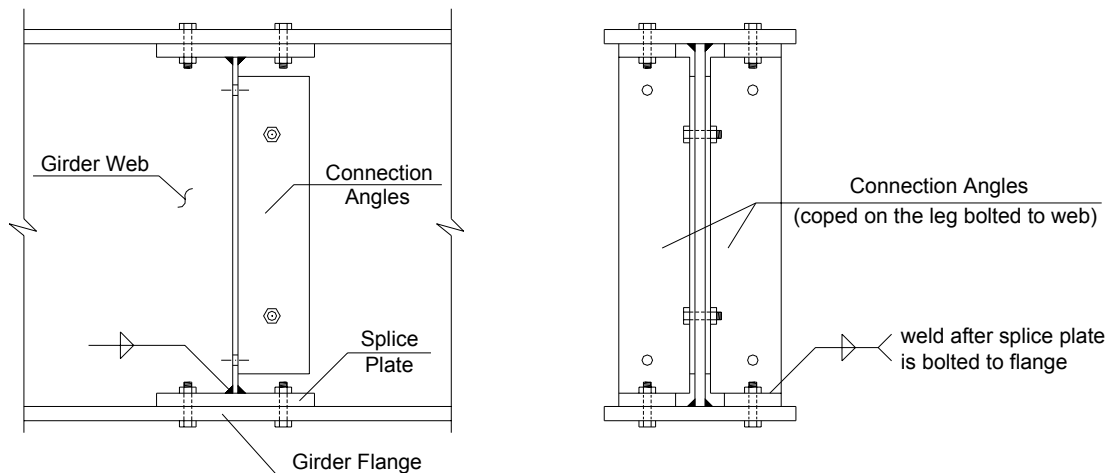


**FIGURE 2-6: Connection Angle Bolted to Both Girder Web and Flanges  
[Nebraska Department of Roads]**

### **2.3.4 Directly Bolted Connection Angle Detail**

The preceding three connection details are designed to provide rigid load paths for

transmitting forces from the transverse members into the longitudinal girders. Either transverse connection plates or angles are used and are welded or bolted to both the web and flanges, so that the girder cross sections are rigid enough to resist the out-of-plane distortion. The detail shown in Figure 2-7, however, is purposely designed to make the girder section more flexible. The diaphragm is shop welded to the connection angles and then field bolted directly to the girder web. No transverse connection plates or angles are used therefore the excessive constraints at the web-to-flange intersections are released. The forces transmitted by the diaphragm are evenly distributed to the girder web by high strength bolts, thus the effect of stress concentration at the web gap is extremely reduced. As long as the open web section between the flange and the diaphragm is deep enough, the secondary stresses developed in this portion of the girder web would not induce fatigue cracks. This detail is used by Illinois DOT for rolled beams or welded plate girders less than 1.05 m (3.5 ft) in depth. The policy of Illinois DOT is to minimize the use of transverse intermediate stiffeners by thickening the girder webs, since this is usually more economical for fabrication. Therefore, web buckling and torsion usually are not problems for these shallow girders. In addition, potential fatigue problems with the connection welds perpendicular to the applied tensile stresses could also be avoided by eliminating transverse stiffeners and connection plates.

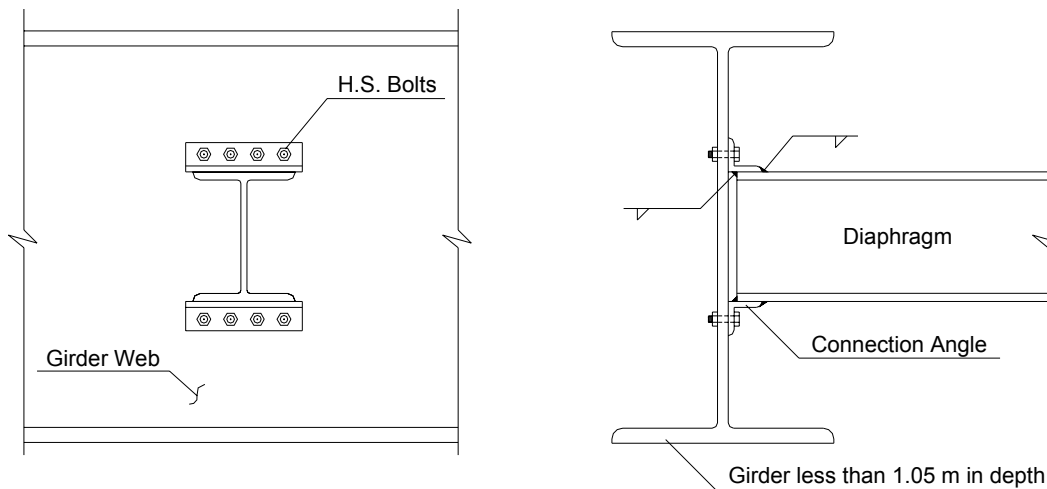


**FIGURE 2-7: Diaphragm bolted directly to girder web [Illinois DOT]**

Miller [1997] studied cost vs. performance of different connection plate details as related to girder flanges, since these are the most commonly used methods for transverse member to girder connections. As summarized in Table 2-1, the cost of a welded connection is much lower than a bolted one, therefore this detail is recommended whenever appropriate. The bolted detail is only necessary in the regions of the flange experiencing high stress ranges, and preferably the option with bolted splice plate should be used because it is cheaper than that with the bolted angle. The expenses for the other two connection types are not available. The all bolted connection angle detail should be much more expensive than both options of the bolted connection plate details. The directly bolted connection angle detail, however, has limitations for girder depth and can not be used for connecting floor-beams or cross frames. Thus these two types of connections are only employed by individual DOTs, whereas the detail of using connection plates, either by welding or bolting to the girder flanges, is widely accepted by different states during normal design practice.

**Table 2-1: Cost Comparison of Different Connection Plate to Girder Flange Connections**

Type of Connection	Illustration	AASHTO Fatigue Detail Category	Cost (per connection)
Welded	Figure 2-4	C'	\$6
Bolted Splice Plate	Figure 2-5, Option 1	B	\$69
Bolted Angle	Figure 2-5, Option 2	B	\$88

## 2.4 Retrofitting Distortion-Induced Fatigue

Numerous retrofit schemes with the objective of repairing distortion-induced fatigue have been proposed during the past 20 years. Some have been used in many actual bridge retrofits, others are still being researched. Although out-of-plane fatigue cracks occur mainly at the small web gap area, the formation of cracking in different bridges varies due to different structural systems and local geometries. The repair methods therefore should also be considered accordingly for different situations. Following is a summary of the techniques that have been previously used for repairing fatigue cracks.

### 2.4.1 Hole Drilling

The traditional repair method shown in Figure 2-8 consists of drilling a hole at the crack tip. The hole diameter is sized to be at least  $2\rho$ , where  $\rho$  is determined by Equation 2-1 [Barsom and Rolfe, 1999].

$$\frac{\Delta K}{\sqrt{\rho}} < 4\sqrt{\sigma_y} \quad (\text{for } \sigma_y \text{ in ksi}) \quad (2-1)$$

$\Delta K$  is the stress intensity factor range and  $\sigma_y$  is the yield strength of the specified steel. This repair is especially effective when arresting crack propagation in low stress regions. However, cracking may recur if the hole size is not large enough or the stress range at the crack location

increases. If this is the case, a supplemental step can be taken either by cold working the hole or by filling the hole with a pretensioned high strength bolt, as will be described in the sections to follow, so that the crack front is restrained from further propagation. Hole drilling is easy to perform and should be used wherever possible even when other repairs are also employed at the same time.

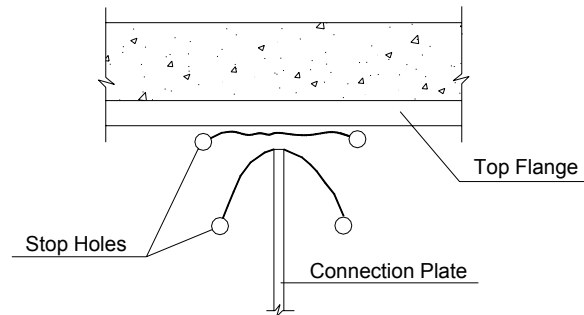


**FIGURE 2-8: Stop Holes Drilled at Crack Ends**

#### **2.4.2 Cold Expansion**

Cold expansion is an approach mostly used in aircraft and railway rails for fatigue life enhancement of rivet or bolt holes. It is often performed by pulling a tapered mandrel, such as used in the split sleeve process [Cannon et al., 1986], through one side of the hole to the other, in order to expand the hole diameter and to produce plastic deformation in the periphery. A zone of residual compressive stresses, both radially and circumferentially, is then formed, so that the initial fatigue resistance of the area surrounding the hole can be greatly improved. As schematically illustrated in Figure 2-9(a) and (b), Cannon et al. [1986] addressed in detail the mechanism of cold expansion as follows:

*“Cold expansion of a hole by forcing an oversize hard tool through it ideally results in material being plastically deformed in the radial and circumferential directions. Following removal of the tool the bulk, still elastic, material surrounding the hole attempts to force the plastically deformed material*

*to return to its original position and the result is that the band of material around the hole experiences compressive residual stresses.”*

However, this method has not been seen in use for the repair of bridge crack details. The stop holes in bridge repairs are often drilled, intercepting the fatigue cracks at the very ends. Since the crack surfaces are stress-free, oversizing the holes by cold expansion would not achieve compressive stresses at the crack vicinity. In other words, the crack introduces a “fuse” so that the compression zone is washed out. As shown in Figure 2-9(c), due to the existence of crack on the hole circumference, the material can be pulled through the hole easily and the crack is forced to open when the expansion force is exerted. Last but not least, the cracks often form at plate-to-plate connection fillet welds, which makes it difficult to accommodate tools (such as puller unit) needed for cold expanding.

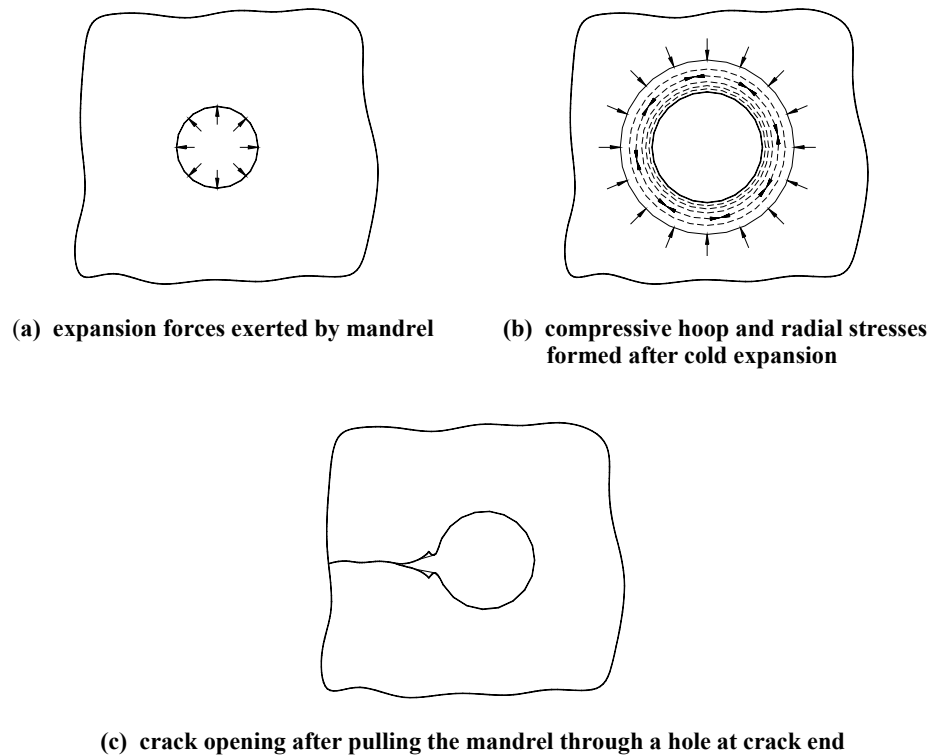


**FIGURE 2-9: Cold Expansion Used to Improve Fatigue Resistance of Drilled Holes**

Though more of a crack prevention method, cold expansion can still be used for shallow crack repair. The crack surface should be gouged out first and ground smooth before cold expansion is to be performed. The repair hole surface should be carefully examined after drilling. If the cracks are found to have propagated deep into the member thickness, cold expansion should not be used at this location.

In most cases, however, installing pretensioned bolts is a more cost-effective and widely used method of strengthening the repair holes, as will be introduced in section 2.4.3.

#### **2.4.3 Filling Drilled Holes with Pretensioned Bolts**

Preloaded high-strength bolts are often used to prevent cracks from reinitiating at the drilled holes. The bolt pretension imposes local compressive stresses perpendicular to the member surface around the hole, creates friction between the faying surfaces, and effectively keeps the crack from recurring. It has been used very often for the repair of out-of-plane fatigue cracking in the web gap region, in concert with the hole drilling approach. That is to say, holes are drilled and then filled with torqued bolts.

#### **2.4.4 Stiffening the Web Gap**

Hole drilling alone can only stop the growth of existing cracks, not the formation of new cracks. Some other measures have to be taken to make the floor-beam (diaphragm, cross-frame) to girder connection either more rigid or more flexible, so that not only are the existing cracks arrested, but also no more cracks develop. If stiffening the web gap is desired, then either a welded or a bolted connection plate detail (Figure 2-10 and 2-11, respectively) may be used.

The welded repair detail (Figure 2-10) is the simplest, but it can only resist stress ranges up to AASHTO fatigue detail Category C'. Though it is easy to perform, the quality of field welding is a concern during the repair. Sandblasting might not be able to clean the repair area

thoroughly before welding, leaving paint, dirt, or other impurities in the root pass between the connection plate and flange. Overhead field welding is usually undesirable, and if it is carried out under traffic, structure vibration could cause micro-cracks to occur in the heat-affected zone during solidification. To achieve good quality welds, it is important that the repair area be properly cleaned and the bridge preferably be closed to traffic prior to the retrofit.

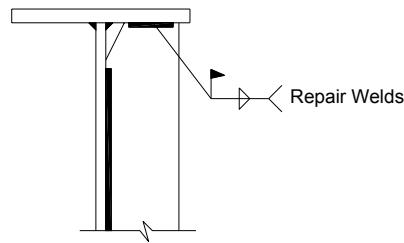


**FIGURE 2-10: Stiffening Web Gap by Welding Connection Plate to Girder Flange**

A bolted detail repair can improve the fatigue resistance to detail Category B. As shown in Figure 2-11(a) and (b), either an angle or a T-section can be used to bolt the connection plate to the girder flange. However, if the repair is performed at the top flange, part of the deck slab has to be removed for bolt installation.

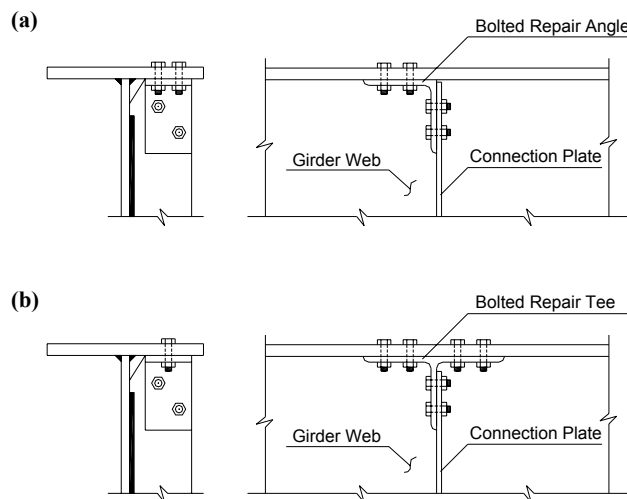


**FIGURE 2-11: Stiffening Web Gap by Bolting Connection Plate to Girder Flange**

### **2.4.5 Bolted Splices**

If large fatigue cracks have developed deep into the girder web, the load-carrying capacity of the main structural member is impaired, which may affect the structural integrity of the bridge. This is especially of concern when the cracks are located in a tension zone. As shown in Figure 2-12, the repair can be performed by removing the original connection plates and bolting reinforcing splices (or coverplates) on both sides of the web. New connection plates also need to be connected rigidly to girder flanges, either by welding or bolting. Thus the cracked web is stiffened and the girder section properties are restored by this retrofit.

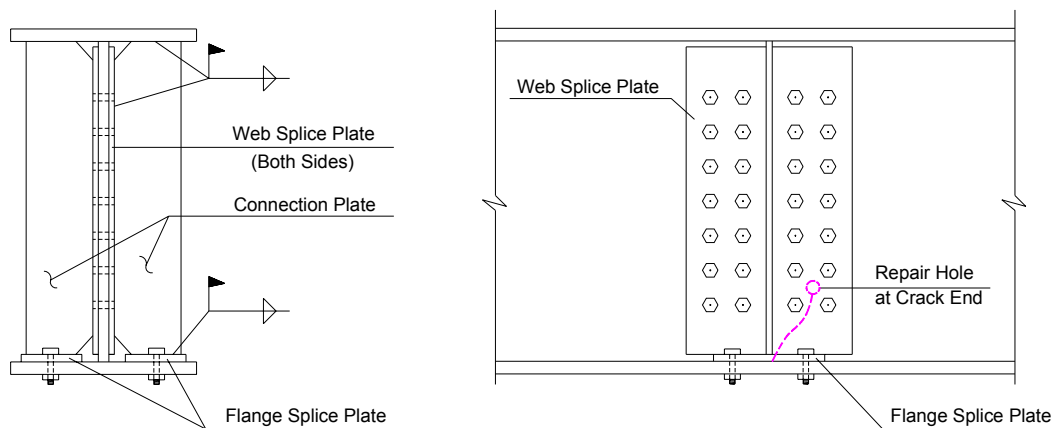


**FIGURE 2-12: Reinforcing Splices Used for Restoring Girder Section Properties**

### **2.4.6 Cutting the Connection Plate Short**

This method was first used in 1980 for the retrofit of the Des Moines (Polk County) Bridge [Fisher, 1984]. It has since been used by Iowa DOT on about 50 two-girder bridges experiencing small web gap cracks. To date, none of these bridges have experienced renewed cracking after the repair. Bridges in other states, such as the Lexington Avenue Bridge (Minnesota) [Dexter & Fisher, 1996], the Poplar Street Bridge Approaches (Illinois) [Koob et al.,

1985], and the Midland County Bridge (Texas) [Keating et al, 1996], were also repaired by employing this approach at the web gap locations. As illustrated in Figure 2-13, part of the connection plate is cut back so that the area of the girder web below the flange is sufficiently flexible to accommodate the out-of-plane rotation. Both field and laboratory tests showed that the secondary stress is significantly reduced after the connection is softened. The cut surface should be well finished to prevent crack reinitiation. To efficiently release the restrained web, a minimum cut-short dimension of 12 in. or 20 times of the web thickness, whichever is larger, is recommended for the connection plate [NCHRP 336, 1990].

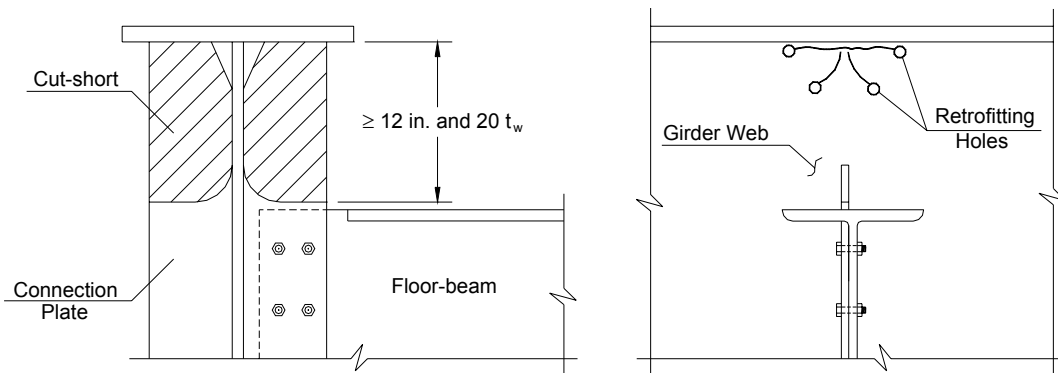


**FIGURE 2-13: Releasing Web Gap Stresses by Cutting the Connection Plate Short**

#### **2.4.7 Diaphragm Removal**

Diaphragms and cross-frames are important during construction because they provide lateral bracing to the girders and stabilize the entire structural system. Once the deck slab is placed, they are no longer needed if construction stability is their only function. Removing interior diaphragms can completely eliminate the secondary stresses that cause fatigue cracks in the girder web, but it can also increase the in-plane bending stresses in the main girders.

Stallings et al. [1996 & 1999] performed field testing of both completely and partially removing

diaphragms of two Alabama DOT bridges. The findings indicated that a 15 % increase in girder stress can reasonably be expected after the repair. Thus it is recommended that repair of out-of-plane fatigue by diaphragm removal only be considered for bridges with rating factors exceeding 1.15.

This repair method should be used with caution since it would increase the girder stresses and decrease the structural resistance against unexpected loading conditions such as earthquake or vehicle collisions. Care should also be taken to make sure that any subsequent removal of the concrete slab considers girder stability.

#### **2.4.8 Bolt Loosening**

Wipf et al. [1998] investigated the effect of repair by loosening the cross-frame-to-connection-plate bolts on five Iowa DOT bridges. Field measurement indicated that the maximum web gap stress ranges at the tested locations were reduced by 25 to 85%, the maximum out-of-plane distortion was reduced by 20 to 88%, and the maximum forces in the cross-frame diagonals were reduced by 73 to 95%. Compared with the diaphragm removal method, bolt loosening has advantages in that it is easier to perform on the site, does not increase girder bending stresses, provides lateral resistance in case of extreme events, and by retightening bolts stabilizes the structure when the deck needs to be replaced.

#### **2.4.9 Diaphragm Repositioning**

This method has been used in the repair of four Minnesota DOT bridges that experienced fatigue cracking in the web gaps close to girder top flange. The performance of the repair is satisfactory to date. As shown schematically in Figure 2-14, diaphragms were originally located near the girder top flanges. To release the constraints at the cracked area, the diaphragms were lowered to rest on the bottom flanges. At a minimum, stress is decreased in the affected areas by

a factor of two. This repair option has similar advantages to bolt loosening when compared to diaphragm removal.

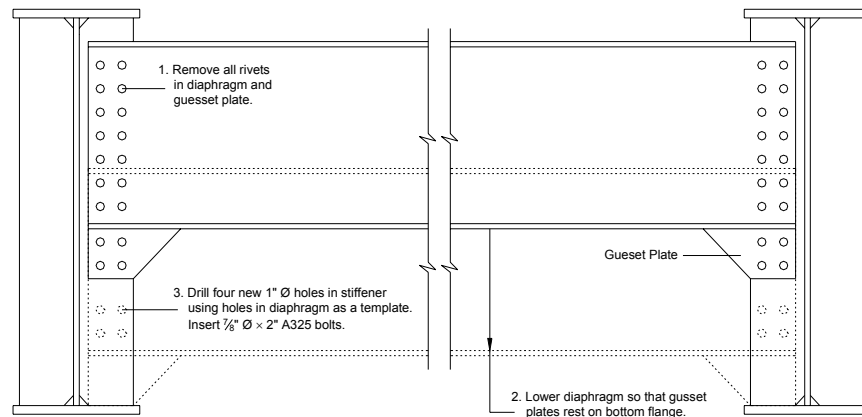


**FIGURE 2-14: Diaphragm Repositioning [Minnesota DOT]**

---

#### **2.4.10 Rewelding**

This repair method usually requires gouging out the existing cracked welds before the new welds are applied; and grinding smooth the rewelded surface after the new welds are filled. Although not recommended by many DOTs due to the expensive labor required to guarantee sound weld quality and smooth surface finishing, it is the last choice if other repair methods cannot effectively stop the crack growth. Gregory et al. [NCHRP 321, 1989] studied the repair of fatigue cracking by welding and provided guidance for achieving good quality welds. The experimental work conducted for this research showed that rewelding, if well performed, could at least restore the original member capacity and provide the same fatigue life as the original shop welds.

---

#### **2.4.11 Peening**

Peening is used to inhibit the cracking process by impacting the toes of weld terminations with pneumatic hammer or automatic shot peening equipment. Residual compressive stresses

are introduced and fatigue resistance can be improved by one category at the treated area. Peening has been used for many cover plate end reinforcement [Welsch, 1990] and is most effective when arresting propagation of shallow cracks [Fisher, 1998]. Figure 2-15 illustrates one of the repair options proposed for the Poplar Street Bridge Approaches [Koob et al., 1985]. In addition to the welded repair, peening is recommended to be applied to the toes on the flange plate along the weld lengths. This implementation enhances the fatigue resistance of the repair welds. Only the weld toe on the flange needs to be peened because this side is perpendicular to the main girder flexural stress range.

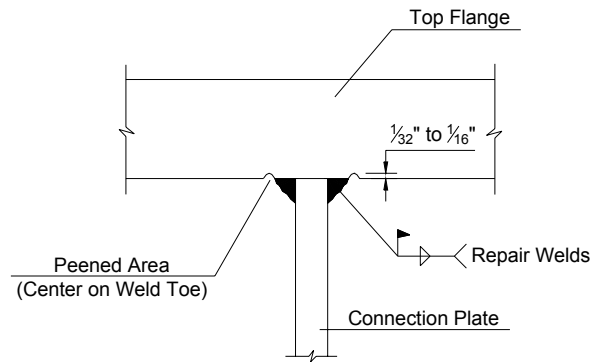


**FIGURE 2-15: Peening Applied in Addition to the Welded Retrofit** [Koob et al., 1985]

#### 2.4.12 Gas Tungsten Arc Remelting

The gas tungsten arc process (GTA), also referred to as tungsten inert gas process (TIG), involves remelting base metal and fillet weld by moving the tungsten electrode along the weld toe. Small cracks, if exist, are therefore removed by melted weld and the weld quality can be improved upon solidification. This method removes micro-discontinuities and reduces the stress concentration at the weld toe. Fatigue resistance can be increased by one category after the repair [Fisher, 1998]. However, remelting is difficult to perform for in-service bridges due to vibration.

#### **2.4.13 Ultrasonic Impact Treatment**

The ultrasonic impact treatment (UIT) is a former Russian technology first used in 1972 for the Soviet Nuclear Naval program on the weld improvement of submarine hulls. It was introduced to the United States during the late 1990s and has since then proved successful in fatigue enhancement of welded details of highway and railway bridges. The UIT equipment uses ultrasonic transducers to convert electrical harmonic vibrations to physical impulses and transfers energy to the weld surfaces through oscillating steel pins. The treatment introduces compressive residual stresses at the weld toes, which leads to the relief of stress concentration and the improvement of fatigue resistance at the welded details. Takamori & Fisher [2000] conducted laboratory tests of UIT treatment on steel girder cover plates and transverse connection stiffeners. The results indicated a minimum improvement of fatigue resistance from Category E' to D at cover plate end welds and from Category C' to B at connection stiffener to web and flange welds. Same fatigue enhancement of transverse stiffener weld toes was also observed from the laboratory studies carried out by Wright [1996]. Uppal et al. [2002] performed UIT testing on vertical stiffener welds of a railway bridge subject to heavy axle loads. The treatment was found able to penetrate the entire web thickness and reduce the residual tensile stresses at the weld toes by at least 8 ksi. Other research findings of this technology were reported by Statnikov [1997], Haagensen et al. [1998], and Fisher et al. [2001]. All these studies showed significantly improved performance of weld joints due to UIT treatment.

Conventional post weld treatment techniques such as peening and GTA remelting can also improve the weld toe characteristics, but are usually labor intensive and less environmentally beneficial. For example, traditional peening procedure operates at a low frequency between 50~100 Hz, which requires considerable effort from the operator in order to

keep the tool steadily along the weld toe line. The procedure is usually time-consuming, and significant vibration and noise from the instrument expose the operator to an uncomfortable working environment. The UIT method operates at a high frequency of 27 kHz with much lower level of vibration and noise. The equipment is lightweight and user friendly, so it is easy to operate during field applications. When applied to the same weld details, UIT costs significantly less than the traditional methods. It only takes a few minutes to complete a single treatment and requires no traffic disruption. The treated areas may also be able to develop a protective layer that provides resistance to corrosion and abrasion. Due to these advantages, UIT has been used more frequently in recent years as a replacement of conventional peening and GTA remelting for bridge maintenance and retrofit.

#### **2.4.14 Using Composite Materials**

Bassetti et al. [2000] studied retrofitting fatigue cracks by using newly developed composite materials such as prestressed carbon fiber laminates. Prestressed Carbon Fiber Reinforced Polymers (CFRP) strips oriented perpendicular to the crack faces could slow down or even completely stop crack propagation. Experimental testing of a retired riveted railway bridge is currently underway in Switzerland. The application of this material is still in the research phase.

### **2.5 Stay Alert to Unforeseen Cracking and Repair Failure**

In some occasional cases, a presumably crack-free detail can become prone to fatigue when subjected to unexpected local constraints; or, a seemingly effective retrofit may turn out to be unsuccessful after a certain period of time in service. Cracks can reinitiate from the original locations, propagate further into the structural members, or develop in the newly repaired details. Awareness of these unanticipated cracking conditions is important to bridge engineers and

inspectors as demonstrated by the following two cases.

### **2.5.1 Bridges over I-10, Phoenix, Arizona**

The diaphragm-to-girder connection plate in these bridges was welded to both girder web and top flange as per design requirement. However, as shown in Figure 2-16(a), over 60 locations were found with diagonal cracks that initiated from the top of the connection-plate-to-web welds, and a few locations also developed cracks along the horizontal connection-plate-to-top-flange welds [Stallings, 2001]. Apparently, unpredicted high-magnitude secondary stresses that are not considered by the normal design process had occurred at the diaphragm-girder connections and caused fatigue cracking in these bridges.

The current design specifications simply require that a rigid connection-plate-to-flange attachment be used to prevent distortion-induced fatigue in web gaps. Thus from a designer's point of view, the secondary stresses in the web gaps have already been taken care of by employing this rigid connection detail, and whether a welded (Category C') or a bolted (Category B) connection should be used depends upon the girder flange in-plane flexural stresses, which are stresses actually caused by load-induced fatigue. However, what bridge engineers always neglect is the fact that the secondary stresses can develop at places other than web gaps and can develop even when the connection plate is welded or bolted to the girder flanges. These stresses are usually insignificant and not taken into account in fatigue examinations. However, in cases such as these Arizona DOT bridges, due to the special structural interaction at the diaphragm-girder connection, the secondary stresses could be much higher than the primary girder flange stresses, and could be located in components other than flanges or webs, such as in connection stiffeners. These distortion-induced stresses are not quantified by the current design code and could overstress the welds or plates even if the main

girder stresses are satisfactory.

Repair to the uncracked connection plates in those bridges was performed by bolt removal, as shown in Figure 2-16(b), to reduce stress ranges at the critical details; while the cracked locations were repaired by removing a portion of the connection plate so that the constraints at the top connection plate end were relaxed.

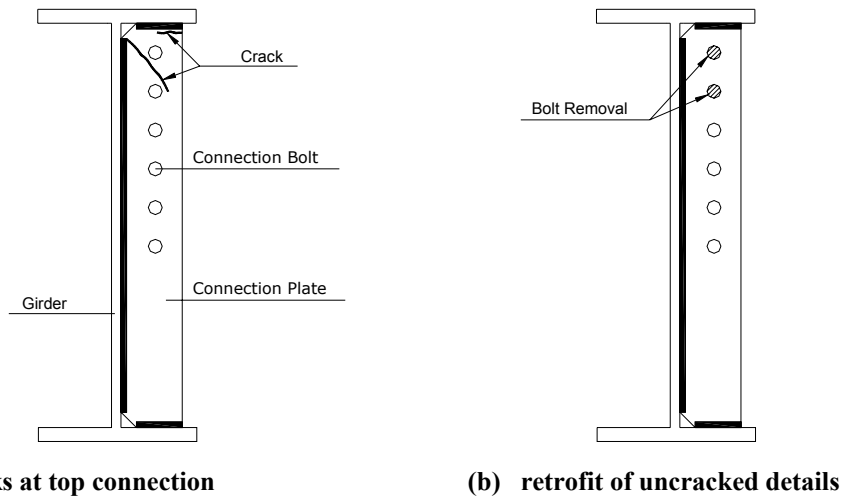
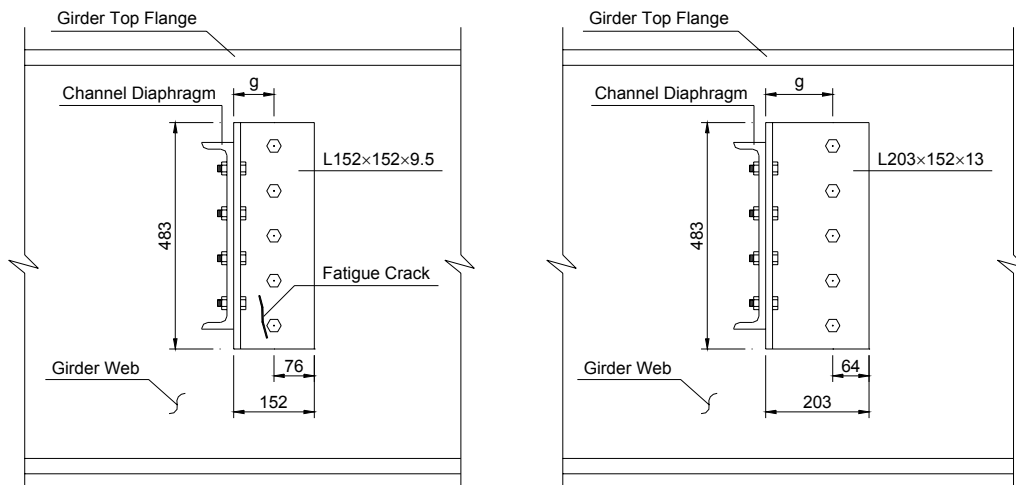


**FIGURE 2-16: Connection Plate Detail used by Bridges over I-10 in Phoenix, Arizona**  
[Stallings, 2001]

### 2.5.2 Bridges in Birmingham, Alabama

When web gap fatigue cracking was identified in many Alabama DOT multi-girder steel bridges, repairs were conducted by replacing the transverse connection stiffeners with bolted connection angles, as shown in Figure 2-17(a). The diaphragms were also lowered to a level that allows flexible out-of-plane movement of the girder web. However, new crack development was soon observed in the replacement angles due to bending of the angle leg bolted to the girder web. Cracks often occurred from the bottom connection bolt, on the front angle face underneath the washer or bolt head, and then propagated both upward and downward through the thickness. Both the field investigation [Cousins et al., 1998] and laboratory study [Cousins & Stallings,

1998] carried out later indicated that the repair angles were unexpectedly subjected to high stress ranges and could only sustain a service life of 1 or 2 years. The new retrofit method recommended by the researchers was to use repair angles with a longer gauge length, as shown in Figure 2-17(b).



\* Note: All dimensions are in (mm).

(a) connection angle with short gage size      (b) connection angle with long gage size

**FIGURE 2-17: Connection Angle used for Web Gap Crack Repair in the Alabama DOT Bridges [Cousins et al., 1998; Cousins & Stallings, 1998]**

Other unsuccessful repairs such as crack extension through the repair holes were also seen quite often during bridge inspections. Retrofitting bridge fatigue thus is no easy task and needs careful consideration for each repair procedure to be carried out properly. If an unknown or unfamiliar crack scenario is encountered, it is important that experimental or theoretical stress investigations be performed before an appropriate retrofit plan is determined. Periodic inspections are also needed even after the bridge has been repaired.

## Chapter 3

### Fatigue Performance Evaluation

This chapter presents the fatigue life and stress range evaluation procedures used in the study. Loading is specified according to the AASHTO *Guide Specifications for Fatigue Evaluation of Existing Steel Bridges* [1990]. The experienced fatigue life of the crack details is estimated based on knowledge of fracture mechanics. The performance and remaining service life of the repair details are evaluated by following fatigue design criteria of the current AASHTO *LRFD Bridge Design Specifications* [1998].

#### 3.1 Loading

The single parameter that is most important to bridge fatigue evaluation is the stress range caused by truck loading. Based on the AASHTO *Guide Specifications for Fatigue Evaluation of Existing Steel Bridges* [1990], an HS15 fatigue truck with gross weight of 54 Kips is specified as loading for the finite element investigations of this research. Assuming the road surfaces are smooth, an additional 10% increment of individual wheel load is considered during the analysis to account for the impact effect [AASHTO Guide Specifications, 1990]. The spacing between the rear two axles is kept constant at 30 ft according to the Guide Specifications and the KDOT rating requirement.

In terms of wheel load lateral distribution, the transverse position of the truck across the roadway width can cause different stress magnitude in a structural component. The NCHRP Report 299 [1987] recommended that a single fatigue truck be positioned at the center of the shoulder lane for fatigue evaluation. Although a truck located in other traffic lanes sometimes causes much higher stress in the structural member under investigation, this is not considered as the typical condition for fatigue since most of the truck traffic occurs in the shoulder lane. The

AASHTO Guide Specifications [1990] also require that this truck positioning be used if the finite element method is employed during fatigue analysis. Therefore, this research follows the preceding two references and studies the stress variation of bridge details by moving the HS15 fatigue truck along the centerline of the shoulder lane.

### **3.2 Crack Growth Characteristics Defined by Fracture Mechanics**

The fatigue life evaluation procedures provided by the AASHTO Guide Specifications [1990] and the NCHRP Report 299 [1987] are used for the intact members subjected to primary stresses. For the conditions of secondary bending and cracked or repaired members, these procedures are not applicable. Therefore, fracture mechanics principles are used in this research to assess the consumed fatigue life of the out-of-plane crack details.

#### **3.2.1 Stress Intensity Factor $K_I$**

Linear-elastic fracture mechanics (LEFM) uses the concept of stress intensity factor,  $K_I$ , to describe the intensity of the stress field ahead of a sharp crack contained in any structural component. It has a general expression of

$$K_I = \sigma \sqrt{\pi a} F \quad (3-1)$$

where  $\sigma$  is the normal stress away from the crack,  $a$  is the crack size, and  $F$  is the geometry factor. The unique aspect of the stress intensity factor, as can be observed from Equation 3-1, is that it correlates the local stress concentration to the remotely applied global stress. Figure 3-1 gives  $K_I$  expressions of the three most often seen crack geometries.

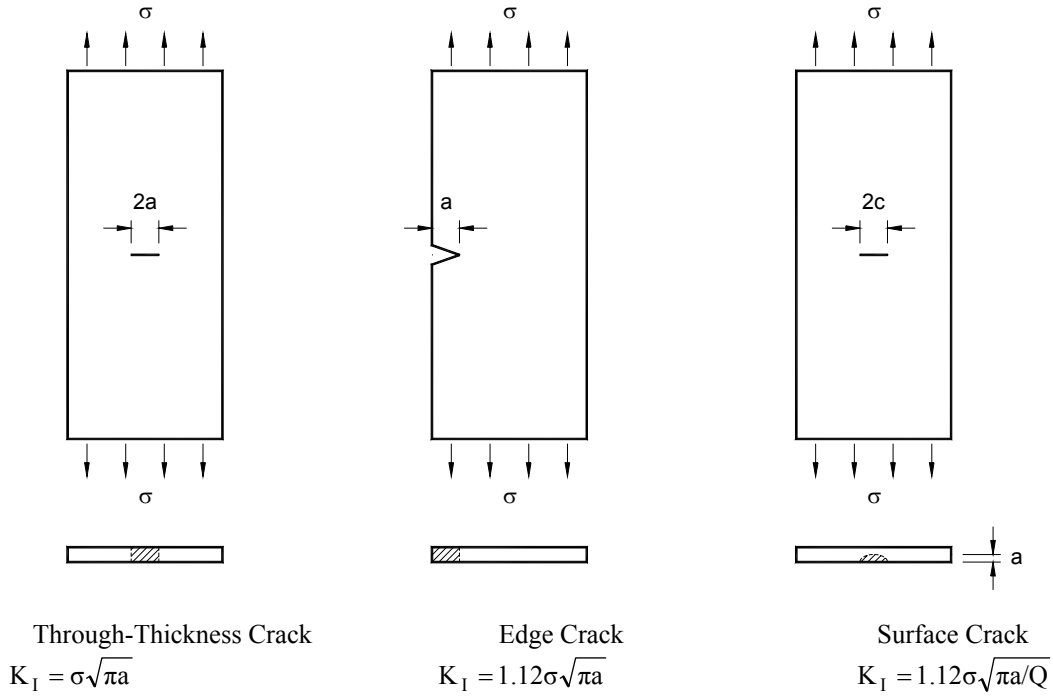


**FIGURE 3-1:  $K_I$  Values for Three Basic Crack Geometries [Barsom and Rolfe, 1999]**

Based on the theory of linear elasticity, when a certain crack size is introduced into a structural component, as shown in Figure 3-2, the stresses and strains in front of the crack are extremely large, changing proportionally to  $1/\sqrt{r}$ , where  $r$  is the distance from the crack tip. In reality, however, plastic deformation occurs in the vicinity of the crack tip and a region of yielding forms. Hence the infinite stress never occurs. The region  $2r_{\text{yield}}$  within which the material yields is called the plastic zone. If the plastic zone is sufficiently small, LEFM theory is still applicable in a region outside of it, called the  $K$ -field, or the region of  $K$ -dominance, as illustrated in Figure 3-3 [Dowling, 1999]. For a large plastic zone, however, this  $K$ -field will be “blown out” and the elastic stress field equations will not be effective near the crack tip. Therefore, when defining the stress intensity factor  $K_I$ , it is important that this plastic zone be small enough so that LEFM theory can be applied.

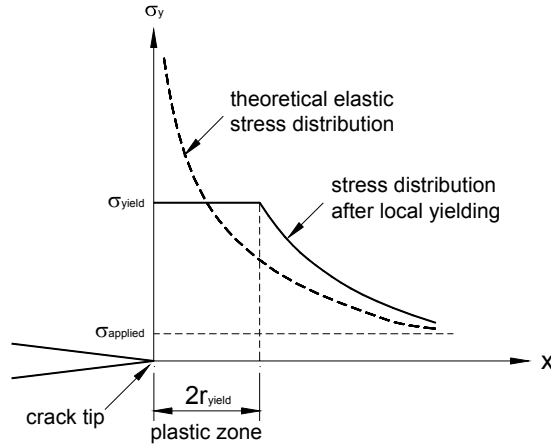


**FIGURE 3-2: Distribution of  $\sigma_y$  Stress Component at the Crack Tip Region**  
[Barsom and Rolfe, 1999]

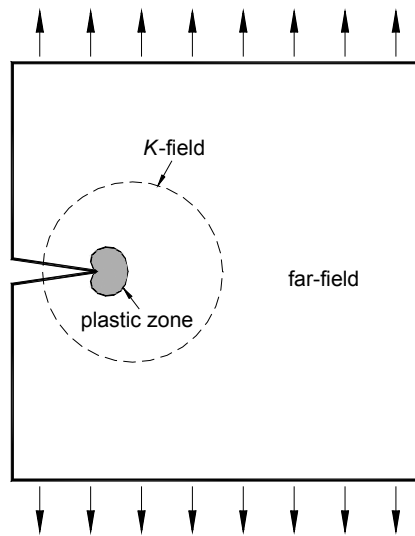


**FIGURE 3-3:  $K$ -field Outside of the Plastic Zone** [Dowling, 1999]

The critical stress intensity factor, or the fracture toughness,  $K_{IC}$ , is the upper limit of the stress intensity factor  $K_I$ . It is a material property varying in accordance with the service temperature, the loading rate, and the constraint of the crack detail. The fracture mechanics design criteria require that  $K_I$  should not exceed  $K_{IC}$  for structure members to be fracture-

resistant. Figure 3-4 illustrates the relationship between the three governing factors for control of brittle fracture: the applied stress  $\sigma$ , the crack size  $a$ , and the material toughness  $K_{IC}$ .

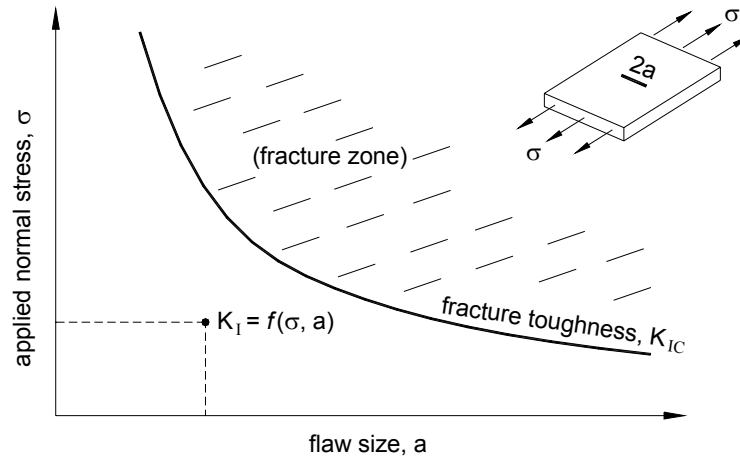


**FIGURE 3-4: Schematic Relation among Stress, Flaw Size, and Material Toughness**  
[Barsom & Rolfe, 1999]

### 3.2.2 Fatigue Crack Propagation

For structural components subjected to fluctuating fatigue stress,  $\Delta\sigma$ , the appropriate fracture mechanics parameter used for crack growth evaluation is correspondingly the stress intensity range,  $\Delta K$ . The fatigue crack propagation of normal structural steels and weldments is described by the curve shown in Figure 3-5. The behavior can be divided into three regions and idealized by three straight lines on a log-log plot. Region I represents a crack growth threshold. The stress intensity range corresponding to the lower left line is a threshold value designated as  $\Delta K_{th}$ . If  $\Delta K$  is lower than  $\Delta K_{th}$ , crack growth does not occur. However, in most existing bridge weldments, initial flaw sizes are large enough so that this threshold is exceeded and the fatigue crack propagation falls into the second part of the curve. For ferrite-pearlite steels, the crack growth rate of Region II can be expressed by the following formula [Barsom & Rolfe, 1999]:

$$\frac{da}{dN} = 3.6 \times 10^{-10} \Delta K^{3.0} \quad (3-2)$$

where:  $a$  = crack size, in.

$N$  = fatigue life, number of cycles.

$\frac{da}{dN}$  = the change in crack length per stress cycle.

$\Delta K$  = stress intensity range, ksi $\sqrt{\text{in.}}$ .

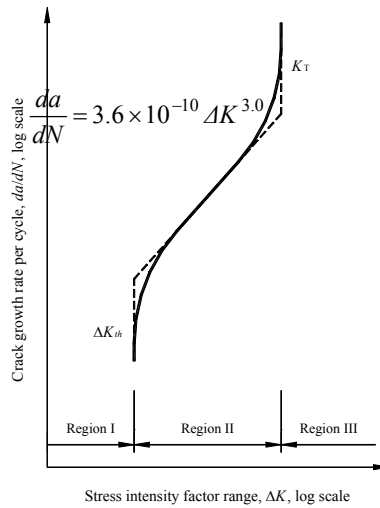


**FIGURE 3-5: Fatigue Crack Growth of Typical Structural Steels [Barsom & Rolfe, 1999]**

The third portion of the curve shows an extremely rapid crack propagation occurring at the end of the fatigue life. The vertical straight line to the upper right indicates an infinite crack growth rate. The level of  $\Delta K$  corresponding to Region III has not been well established.

However, specimens tested under zero-to-tension loading show that the transition from Region II to Region III occurs at a constant value of crack tip opening displacement, CTOD, or  $\delta_T$ , of 0.0016 in., and has a relationship of [Barsom & Rolfe, 1999]

$$\delta_T = \frac{K_T^2}{E \sigma_{flow}} = 1.6 \times 10^{-3} \text{ in.} \quad (3-3)$$

where:  $K_T$  = stress intensity range value at the onset of fatigue crack growth acceleration, corresponding to stress ratio

$$R = \sigma_{min} / \sigma_{max} = 0.$$

$E$  = Young's modulus, 29000 ksi for steel materials.

$\sigma_{flow}$  = flow stress, which is the average of the yield and tensile strengths.

It should be noted that this correlation is obtained from zero-to-tension loading condition, that is,  $K_T = \Delta K = K_{max}$ , therefore Equation 3-3 is an approximate method and should be used with caution when the stress ratio is not equal to zero. For structural steel, Equation 3-3 can be rewritten as [NCHRP 299, 1987]

$$K_T = \sqrt{\delta_T E \sigma_{flow}} = 7 \sqrt{\frac{\sigma_y + \sigma_t}{2}} \quad (3-4)$$

where  $\sigma_y$  is the yield strength and  $\sigma_t$  is the tensile strength, both in ksi.

### **3.2.3 Fatigue Life Evaluation**

From Figure 3-5 it can be concluded that the fatigue life of a crack detail is spent mostly in Region II. To calculate the total number of cycles for crack propagation, Equation 3-2 is rearranged as shown in Equation 3-5 by integrating the crack growth expression from the initial size,  $a_{initial}$ , to the critical size,  $a_{critical}$ .

$$N = \int dN = \int_{a_{initial}}^{a_{critical}} \frac{da}{3.6 \times 10^{-10} \Delta K^{3.0}} \quad (3-5)$$

However, for many crack configurations, the stress intensity range  $\Delta K$  is not a simple function of crack size  $a$ , and mathematic difficulties can be encountered for the direct integration of Equation 3-5. Thus numeric integration is often used to accumulate the stress cycles  $\Delta N$  consumed by each crack growth increment  $\Delta a$ . The case study of the Arkansas River Bridge presented in Chapter 5 will illustrate in detail how the aforementioned procedures are used for the estimation of the expended fatigue life of crack details. Only one of the five case bridges is

analyzed for the experienced fatigue cycles at the crack locations, because this is of less significance as compared to the fatigue evaluation of the retrofit details.

### **3.3 AASHTO LRFD Fatigue Design Provisions**

As already mentioned, the procedures for life prediction of bridge post-retrofit details are not addressed by either the AASHTO Guide Specifications for Fatigue Evaluation of Existing Steel Bridges [1990] or the NCHRP Report 299: Fatigue Evaluation Procedures for Steel Bridges [1987]. Although the bridges have been in service for many years, the repaired details should be considered more appropriately as newly constructed. Therefore, the fatigue provisions of the current AASHTO LRFD Bridge Design Specifications [1998] are adopted in this research to evaluate the fatigue performance of different repair methods. This section reviews the design criteria of the AASHTO LRFD fatigue limit state, explains their applicability to the process of repair evaluation, and introduces the background for the development of the infinite life concept.

#### **3.3.1 AASHTO Fatigue Detail Categories**

In the current AASHTO LRFD Specifications [1998], bridge components and details are grouped into eight categories according to their resistance against load-induced fatigue. In general, Category A refers to plain members; B is for base metal or welded connections in built-up members without attachments, usually with the welds oriented parallel to the direction of applied stress; C applies to fillet or groove welded attachments less than 2 in. long or with transition radius between 6 in. and 24 in.; D is assigned to welding of attachments longer than 2 in. but shorter than 4 in., or with 2~6 in. transition radius, or with unequal plate thickness; E includes coverplate end weldments, attachments with longer than 4 in. welds, or with less than 2 in. transition radius, or with end welds not ground smooth. As shown in Figure 3-6, for each detail category, the  $S-N$  curve indicates two types of fatigue behavior: a finite life represented by

the solid line and an infinite life represented by the dashed line. For any point on the curve, the number of loading cycles is the fatigue life that the detail can sustain prior to crack initiation, and the stress range is the fatigue resistance associated with that level of design life. The larger the required number of repeated loading, the lower the allowable stress range. The stress range corresponding to the horizontal dashed line is the constant amplitude fatigue threshold,  $(\Delta F)_{TH}$ , below which longer than  $2 \times 10^6$  cycles of fatigue life will take place for all detail categories.

When the stress range is below  $\frac{1}{2}(\Delta F)_{TH}$ , fatigue crack propagation would not occur and an infinite number of loading cycles can be expected.

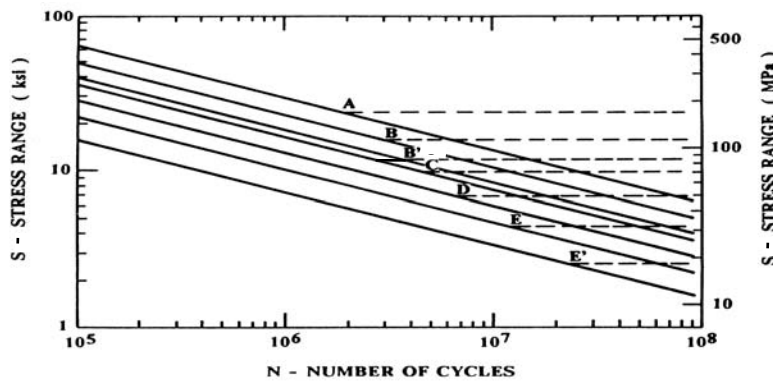


**FIGURE 3-6: S-N Curves for AASHTO Fatigue Detail Categories [AASHTO LRFD, 1998]**

### 3.3.2 Applicability to Repair Evaluation

In terms of design, the relationship between fatigue load and resistance at any detail should satisfy Equation 3-6 [AASHTO LRFD Equation C6.6.1.2.2-1, 1998]

$$\eta \gamma (\Delta f) \leq \phi (\Delta F)_n \quad (3-6)$$

where:  $\eta$  = load modification factor, 1.0 for fatigue limit state.

$\gamma$  = load factor, 0.75 for fatigue limit state.

$(\Delta f)$  = live load stress range due to HS20 design truck, ksi.

$\phi$  = resistance factor, 1.0 for fatigue limit state.

$(\Delta F)_n$  = nominal fatigue resistance, ksi.

Note that the live load caused by the HS20 design truck (72 Kips) multiplying by 0.75 load factor is equivalent to that caused by the HS15 fatigue truck (54 Kips). The truck loading used for the fatigue calculation is thus consistent between the LRFD Specifications [AASHTO, 1998] and the Guide Specifications [AASHTO, 1990].

However, there are also discrepancies between the two specifications, as would be expected since the former is aimed at design of new bridges while the latter is used for the evaluation of old bridges. The first difference can be seen in the consideration of the effect due to dynamic impact. The LRFD Specifications assign an increase of 15% to the truck gross weight for fatigue and fracture limit states design [AASHTO LRFD Table 3.6.2.1-1, 1998], while the Guide Specifications assign an increase of 10% to 30%, depending on the roughness of the road surfaces [AASHTO Guide Specifications 2.4, 1990]. This research is focused on the cracking and repair evaluation of existing steel bridges, not the design of new bridges, so the provisions of the Guide Specifications are followed. Assuming smooth road surfaces, a 10% increase is applied to the fatigue truck for loading of the finite element models.

The second disparity between the two specifications is the lateral load distribution. The Guide Specifications allow a 0.96 reduction factor if a rigorous method, such as the finite element method, is used for the evaluation, and when a single fatigue truck is moved along the centerline of the shoulder traffic lane [AASHTO Guide Specifications 2.6 Alternative 2, 1990]. However, this factor is conservatively not used in this research. For the LRFD Specifications, no reduction factor is specified if refined analysis methods (including finite element method) are

used, but the single design truck is required to be positioned transversely and longitudinally to obtain the maximum stress range at the detail under consideration, regardless of the position of traffic or design lanes on the deck [AASHTO LRFD 3.6.1.4.3a, 1998]. This is explained in the Commentary of the LRFD Specifications as follows: *“If it were assured that the traffic lanes would remain as they are indicated at the opening of the bridge throughout its entire service life, it would be more appropriate to place the truck at the center of the traffic lane which produces maximum stress range in the detail under consideration. But because future traffic patterns on the bridge are uncertain and in the interest of minimizing the number of calculations required of the designer, the position of the truck is made independent of the location of both the traffic lanes and the design lanes”* [AASHTO LRFD C3.6.1.4.3a, 1998]. Since the LRFD Specifications are used in this research for the evaluation of bridges that are about 30 to 50 years old, existing conditions in the bridges need to be considered. For all the five bridges under investigation, the traffic lanes are already determined and will remain unchanged in the future. When defining the single-lane average daily truck traffic ( $ADTT_{SL}$ ), the LRFD Specifications also agree that *“On a typical bridge with no nearby entrance/exit ramps, the shoulder lane carries most of the truck traffic”* [AASHTO LRFD C3.6.1.4.2, 1998]. Therefore the use of shoulder lane as the most heavily traveled lane in the bridge by a single truck is also acceptable for the fatigue analysis using the LRFD Specifications. The two specifications are in agreement on this point when the actual traffic condition of the bridge is considered.

So the load term on the left side of Equation 3-6 can be replaced by the stress range resulting from the loading condition specified in section 3.1. To be consistent with the stress range designation used in the following chapters, all the parameters on the load side of Equation 3-6 are combined and represented by  $\Delta\sigma$ . Equation 3-6 can then be rewritten as

$$\Delta\sigma \leq (\Delta F)_n \quad (3-7)$$

where  $\Delta\sigma$  is the stress range that will be calculated by finite element analysis at the repaired details. The right side term, the nominal fatigue resistance, has an expression as shown by Equation 3-8 [AASHTO LRFD Equation 6.6.1.2.5-1, 1998] and is graphically illustrated in Figure 3-6 [AASHTO LRFD Figure C.6.6.1.2.5-1, 1998].

$$(\Delta F)_n = \left( \frac{A}{N} \right)^{\frac{1}{3}} \geq \frac{1}{2} (\Delta F)_{TH} \quad (3-8)$$

where:  $A$  = detail category constant, listed in Table 3-1.

$N = (365)(75)n(ADTT)_{SL}$ , the number of stress range cycles targeting 75 years design life.

$n$  = number of stress range cycles per truck passage, as shown in Table 3-2.

$(ADTT)_{SL}$  = the number of trucks per day in a single-lane averaged over the design life.

$(\Delta F)_{TH}$  = constant amplitude fatigue threshold, listed in Table 3-1.

**TABLE 3-1: Detail Category Constant A and Fatigue Thresholds  $(\Delta F)_{TH}$**

Detail Category	Constant, $A^a$ ( $\times 10^8$ ksi <sup>3</sup> )	Fatigue Threshold, $(\Delta F)_{TH}^b$ (ksi)
A	250.0	24.0
B	120.0	16.0
B'	61.0	12.0
C	44.0	10.0
C'	44.0	12.0
D	22.0	7.0
E	11.0	4.5
E'	3.9	2.6

Note: <sup>a</sup>From AASHTO LRFD [1998] Table 6.6.1.2.5-1.

<sup>b</sup>From AASHTO LRFD [1998] Table 6.6.1.2.5-3.

**Table 3-2 Cycles per Truck Passage,  $n^a$**

Longitudinal Members	Span Length	
	> 40 ft	≤ 40 ft
Simple Span Girders	1.0	2.0
Continuous Girders		
1. near interior support <sup>b</sup>	1.5	2.0
2. elsewhere	1.0	2.0
Cantilever Girders	5.0	
Trusses	1.0	
	Spacing	
Transverse Members	> 20 ft	≤ 20 ft
	1.0	2.0

Note: <sup>a</sup>From AASHTO LRFD [1998] Table 6.6.1.2.5-2.

<sup>b</sup>A distance equal to one-tenth the span on each side of an interior support is considered to be near the support.

The number  $N$  in Equation 3-8 can be explained as the total number of stress range cycles that would occur in the entire bridge life. The design life considered during the overall development of the LRFD Specifications is 75 years. However, for a repaired detail in an existing bridge, such a long life may not be easy to reach. If that is the case, Equation 3-7 would not be satisfied, but the remaining service life can be calculated by solving Equation 3-8 for  $N$  to yield

$$N = \frac{A}{(\Delta\sigma)_n^3} \quad (3-9)$$

Depending on the future traffic flow of the bridge, the number of years that the repaired detail would sustain,  $N_Y$ , can be computed as

$$N_Y = \frac{N}{(365)n(ADTT)_{SL}} \quad (3-10)$$

Based on the foregoing discussion, the AASHTO LRFD Specifications [1998] will be

used in the study of all five case bridges to evaluate the stress and remaining service life of the bridge repair details. The method presented in this section is based on careful comparison between the design criteria and the existing bridge conditions, and should not be applied arbitrarily to the repair evaluation of other bridges except when the same examination procedures are carried out.

Most of the provisions mentioned in this section, from either the *LRFD Bridge Design Specifications* [1998] or the *Guide Specifications for Fatigue Evaluation of Existing Steel Bridges* [1990], are declared to be only applicable to conditions of load-induced fatigue. This is because the mathematical determination of secondary stress is usually not required by the codes and is not possible to be achieved by using normal design or evaluation procedures as for primary stress. However, as long as the detail under consideration has already been classified as one of the fatigue detail categories and its stress condition is known, for example, from finite element analysis, the evaluation procedures stated above should also be applicable to the distortion-induced fatigue.

### **3.3.3 Infinite Life Fatigue Limit**

The  $\frac{1}{2}(\Delta F)_{TH}$  term in Equation 3-8 represents the fatigue resistance corresponding to infinite life. The LRFD Specifications describe the 0.5 factor as a consideration for higher traffic volume bridges, which requires that the maximum stress range be less than the constant amplitude fatigue threshold. The maximum stress range is assumed to be twice the live load stress range caused by single fatigue truck [AASHTO LRFD C6.6.1.2.5, 1998]. Instead of multiplying by a factor of 2 on the load side of Equation 3-8, a 0.5 factor is applied on the resistance side to take into account the possible occurrence of heavy truck loading. Since the fatigue live load stress range is calculated by using an HS20 design truck with 0.75 load factor,

or an effective HS15 truck, the LRFD Specifications actually imply the maximum stress range caused by an HS30 truck.

The constant amplitude fatigue threshold in the *LRFD Bridge Design Specifications* [1998] is equal to the allowable fatigue stress range for over 2 million cycles on redundant load path structures in the *Standard Specifications for Highway Bridges* [1996]. The 2 million cycles was assumed to be infinite life condition in the early era of fatigue design when available test data were mainly from small plate specimens. This was later found to be unconservative when compared with results obtained from full-size experiments. As shown in Figure 3-6, except for Category A base metal detail, 2 million cycles of loading does not correspond to the fatigue limit or crack growth threshold for other structural details.

The  $S-N$  curves in Figure 3-6 are derived from a large number of full-scale fatigue test data with a 97.5% survival limit and are based on constant amplitude loading [Dexter and Fisher, 2000]. Laboratory experiments indicate that if a constant magnitude of repeated loading below  $(\Delta F)_{TH}$  is applied, noticeable cracking would not occur and the test detail can carry unlimited number of load cycles. However, in reality the bridges are subjected to variable amplitude traffic loading, thus stress ranges caused by actual trucks crossing the bridge change continuously and randomly. Experimental results obtained from full-scale variable amplitude fatigue tests show that if 0.01% of the stress ranges exceed  $(\Delta F)_{TH}$ , fatigue cracking can still occur [NCHRP 354, 1993]. This observation can be explained schematically by Figure 3-7.  $S_e$  is the effective stress range developed based on the cubic root of the mean cube (rmc) of the stress ranges:

$$S_e = [\sum (n_i / N_{total}) S_i^3]^{1/3} \quad (3-11)$$

where  $n_i$  is the number of cycles for stress range  $S_i$ , and  $N_{total}$  is the total number of stress range cycles in the distribution.  $S_{max}$  refers to the fatigue limit state stress range associated with an

exceedance probability of 0.01%. Obviously Case 1 is in the finite life regime and Case 3 is in the infinite life regime. For Case 2, the effective stress range is below the constant amplitude fatigue threshold  $(\Delta F)_{TH}$ , but more than 0.01% of the stress ranges are over  $(\Delta F)_{TH}$ , thus an infinite life is impossible.

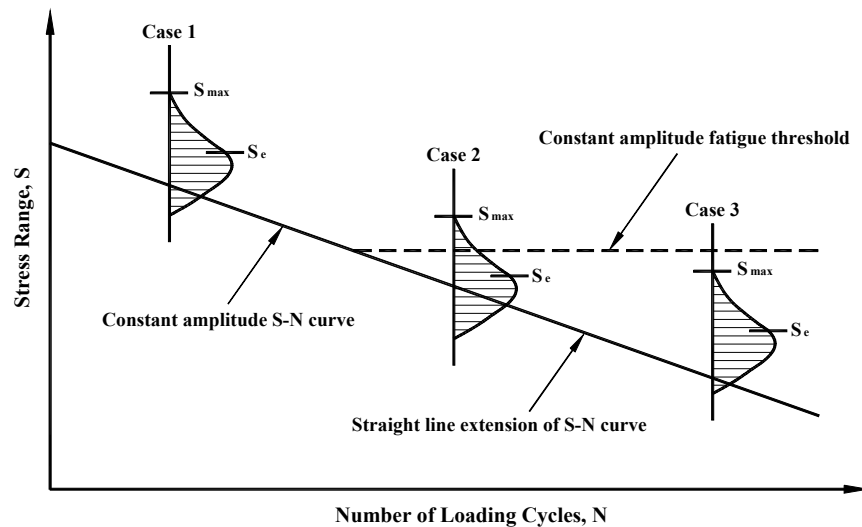


**FIGURE 3-7: Relationship between the Spectrum of Applied Stress Ranges and the  $S$ - $N$  Curve [Dexter & Fisher, 2000]**

To establish a safety margin for infinite life, a heavy truck that can cause less than 0.01% probability of exceedance needs to be specified. The statistics of the gross vehicle weight histogram in NCHRP Report 299 [1987] shows that an HS45 truck has an exceedance probability of 0.023%, which is close to, but has not yet reached the requirement of 0.01%. The NCHRP Report 299 thus recommends that “*if the assumption is made that fatigue is governed by individual truck occurrences, the expected maximum truck weight will be approximately 3 times the effective truck weight*”. Notice that if HS45 is considered, the reduction factor for constant amplitude fatigue threshold in the right term of Equation 3-8 should be  $\frac{1}{3}$ , not  $\frac{1}{2}$ . In fact, the reduction factor recommended in the Commentary of the AASHTO Guide Specifications is

0.367, very close to  $\frac{1}{3}$ . The HS30 truck implied by the LRFD Specifications is apparently a lighter heavy truck, compared with the HS45 truck required by the Guide Specifications and the NCHRP Report 299. This is because the design based on the maximum truck weight of HS45 has resulted in overly conservative life estimates compared to the observed field behavior [Dexter and Fisher, 2000]. In order to match the actual field conditions, the LRFD Specifications purposely loosen the design requirement by increasing the lower bound of the fatigue resistance by 50%, i.e. using  $\frac{1}{2}$  instead of  $\frac{1}{3}$  as the reduction factor for  $(\Delta F)_{TH}$ . So when the design stress range is controlled below one half of the constant amplitude fatigue threshold, a theoretically infinite life will occur at the detail.

Although the current LRFD Specifications allow higher infinite life fatigue resistance than the Guide Specifications, it may still be difficult to reach for a repaired detail, as will be illustrated later in the retrofit studies. In that case, Equation 3-9 and 3-10 need to be used to find the remaining service life of the details under consideration.

## Chapter 4

### Applied Finite Element Procedures

Stresses driven by out-of-plane distortion are considered as secondary stresses and are not accounted for during structural analysis. Current bridge design specifications prevent distortion-induced fatigue through requirement of using rigid attachment between girder flanges and connection stiffeners, but procedures for determination of secondary stresses are not addressed. The stress range magnitude is the governing parameter for rating of existing bridges and evaluation of fatigue repair approaches. Finite element studies are therefore performed in this research, both extensively and intensively, to provide comprehensive stress analysis at the transverse-to-longitudinal member connection details. Detailed investigation procedures and analytical results are presented in case studies from Chapters 5 to 9. This chapter reviews the computational work conducted by other studies and introduces the general finite element modeling approaches used in this research.

#### 4.1 Related Work

Due to computational cost constraints, only a small number of finite element studies were conducted during the early stage of research for steel bridge fatigue cracking and repair evaluation. Many of these studies were performed more on what would by present standards be considered small-size conceptual models as supplements to experimental investigations. A review of previous work provides good insight into what effective modeling strategies and approaches are appropriate for the case studies of this research.

NCHRP Report 227 [1980] studied stresses of girder web gussets for lateral bracing through modeling of a testing girder. Three levels of discretized models were constructed to

evaluate the out-of-plane behavior at the gusset-to-web connections. The first model consisted of a half span of the girder [Figure 4-1(a)]. The second model was cut from the first model with only a short length of the girder subjected to testing load [Figure 4-1(b)]. The third model was further abstracted from the second model including part of the girder web, transverse stiffener, and gusset plate [Figure 4-1(c)]. Each submodel was linked to its supermodel by enforcing the model boundary conditions of displacements and rotations obtained from the supermodel. In other words, the degrees of freedom (DOFs) of the cut-lines in the original model were applied as boundary conditions for the derivative cut model. All three models were meshed with a limited number of elements in order to save computation time. The analytical results were found to be in agreement with the experimental data.

NCHRP Report 336 [1990] also conducted a restricted size finite element analysis at the web-stiffener-gusset connection to determine the lateral bracing requirements and the driving forces needed during the experimental study for the web gap out-of-plane distortion. Only half of the testing girder was modeled due to symmetry (Figure 4-2). Some structural components were meshed by degenerated element types in order to simplify the analysis. For example, the flanges were modeled by truss elements and the concentrated load stiffener and the transverse connection plate were modeled with beam elements. All these elements were then superimposed on the web plane, which was meshed by plate elements. The web area close to the stiffener and gusset intersection was modeled with small-size plate-bending elements. The web area further away was modeled with large-size plane-stress elements. The transition region between the coarse and refined mesh was formed by triangular elements. Instead of approaching the solution through multi-level discretizations as performed in NCHRP Report 227 [1980], this research used a single model with varying degrees of refinement to investigate stresses at the critical

location. The results were used to direct the setup and adjustment of the test specimens. The predicted out-of-plane behavior was generally consistent with the experimental measurements.

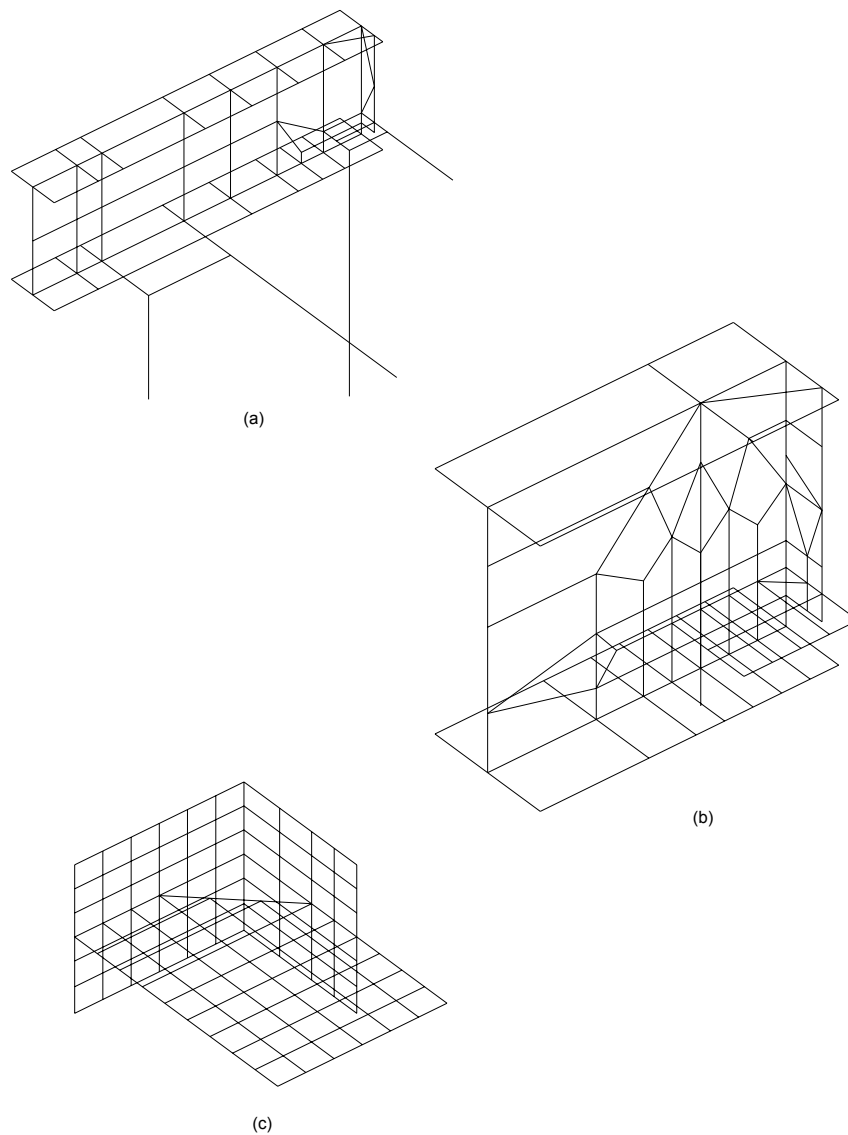


**FIGURE 4-1: Finite Element Models for the Web-Gusset-Stiffener Connection [NCHRP 227, 1980]**

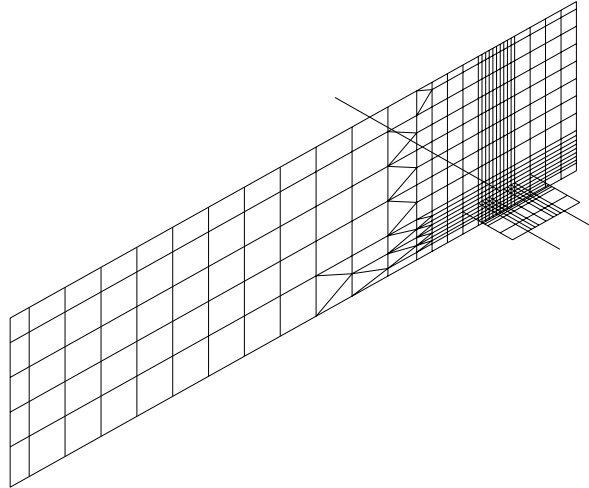
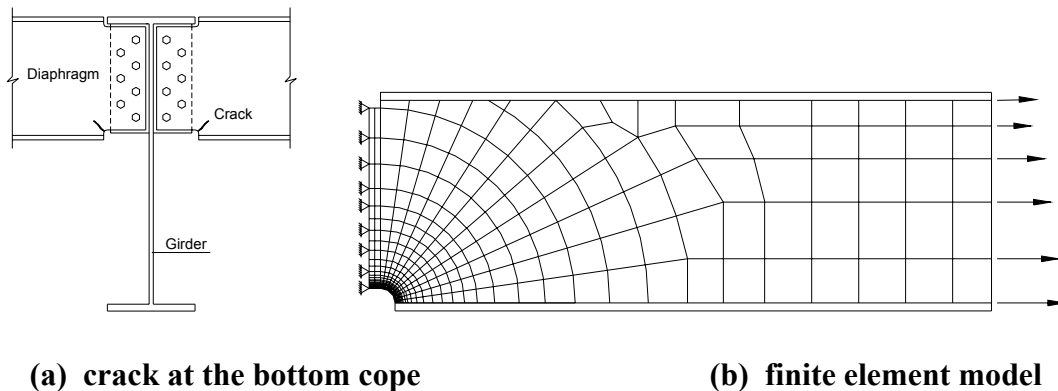


**FIGURE 4-2: Finite Element of Web, Gusset Plate, and Lateral Braces [NCHRP 336, 1990]**

Zwerneman et al. [1993] studied out-of-plane fatigue cracking developed in coped diaphragm to girder connections of an Oklahoma DOT bridge [Figure 4-3(a)]. Both field and laboratory tests were also carried out in addition to finite element studies during the research. The diaphragm was modeled with eight-node isoparametric elements at the web and plane-truss elements at the flanges [Figure 4-3(b)]. The length of the model was three times the depth of the diaphragm. The nodes on left side of the model were pinned to simulate the bolt line, and those on the right side of the model were subjected to a moment able to introduce the effect of out-of-plane distortion. The field test data indicated a composite interaction between the diaphragms and the deck slab. Therefore, the right side of the finite element model had imposed loads producing the stress gradient applicable under fully composite girder action. Three repair models were also analyzed for the diaphragm subjected to the same loading condition: 1) replacing existing diaphragms with uncoped diaphragms, 2) smoothing the cope with a tapered transition, and 3) relaxing the connection by bolt removal. The third repair option, removing connection bolts close to the bottom cracked diaphragm flange, proved to be the most effective.

Based on the model analyses, all three retrofit methods were then further studied through laboratory tests. The conclusions drawn from the experimental and analytical repair investigations were the same. A similar finite element study for distortion-induced fatigue cracking at coped floor-beam to girder connections was performed by Walker et al. [1992] for the Mahomet Bridge (Illinois DOT) on I-74 over the Sangamon River.



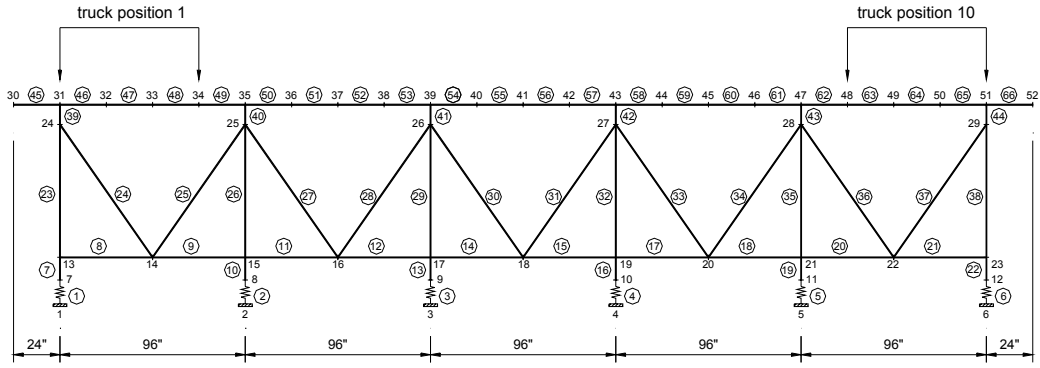
**(a) crack at the bottom cope** **(b) finite element model**

**FIGURE 4-3: Fatigue Study for Coped Diaphragm to Girder Connection**  
[Zwerneman et al., 1993]

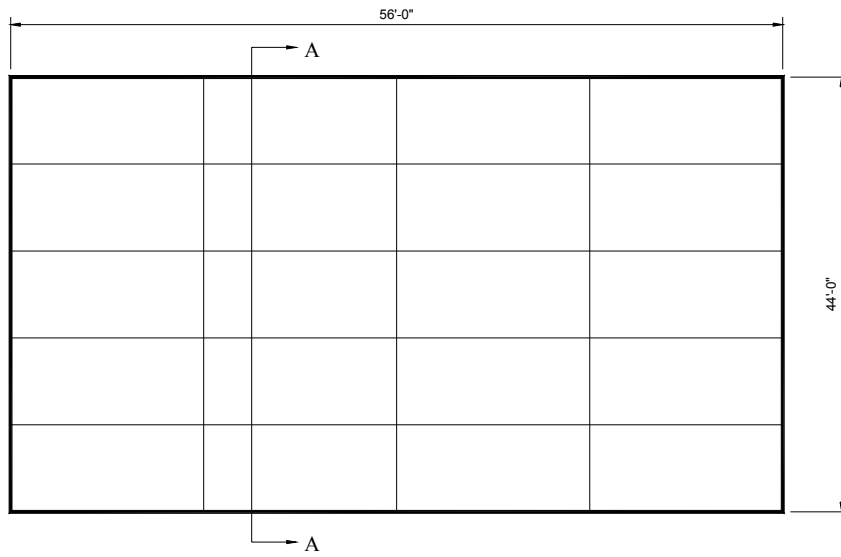
Ross et al. [1994] investigated a multi-girder/cross-frame bridge of the New Mexico Highway and Transportation Department with the intent of developing design loads for cross-frame members. Both 2-D and 3-D finite element models were built as shown in Figure 4-4 to evaluate forces carried by each cross-frame member under AASHTO design truck load. The computer program ANSYS education version was used for the analysis. In the 2-D model, all the structural components were modeled by beam elements, with top flanges embedded into the deck for composite action and the bottom flanges omitted in favor of spring boundary elements. The two 16 Kips wheel loads of the HS20 truck were applied to the deck and were moved from the left to right of the bridge lanes for a total of ten transverse loading positions. The software version used in this study allowed only a limited number of nodal DOFs, so the bridge length

was shortened to 56 ft in the 3-D model instead of the actual 140 ft, and a non-skewed layout was used instead of the actual skew. An HS20 design truck (72 Kips) was first moved along the bridge length at intervals of 3.5 ft. The critical longitudinal location was found to occur when the drive axle was at the mid girder span. The truck was then placed transversely over the deck for 18 load cases to determine the maximum forces occurring to the cross-frame members. The computer solutions obtained from both the 2-D and 3-D analyses were then used to guide the strain gauging arrangement for field testing.

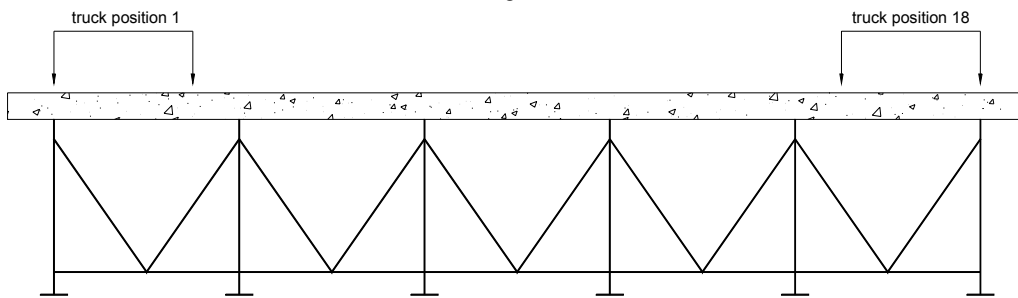
Tedesco et al. [1995] conducted finite element analysis for an Alabama DOT steel bridge to evaluate the effect of diaphragm removal in retrofitting distortion-induced fatigue. The analysis was carried out on a supercomputer so that the entire bridge structure was modeled as shown in Figure 4-5. Four-node shell elements were used for deck slab and girder flanges. Three-node plate-bending elements were used for webs. Beam elements were used for diaphragms. Rigid link elements and truss elements were used between diaphragms and girder webs. In addition, rigid link elements were also used to connect flange to web elements as well as flange to deck elements. Analyses were carried out for conditions both with and without diaphragms, using the ADINA finite element software package. The results indicated that after diaphragm removal the girder flexural stress and vertical deflection were increased maximally by 8% and 9%, respectively; the maximum positive deck bending moment was increased by 14%; and the maximum negative deck bending moment was decreased by almost 100%. Therefore, diaphragm removal can not only eliminate the secondary stresses, but improve the deck performance as well. The corresponding field testing results of this bridge was carried out by Stallings et al. [1996].



(a) 2-D finite element model



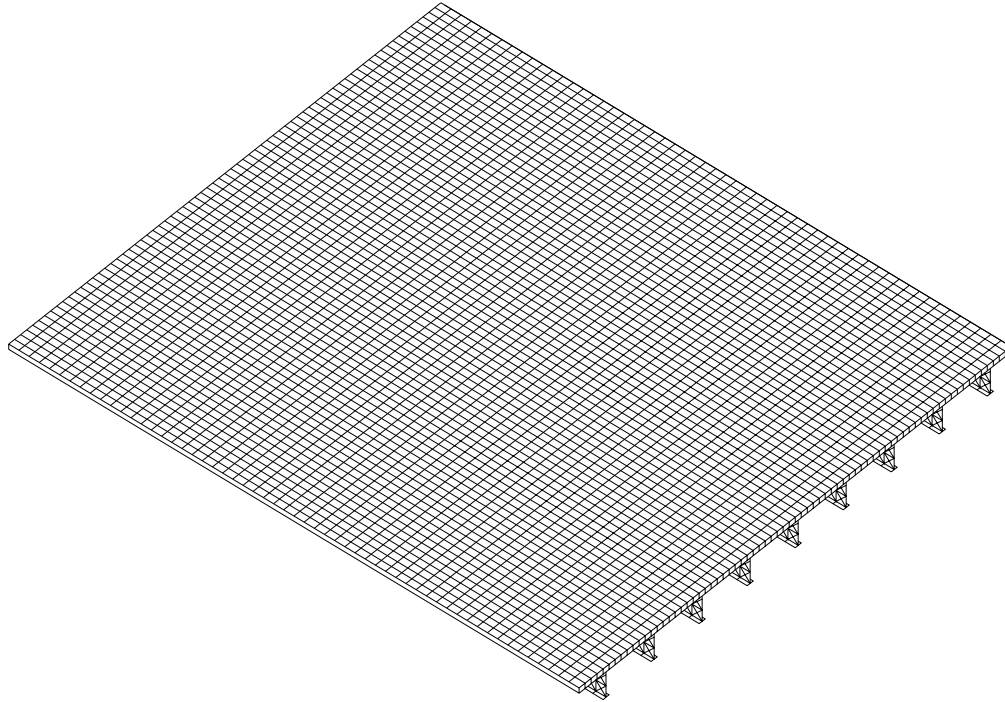
Bridge Plan



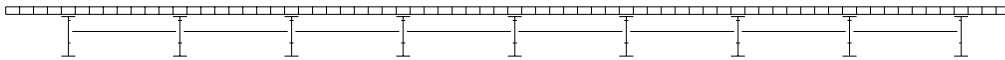
Section A-A

(b) 3-D finite element model

FIGURE 4-4: Investigation of Design Load for Cross-Frame Members [Ross et al., 1994]



(a) 3-D finite element for whole bridge span



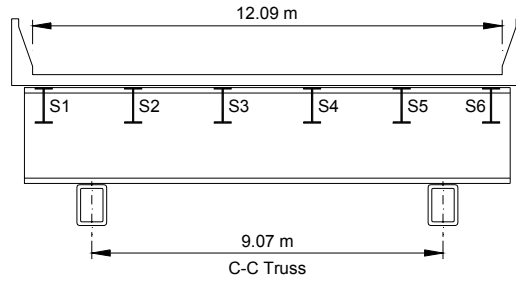
(b) model cross section

**FIGURE 4-5: Finite Element Analysis for Girder-Diaphragm Interaction**  
[Tedesco et al., 1995]

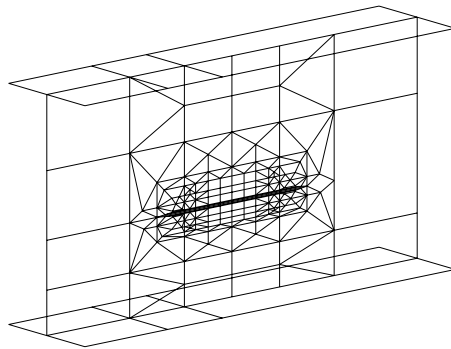
Lai [1996] studied fatigue cracking at stringer to floor-beam connections in a truss bridge [Figure 4-6(a)] using two levels of finite element models. The STAAD-III computer program was adopted in this research for model construction and stress investigation. The Level One model included a portion of the bridge deck, stringers, floor-beams, and trusses, and was loaded by an HS15 fatigue truck along the center of each traffic lane. This model described the overall behavior of the bridge and provided forces to be applied to the Level Two model. The Level Two model consisted of a floor-beam with refined mesh at the stringer to floor-beam connection, as shown by Figure 4-6(b). The fatigue stress and crack growth behavior were then studied

based on the results obtained from the Level Two model and linear elastic fracture mechanics (LEFM) theory. Two retrofit approaches were also investigated using finite element methods. The first approach was to reduce the connection stiffness by hole drilling and saw cutting to form a “dog bone” or “dumbbell” shape in the floor-beam web [Figure 4-6(c)]. The second approach was to increase the stiffness at the connections by bolting an angle bracket to both the stringer bottom flange and the floor-beam web. The maximum stresses were reduced by 29% and 60%, respectively, for the two repairs.

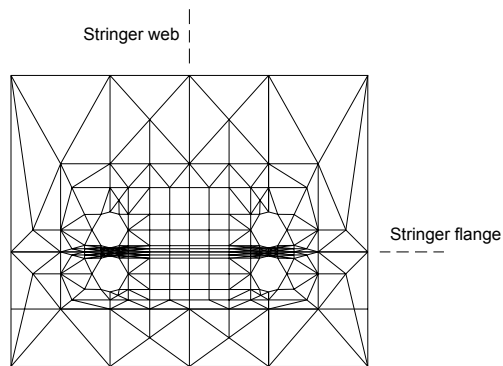
Keating et al. [1996] performed a parametric study using finite element models to investigate the stress concentration effect of multiple drilled holes and large flame cut holes that could be used in the repair of web gap fatigue cracking. Models with different hole size, shape, and orientation were analyzed using the finite element program SAP90. The results were then combined with experimental data obtained from laboratory tests to help develop guidelines for the use of multiple drilled holes and flame cut holes in crack repair. Figure 4-7 shows schematically the finite element models of several different hole geometries studied during the investigation.



(a) bridge cross section

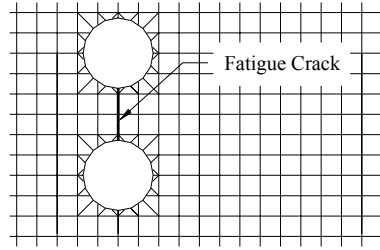


(b) Level Two model

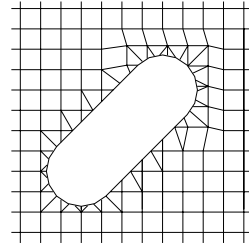


(c) "dumbbell" repair model

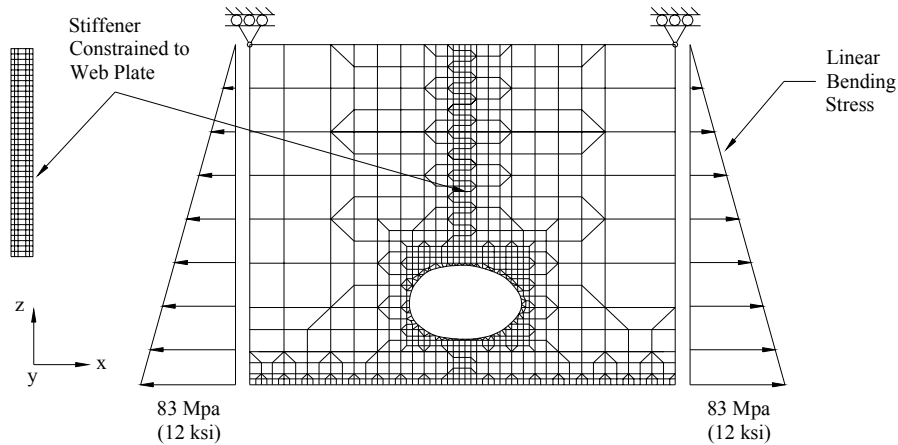
**FIGURE 4-6: Crack and Repair Analysis at Stringer to Floor-Beam Connection [Lai, 1996]**



(a) simulated crack with drilled holes



(b) repair with 45° slotted holes



(c) mesh and loading condition for girder web with flame cut holes

**FIGURE 4-7: Finite Element Analyses for Drilled Holes and Flame Cut Holes [Keating et al., 1996]**

## 4.2 Submodeling

The foregoing research studies provide valuable guidance. One of the highlights of the previous work is the use of multi-level modeling schemes. In order to properly characterize the behavior of out-of-plane distortion while minimizing computational time, it is wise to use different levels of refinement for models as the localized region of fatigue stress is approached. The software used in this project for model implementation is ANSYS 5.6 [2000] academic version, having an upper limit node number of 128,000. This is sufficient for the model sizes required for this research. For each of the five KDOT bridges under investigation, a two-level modeling approach is used, with the large model simulating the globe structure behavior under truck loading, and the small model revealing the local stress field at the crack prone details. The analyses for four out of

the five bridges (the Arkansas River Bridge, the Winfield Bridge, the Hump Yard Bridge, and the Tuttle Creek Bridge) are carried out using the coarse-to-fine submodeling technique supported by ANSYS. The load path for the Westgate Bridge is clearly defined, so stick frame model analysis is performed instead of coarse model analysis when the structure global behavior is studied, as explained in Chapter 6. The local stress condition of this bridge is also investigated by using refined finite element models.

Submodeling is a finite element method used to approach more satisfactory results in an area of interest. For example, the element mesh of a full-size bridge model is usually too coarse to provide accurate stress results at the crack sensitive details. To solve this problem, either the whole large model is analyzed again with greater mesh refinement, or a separate submodel with only the connection under consideration is created for detailed investigation. The first option is obviously computationally expensive. Therefore the second option, the submodeling method, is used in this research to study the stress concentration effect at the crack details. To link the analysis between the coarse model and the submodel, an appropriate data mapping process needs to be specified.

Submodeling is fundamentally a displacement-imposed method. Although the coarse model is not able to produce accurate results at the stress concentration point, the results away from that location may be good enough, because the solutions at those distant regions are relatively stable and are not sensitive to the change of the element size. Therefore, it is the modeler's job to decide to what extent the boundary of the submodel should be defined so that the displacement results from the coarse model can be correctly used and satisfactory stress results can be obtained in the region of interest.

Figure 4-8 shows the schematic relationship between the coarse model and the submodel. The connection stiffener to girder web and flange intersection is the area subjected to high stress gradient, therefore the submodel only needs to include part of the structural components around this region. The bold lines in Figure 4-8(a) represent a cut boundary on the coarse model. The area within this boundary is abstracted and finely meshed for the formation of the submodel, as shown in Figure 4-8(b). The element type, material properties, and geometry coordinates of the submodel should be kept the same as those of the corresponding coarse model along the cut boundary. The geometry inside the submodel, however, can be changed when necessary. Comparing Figures 4-8(a) and (b), it can be observed that there are three places that are modified during the submodeling: the inside corner of the connection stiffener end is clipped; the diaphragm is terminated short of the web-to-stiffener connection so that only the stiffener is directly connected to the web; and the bottom stiffener end is separated from the flange. The coarse model would be cumbersome if these local details had to be considered. Yet for the submodel it is not difficult to implement these details. As long as the modified regions are away from the cut boundary, the results are not significantly affected.

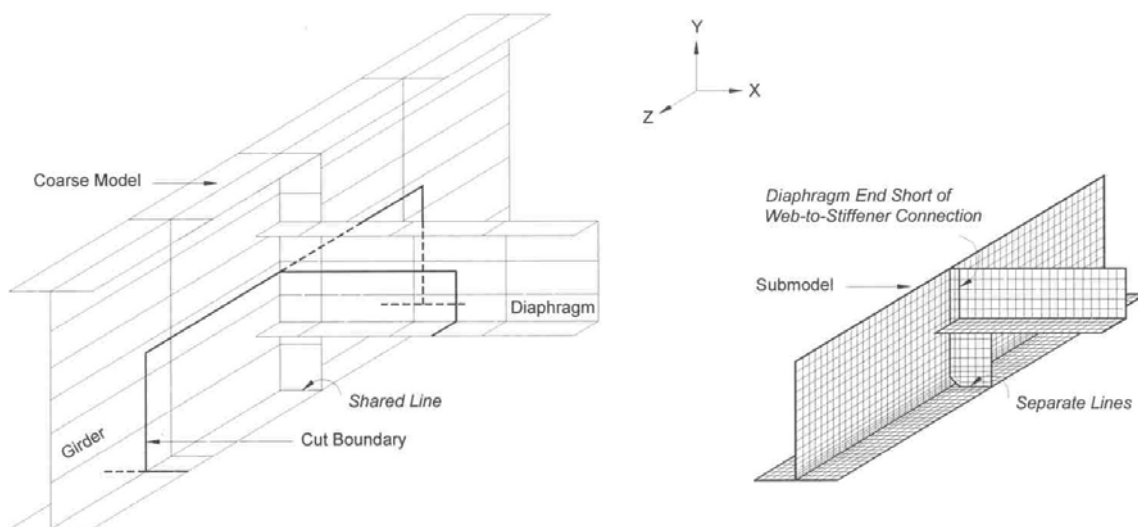


**FIGURE 4-8: Coarse Model vs. Submodel**

To link the submodel with the coarse model, the displacements calculated on the cut boundaries of the coarse model are specified as the boundary conditions for the submodel. This procedure is called cut boundary DOF interpolation. Because the submodel is completely independent of the coarse model, the nodal displacements along the submodel cut boundary are calculated by interpolating the DOF results from the coarse model using the element shape functions. This is based on Saint-Venant's principle, which states that if an actual loading condition is replaced by a statically equivalent system, the distribution of stress and strain is altered only near the regions of load application. For the submodel of Figure 4-8, this implies that the displacements calculated by cut boundary interpolation will not change the results at the stress concentration region, as long as it is far enough away from the cut boundary. The submodeling method, therefore, is also called the cut-boundary displacement method.

The major steps for conducting a submodeling analysis can be summarized as follows:

- 1) Build and analyze the coarse model;
- 2) Create the submodel, record the cut boundary nodal coordinates;
- 3) Go back to the coarse model and perform cut boundary DOF interpolation;
- 4) Return to the submodel, apply interpolated DOFs, and analyze the submodel;
- 5) Check if the distance between the stress concentration and the cut boundary is sufficient.

### **4.3 Modeling Noncomposition Action**

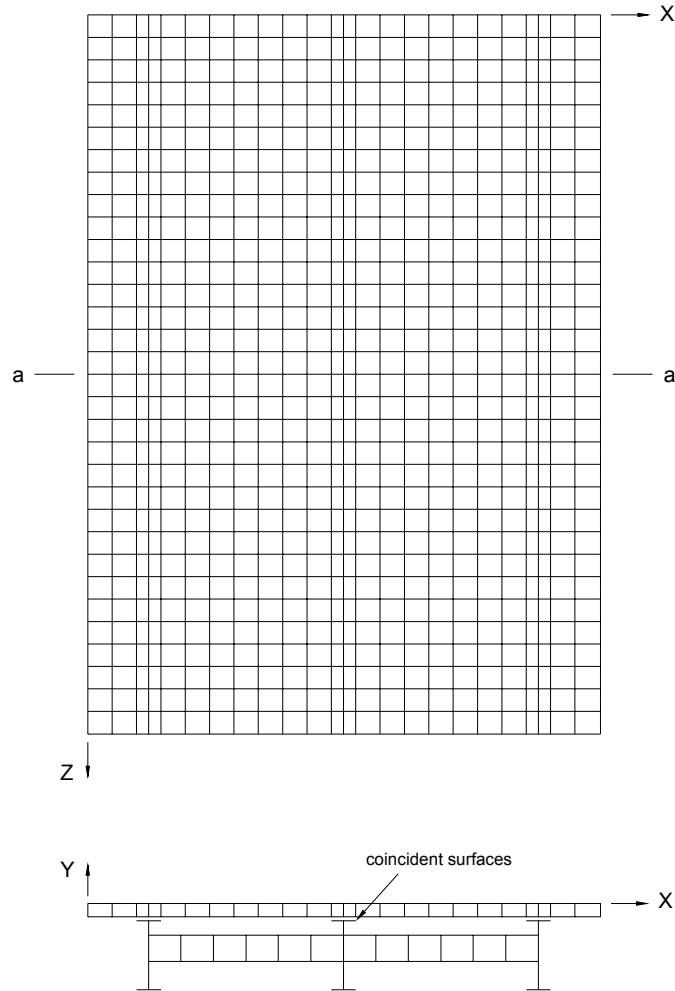
All five KDOT bridges selected for this study are noncomposite. The most accurate finite element approach for modeling the noncomposite behavior is to perform a contact analysis, taking into account the friction between the concrete slab and the steel girder. However, finite element contact problems are highly nonlinear and require significant computer resources to

solve models of large size, such as the coarse models investigated by this research. Another difficulty of performing contact analysis is the need to determine bond between the two contact surfaces. Although many bridges are designed and constructed as noncomposite, they actually exhibit composite action under service loads due to the chemical bond and the friction between the two different materials. The actual interaction could change from almost fully composite, to partially composite, and to completely noncomposite, depending on the years of service and the loading conditions [Aktan, 1994]. The AASHTO *Guide Specifications for Fatigue Evaluation of Existing Steel Bridges* [1990] uses the adjustment of the girder section modulus to include the possible composite action in noncomposite bridges. Section 2.7.1 of the Guide Specifications defines as follows the member section used for stress range calculation of bridges with noncomposite concrete decks: *“If there is no visual indication of separation between the deck and steel section, use either the full composite section or the steel section alone increased by 30% for the positive bending portion of the moment range and the steel section alone increased by 15% for the negative bending portion of the moment range. If there is visual indication of separation between the deck and steel section, use the steel section alone for both the positive and negative bending portions of the moment range.”* The bond between the slab and girder decreases as the bridge is subjected to continuous impact load for years. Unless field experiments are conducted, it is hard to determine to what extent the noncomposite or composite action has been reached. For conservative purposes, KDOT directed that all five bridges be analyzed as fully noncomposite since they have been in use for 25 ~ 45 years. The deck slab is allowed to slide independently upon the girders and no friction needs to be considered between the concrete slab and steel sections as was originally designed. Therefore linear coupled degrees of freedom

are used instead of nonlinear contact elements to simplify the finite element analysis of the bridges.

Coupling forces two or more DOFs to take the same value. In order to model the bridge noncomposite behavior, it is assumed that the corresponding deck and girder contact surface nodes will displace the same in the vertical and transverse directions, but independently in the longitudinal direction. As shown in Figure 4-9, to create coupled DOF sets, the deck bottom surface and the girder top flange are meshed with a series of coincident nodes. Each pair of coincident nodes are “buttoned” together both for the transverse (X) and vertical (Y) DOFs, but “untied” for the longitudinal (Z) DOF so that the model can behave noncompositely. However, as an exception, those coincident nodes on the mid-span girder sections (line a-a in Figure 4-9) are also coupled for the longitudinal DOF in order to keep the model stable during computation.

Since coupled sets are not specified for the longitudinal DOF, penetration will occur at the interface by allowing free slippage between the deck and girder along this direction. To find out how this would affect the accuracy of the results, a number of small-size finite element models are analyzed first to examine the applicability of the coupling method to modeling noncomposite action. In the following examples, all DOFs of the coincident nodes on the two contact surfaces are coupled except that along the beam longitudinal direction. The first two cases are rectangular beams stacked on one another with identical geometry and material properties, and the next two cases model bridge girders with slab-on-girder cross sections. The stresses obtained from the finite element analysis are compared with those calculated based on the ideal beam bending stress formula.



Note:  
 All coincident nodes are coupled for X and Y DOF.  
 Coincident nodes along line a-a are also coupled for Z DOF.

**FIGURE 4-9: Schematic of Coupled DOF Sets Used for Modeling Bridge Noncomposite Action**

**4.3.1 Example 4.1**

As shown in Figure 4-10(a), two beams are stacked and subject to a uniform load of 1 Kip/in. The maximum and minimum stresses at the beam mid-span are calculated as:

$$M = wl^2/8 = (1)(15)^2/8 = 28.125 \text{ Kips-in}$$

$$I = (1)(1)^3/12 = 0.083 \text{ in}^3$$

$$\sigma = Mc/2I = (28.125)(0.5)/(2 \times 0.083) = \pm 84.375 \text{ ksi}$$

The finite element result is shown in Figure 4-10(b). The top and bottom fiber stresses at the mid-span of the underlying member (Beam B) are used for verification:

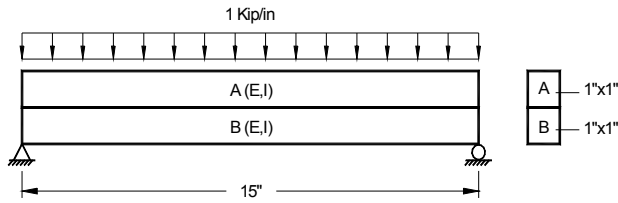
$$\text{Top fiber: } \sigma_t = 84.456 \text{ ksi}$$

$$\text{Error} = (84.456 - 84.375)/84.375 = 0.1\%$$

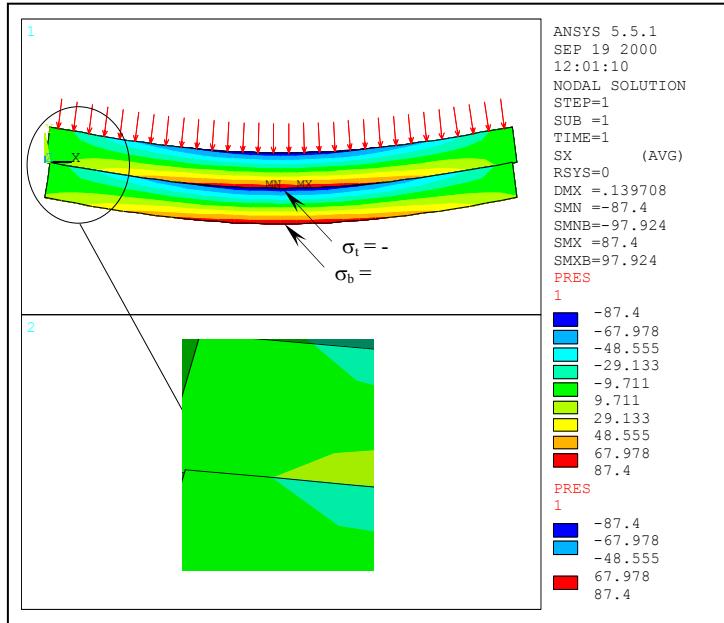
$$\text{Bottom fiber: } \sigma_b = -86.743 \text{ ksi}$$

$$\text{Error} = (86.743 - 84.375)/84.375 = 2.8\%$$

The stresses at the beam top and bottom edges are almost symmetric and they are very close to the results calculated by the beam bending stress formula. Figure 4-10(b) shows the stress distribution and the deflected shape of the finite element model. It can be observed that the bending stress contour is almost identical for the two beams and sliding occurs on the interface. Beam A and B are therefore acting noncompositely. Small penetration of the coincident surfaces is also observed as shown in the zoomed-in window of Figure 4-10(b). However, this does not have much effect on the model behavior since the stress results are very close to the ideal bending solution.



(a) member geometry and loading



(b) FEM output showing slippage and penetration on the contacting surfaces

FIGURE 4-10: Simply Supported Rectangular Beams

### 4.3.2 Example 4.2

A two-span structure is shown in Figure 4-11(a). Beam A and B are stacked and subject to a concentrated load of 20 Kips at the middle of each span. The stresses at the beam mid-span and mid-support sections are calculated as:

Stresses at the mid-span

$$M = (5/32)Pl = (0.15625)(20)(10) = 31.25 \text{ Kips-in}$$

$$\sigma = Mc/2I = (31.25)(0.5)/(2 \times 0.083) = \pm 93.75 \text{ ksi}$$

Stresses at the mid-support

$$M = (3/16)Pl = (0.1875)(20)(10) = 37.50 \text{ Kips-in}$$

$$\sigma = Mc/2I = (37.50)(0.5)/(2 \times 0.083) = \pm 112.50 \text{ ksi}$$

The finite element output is illustrated in Figure 4-11(b). The result of the bottom member is used to verify the stresses at the mid-span section, and the result of the top member is used to verify the stresses at the mid-support section. This is because stress concentration would occur at nodes and elements close to the loading and constraint points. Results obtained from these regions should be avoided or used with caution.

Stresses at the mid-span

$$\text{Top fiber: } \sigma_t = -94.385 \text{ ksi}$$

$$\text{Error} = (94.385 - 93.75)/93.75 = 0.7\%$$

$$\text{Bottom fiber: } \sigma_b = 86.167 \text{ ksi}$$

$$\text{Error} = (86.167 - 93.75)/93.75 = -8.1\%$$

Stresses at the mid-support

$$\text{Top fiber: } \sigma_t = 100.416 \text{ ksi}$$

$$\text{Error} = (100.416 - 112.50)/112.50 = -10.7\%$$

$$\text{Bottom fiber: } \sigma_b = -110.310 \text{ ksi}$$

$$\text{Error} = (110.310 - 112.50)/112.50 = -1.9\%$$

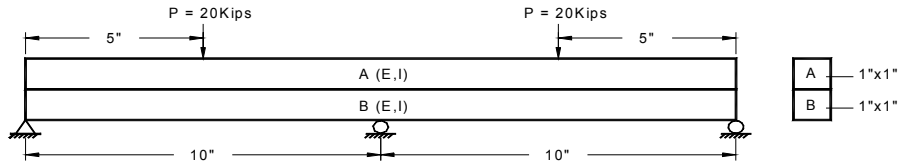
The stress errors are all less than 11%. In general, the bending stress distributions of the two beams are the same and the stresses at the top and bottom edges for each beam section are very close. Slippage on the interface along the beam longitudinal direction is also observed as shown in Figure 4-11(b). The two beams thus deflect consistently as well as independently. Penetration occurs again at the coincident surfaces, as shown in the bottom window of Figure 4-11(b), but the beam noncomposite action is not greatly affected.

Example 4.1 and 4.2 demonstrate that the coupled DOFs can be used to model the

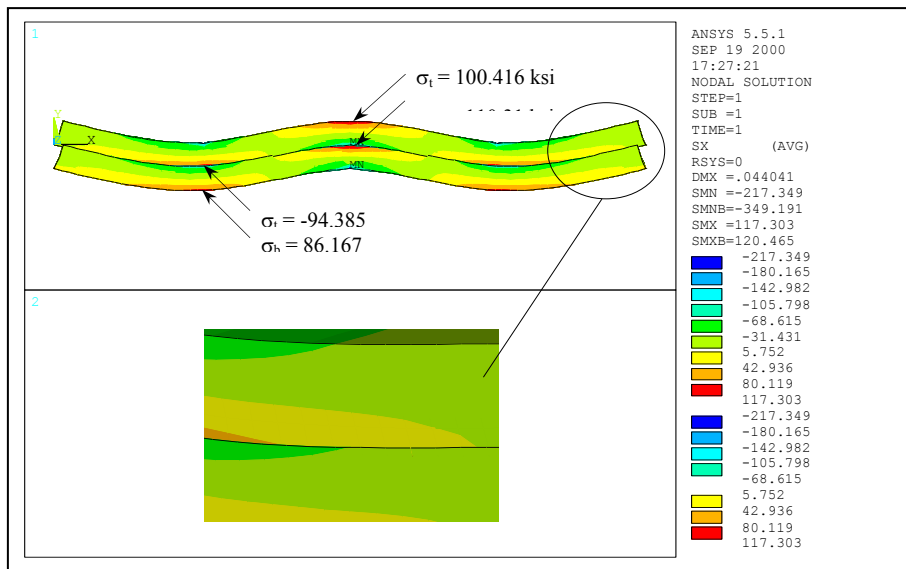
noncomposite action for members of simple geometry and with matching material properties.

Example 4.3 and 4.4 illustrate the accuracy of this method in modeling the noncomposite

behavior for concrete-slab-on-steel-girder bridge sections.



(a) member geometry and loading condition



(b) FEM output showing bending stress distribution and

FIGURE 4-11: Two-Span Rectangular

### 4.3.3 Example 4.3

A simply supported slab-on-girder bridge member is shown in Figure 4-12(a). Two concentrated loads of 200 Kips are applied on top of the deck at 5 ft from each end of the beam. The member sections between the two load points are subject to constant bending moment. The stresses of the steel sections within this region are calculated as:

$$E_s = 29000 \text{ ksi}$$

$$E_c = 57\sqrt{f'_c} = 57\sqrt{3000} = 3122 \text{ ksi}$$

$$n = E_s / E_c = 29000/3122 = 9$$

$$I_s = (0.65)(35-1.02)^3/12 + 2[(12)(1.02)^3/12 + (12)(1.02)(17.5)^2] = 9624 \text{ in}^4$$

$$I_c = (108)(8.25)^3/12 = 5054 \text{ in}^4$$

$$I = (I_s + I_c / n) = (9624 + 5054/9) = 10186 \text{ in}^4$$

$$M = Pa = (200)(5 \times 12) = 12000 \text{ Kips-in}$$

$$\sigma = Mc/I = (12000)(17.5)/(10186) = \pm 20.617 \text{ ksi}$$

Results obtained from the finite element computation are shown in Figure 4-12(b). The stresses of the girder flanges at the mid-span section are used for verification:

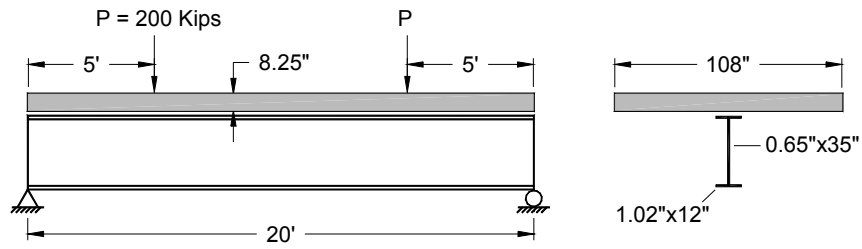
$$\text{Top flange: } \sigma_t = -20.303 \text{ ksi}$$

$$\text{Error} = (20.303 - 20.617)/20.617 = -1.5\%$$

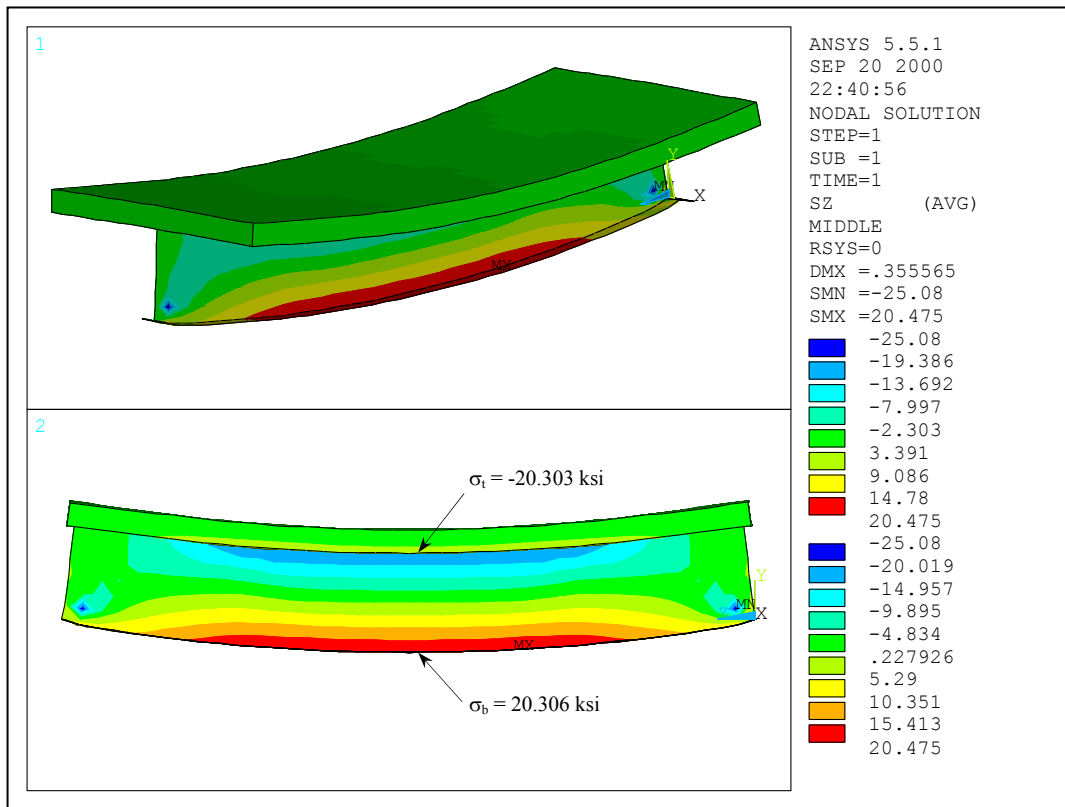
$$\text{Bottom flange: } \sigma_b = 20.306 \text{ ksi}$$

$$\text{Error} = (20.306 - 20.617)/20.617 = -1.5\%$$

The stress values are therefore very close to the ideal bending solution. The girder web stress contour in the bottom window of Figure 4-12(b) shows that the center half of the girder length is in a region of pure bending and the stresses are symmetric about the web centerline. Relative slip occurs between the deck slab and the girder top flange as shown by the displaced outline. The bridge section is therefore apparently noncomposite. Penetration still exists but is too small to be seen at the graphical scale of this example.



(a) member geometry and loading condition



(b) FEM bending stress distribution and deflected shape

FIGURE 4-12: Simply Supported Noncomposite Bridge Section

#### 4.3.4 Example 4.4

A two-span slab-on-girder bridge is subject to a point load of 200 Kips as shown in Figure 4-13(a). The maximum stresses of the steel sections at the center of each span are calculated as:

Stresses at the left mid-span section:

$$I = (I_s + I_c / n) = 10186 \text{ in}^4 \text{ (from Example 4.3)}$$

$$M = (13/64)Pl = (0.2031)(200)(20 \times 12) = 9750 \text{ Kips-in}$$

$$\sigma = Mc/I = (9750)(17.5)/(10186) = \pm 16.751 \text{ ksi}$$

Stresses at the right mid-span section:

$$M = (3/64)Pl = (0.0469)(200)(20 \times 12) = 2250 \text{ Kips-in}$$

$$\sigma = Mc/I = (2250)(17.5)/(10186) = \pm 3.866 \text{ ksi}$$

Compared with the results obtained from the finite element computation, as illustrated in Figure 4-13(b):

Stresses at the left mid-span section:

$$\text{Top flange: } \sigma_t = -16.965 \text{ ksi}$$

$$\text{Error} = (16.965 - 16.751)/16.751 = 1.3\%$$

$$\text{Bottom flange: } \sigma_b = 15.306 \text{ ksi}$$

$$\text{Error} = (15.306 - 16.751)/16.751 = -8.6\%$$

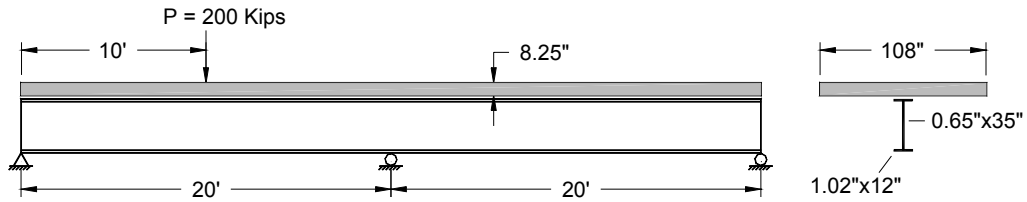
Stresses at the right mid-span section:

$$\text{Top flange: } \sigma_t = 3.590 \text{ ksi}$$

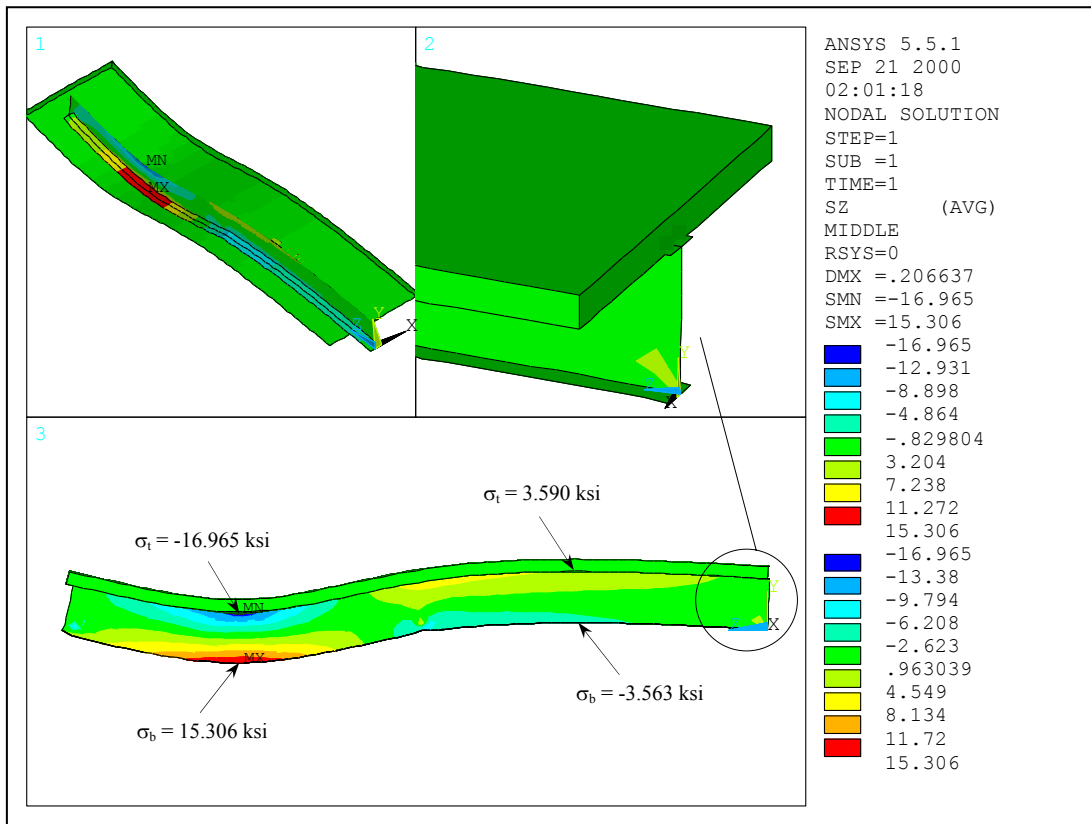
$$\text{Error} = (3.590 - 3.866)/3.866 = -7.1\%$$

$$\text{Bottom flange: } \sigma_b = -3.563 \text{ ksi}$$

$$\text{Error} = (3.563 - 3.866)/3.866 = -7.8\%$$



(a) member geometry and load condition



(b) FEM bending stress distribution and deflected shape

FIGURE 4-13: Two-Span Noncomposite Bridge

The errors are all below 10%. Except at the support regions, the tensile and compressive zones for most of the girder sections are symmetric about the web centerline. The deck slab slides relative to the top of the girder as shown by the displaced contour in Figure 4-13(b). The slip between the contact surfaces is unsymmetric in this example because the load is applied only on one span of the beam. The interface penetration is again very small and hard to detect even in the zoomed-in detail. This example, together with Example 4.3, shows that the coupling method can also be used to model the noncomposite behavior of the slab-on-girder bridge sections.

No more than two-span cases are considered for the pilot models, because the finite element investigations for the five KDOT bridges are limited to no more than two continuous spans in order to control the model size. Small errors were observed as compared with the results calculated based on ideal bending. This is caused by the small penetration occurring at the contact surfaces, the way the loads and support conditions are applied on to the finite element models, the element size or mesh density used during model construction, and the difference between the principles followed by traditional beam flexural stress calculation and the finite element computation. As long as the area of interest is away from the loading or supporting point, the results are satisfactory. The four testing examples thus validate the coupling method in simulating the noncomposite behavior for bridge coarse models.

#### **4.4 Other Considerations for Model Validation**

All the four bridges investigated in this study using the submodeling method have multiple continuous spans. To control the model size and save computation time, only one or two spans of the bridges are built into the coarse model. The coarse model of the Arkansas River Bridge includes two spans of the bridge adjacent to an expansion joint. The coarse models of the other three bridges include only one of the typical continuous spans. The boundary conditions used at

the model end sections are assumed pinned if the girders are interrupted at an expansion joint and fixed if the bridge is continuous over the pier. A trial analysis has been conducted comparing a single span model and an equal 3-span model of a continuous bridge, both fixed at the girder end sections. The difference of web gap stresses is found only about 5% in the most affected details as indicated by the submodel results. The girder in-plane flexural stresses are found to be more sensitive to this boundary condition assumption, but are not relevant parameters for this study. The simplification of using fixed DOFs for the continuous support is therefore determined to have no significant effect on the girder out-of-plane behavior and secondary distortion-induced stresses as explored in this study.

The first case study, the Arkansas River Bridge, is modeled using 20-node brick elements for the concrete slab and 8-node shell elements for the steel plates. The analysis results were not significantly different from those obtained for the same model using lower order 8-node brick elements and 4-node shell elements. Therefore, lower order element types are used during the coarse model and submodel analyses of the other three bridges studied using submodeling: the Winfield Bridge, the Hump Yard Bridge, and the Tuttle Creek Bridge. This follows the recommendation of the ANSYS software that lower order linear elements be used instead of higher order quadratic elements, as long as their degenerated forms (triangular 2-D or tetrahedral 3-D elements) are avoided at critical regions and certain mesh refinement requirements are satisfied. Normally, this practice yields results with the same or better accuracy at less expense.

The element mesh size in the vicinity of the crack initiation site is controlled at a level that further refinement does not produce a significant stress increment. Theoretically, when linear analysis is performed, the stresses at the concentration point tend toward infinity if the mesh size is continuously reduced. In reality, however, a plastic zone is formed at the critical

location. Since the plastic zone of all the details under consideration is very small, instead of using nonlinear analysis to find the size of the plastic zone for different submodels, linear analysis is performed in this study. A uniform mesh density is used at the concentration regions. In particular, for the four bridges experiencing web gap cracking (the Westgate Bridge, the Winfield Bridge, the Hump Yard Bridge, and the Tuttle Creek Bridge), the mesh size within the web gap depth is all controlled at 0.25 in. As presented later in the chapters of case studies, the out-of-plane stress results are found stable at this mesh refinement and comparable to the field and laboratory test data reported by other research [Koob et al., 1985; Fisher et al., 1987; Stallings et al., 1993; D'Andrea et al., 2001].

Principle stresses are normally used for identification of crack initiation sites in finite element analysis. In this research, however, the axial stresses are more appropriate for interpretation of the cause of fatigue cracking, because the models are built purposely with the potential crack paths oriented perpendicular to the axial stresses. As presented in Chapters 5 to 9, the axial stresses provide rational and satisfactory explanation for the crack initiation and development observed in each bridge. This is consistent with the fundamental fracture Mode I assumption that only the stress component normal to the crack path is responsible for the crack growth.

## Chapter 5

### Case Study 1: The Arkansas River Bridge

Cracks in the Arkansas River Bridge are classified as: 1) broken welds at the stringer to floor-beam connections; 2) vertical cracks at the expansion joints; and 3) horizontal cracks due to out-of-plane distortion at the floor-beam to exterior girder connections. About 110 cracks were observed in the bridge, more than one-third of them being distortion-driven. However, unlike the cracks found in most other bridges, the Arkansas River Bridge developed out-of-plane fatigue cracking at a distance away from the small web gap area. The crack condition is severe at some locations and could affect major structural members if propagation continues. The main scope of this case study is thus directed toward the stress analysis and repair evaluation of the cracks caused by out-of-plane distortion.

#### 5.1 Description of the Bridge Structure

The Arkansas River Bridge [KDOT Bridge No. 96-78-244.38(064)] was designed in 1949 and constructed in 1955. It is located on highway K-96 over the Arkansas River, 1.28 miles south of 5<sup>th</sup> Avenue in Hutchinson, Kansas. The superstructure is composed of a typical noncomposite girder/floor-beam/stringer system, as shown in Figure 5-1 and Figure 5-2. The bridge has four main girders extending 1020 ft longitudinally from northeast to southwest, with 17 equal spans of 60 ft. The girders are continuous except at two expansion joints, which divide the bridge length into three units. Transverse floor-beams are connected to the girders at the third points within each span and at the pier locations. Stringers are continuous on top of the floor-beams. An 8<sup>1</sup>/<sub>4</sub> in. reinforced concrete slab is supported by the girders and the stringers. The bridge roadway width is 52 ft, including four 12 ft traffic lanes and two 2 ft shoulders. The sidewalk,

one on each side of the bridge, is 4 ft 2½ in. wide. Thus the total bridge cross section width is 60 ft 5 in. All of the main structural members are rolled steel sections. The girder sections are W36×160 and W36×170, the floor-beams are W21×68 and W21×62, and the stringers are W14×43 and W16×45. Girder transverse stiffeners are used as floor-beam connection plates.

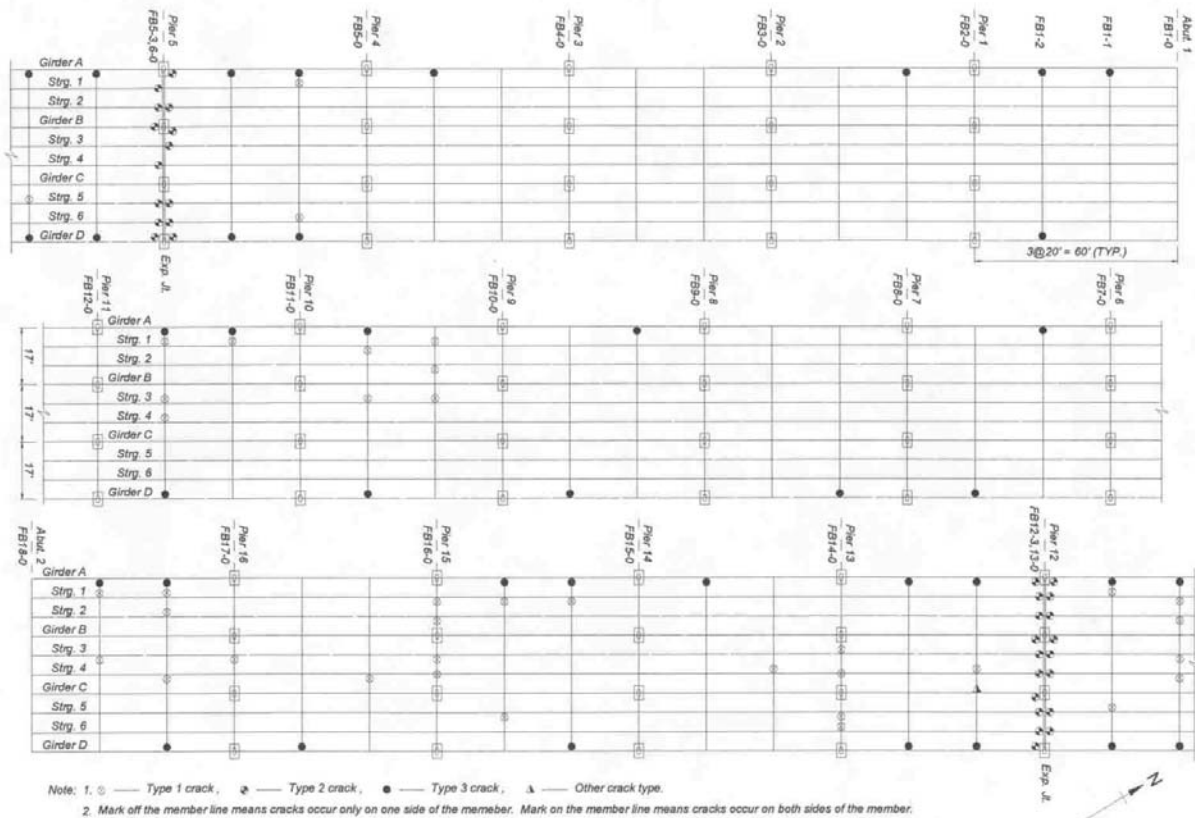


**FIGURE 5-1: Frame Plan and Crack Distribution of the Arkansas River Bridge**

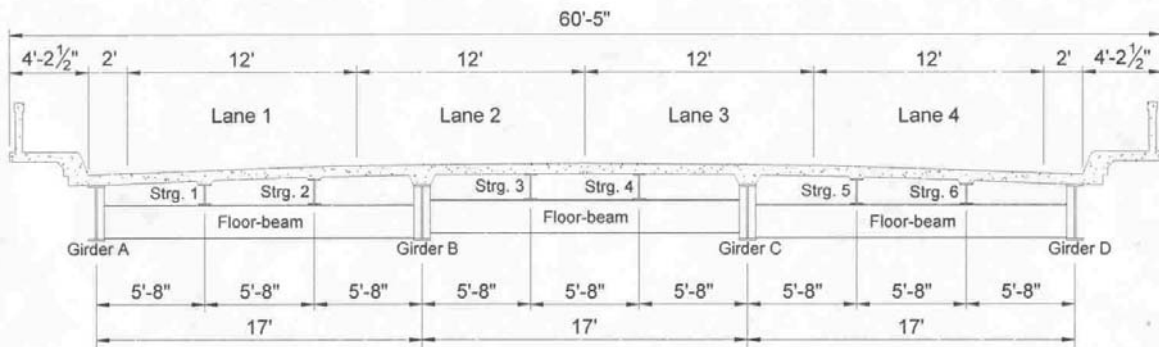


**FIGURE 5-2: Cross Section of the Arkansas River Bridge**

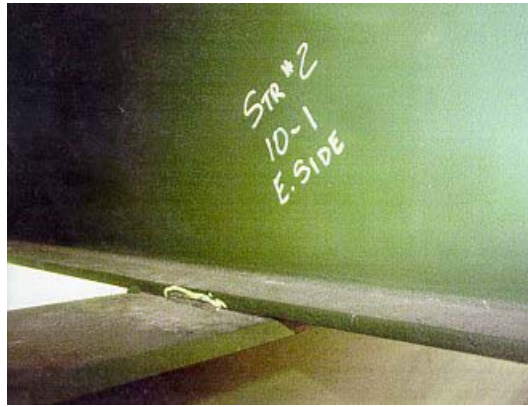
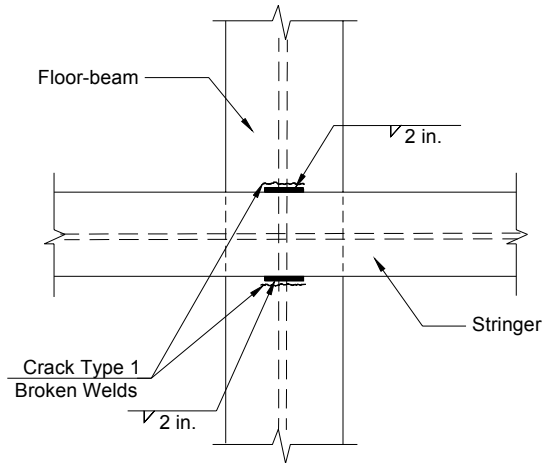
The 1993 KDOT traffic survey predicted a 12,500 daily traffic for the Arkansas River Bridge in the year 1996. The contribution due to the medium and heavy trucks are 3% and 8%, respectively. Because the bridge is designed for four-lane traffic, the average daily truck traffic for a single lane is estimated to be

$$(ADTT)_{SL} = (3\% + 8\%) (12,500) / 4 = 344 \quad (5-1)$$

This indicates a low traffic volume on the bridge. In addition, a bypass for the city of Hutchinson is currently under construction. It is estimated that the traffic volume of the Arkansas River Bridge will be even less after the new bypass is completed.

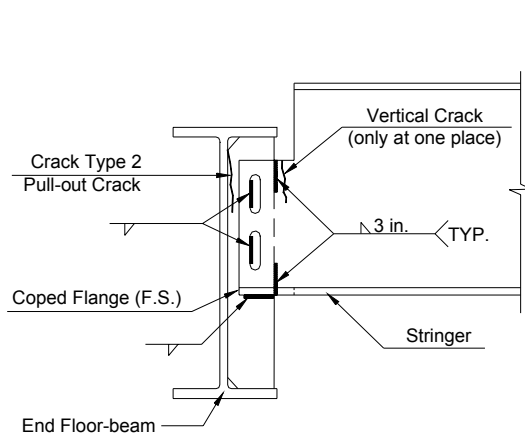
## **5.2 Fatigue Crack Observation**

During a scheduled bridge inspection in April 1995 and a follow-up inspection in May 1996, the KDOT Special Inspection Team identified a large number of fatigue cracks in the Arkansas River Bridge. Figure 5-1 shows the overall distribution of the cracks in the bridge. Cracks in the superstructure steel members are categorized into three major types. Type 1 cracks are broken welds at the stringer to floor-beam connections, as shown in Figure 5-3. Type 2 cracks occur at the expansion joints, either as pull-out cracks at the stringer to floor-beam connections, as shown in Figure 5-4(a), or as vertical cracks at the floor-beam to girder connections, as shown in Figure 5-4(b). Type 3 cracks are horizontal cracks developed at the floor-beam to exterior girder connection stiffeners, as shown in Figure 5-5.

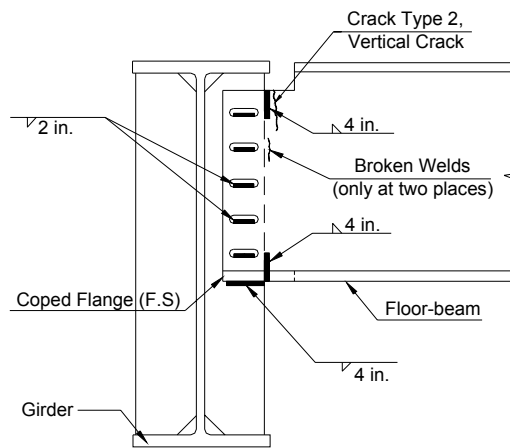


(a) typical stringer to floor-beam connection (b) broken welds marked during inspection

FIGURE 5-3: Type 1 Fatigue Cracking

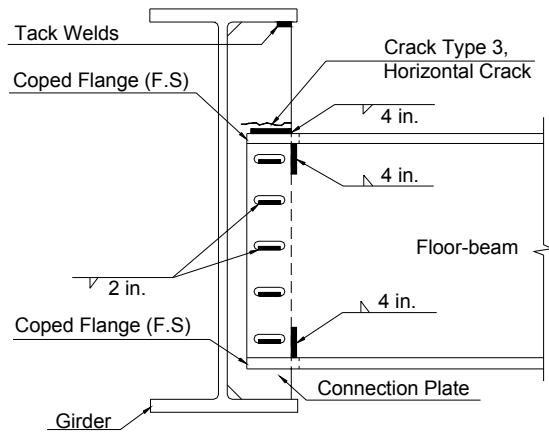


(a) pull-out crack at the stringer to floor-beam



(b) vertical crack at the floor-beam to girder connection

FIGURE 5-4: Type 2 Fatigue Cracking



**(a) typical floor-beam to exterior girder connection**



**(b) out-of-plane fatigue cracks in Girder A, Floor-beam 5-2**

**FIGURE 5-5: Type 3 Fatigue Cracking**

Table 5-1 summarizes the three types of fatigue cracking in the Arkansas River Bridge. The number of Type 1 crack for April 95 is listed as “Not Available” since this type of crack was not looked for in the 1995 inspection.

Also included in Table 5-1 and Figure 5-1 is an exceptional case, described as “other” crack type. Unlike the foregoing three crack types, this type of crack is found only at one place in the bridge at a floor-beam to interior girder connection.

**TABLE 5-1: Fatigue Crack Characteristics of the Arkansas River Bridge**

Crack Type	Crack Description		Number of New Crack Locations		Total Crack Number
			April 95	May 96	
1	Broken Welds at Stringer to Floor-beam Connections		N. A.	38	38
2	Cracks at the Expansion Joints	Pull-out Cracks at the Stringer to Floor-beam Connections	21	0	32
		Vertical Cracks at the Floor-beam to Girder Connections	11	0	
3	Horizontal Cracks in the Transverse Stiffeners at the Floor-beam to Exterior Girder Connections		34	5	39
Other	Vertical Crack at Floor-beam to Interior Girder Connection		1	0	1
Total Crack Number					110

***5.2.1 Crack Type 1 — Broken Welds at the Stringer to Floor-beam Connections***

The stringer/floor-beam system of this bridge consists of the longitudinal stringers sitting on top of the transverse floor-beams. Both edges of the stringer’s bottom flange are welded to the top flange of the floor-beam with 2 in. long fillet welds, as shown in Figure 5-3(a). Cracks initiated from one end of the weld termination and propagated to the other end under traffic loading, detaching the stringer completely from the floor-beam [Figure 5-3(b)]. However, even if the connection welds are broken, the load path from the stringer to floor-beam still remains intact. Therefore, Type 1 cracks do not affect the load carrying capacity of the bridge and no repair is needed at this crack location.

***5.2.2 Crack Type 2 — Fatigue Cracks at the Expansion Joints***

The Arkansas River Bridge has expansion joints located at Pier No. 5 and Pier No. 12. Two different crack details were observed at the expansion joints.

The first detail is found at the stringer to floor-beam connections. Cracks are mostly formed at the top end of the connection stiffener to floor-beam web weld, as shown in Figure 5-

4(a). This is reported as a “pull-out” crack. Only one connection also developed a crack at the top of the coped stringer web to floor-beam stiffener weld, which is reported as a “vertical” crack. During the 1995 inspection, 21 stringer to floor-beam connections at the expansion joints were found with fatigue cracks. Many of them have developed pull-out cracks on both sides of the stiffener. No new cracks were observed during the 1996 inspection, but 9 out of the original 21 cracks have propagated downward with growths ranging from  $\frac{1}{8}$  to  $1\frac{1}{4}$  in. Some even propagated into the floor-beam web.

The second detail is located at the floor-beam to girder connections. Cracks are mostly formed at the coped floor-beam web to girder bearing stiffener welds, as illustrated in Figure 5-4(b). This is reported as a “vertical” crack. During the 1995 inspection, 11 floor-beam to girder connections at the expansion joints were found to have developed fatigue cracking. Nine of the 11 are vertical cracks in the top connection welds. The remaining 2 are broken tack welds located between the top and bottom connection welds. As illustrated in Figure 5-4(b), there should be only two 4 in. vertical welds (one at the top and the other one at the bottom) at the floor-beam web to stiffener connection according to the original design. Tack welds were not specified, but were left after construction. No new cracks were reported in the 1996 inspection. However, 8 of the previous 11 locations were observed with crack growth. The maximum growth is about  $1\frac{1}{2}$  to 2 in. At the connection of Girder A and Floor-beam 5-3, the vertical weld failed completely on the east side, causing a 1 in. drop of the floor-beam at this end.

Both the pull-out and the vertical cracks developed from the top end of the weld connection between the longitudinal and transverse members, and then propagated vertically downward. There are 40 places at the two expansion joints where the longitudinal members (girders and stringers) and the transverse members (floor-beams) are connected, as shown in

Figure 5-1. Thirty-two (or 80%) of them have developed Type 2 cracks. These cracks could cause structural damage to some extent, both at the stringer to floor-beam connections and at the floor-beam to girder connections. However, no collapse mechanism would form in either case due to the structural redundancy at the bridge piers. An economical and simple retrofit is recommended by adding additional floor-beams along side the existing floor-beams at the expansion joints. No other repair technique (such as hole drilling) is needed. However, the crack propagation needs to be monitored until the repair is performed.

### **5.2.3 Crack Type 3 — Out-of-Plane Fatigue Cracks at the Floor-beam to Exterior Girder Connections**

Type 3 cracks developed at the floor-beam to exterior girder connections at the third points of girder spans. As shown in Figure 5-5(a), the floor-beam is connected to the stiffener by a 4 in. long horizontal weld at the top flange and two 4 in. long vertical welds at the web. In addition, there are five 2 in. long horizontal welds placed in slotted holes along the floor-beam web depth. Cracks initiated from the edge of the connection plate, at the place where the horizontal weld toe is located, and then propagated along the weld towards the girder web [Figure 5-5(b)]. Apparently, this type of crack is caused by out-of-plane floor-beam end moment. The tack weld connecting stiffener to girder top flange was found not broken. No web gap cracks developed at the stiffener-web-flange connections in this bridge.

Type 3 cracks were observed over much of the bridge. There are 68 floor-beam to exterior girder connections that are not at the bridge piers, as shown in Figure 5-1. Thirty-nine of them have developed Type 3 cracks. None of these cracks were found at the expansion joints or the negative moment regions, that is, at the floor-beam to girder connections at the bridge piers. This is because no differential girder deflections could occur at bridge supports. Also, no Type 3 cracks were found at the floor-beam to interior girder connections, because the

differential girder deflections are relatively small at these locations.

During the 1995 inspection, 34 cracks of this type were identified. In 1996, five new cracks were observed. Also during the 1996 inspection 14 out of the previous 34 crack locations were found with crack growth of about  $\frac{1}{8}$  to  $1\frac{1}{4}$  in. At the west side of Girder D and Floor-beam 13-1 connection, the horizontal crack even continued to propagate downward along the vertical stiffener-to-web welds by  $\frac{1}{2}$  in. Of the total 39 cracks found in the floor-beam to girder connections, the crack formed at the west side of Girder D, Floor-beam 13-1 has the maximum horizontal crack length of 5 in., and the crack formed at the east side of Girder A, Floor-beam 1-1 has the next maximum crack length of 4 in.

#### **5.2.4 Other Crack Type — Vertical Crack at the Floor-beam to Interior Girder Connection**

An exceptional crack type is found located in the west girder side of the connection between Floor-beam 13-1 and interior Girder C. As shown in Figure 5-6, the crack initiated from the top end of the floor-beam web to connection stiffener weld, and then progressed vertically downward. The crack shape is the same as those observed in Type 2 vertical cracks at the floor-beam to girder connections, but it is not located at the expansion joint, and is caused by out-of-plane distortion. Only one place in the bridge developed this type of crack, and the crack condition is not severe. The crack length is  $\frac{3}{4}$  in. observed during the 1995 inspection, and there is no indication of further propagation as per the 1996 inspection. The simplest way to repair this crack is to gouge out the original cracked weld and reweld the connection.

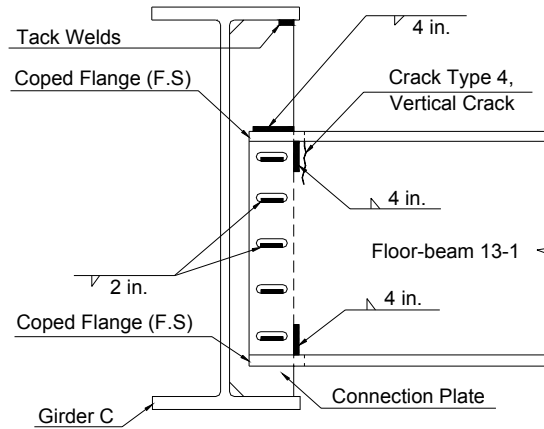


**Figure 5-6: Other Type of Fatigue Cracking**

Longitudinal girders are the primary load carrying members of the bridge. The Type 3 distortion-induced cracking in the connection plates provides a direct path for cracks to grow into the girder web, hence, jeopardizing the structural integrity of the bridge. To date, no cracks have been found to have propagated into the girder web. However, due to the importance of the floor-beam to girder connection, a thorough investigation for this type of crack should be conducted and an appropriate retrofit plan should be carried out to prevent crack propagation. The remaining part of this chapter thus focuses only on the study of the Type 3 fatigue cracking.

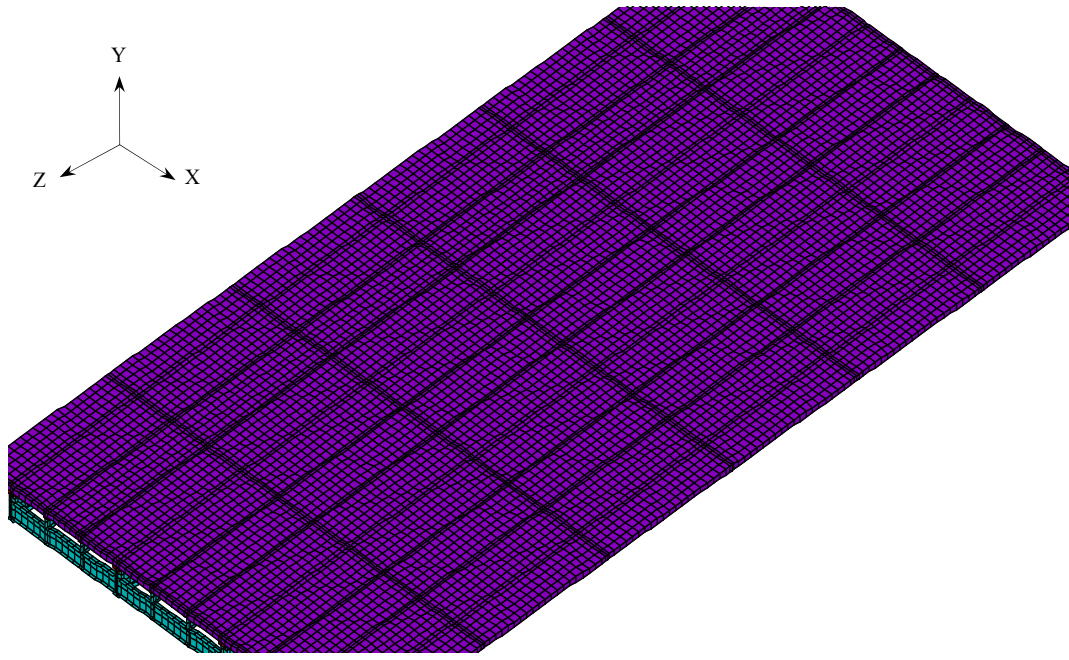
### **5.3 Finite Element Stress Analysis for Type 3 Cracks**

The out-of-plane distortion occurring at the floor-beam to exterior girder connections results from a three-dimensional interaction between different structural members under traffic loading. The connections are actually semi-rigid, according to the weld arrangement shown in Figure 5-5. To accurately interpret the stress field around the crack region, two consecutive procedures from coarse to refined model analyses are performed as follows. For issues regarding modeling techniques and fatigue evaluation procedures, see Chapters 4 and 5.

### **5.3.1 Coarse Model**

The bridge inspection result shows that Span No. 11 and 12 contain the largest number of fatigue cracks identified in the structure, therefore these two spans of the bridge are selected for detailed investigation. As shown in Figure 5-7, all the bridge superstructure components (flanges, webs, stiffeners, and deck) between Pier No. 10 and 12 are built into a large, coarse finite element model. This coarse model consists of 27,390 elements and 74,633 nodes, and requires at least 7 GB computer hard drive space to run the calculation. Figure 5-8 shows the element combination at a typical girder section. The steel members are modeled by eight-node shell elements along the center of the plate thickness. The deck slab is modeled by 8-node brick elements. The haunch between the deck slab and the girder (or stringer) top flange is modeled by 20-node brick elements. However, these 20-node brick elements are actually degraded to 16-node in order to form a transition between the linear deck brick elements and the quadratic flange shell elements. The four midside nodes of the haunch element surface connecting to the deck are removed. Coincident surfaces are generated at the places where the haunch bottom surface and the girder (or stringer) top flange are in contact. To model the noncomposite action between the deck and the girders (or stringers), each pair of the coincident nodes is coupled in the X and Y direction degrees of freedom. The Z direction degree of freedom is not coupled so that the deck and the girder (or stringer) can slide relative to one another along the bridge longitudinal direction. The boundary conditions applied to the coarse model at the pier locations are also shown in Figure 5-8. Pier No. 12 is an expansion joint, so the girder ends at this location should be modeled as rollers. The girder ends at Pier no. 10 should be approximated as fixed because the actual girders are continuous across the pier but the finite element model has to terminate at this point. The supports at Pier No. 11 should also be modeled as rollers since the girders are

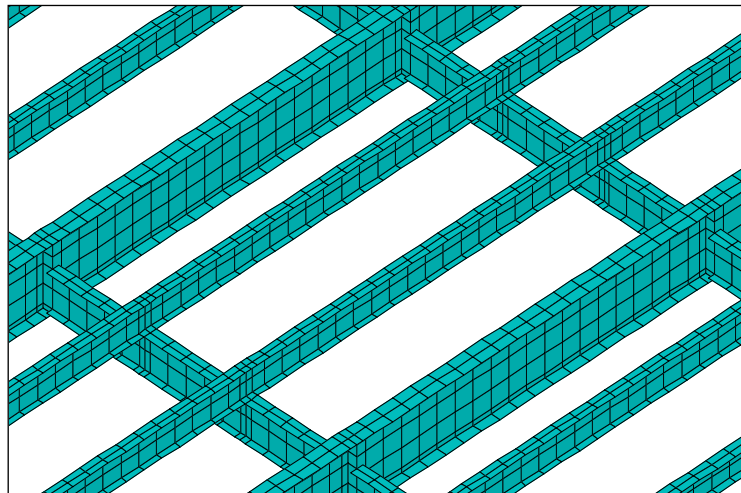
continuous across this location. Thus, the nodes at the girder bottom flanges along the centerlines of Pier No. 11 and 12 are restrained from translation in X and Y directions and rotation about Y and Z axes, while the girder bottom flange nodes along the centerline of Pier No. 10 are fixed for all translational and rotational degrees of freedom. The concrete modulus of elasticity is specified according to the American Concrete Institute (ACI) standard of  $57\sqrt{f'_c}$ , where  $f'_c$  (3000 psi for the concrete used in this bridge) is the compressive strength of concrete at 28 days.



(a) isometric view of the coarse model

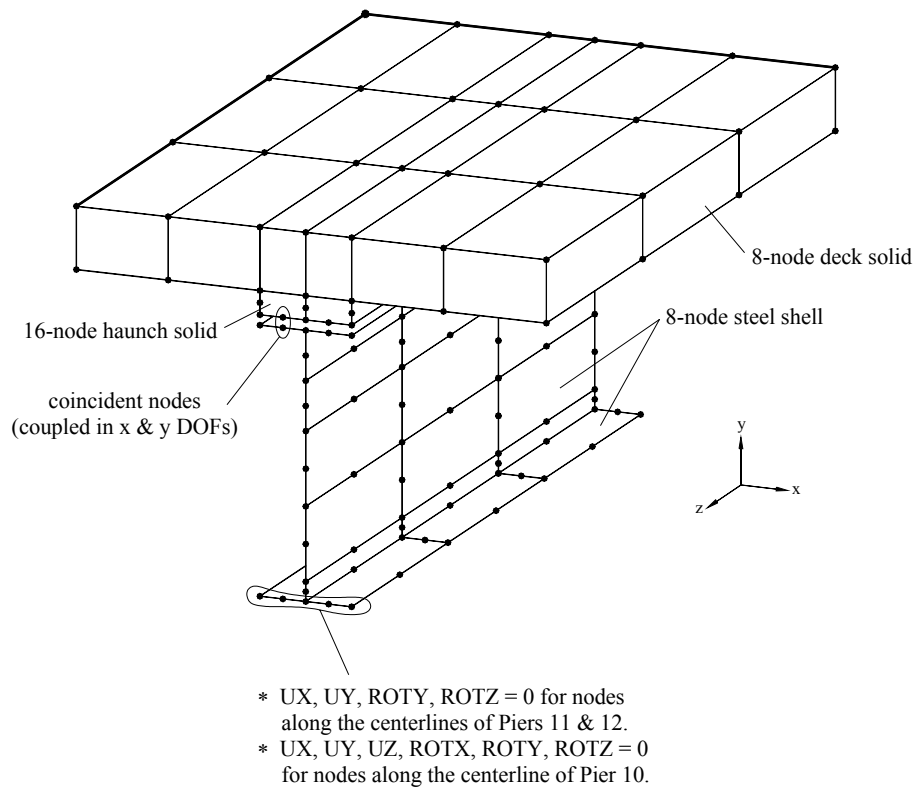


(b) cross section of the coarse model at the bridge pier



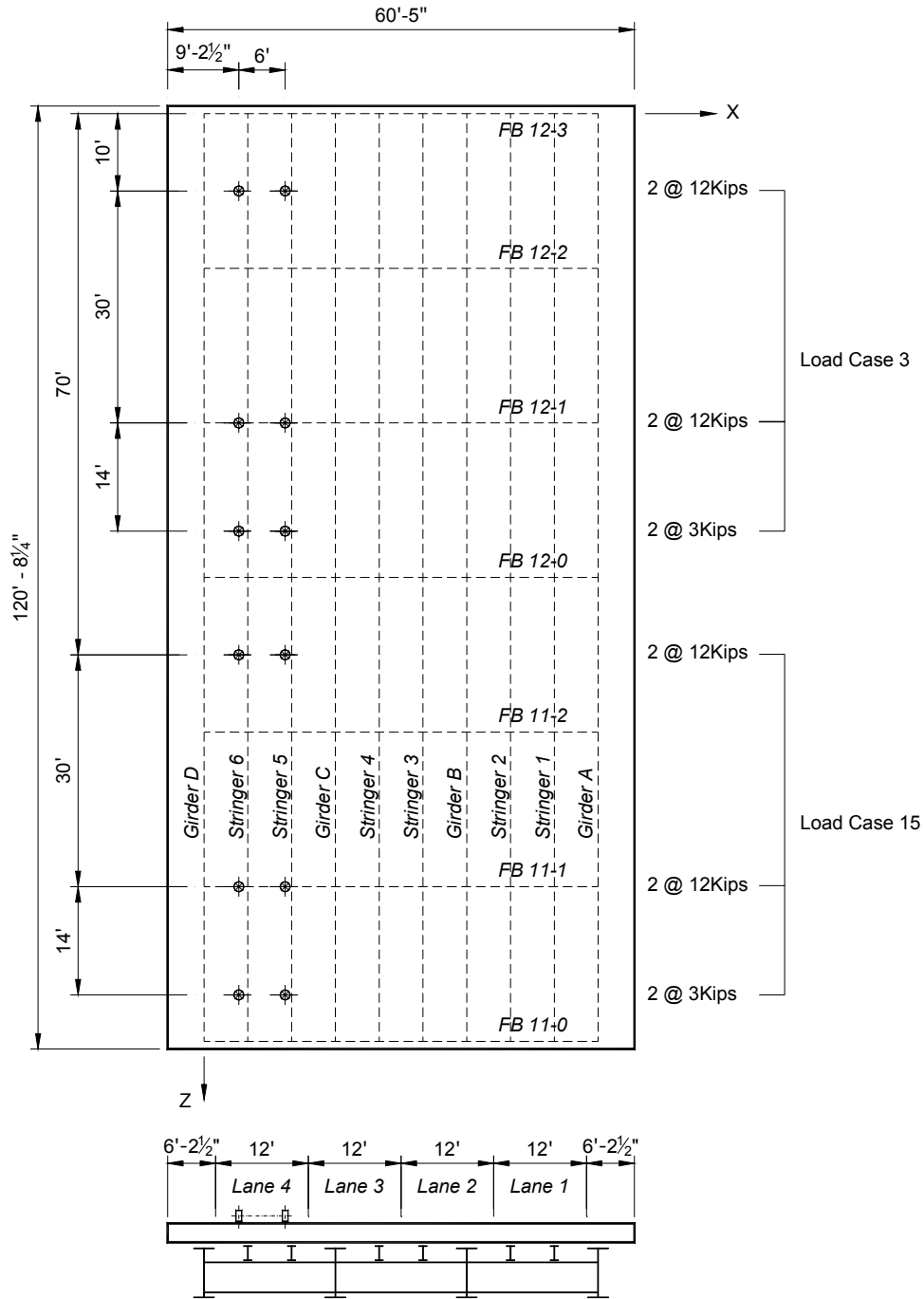
(c) element mesh of steel members under concrete deck

**FIGURE 5-7: Coarse Model of the Arkansas River Bridge Superstructure from Pier No. 10 to 12**



**FIGURE 5-8: Element Combination at a Typical Girder Section for the Coarse Model**

An HS15 fatigue truck is applied to conduct the coarse model analysis. As shown in Figure 5-9, the truck is positioned at the center of Lane 4, the driving lane close to Girder D. The distance between the exterior wheels and the deck edge is 9 ft 2½ in. Wheel loads are applied directly as nodal forces on top of the deck elements. Twenty load cases are performed by moving the truck from Pier No. 12 to Pier No. 10 in increments of 5 ft. The crack opening stresses for all the floor-beam to exterior girder connections are examined and the highest stress range is observed at Floor-beam 12-1 to Girder D connection, with the maximum stress occurring at load case 3 and the minimum stress occurring at load case 15. Figure 5-9 shows the truck location of these two load cases.



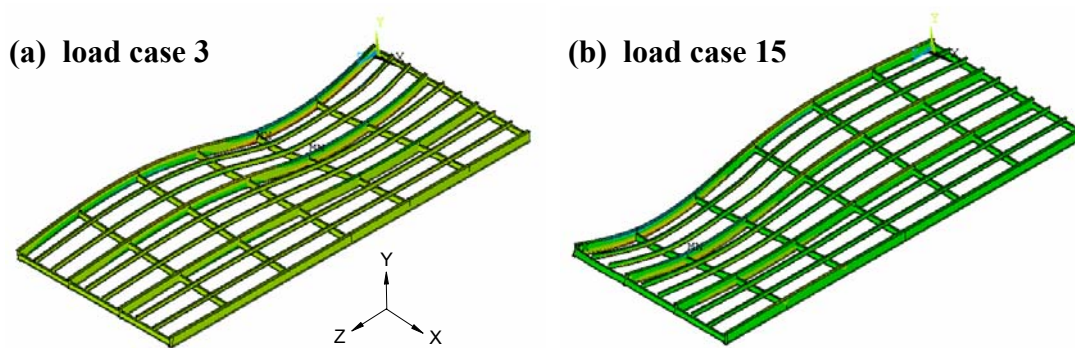
**FIGURE 5-9: Truck Location for Load Cases 3 and 15**

Figure 5-10 shows the overall deflection of the coarse model at load cases 3 and 15.

Deck elements are excluded from the plot in order to show the outline of the steel members.

Figure 5-11 shows the maximum stress that occurs at Floor-beam 12-1 to Girder D connection in

load case 3. The stress concentration is located at the floor-beam top flange to girder connection plate intersection, marked by point C in the figure. This is also the place where the out-of-plane fatigue cracking initiates in the actual bridge detail. Crack opening stress is in the vertical Y direction because the crack grows horizontally. For each load case, the extreme Y-stress occurring at point C could either be in tension, if the out-of-plane bending moment is negative at the floor-beam end; or in compression, if the out-of-plane bending moment is positive at the connection. The relative sliding between the haunch bottom surface and the girder (or stringer) top flange can also be observed from Figure 5-11.



**Figure 5-10 Deflection of steel members (deck elements are hidden)**

A fully composite model is also constructed during the investigation by merging all the coincident nodes at the girder-slab interface, in order to see the difference between the composite and noncomposite behavior of the bridge, and to explain to what extent this would influence the out-of-plane distortion. Results obtained for the connection of Figure 5-11 are used for the following discussion. Point A at the girder top flange and point B at the girder bottom flange are evaluated for the in-plane bending stress,  $\sigma_z$ , and point C at the crack initiation point is evaluated for the out-of-plane bending stress,  $\sigma_y$ . Table 5-2 lists the average nodal solution of

load case 3 for the specified locations of both the noncomposite and composite models. The bending stresses for the noncomposite case are -1.939 ksi at point A and 1.902 ksi at point B, which shows a symmetric stress distribution along the girder height. The bending stresses at the same girder section for the composite situation, however, are much lower, as can be predicted due to the interaction between the girder section and the deck slab. The top flange stress is 0.028 ksi at point A and the bottom flange stress is 1.371 ksi at point B. The neutral axis, therefore, lies above the steel section. Another big difference between the two models can be observed from the vertical girder deflection at this connection: 0.194 in. for the noncomposite condition, but only 0.076 in. for the composite condition. The in-plane flexural stiffness is increased significantly due to the bridge composite action. However, the performance caused by the out-of-plane distortion at this floor-beam to girder connection does not show much difference between the noncomposite and composite analysis results. The out-of-plane crack opening stress at point C is 3.783 ksi for the noncomposite model, and 3.294 ksi for the composite model. Only a small variation is observed. The same comparison procedure is then carried out to look at the results of other load cases and also at other floor-beam to girder connections. In most cases, the investigation shows a great difference between the noncomposite and composite results of the girder in-plane bending stress and vertical deflection. The out-of-plane bending stress, however, is not affected much by the composite or noncomposite action of this bridge.

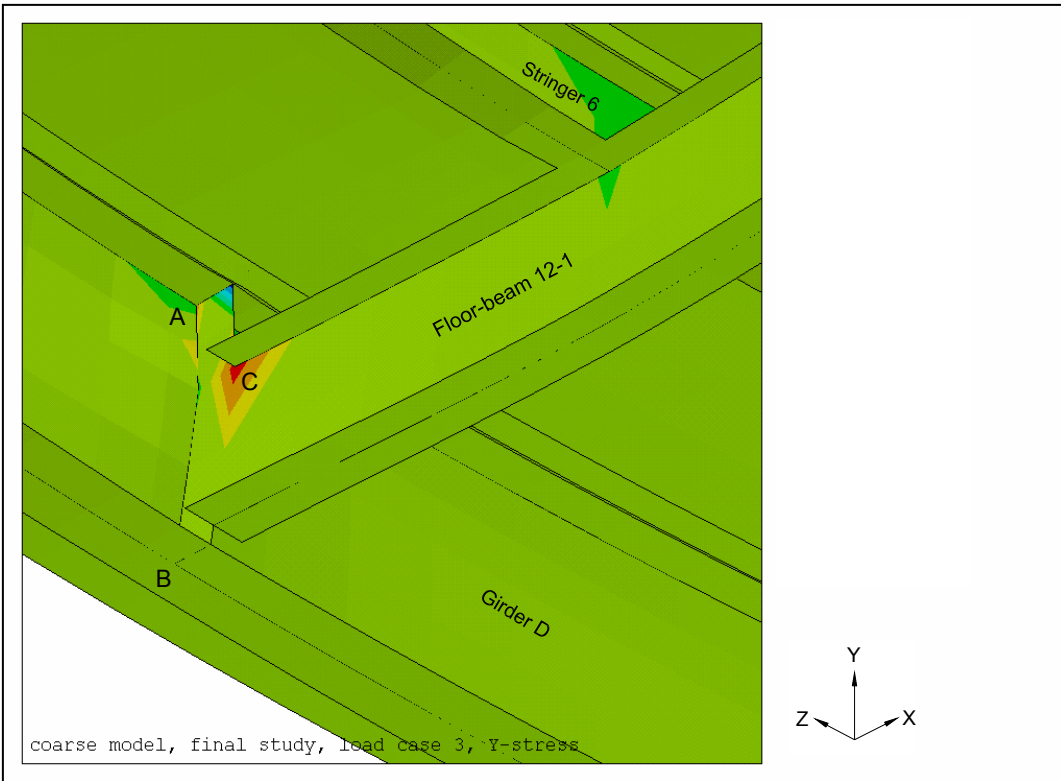


**FIGURE 5-11: Stress Concentration Occurring at Floor-Beam 12-1 to Girder D Connection at Load Case 3 (viewed from underneath the bridge)**

**Table 5-2: Comparison of noncomposite and composite analysis results for Floor-beam 12-1 to Girder D connection at load case 3 based on coarse model study**

Location in Figure 3-9	Data Evaluated	Noncomposite Results	Composite Results
A	In-plane bending stress at girder top flange, $\sigma_z$	-1.939 ksi	0.028 ksi
B	In-plane bending stress at girder bottom flange, $\sigma_z$	1.902 ksi	1.371 ksi
C	Out-of-plane bending stress at crack initiation point, $\sigma_y$	3.783 ksi	3.294 ksi
A, B, and C	Girder vertical deflection, $u_y$	-0.194 in.	-0.076 in.

The data listed in Table 5-2 are based on the coarse finite element model and are used only for the comparison between the noncomposite and composite analyses. The element mesh at this stage is not fine enough to produce satisfactory results, especially at the stress concentration point. To obtain an acceptable solution for the area of interest, a submodel needs to be built in order to conduct more detailed investigation of that region. The connection of Floor-beam 12-1 and Girder D is chosen for the subsequent submodeling since it experiences the highest stress range of all the floor-beam to girder connections of the coarse model.

### **5.3.2 Submodel**

Figure 5-12 shows the cut-off sections selected for submodeling. Compared to the coarse model [Figure 5-12(a)], the submodel [Figure 5-12(b)] geometry is modified at two places: the floor-beam flange cope and the connection plate width. As shown in Figure 5-12(a), for simplification purpose, the floor-beam flanges in the coarse model are stopped when they come to the connection plate, and the connection plate width is set the same as half of the girder flange width (6 in.). It reduces the model size and saves a lot modeling and computing time for the coarse model when these local details are neglected. To incorporate these details in the submodel

is much easier for the modeling procedure and the results should not be significantly affected since the modified region and the area of interest are away from the cut boundary. As shown in Figure 5-12(b), the coped floor-beam top flange is included and the actual connection plate width (5 in.) is used for the submodel. To make sure the solution of the submodel is not changed by the local details, another submodel is created for comparison, with exactly the same geometry as cut from the coarse model. The average nodal solution at the stress concentration point shows only 2 percent difference before and after the changes are made. Thus the modification included in the submodel is acceptable.

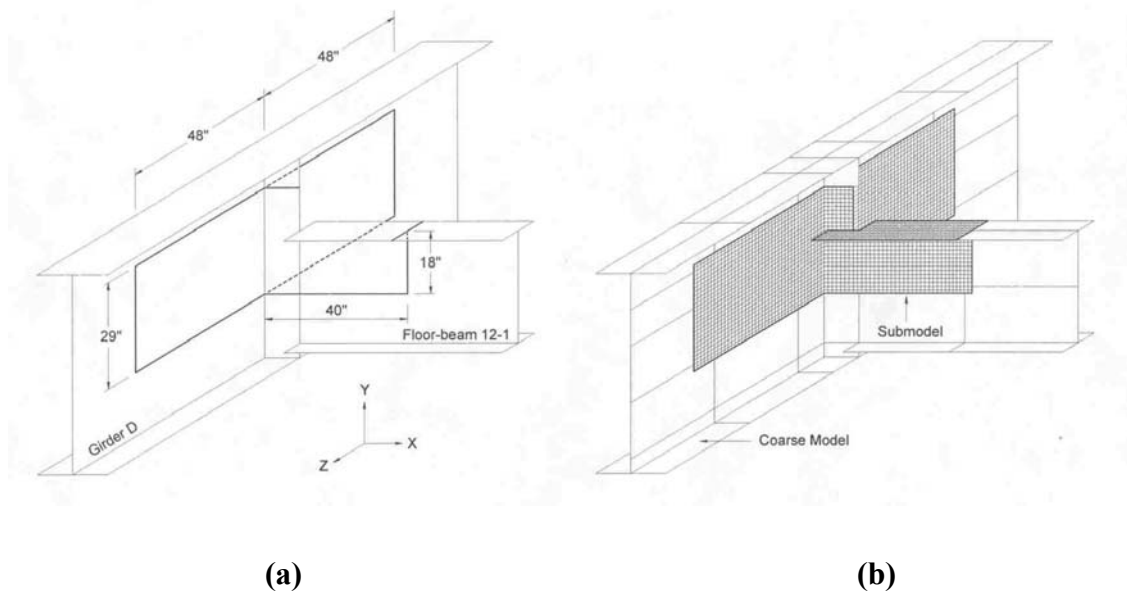


**FIGURE 5-12: Submodeling of the Crack Region**

For all twenty load cases, the cut boundary DOF interpolation is performed and the analysis for the submodel is conducted. The computed Y direction stresses for each load case at the stress concentration point and the point 3 in. above it are tabulated in Table 5-3. Figure 5-13 shows schematically the stress variation of these two locations corresponding to different load cases. The plotted curves indicate that the entire 20 load cases can be divided into two major stress cycles. The first one starts at load case 1 and ends at load case 6. The second one starts at

load case 6 and ends at load case 15. Load cases 15 to 20 could also be counted as part of the second stress cycle, since the truck loading positions are away from the investigated connection and no more peak stresses would occur during these load cases.

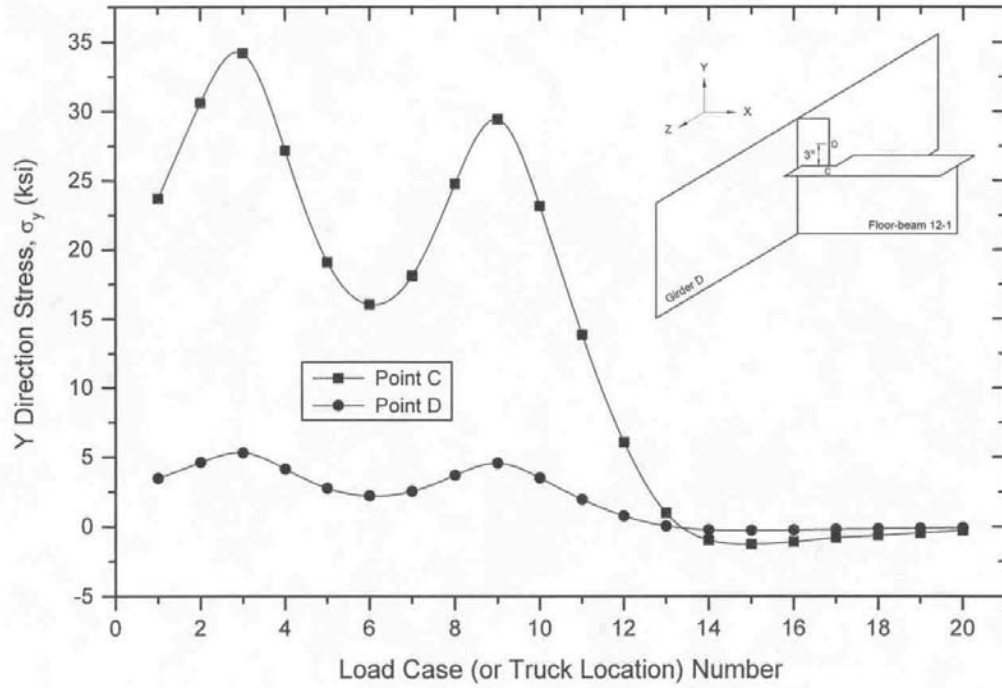


**FIGURE 5-13: Out-of-Plane Stress Variation at Floor-Beam 12-1 to Girder D Connection**

**Table 5-3 Y direction stresses obtained from the submodel analysis**

load case	Y-stress, $\sigma_y$ (ksi)		extreme cases
	stress concentration point <sup>a</sup>	3" above the concentration <sup>b</sup>	
1	23.7050	3.4771	Max.
2	30.6010	4.6164	
3	34.1720	5.3143	
4	27.1510	4.1404	
5	19.0860	2.7537	
6	16.0170	2.2080	
7	18.1020	2.5495	
8	24.7540	3.7017	
9	29.4240	4.5672	
10	23.1310	3.4965	
11	13.8410	1.9528	
12	6.0730	0.7669	
13	0.9611	0.0324	
14	-0.9836	-0.2404	Min.
15	-1.2770	-0.2821	
16	-1.0960	-0.2505	
17	-0.8105	-0.1993	
18	-0.6442	-0.1629	
19	-0.4631	-0.1265	
20	-0.2779	-0.0867	

Note: <sup>a</sup>marked as point C in Figures 5-13 & 5-14.

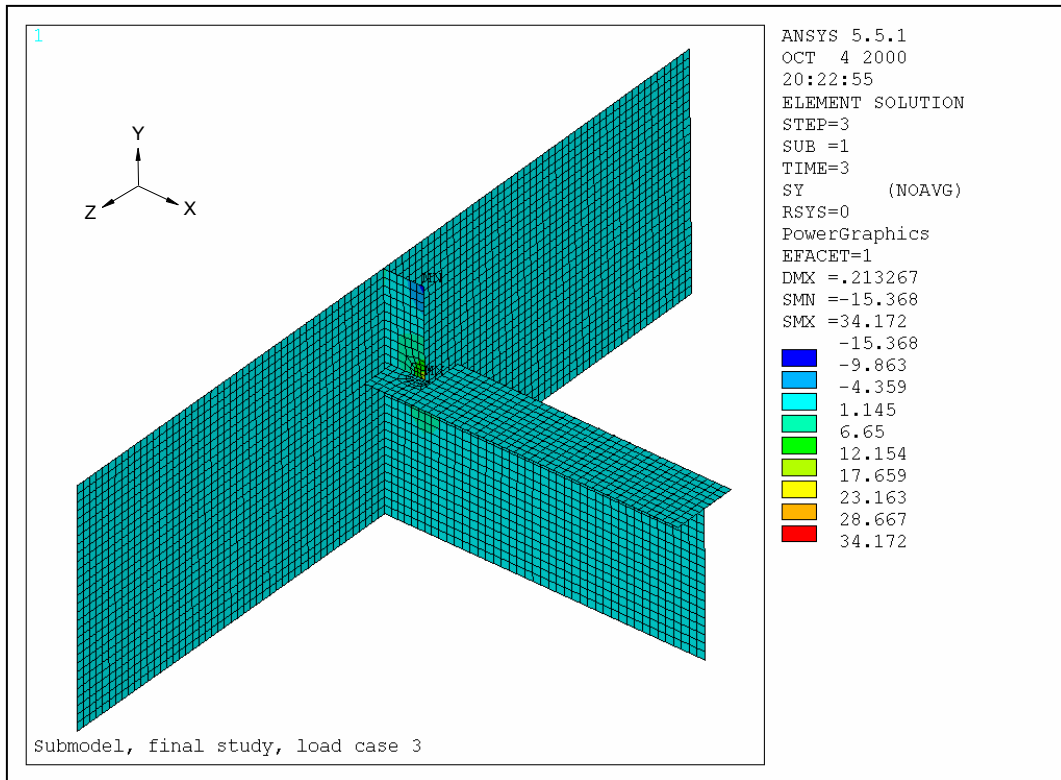
<sup>b</sup>marked as point D in Figures 5-13 & 5-14.

Both point C at the stress concentration and point D located 3 in. above have the same stress fluctuation pattern. However, the amplitude of stress variation at point C is much higher due to the effect of stress concentration. This is the place where the actual out-of-plane fatigue cracks originate in the bridge. As listed in Table 5-3, the submodel solution shows that the maximum tensile stress at point C is 34.172 ksi, occurring at load case 3, and the maximum compressive stress is -1.277 ksi, occurring at load case 15. This is the same location where the highest stress range was observed in the coarse model analysis. However, the numerical values are extremely different. Recalling the results listed in Table 5-2 for the coarse model, the Y-stress for the same point C at load case 3 is only 3.783 ksi, which is about one tenth of the

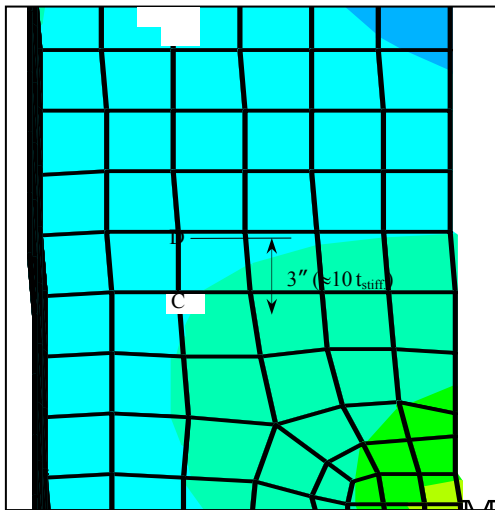
submodel solution. The finely meshed submodel thus presents the stress condition around the localized region with much more accuracy.

Figure 5-14 shows the Y direction stress contour for the submodel at load case 3, based on ANSYS element solution. Figure 5-14(a) shows the overall element mesh and stress distribution of the submodel. Figure 5-14(b) and (c) illustrate the detailed stress condition at the floor-beam top flange to stiffener plate connection. The elements around the crack initiation point are doubly refined in order to obtain more accurate results at this location. From the stress distribution contour it can be noted that the out-of-plane bending effect is highly localized. The maximum stress at the concentration point is close to yielding, but the stress a few inches away soon decreases to a very small value. This also happens in the other load cases. The stress within the concentration area changes abruptly, while those on the rest of the model remain stable and low.

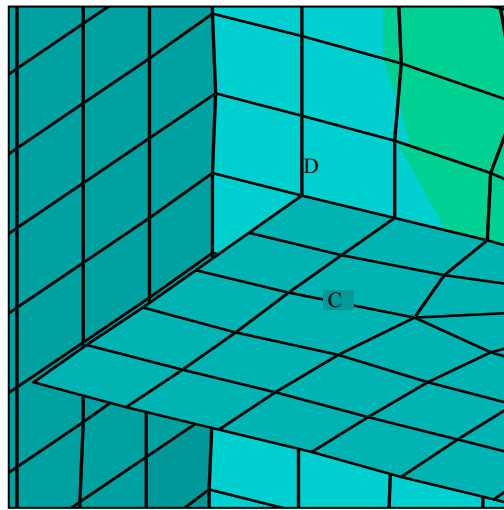
The region of stress concentration is confined within the area of the stiffener plate, as shown in Figure 5-14(b). Theoretically, the stress at the concentration point C can approach infinity for a linear analysis. The finer the element mesh used around this point, the higher the calculated crack opening stress. In the actual structure, a plastic zone will form around the concentration point when the stresses reach yielding. However, for most of the bridge crack details, this plastic zone is very small and non-linear analysis is not needed. Thus, it is the modeler's decision to choose a reasonably small element mesh size at the stress concentration area so that the computed peak stress magnitude is accurate and stable enough to explain the crack opening phenomenon. In some circumstances, it does take a few trial and error adjustments before the result reaches stable.



(a) overall  $\sigma_y$  stress distribution for the submodel



(b) shape of stress concentration area



(c) stress concentration point

Figure 5-14 Submodel element solution for Y direction stress at load case 3

The stress intensity factor expression given by Equation 3-1,  $K_I = \sigma \sqrt{\pi a} F$ , requires that a far field stress  $\sigma$  be used to determine the stress intensity of the crack region. Therefore, before  $K_I$  factor can be calculated, a normal stress outside the concentration zone should be determined first. For this study, the location 3 in. above the stress concentration point is used to specify the normal stress, as indicated by point D in Figure 5-13 and 5-14(b), (c). The distance between points C and D is close to ten times the stiffener plate thickness and is assumed to be far enough away from the stress concentration. This assumption is conservative, as the stresses further away soon decrease to zero. As known from Table 5-3, the maximum stress at point D is 5.314 ksi at load case 3, and the minimum stress is -0.282 ksi at load case 15. Calculation of the stress intensity factor and its application for fatigue life evaluation will be presented in section 5.4.

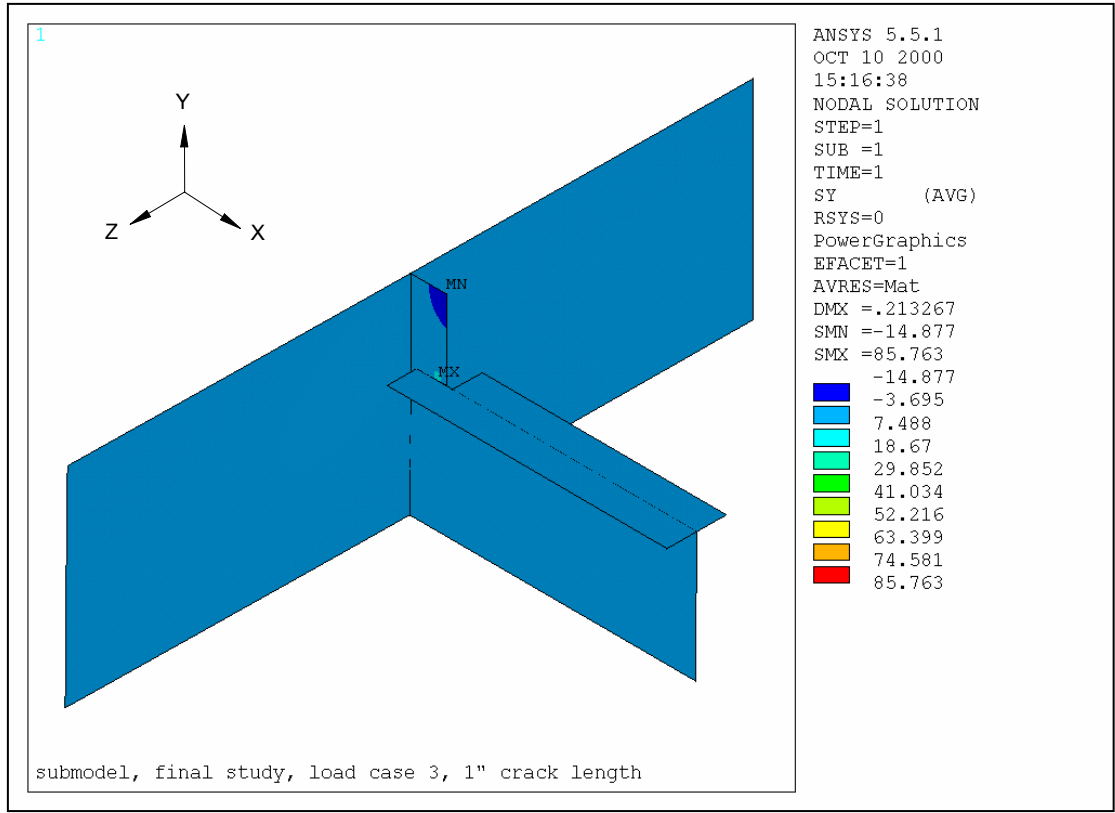
### **5.3.3 Unzipping fatigue cracks**

Different out-of-plane crack dimensions have been observed in the Arkansas River Bridge at the floor-beam to exterior girder connections. Therefore it is interesting to know how the stress field at the concentration region changes when the crack grows progressively. A series of coarse-to-fine submodeling analyses are conducted by introducing crack sizes from 0.5 in. to 4 in., with an extension of 0.5 in. for each unzipping step. Only linear finite element analysis is carried out, and the following parameters obtained from the ANSYS results are studied for the effect of crack growth: the normal stresses, the crack mouth opening displacements, and the stress intensity factors.

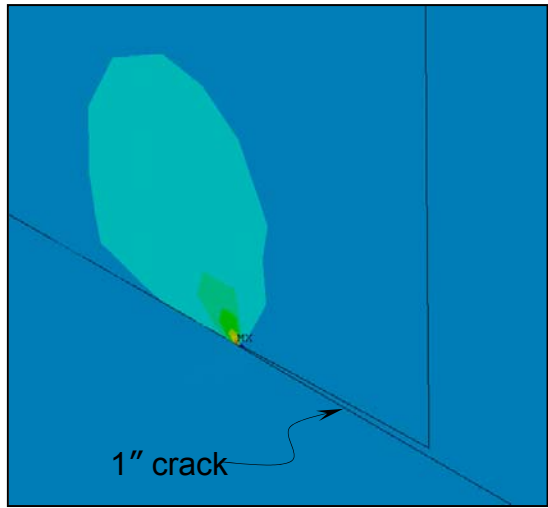
Figure 5-15 shows the finite element solution for the submodel of 1 in. crack. Most places on the model indicate close to zero stresses and the stress concentration is localized only in a small area around the crack tip. As already predicted, the stresses and strains at the crack tip are singular due to the linear elastic analysis. To pick up the singularity in the strain, the two

crack faces are modeled as coincident lines in the fracture model, and the first row of elements around the crack tip are reduced to the shape of isosceles triangles with midside nodes placed at the quarter points. Such elements are called singular elements; they have the same node at the crack tip. ANSYS allows controlling the size of the elements of the first two rows around the crack tip. As shown in Figure 5-15©, the radius of the crack tip elements is 0.02 in., and the size of the second row elements is 0.04 in. Although non-linear analysis is not performed, the plastic zone size is very small as can be estimated approximately from the linear elastic stress contour. Load case 3 again is found to have the severest stress condition; therefore results from other load cases are not reported.

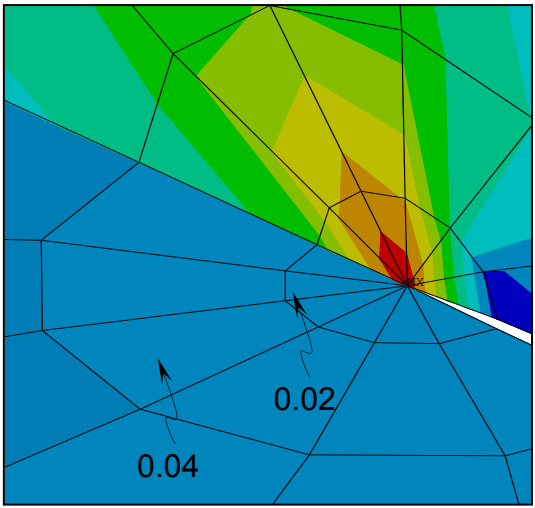
The same modeling procedure is carried out for study of the floor-beam to girder connections of different crack dimensions. For every 0.5 in. crack growth, the geometry of both the coarse model and the corresponding submodel is modified for a new set of analysis, and the ANSYS computation is performed for load case 3 only. By using submodeling method, the cut boundary interpolation provides a consistent displacement mapping procedure between the coarse and the refined models, thus the changes of the out-of-plane rotational stiffness can be directly and accurately presented through the finite element solution. Figure 5-16 shows that for a specified crack size  $a$ , the Y direction stress at 3 in. above the crack tip, point E', is defined as the normal stress, and the maximum relative displacement between the two coincident crack surfaces is measured as the crack mouth opening displacement, CMOD. The stress at the crack tip, point E, is always much higher than yielding due to the stress concentration effect, and thus is not used for evaluation.



(a) overall stress distribution in the submodel

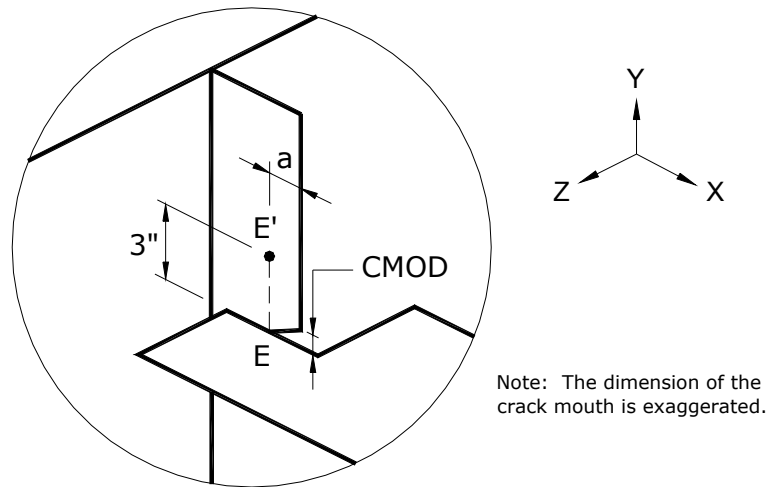


(b) stress concentration



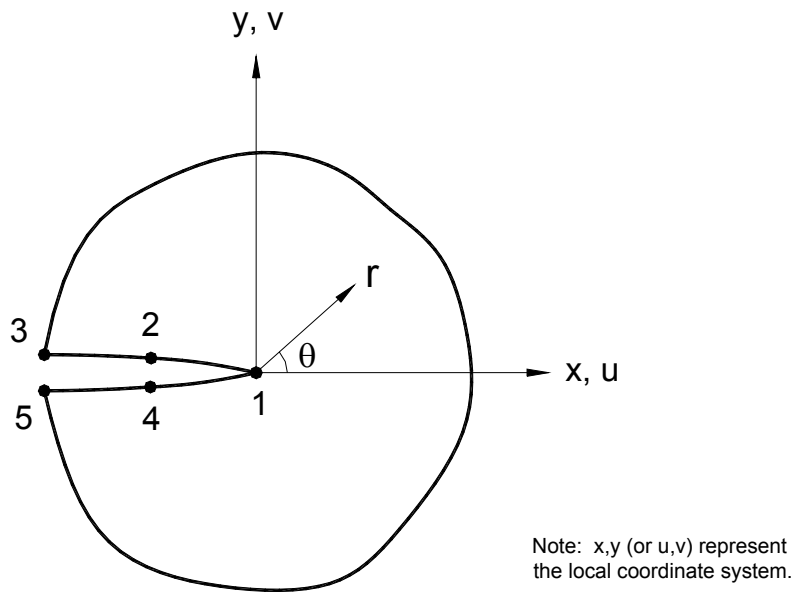
(c) stress field ahead of crack tip

**FIGURE 5-15: Load Case 3 Y-Stress Contour of the Submodel with 1 inch Crack**



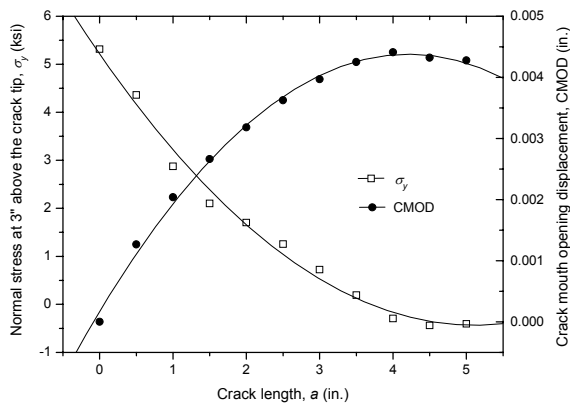
**FIGURE 5-16: Schematic Showing Locations for Normal Stress and CMOD Measurement**

Plane stress condition is assumed for analyzing the fracture terms. ANSYS calculates stress intensity factors based on the displacements along the specified crack path as shown in Figure 5-17. A local crack tip coordinate system has to be established first with X axis oriented parallel to the crack face and Y axis oriented perpendicular to the crack face. The crack path is then defined by specifying five nodes along the crack surfaces: one at the crack tip, and two on each of the crack faces. The fracture parameters obtained from the submodel analyses for different crack sizes are listed in Table 5-4 and are plotted in Figure 5-18 and 5-19.



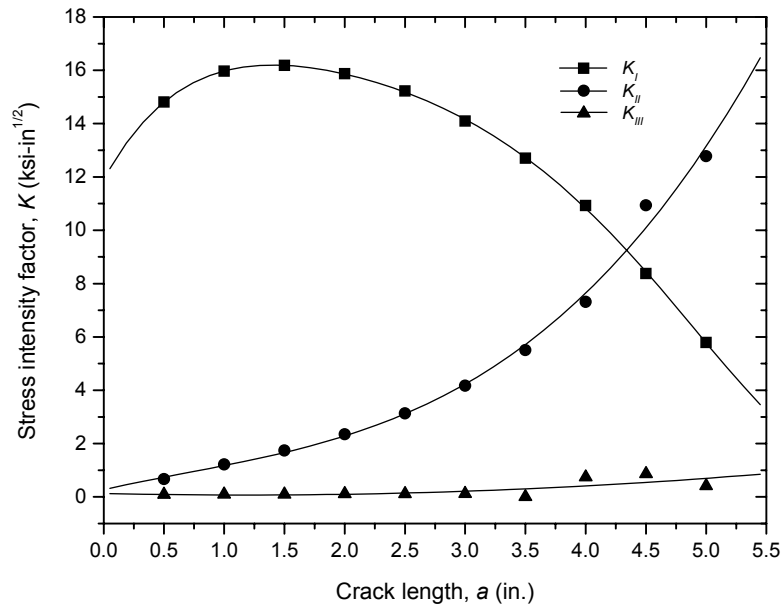
**FIGURE 5-17: ANSYS Typical Path Definition for a Full Crack Model**

Figure 5-18 shows the normal stress and CMOD development corresponding to the crack growth. The normal stress decreases gradually when the crack is unzipped and even becomes negative when the crack propagates to above 4 in. This indicates that the stress field around the crack region is relaxed and the restraint at the floor-beam to girder connection is softened when the crack size increases, thus slowing down the crack opening process. However, the crack propagation is not able to be self-stabilized, because the stresses ahead of the crack tip are still in tension and will continue to pull the crack apart though in a relatively slower manner.



**FIGURE 5-18: Correlation of Normal Stress and CMOD with Crack Growth**

Figure 5-19 describes the change of stress intensity factors with respect to the increase of crack size. Of the three basic modes of crack surface displacements, the opening mode (Mode I) is predominant when crack size is less than 4 in., and the relationship of  $K_I > K_{II} > K_{III}$  can be identified during the earlier 80percent of the fatigue crack development. When crack size exceeds 4 in., the shearing mode (Mode II) becomes the governing element of the fracture behavior. In general,  $K_I$  drops down when crack size increases, which confirms that the stress condition that tends to open the crack apart is alleviated with the increase of crack length. The  $K_{II}$  value, however, goes up with the increasing crack size, as the sliding mode starts to show its effect when the crack opening process slows down.  $K_{III}$  factor remains close to zero throughout the whole crack propagation, because most of the out-of-plane displacements at the crack faces occur in the plane of the stiffener plate, and thus cracking in the mode of tearing (Mode III) is not sufficiently formed.



**FIGURE 5-19: ANSYS Stress Intensity Factor Results for Three Basic Crack Modes**

**TABLE 5-4: ANSYS Load Case 3 Solutions for Submodels of Different Crack Sizes**

Crack Size a (in.)	Normal Stress $\sigma_y$ (ksi)	CMOD ( $\times 10^{-3}$ in.)	Stress Intensity Factors (ksi $\sqrt{\text{in.}}$ )		
			$K_I$	$K_{II}$	$K_{III}$
0.5	4.358	1.267	14.810	0.664	0.0882
1.0	2.874	2.038	15.967	1.218	0.0928
1.5	2.099	2.662	16.182	1.738	0.0965
2.0	1.703	3.181	15.875	2.347	0.1080
2.5	1.255	3.625	15.221	3.134	0.1109
3.0	0.723	3.970	14.096	4.170	0.1153
3.5	0.190	4.250	12.704	5.506	0.0004
4.0	-0.294	4.410	10.928	7.312	0.7400
4.5	-0.440	4.321	8.373	10.937	0.8612
5.0	-0.406	4.276	5.793	12.779	0.4096

Only the results of load case 3 are discussed in this section. For the analysis of all the fracture models of different crack sizes, this is always the case that causes the severest crack opening stresses, the largest crack opening displacements, and the highest stress intensity factors. Those load cases that cause crack closure are not investigated, because the stiffener section, although cracked, is not really reduced when carrying the compressive stresses under the positive out-of-plane bending moment. Therefore they are assumed to have the same stress results as obtained from the uncracked submodel at the corresponding load cases.

#### 5.4 Fatigue Life Evaluation

The fracture mechanics theories addressed in section 3.2 are adopted in this section to evaluate fatigue life for the out-of-plane crack details of the Arkansas River Bridge. As indicated by Equation 3-5 for the stress cycle integration, the problem now reduces to the determination of the stress intensity range  $\Delta K$ . In particular,  $\Delta K_I$ , the stress intensity range for Mode I, the opening mode, should be used for stress cycle calculation, as it is the governing parameter that is

responsible for the out-of-plane fatigue cracking. The geometry and the stress distribution at the crack locations of this bridge do not match those of the standard crack types such as shown in Figure 3-1, thus special assumptions need to be proposed when solving  $\Delta K_I$  for the crack details. Two different methods are discussed in sections 5.4.1 and 5.4.2 to show the different approaches used in this study for fatigue life estimation. The first method uses the traditional stress intensity factor formula of a single edge crack under uniform loading. The second method uses the stress intensity factors obtained directly from the ANSYS crack unzipping analysis. Both results are then used to compare with the data provided by KDOT traffic count.

**5.4.1 Fatigue Life Calculated by Using Conventional  $K_I$  Formula**

The  $K_I$  formula in Equation 3-1 shows that the stress intensity factor is a function of the crack size  $a$ , the far field stress  $\sigma$ , and the geometry factor  $F$ . For a thin plate with an edge notch under the constant amplitude fatigue loading  $\Delta\sigma$ , as shown in Figure 5-20, the stress intensity range at the crack tip can be written as:

$$\Delta K_I = \Delta\sigma \sqrt{\pi a} F(a/b) \tag{5-2}$$

where:  $\Delta\sigma$  = normal stress range, ksi.

$F(a/b)$  = geometry factor for single edge crack, depending on the ratio of the crack size  $a$  vs. the plate width  $b$ .

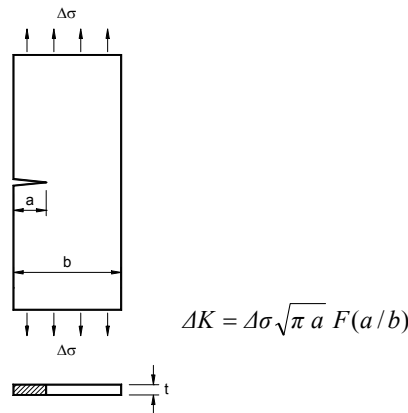


**FIGURE 5-20: Single Edge Notched Plate**

The horizontal crack developed in the stiffener plate of the Arkansas River Bridge is shaped like an edge crack, but the stresses in the far field are not uniform. The coarse-to-fine submodeling analysis carried out in section 5.3.3 shows that the normal stress at 3 in. above the crack tip decreases when the crack size increases. As illustrated in Figure 5-21, in order to use Equation 5-2, the maximum Y direction stress range occurring at point D, 3 in. above the crack initiation point C, is used and is assumed to be constant throughout the entire crack propagation. The maximum and minimum stresses at this point occur in load cases 3 and 15, respectively, as previously mentioned in section 5.3.2. The “nominal” uniform stress range for the cracked stiffener plate could then be obtained by finding the differential value between the two extremes:

$$\Delta\sigma = \sigma_{\max} - \sigma_{\min} = 5.314 - (-0.282) = 5.6 \text{ ksi} \quad (5-3)$$

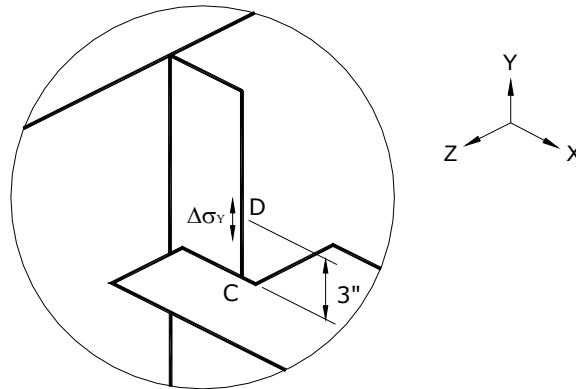


**FIGURE 5-21: Location of the Maximum Normal Stress Range Used for Fatigue Life Calculation**

The geometry factor  $F(a/b)$  for single edge crack is available in different mathematical expressions. The three most commonly used empirical formulas are given in Equation 5-4 to 5-6 [Tada et la, 2000]. The first expression was proposed by Gross and Brown using least squares fitting, and the other two were presented by Tada.

- a. Gross (1964) and Brown (1966), 0.5% accuracy for  $a/b \leq 0.6$

$$F(a/b) = 1.122 - 0.231(a/b) + 10.550(a/b)^2 - 21.710(a/b)^3 + 30.382(a/b)^4 \quad (5-4)$$

- b. Tada (1973), better than 1% accuracy for  $a/b < 0.2$ , 0.5% accuracy for  $a/b \geq 0.2$

$$F(a/b) = 0.265(1 - a/b)^4 + \frac{0.857 + 0.265a/b}{(1 - a/b)^{3/2}} \quad (5-5)$$

- c. Tada (1973), better than 0.5% accuracy for any  $a/b$

$$F(a/b) = \sqrt{\frac{2b}{\pi a} \tan \frac{\pi a}{2b}} \cdot \frac{0.752 + 2.02(a/b) + 0.37(1 - \sin \frac{\pi a}{2b})^3}{\cos \frac{\pi a}{2b}} \quad (5-6)$$

The  $F(a/b)$  factors corresponding to different  $a/b$  ratios are listed in Table 5-5 for the above three equations. Figure 5-22 shows that the  $F(a/b)$  values calculated by different methods are almost the same until  $a/b$  reaches 0.6, after which the curves diverge, with the two Tada curves remaining close together, while the Gross and Brown curve rises more slowly. For most steels, because  $F(a/b)$  increases rapidly after  $a/b$  exceeds 0.5, the stress intensity factor  $K_I$  soon reaches its upper limit, the critical stress intensity factor, or the fracture toughness,  $K_{IC}$ . Therefore,  $F(a/b)$  data for  $a/b > 0.5$  are not frequently used.

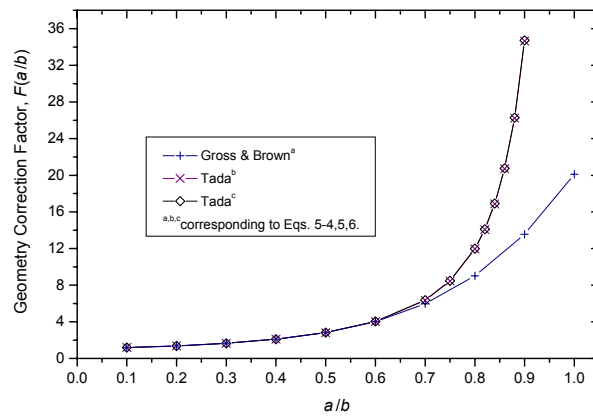


**FIGURE 5-22: Change of Geometry Factors vs.  $a/b$  Ratio for Different  $F$  Formulas**

**TABLE 5-5: Geometry Correction Factors for a Single Edge Notched Plate**

$a/b$	$\pi a/2b$	$F(a/b)$		
		Gross & Brown <sup>a</sup>	Tada <sup>b</sup>	Tada <sup>c</sup>
0.1	0.157	1.1857	1.2086	1.1957
0.2	0.314	1.3727	1.3803	1.3667
0.3	0.471	1.6621	1.6627	1.6551
0.4	0.628	2.1059	2.1064	2.1080
0.5	0.785	2.8291	2.8153	2.8266
0.6	0.942	4.0295	4.0229	4.0432
0.7	1.100	5.9780	6.3466	6.3755
0.8	1.257	9.0181	11.9522	11.9926
0.9	1.414	13.5666	34.6428	34.7187
1.0	1.571	20.1130	$\infty$	$\infty$

Note: <sup>a, b, c</sup> Formulas are provided by Equations 5-4, 5 and 6.

Either one of the three aforementioned formulas can be used for Equation 5-2, because the  $F(a/b)$  factors provided by these three methods are almost identical before  $a/b$  reaches 0.6. The first Tada expression, Equation 5-5, is then chosen for the subsequent analysis.

The steel members used in the Arkansas River Bridge were all fabricated from ASTM A373. A review of the mill reports for this bridge indicates that all of the material satisfies the mechanical and chemistry requirements of the specifications. The chemical composition, yielding and tensile strengths of the steels used in this bridge are tabulated in Table 5-6. The respective properties defined by ASTM standard for the A373 steel are listed in Table 5-7. The standard minimum yield and tensile strengths of 32 ksi and 58 ksi, respectively, are then used for Equation 3-4. Thus the stress intensity range at the Region II to Region III transition,  $K_T$ , is about 47 ksi $\sqrt{\text{in}}$ .

The critical stress intensity factor  $K_{IC}$  is a material property varying in accordance with the service temperature, the loading rate, and the constraint of the crack detail. However, the fracture toughness of the steel used in this bridge is not available. Based on information

provided by other researches [Roddis, 1988; Fisher, 1984], an overall  $K_{IC}$  of 80 ksi $\sqrt{\text{in.}}$  is assumed in this study regardless of the influences such as temperature change.

**TABLE 5-6: Ranges of Tested Properties Documented by Mill Reports**

Composition (%)				Yield Strength (ksi)	Tensile Strength (ksi)
C	Mn	P	S		
0.18 ~ 0.27	0.56 ~ 0.76	0.005 ~ 0.026	0.020 ~ 0.035	33.22 ~ 54.51	60.10 ~ 79.03

**TABLE 5-7: Standard Properties Specified for ASTM A373 Steel**  
**[NCHRP 321, 1989]**

Composition (%) (single values are maximum)				Minimum Yield Strength (ksi)	Tensile Strength (ksi)
C	Mn	P	S		
0.30	0.50 ~ 0.90	0.05	0.063	32	58 ~ 75

Now that the stress range and the geometry factor have been determined, the fatigue life of the crack detail can be obtained by combining Equation 3-5 and 5-2. The initial crack size is assumed to be 0.15 in. This was used by Fisher [1984] for the fatigue life evaluation of the out-of-plane web gap cracks in the Des Moines Bridge and the Poplar Street Approach Bridges, and is thus assumed to be a reasonable crack initiation size here for this study. The critical crack size is 5 in., using the stiffener plate width, which is also the maximum crack size that has been observed during the inspection. The number of stress cycles corresponding to any crack size  $a$  can be calculated by substituting  $a$  for  $a_{critical}$  in Equation 3-5. Table 5-8 shows the fatigue life

calculation by accumulating the number of loading cycles obtained within each small segment of crack growth. Notice that at  $a/b = 0.52$ ,  $\Delta K_I$  exceeds  $K_T$ . Past this point the crack grows rapidly and the remaining number of stress cycles is only a small fraction of that experienced before  $K_T$  is reached. At  $a/b = 0.64$ ,  $\Delta K_I$  reaches  $K_{IC}$ , the geometry factor  $F(a/b)$  does not apply further on, and  $\Delta K_I$  is then kept constant of  $80 \text{ ksi} \sqrt{\text{in.}}$  until  $a_{critical}$  is reached. The total number of loading cycles calculated based on this method is  $5.733 \times 10^6$ .

#### **5.4.2 Fatigue Life Calculated by Using ANSYS $K_I$ Results**

The submodeling analysis carried out for the crack unzipping process yields the finite element based  $K_I$  results at the crack tip for every 0.5 in. crack growth. As discussed in section 5.3.3, the stress intensity factors are calculated according to a path composed of five nodes specified along the crack surfaces. The maximum  $K_I$  factors for all crack sizes occur at load case 3, which are tabulated in Table 5-5 and plotted in Figure 5-19. The minimum  $K_I$  factors are considered to be zero for those load cases that cause crack closure. Thus,  $K_I$  factors of load case 3 are used for stress intensity range  $\Delta K_I$  and Equation 3-5 can be used directly to calculate the total number of loading cycles sustained by the crack detail.

**TABLE 5-8: Fatigue Crack Growth Calculation Assuming Single Edge Crack**

$a_o$ (in.)	$a_f$ (in.)	$a_{avg}$ (in.)	$a_{avg} / b$	$F(a/b)$ [Eq. 5-5]	$\Delta K_I$ (ksi $\sqrt{\text{in.}}$ )	$\Delta N$ ( $\times 10^6$ cycles)	$\Sigma N$ ( $\times 10^6$ cycles)
0.15	0.25	0.200	0.04	1.147	5.094	2.102	2.102
0.25	0.35	0.300	0.06	1.165	6.332	1.094	3.196
0.35	0.45	0.400	0.08	1.185	7.439	0.675	3.871
0.45	0.55	0.500	0.10	1.209	8.483	0.455	4.326
0.55	0.65	0.600	0.12	1.236	9.500	0.324	4.650
0.65	0.75	0.700	0.14	1.266	10.514	0.239	4.889
0.75	0.85	0.800	0.16	1.300	11.543	0.181	5.070
0.85	0.95	0.900	0.18	1.338	12.601	0.139	5.209
0.95	1.05	1.000	0.20	1.380	13.701	0.108	5.317
1.05	1.15	1.100	0.22	1.427	14.853	0.085	5.401
1.15	1.25	1.200	0.24	1.478	16.069	0.067	5.468
1.25	1.35	1.300	0.26	1.534	17.360	0.053	5.521
1.35	1.45	1.400	0.28	1.595	18.737	0.042	5.564
1.45	1.55	1.500	0.30	1.663	20.212	0.034	5.597
1.55	1.65	1.600	0.32	1.736	21.799	0.027	5.624
1.65	1.75	1.700	0.34	1.817	23.510	0.021	5.645
1.75	1.85	1.800	0.36	1.905	25.363	0.017	5.662
1.85	1.95	1.900	0.38	2.001	27.376	0.014	5.676
1.95	2.05	2.000	0.40	2.106	29.568	0.011	5.687
2.05	2.15	2.100	0.42	2.222	31.963	0.009	5.695
2.15	2.25	2.200	0.44	2.349	34.587	0.007	5.702
2.25	2.35	2.300	0.46	2.489	37.473	0.005	5.707
2.35	2.45	2.400	0.48	2.644	40.658	0.004	5.711
2.45	2.55	2.500	0.50	2.815	44.183	0.003	5.715
2.55	2.65	2.600	0.52	3.005	48.102 <sup>a</sup>	0.002	5.717
2.65	2.75	2.700	0.54	3.217	52.475	0.002	5.719
2.75	2.85	2.800	0.56	3.455	57.379	0.001	5.720
2.85	2.95	2.900	0.58	3.721	62.903	0.001	5.722
2.95	3.05	3.000	0.60	4.023	69.161	0.001	5.722
3.05	3.15	3.100	0.62	4.365	76.291	0.001	5.723
3.15	3.25	3.200	0.64	—	80.000 <sup>b</sup>	0.001	5.724
3.25	3.35	3.300	0.66	—	80.000	0.001	5.724
3.35	3.45	3.400	0.68	—	80.000	0.001	5.725
3.45	3.55	3.500	0.70	—	80.000	0.001	5.725
3.55	3.65	3.600	0.72	—	80.000	0.001	5.726
3.65	3.75	3.700	0.74	—	80.000	0.001	5.726
3.75	3.85	3.800	0.76	—	80.000	0.001	5.727
3.85	3.95	3.900	0.78	—	80.000	0.001	5.727
3.95	4.05	4.000	0.80	—	80.000	0.001	5.728
4.05	4.15	4.100	0.82	—	80.000	0.001	5.728
4.15	4.25	4.200	0.84	—	80.000	0.001	5.729
4.25	4.35	4.300	0.86	—	80.000	0.001	5.730
4.35	4.45	4.400	0.88	—	80.000	0.001	5.730
4.45	4.55	4.500	0.90	—	80.000	0.001	5.731
4.55	4.65	4.600	0.92	—	80.000	0.001	5.731
4.65	4.75	4.700	0.94	—	80.000	0.001	5.732
4.75	4.85	4.800	0.96	—	80.000	0.001	5.732
4.85	5.00	4.925	0.99	—	80.000	0.001	5.733

Note: <sup>a</sup> $\Delta K_I$  exceeds  $K_{T_s}$ , crack growth rate starts to accelerate.

<sup>b</sup> $\Delta K_I$  reaches the upper limit  $K_{Ic}$ .

**Table 5-9 Fatigue crack growth calculation using ANSYS  $K_I$  factors**

$a_o$ (in.)	$a_f$ (in.)	$a_{avg}$ (in.)	$\Delta K_I$ (ksi $\sqrt{\text{in.}}$ )	$\Delta N$ ( $\times 10^6$ cycles)	$\Sigma N$ ( $\times 10^6$ cycles)
0.15	0.25	0.200	11.447	0.185	0.185
0.25	0.35	0.300	12.568	0.140	0.325
0.35	0.45	0.400	13.689	0.108	0.433
0.45	0.55	0.500	14.810	0.086	0.519
0.55	0.65	0.600	15.041	0.082	0.601
0.65	0.75	0.700	15.273	0.078	0.679
0.75	0.85	0.800	15.504	0.075	0.753
0.85	0.95	0.900	15.736	0.071	0.824
0.95	1.05	1.000	15.967	0.068	0.893
1.05	1.15	1.100	16.010	0.068	0.960
1.15	1.25	1.200	16.053	0.067	1.027
1.25	1.35	1.300	16.096	0.067	1.094
1.35	1.45	1.400	16.139	0.066	1.160
1.45	1.55	1.500	16.182	0.066	1.226
1.55	1.65	1.600	16.121	0.066	1.292
1.65	1.75	1.700	16.059	0.067	1.359
1.75	1.85	1.800	15.998	0.068	1.427
1.85	1.95	1.900	15.936	0.069	1.496
1.95	2.05	2.000	15.875	0.069	1.565
2.05	2.15	2.100	15.744	0.071	1.636
2.15	2.25	2.200	15.613	0.073	1.709
2.25	2.35	2.300	15.483	0.075	1.784
2.35	2.45	2.400	15.352	0.077	1.861
2.45	2.55	2.500	15.221	0.079	1.939
2.55	2.65	2.600	14.996	0.082	2.022
2.65	2.75	2.700	14.771	0.086	2.108
2.75	2.85	2.800	14.546	0.090	2.198
2.85	2.95	2.900	14.321	0.095	2.293
2.95	3.05	3.000	14.096	0.099	2.392
3.05	3.15	3.100	13.818	0.105	2.497
3.15	3.25	3.200	13.539	0.112	2.609
3.25	3.35	3.300	13.261	0.119	2.728
3.35	3.45	3.400	12.982	0.127	2.855
3.45	3.55	3.500	12.704	0.135	2.991
3.55	3.65	3.600	12.349	0.148	3.138
3.65	3.75	3.700	11.994	0.161	3.299
3.75	3.85	3.800	11.638	0.176	3.476
3.85	3.95	3.900	11.283	0.193	3.669
3.95	4.05	4.000	10.928	0.213	3.882
4.05	4.15	4.100	10.930 <sup>a</sup>	0.213	4.095
4.15	4.25	4.200	10.932 <sup>a</sup>	0.213	4.307
4.25	4.35	4.300	10.933 <sup>a</sup>	0.213	4.520
4.35	4.45	4.400	10.935 <sup>a</sup>	0.212	4.732
4.45	4.55	4.500	10.937 <sup>a</sup>	0.212	4.944
4.55	4.65	4.600	11.305 <sup>a</sup>	0.192	5.137
4.65	4.75	4.700	11.674 <sup>a</sup>	0.175	5.311
4.75	4.85	4.800	12.042 <sup>a</sup>	0.159	5.470
4.85	5.00	4.925	12.503 <sup>a</sup>	0.213	5.684

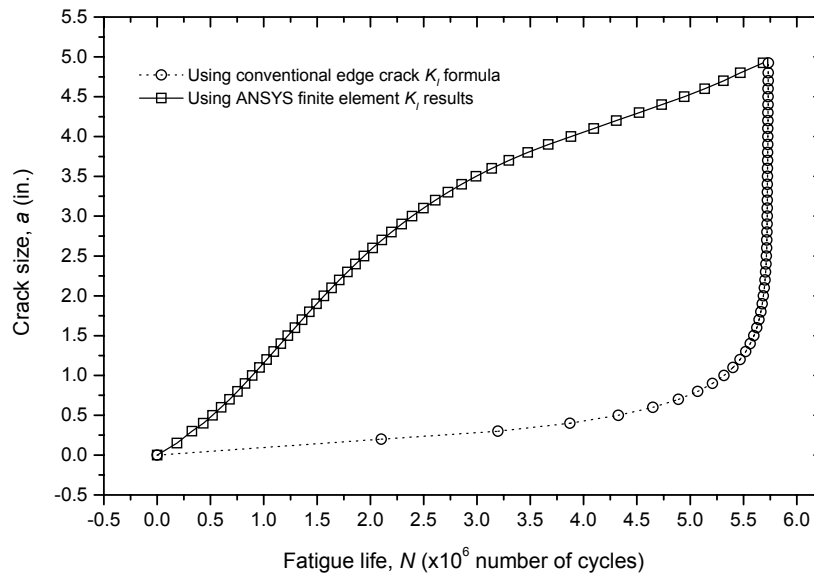
Note: <sup>a</sup> $K_{II} > K_I$  at  $a = 4.5''$  and  $5''$  (Figure 5-19, Table 5-5), therefore  $K_{II}$  is used for  $a > 4''$ .

Table 5-9 shows the spreadsheet developed for crack growth calculation by using the ANSYS  $K_I$  solutions. The same  $a_{initial}$  of 0.15 in. and  $a_{critical}$  of 5 in. are used as in section 5.4.1.

Because the finite element analyses are conducted only for every 0.5 in. crack increment, the  $K_I$  values for other crack lengths in the table are obtained by linear interpolation. It should be noted that  $K_{II}$  values are larger than  $K_I$  at the end of the crack propagation (Figure 5-19). It might be unconservative if only the effect of crack opening mode is considered at that point. Therefore,  $K_{II}$  factors are used to replace  $K_I$  at 4.5 in. and 5 in. crack lengths, and are used for the stress intensity range interpolation of crack sizes larger than 4 in. The stress intensity range for the onset of unstable crack growth  $K_T$  and the critical stress intensity factor  $K_{IC}$  are never reached. The fatigue life obtained by this method is  $5.684 \times 10^6$  cycles.

### **5.4.3 Evaluation of the Different Approaches for Fatigue Life Estimation**

Two different methods are used in sections 5.4.1 and 5.4.2 to estimate the experienced fatigue life of the out-of-plane crack details developed in the Arkansas River Bridge. The crack growth scenarios described by these two methods, however, are different, as can be observed from the  $a$  versus  $N$  curves shown in Figure 5-23.



**FIGURE 5-23: Fatigue Crack Growth Curves Obtained by Using Different  $K_I$  Approaches**

The dotted curve is obtained by using the traditional edge crack  $K_I$  formula. A nominal far field stress range of 5.6 ksi is used and is assumed to be constant throughout the entire cracking procedure. The stress intensity range and the fatigue life are thus mainly functions of the crack dimension. As listed in Table 5-8, the stress intensity range varies from 5.094 ksi  $\sqrt{\text{in.}}$  to 80 ksi  $\sqrt{\text{in.}}$ . Because the fatigue life is inversely proportional to the third power of the stress intensity range, the number of loading cycles within each small crack increment decreases when the crack size increases. The crack growth rate thus increases significantly when the crack propagates into a larger dimension. As indicated by the first horizontal part of the curve, most of the fatigue life is used up at the beginning of the propagation when the crack sizes are very small. Only limited number of life cycles is left for larger crack sizes as shown by the second vertical part of the curve.

The solid curve in Figure 5-23 is based on the  $K_I$  results for different crack dimensions solved directly by ANSYS. The stress intensity factors obtained from this method are much closer to the actual cracking condition. As shown in Table 5-9, the stress intensity range is kept within 10 ~ 17 ksi  $\sqrt{\text{in.}}$ , and no radical change ever occurs during the crack growth. Therefore, a close to linear crack development can be observed, and the rate of crack growth is much more stable as compared with that of the first method.

It is interesting to notice that the two crack growth paths plotted in Figure 5-23 are completely different; however, the final results for the fatigue life estimation are very close. The first method could be used if the crack unzipping analysis is not conducted. As long as the normal stress is determined, the fatigue life could then be calculated. Normally this is a simple approach for most of the nonstandard cracking problems: assign a far field point for nominal stress, assume it to be constant during the propagation, and then use Equation 3-5 to calculate the

fatigue life. The crack growth pattern may not agree with the actual behavior, but the life estimated by this method is usually satisfactory enough. The second method uses the stress intensity factors obtained directly from the finite element analysis for each individual crack dimension; therefore it describes the crack development in a manner close to the exact condition. However, this approach requires a lot modeling and computing time because both the coarse model and the submodel have to be changed for every step of crack growth in order to obtain the actual stress intensity factors at the crack tip. The life ranges presented by the two methods are almost the same.

The traffic information provided by KDOT shows an  $(ADTT)_{SL}$  of 344 (Equation 5-1) in 1996. Assuming the same amount of traffic has occurred throughout the bridge's service, the total number of truck traffic cycles during the past 45 years could then be approximated as

$$\Sigma N = 344 \times 365 \times 45 = 5.650 \times 10^6 \text{ cycles} \quad (5-7)$$

Some factors that may influence the outcome of Equation 5-7 are not included due to lack of information. For example, the  $(ADTT)_{SL}$  number calculated by Equation 5-1 is an average value for all four traffic lanes. It would be more appropriate to use only the truck traffic number of a shoulder lane, which is expected to be higher than 344. In addition, only one stress range cycle per truck passage is considered in Equation 5-7, but the stress variation curves in Figure 5-13 actually indicate two load cycles per truck passage. The stress range of the second load cycle is higher than the first, so it might be more appropriate if the traffic count obtained from Equation 5-7 is multiplied by a factor between 1.0 and 2.0. However, other factors may cause a decrease in the number of life cycles calculated by Equation 5-7. Notice that the  $(ADTT)_{SL}$  value for 1996 is used in the equation and it is assumed to be constant throughout the past 45 years. The real traffic volume on the bridge presumably was less in the early years of service. If this

situation is considered, then a reduction factor should be applied to the equation. All these factors are either unavailable due to lack of information, or difficult to interpret quantitatively from limited knowledge, therefore they are not considered in the traffic count for simplification purposes.

Table 5-10 shows a satisfactory agreement between the life estimates calculated by using fracture mechanics theory and the KDOT traffic count. There is already one connection in the bridge that has developed a horizontal fatigue crack through the whole plate width on one side of the stiffener, and there are several other connections that have developed crack lengths almost to the width of the stiffener. The analysis conducted by this study thus matches the actual fatigue cracking behavior in the field.

**TABLE 5-10: Fatigue Life Estimated by Using Different Approaches**

Method	Assumed parameter	Total number of traffic loading, $\Sigma N$
Fracture mechanics	Single edge crack $K_I$	$5.733 \times 10^6$ cycles
	ANSYS $K_I$	$5.684 \times 10^6$ cycles
KDOT traffic count	$(ADTT)_{SL} = 344$	$5.650 \times 10^6$ cycles

It is important to consider the inherent variability in fatigue life values. Cracking behavior is characterized by large data scatter. Although the values given in Table 5-10 are all about 6 million cycles, much more variation between predicted and actual cycles would still be regarded as in good agreement from a fracture mechanics application point of view. For example, if the modification factor for the number of loading cycles can be determined precisely enough for single truck passage on a shoulder lane, or if a complete truck traffic growth pattern during the past 45 years is available so that the actual  $(ADTT)_{SL}$  values between 1955 and 2000 can be obtained, then the life range calculated by using Equation 5-7 could be changed. In these cases the predicted value of 6 million would still be considered to be in good agreement with the actual condition.

It should be pointed out that the life estimates obtained from the fracture mechanics methods are based on the finite element stress and stress intensity factor results of the crack detail at the Floor-beam 12-1 to Girder D connection, which is the “hottest” spot in the bridge coarse model. The same details at other locations have lower stress ranges under traffic loading, and thus slower crack growth and longer fatigue lives. Only this critical location is investigated for fatigue stress and life evaluation, and it will also be used in the next section for crack repair analysis.

## **5.5 Retrofit Study for Type 3 Out-of-Plane Fatigue Cracking**

### **5.5.1 Repair Guidelines**

Many factors can influence the fatigue life at a crack site, such as the initial crack size, the stress range, and the fracture toughness of the material [Barsom & Rolfe, 1999]. The stress range is the most important since it is the primary driver of fatigue cracking. The crack growth rate is inversely proportional to the cubic power of stress range, thus a slight decrease in stress range could result in a significant increase in fatigue life. The fundamental principles for repair schemes should be aimed at lowering the stress range below the fatigue limit, or to a level where fatigue cracking would not occur within an acceptably large number of loading cycles so that an adequate remaining service life can be obtained.

Cracking matching that of the Arkansas River Bridge has not been documented in previous literature. Based on the information provided by the AASHTO fatigue detail categories and other researches for out-of-plane fatigue investigation, it is reasonable to conclude that the floor-beam coped flange to stiffener weld connection in the Arkansas River Bridge is no better than an AASHTO fatigue Category C detail. To effectively repair the fatigue cracking in the bridge, not only the stress range should be lowered to a satisfactory level, but the fatigue

resistance of the repaired connection should also be improved to a better category, or at least be kept the same as the original detail. In other words, a Category C or better detail should be reached after the out-of-plane horizontal crack in the stiffener plate is repaired.

A series of repair plans are studied in this section for the purposes of eliminating the crack initiation site, reducing the stress variation magnitude, and extending the bridge service life. For each repair option, the finite element coarse-to-fine submodeling analysis is carried out again to investigate the change of local stresses at the concentration region, and the AASHTO LRFD fatigue design criteria addressed in section 3.3 are used to predict the remaining service life of the repaired detail. It is assumed that the out-of-plane fatigue cracks will initiate in the stiffener plate sooner or later, so the recommended repair will be applied to all 68 floor-beam to exterior girder connections at the third points of girder spans, including those places where cracks have not developed yet.

## **5.5.2 Finite Element Repair Analysis**

### ***5.5.2.1 Repair Plan 1 — Add Backup Plate to the Stiffener***

The first repair method is shown in Figure 5-24. An additional 1 in. thick plate is bolted to the back of the existing stiffener to locally reinforce the connection, and a  $\frac{3}{4}$ " diameter hole is placed at the crack tip to arrest the crack propagation. Both the finite element coarse model and the submodel are modified due to the geometry change, and the analysis is performed only for load cases 3 and 15 because these are the two load cases causing the extreme stresses in the model. For the connections that have not developed out-of-plane fatigue cracks, as shown in Figure 5-25(a), both the highest and the lowest stresses occur at point P1 on the edge of the existing stiffener plate where the horizontal weld terminates. This is the same place where cracks originally initiated in the bridge. The maximum stress range is 20.667 ksi, reduced by more than

40% as compared with that of the unrepaired condition (35.449 ksi). However, the stress concentration effect is not greatly mitigated because the stress range is still much higher than the constant amplitude fatigue threshold of a Category C detail. For the cracked connections such as shown in Figure 5-25(b), with the increase of crack length, the maximum Y direction stress range at the hole end eventually decreases to a low magnitude due to the softening effect. However, an increasing X direction stress range is developed at point Q1 on the bottom of the drilled hole circumference. If the hole is placed at the end of the stiffener plate width for a large crack size, this high X direction stress fluctuation may introduce a new vertical crack along the stiffener to girder web weld. The newly bolted backup plate has fatigue resistance of an AASHTO Category B detail. The stress ranges found in this plate are lower than 5 ksi, for either the cracked or uncracked conditions. Therefore the remaining life of the detail after repair depends on the stress variation of the existing stiffener plate. The finite element repair analysis for a submodel containing 4<sup>1</sup>/<sub>4</sub> in. crack shows a 1<sup>st</sup> principal stress range of 21.466 ksi close to X axis direction at point Q1. Assuming the drilled hole surface can have fatigue resistance of a Category B detail, the remaining service life using the proposed repair method is then calculated as shown in Table 5-11.

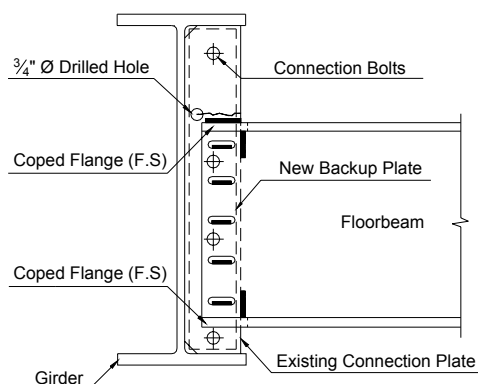


**FIGURE 5-24: Repair Plan 1: Add Backup Plate to the Stiffener**

**TABLE 5-11: Remaining Service Life using Repair Plan 1**

Location of maximum stress range: Q1 [Figure 5-25(b)]		
Category B detail, $A = 120 \times 10^8$ , $(\Delta F)_{TH} = 16$ ksi		
$\sigma_{max} = 21.446$ ksi (load case 3)		
$\sigma_{min} = 0$ ksi (load case 15)		
$\Delta\sigma = \sigma_{max} - \sigma_{min} = 21.446$ ksi $> 0.5(\Delta F)_{TH}$		
$N_Y = A / [(365) n (\Delta\sigma)^3 (ASTT)_{SL}]$		
Percentage of the 1996 truck traffic	Future $(ADDT)_{SL}$	Remaining service life $N_Y$ (year)
100%	344	10
50%	172	19
33%	115	29
25%	86	39

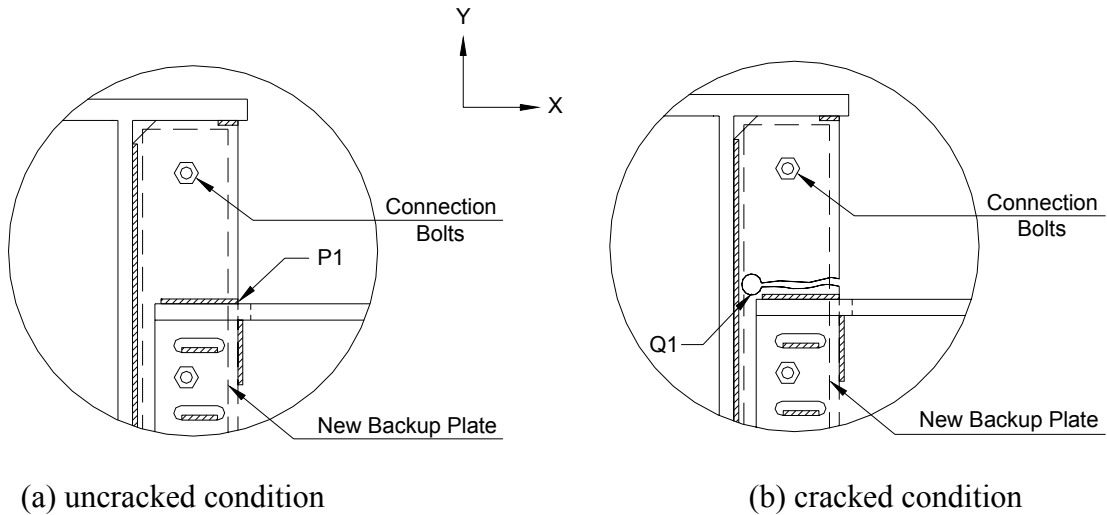


**FIGURE 5-25: Maximum Stress Range Locations for Repair Plan 1**

The number  $n$  in the  $N_Y$  formula is used to consider additional loading cycles that might occur when the truck moves to other locations on the bridge. As previously indicated in Figure 5-13, it seems that two load cycles have occurred when the truck moves from Pier No. 12 to Pier No. 10, and the effect is especially outstanding at the stress concentration point C. However, the

stress range of the second load cycle is much larger than that of the first one, and this double cycle effect is not so noticeable at other locations in the bridge. Therefore, only one full stress range cycle per truck passage is considered during the fatigue life evaluation, using the stress range that of the difference between the maximum and minimum stresses. The *LRFD Bridge Design Specifications* [1998] define the  $n$  value according to the girder span length and the detail location. For any place away from the interior supports and with continuous girder spans longer than 40 ft,  $n$  is specified as 1.0 (Table 3-2). Thus the  $n$  value adopted by the AASHTO LRFD Specifications is consistent with that used in section 5.4.3 for traffic count.

Since the new Hutchinson Bypass will attract a large portion of the traffic and become the main artery for the city, the truck traffic over the Arkansas River Bridge may reduce significantly. Table 5-11 calculates the remaining service life corresponding to the future  $(ADTT)_{SL}$  value considered as a percentage of the 1996 KDOT statistics. The result shows only moderate service life after repair since the stress range is not sufficiently reduced. However, it is still an applicable repair method as long as the truck traffic is low. A disadvantage of using this repair method is that it requires a large number of field drilled holes.

There are many factors that can cause fatigue cracks other than stress fluctuation, such as poor welding quality, large initial defect, residual stress, etc. Of the 68 floor-beam to exterior girder connections off the bridge piers, 39 have developed out-of-plane fatigue cracks of different lengths, while the other 29 are not cracked yet. Theoretically the service life of those 29 uncracked connections should have already been used up. But in fact these connections have been in use for 45 years under very high stress ranges without cracking. In this circumstance, the connections must have good quality welds and very small initial flaw sizes so that they can keep intact even subjected to high stress variations. However, if no repair is performed, cracks will

eventually develop in these locations, which is just a matter of time. The bolted backup plate would only stop crack propagation for a limited number of years unless the truck traffic is significantly reduced. Therefore other repair options are evaluated before the final retrofit plan can be determined.

### 5.5.2.2 Repair Plan 2 — *Cut Short Stiffener Completely*

As illustrated in Figure 5-26, the second repair plan is to completely cut short the stiffener plate from above the floor-beam top flange. The crack and the welds connecting the stiffener plate to the girder web and floor-beam top flange should also be removed. At the intersection of the horizontal and vertical cut lines, a smooth transition is formed by a curve of 0.8 in. radius. The coarse-to-submodel finite element analysis is performed again and the maximum stress range of 33.023 ksi is found at point P2 on the curved cut line. The maximum tensile stress occurs in load case 3 in the direction of the 1<sup>st</sup> principal stress, and the maximum compressive stress occurs in load case 15 in the direction of the 3<sup>rd</sup> principal stress. Both are parallel to the tangent of the curve at point P2. If the cut surface is ground smooth, an AASHTO fatigue Category A detail can be achieved. However, because the maximum stress range is very high, the remaining service life as calculated by Table 5-12 is short.

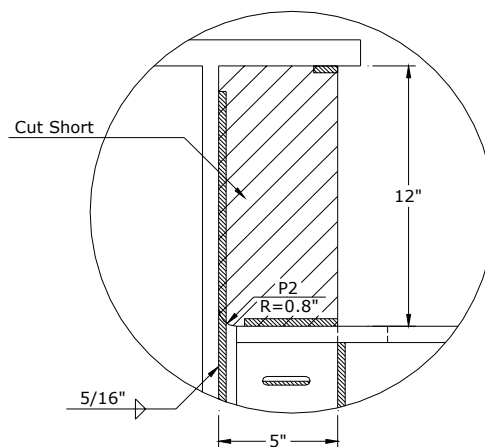


**FIGURE 5-26: Repair Plan 2: Cut Short Stiffener Completely**

**TABLE 5-12: Remaining Service Life using Repair Plan 2**

Location of maximum stress range: P2 (Figure 5-26)		
Category A detail, $A = 250 \times 10^8$ , $(\Delta F)_{TH} = 24$ ksi		
$\sigma_{max} = 31.230$ ksi (load case 3)		
$\sigma_{min} = -1.793$ ksi (load case 15)		
$\Delta\sigma = \sigma_{max} - \sigma_{min} = 33.023$ ksi $> 0.5(\Delta F)_{TH}$		
$N_Y = A / [(365) n (\Delta\sigma)^3 (ASTT)_{SL}]$		
Percentage of the 1996 truck traffic	Future $(ADDT)_{SL}$	Remaining service life $N_Y$ (year)
100%	344	6
50%	172	11
33%	115	17
25%	86	22

This retrofit was used as one of the repair methods for the Des Moines Bridge (Polk County, Iowa) [Fisher, 1984], and has been used since 1980 by Iowa DOT on about 50 two-girder bridges that have developed small web gap cracks. All of them experienced no crack reinitiation after the repair. Although the Arkansas River Bridge has the out-of-plane cracks at a different location, the situation after the repair is the same. The high cyclic stress range at point P2 in Figure 5-26 could form a new crack path along the stiffener plate to girder web weld. The reason why this type of crack is not seen in those Iowa DOT bridges after so many years since they were repaired could be that the cut surfaces were well finished. For example, the repair plan of the Des Moines Bridge required surface smoothness of 250  $\mu$ -in. or less for the horizontal cut line and 125  $\mu$ -in. or less for the vertical cut line. This is much smoother than the requirement of 1,000  $\mu$ -in or less for the surface finish of an AASHTO Category A detail, therefore the initial flaw size is very small and a long fatigue life can be provided. The stress measurement for point P2 at the curved transition region is not available from the Des Moines Bridge, but since it also consists of a girder/floor-beam/stringer system, the load transferred from the stringer to floor-beam should also cause out-of-plane bending stresses at this corner.

It seems contradictory that the theoretical calculation shows only a very short life, but in reality many bridges have been repaired by this means without problem under normal traffic. The Des Moines Bridge, for instance, remains uncracked 20 years after its retrofit. As previously mentioned, the successful application of this repair technique in those Iowa DOT bridges may result from the smooth surface finishing. A similar cutback method was also used by Minnesota DOT on the Lexington Avenue Bridge, but the repair was not successful [Dexter and Fisher, 1996]. Contrary to required recommendations, most of the fillet welds and a portion of the connection plate had been left on the girder web at the cut-short region. Thus cracks soon reinitiated after the retrofit. A clean surface finish therefore is very important to the remaining service life of the connection detail if the cut-short repair is used. Besides, many field testing results indicated that the stresses and stress ranges experienced by a bridge under the actual traffic condition are usually lower than calculated by using an AASHTO HS20 design truck, or an HS15 fatigue truck if the fatigue limit state governs. This might be the other reason why those repaired details in the Iowa DOT bridges are still doing so well.

However, the theoretical analysis conducted in this study indicates a close to yielding stress range at the transition region (point P2 in Figure 5-26). For conservative purposes, this repair method is not recommended for the Arkansas River Bridge, as cracks may reinitiate and propagate downward into the girder web due to the high cyclic stress fluctuation at the curved cut surface. In addition, the remnant of the fillet welds and stiffener plate along the cut edges has to be ground flush with the girder web and floor-beam top flange. If the surface finishing has to be controlled to a smoothness of 250  $\mu$ -in. or less, it will require a large amount of field grinding, causing much difficulty during the retrofit construction.

### 5.5.2.2 Repair Plan 3: Cut Short Stiffener Partially and Drill Holes

Figure 5-27 shows the schematic of the third repair method. To make the cutting process much easier, the stiffener plate is partially cut short, with a  $\frac{3}{4}$  in. vertical stub left on the girder web side and another  $\frac{3}{4}$  in. horizontal stub left above the floor-beam top flange. A smooth transition between the vertical and horizontal cut edges is then formed by a larger curvature of 3 in. radius. The crack is left in place and a  $\frac{3}{4}$  in. diameter hole is drilled at the inner side of the stiffener plate in order to stop the crack when it proceeds to that point. Finite element analyses are carried out for submodels with crack lengths of 2 in. and 4  $\frac{1}{4}$  in. Solution for the 2 in. crack model shows that point P3 on the curved cut line has a maximum stress range of 22.782 ksi. The 4  $\frac{1}{4}$  in. crack model, however, indicates that when crack propagates further and reaches the drilled hole, point Q3 at the bottom of the hole circumference has a maximum stress range of 35.491 ksi. Figure 5-28 shows the first principal stress distribution of load case 3 for the submodels of the two crack lengths. This repair is definitely not a good choice, because the stress at point Q3 has almost reached yielding. Still the remaining life is tabulated as shown in Table 5-13 by using the maximum stress range obtained from the 4  $\frac{1}{4}$  in. crack model.

**TABLE 5-13: Remaining Service Life using Repair Plan 3**

Location of maximum stress range: Q3 (Figure 5-27)		
Category B detail, $A = 120 \times 10^8$ , $(\Delta F)_{TH} = 16$ ksi		
$\sigma_{max} = 35.491$ ksi (load case 3)		
$\sigma_{min} = 0$ ksi (load case 15)		
$\Delta\sigma = \sigma_{max} - \sigma_{min} = 35.491$ ksi $> 0.5(\Delta F)_{TH}$		
$N_Y = A / [(365) n (\Delta\sigma)^3 (ASTT)_{SL}]$		
Percentage of the 1996 truck traffic	Future $(ADDT)_{SL}$	Remaining service life $N_Y$ (year)
100%	344	2
50%	172	4
33%	115	6
25%	86	9

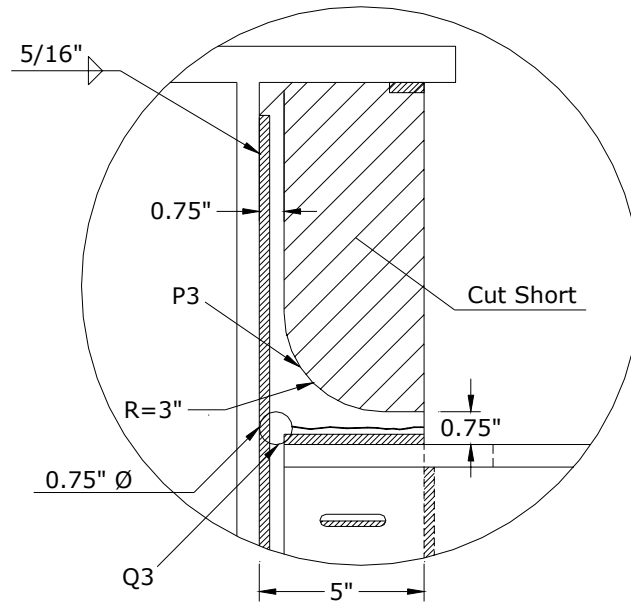
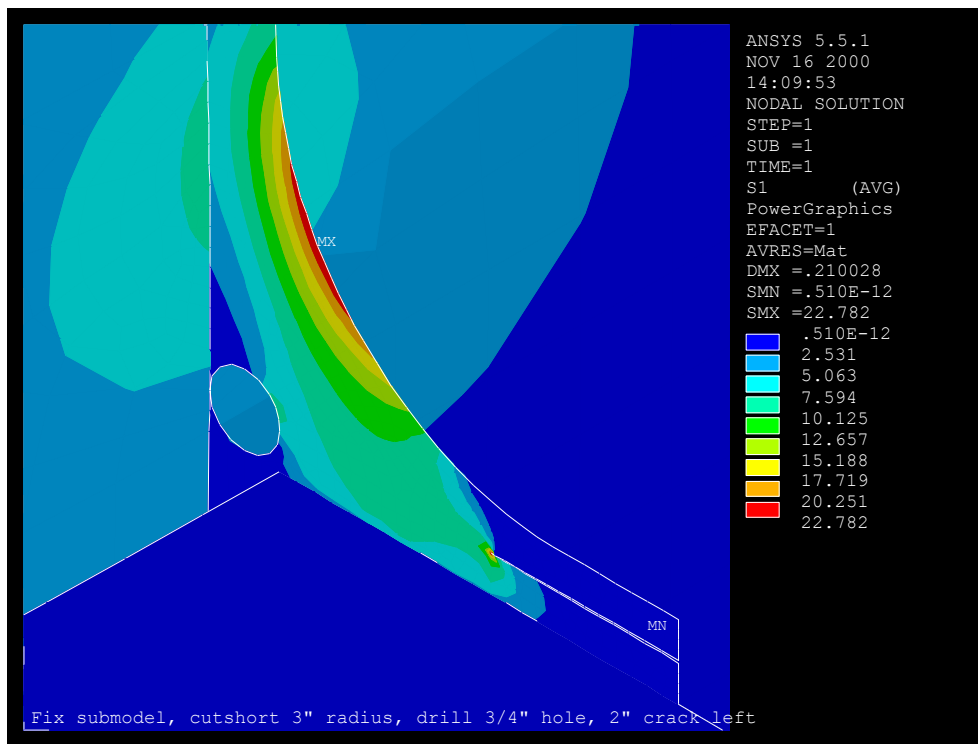


**FIGURE 5-27: Repair Plan 3: Cut Short Stiffener Partially and Drill Holes**

***5.5.2.4 Repair Plan 4 — Cut Short Stiffener Partially and Reweld the Crack***

The fourth repair plan is to partially cut short the stiffener plate and reweld the crack, as shown in Figure 5-29. Finite element submodeling analysis shows that the maximum stress range is located at Point P4 on the curved cut surface with a value of 23.72 ksi. The tensile stress caused by the negative out-of-plane bending moment is in the direction of the 1<sup>st</sup> principal stress, and the compressive stress caused by the positive out-of-plane bending moment is in the direction of the 3<sup>rd</sup> principal stress.

(a)



(b)

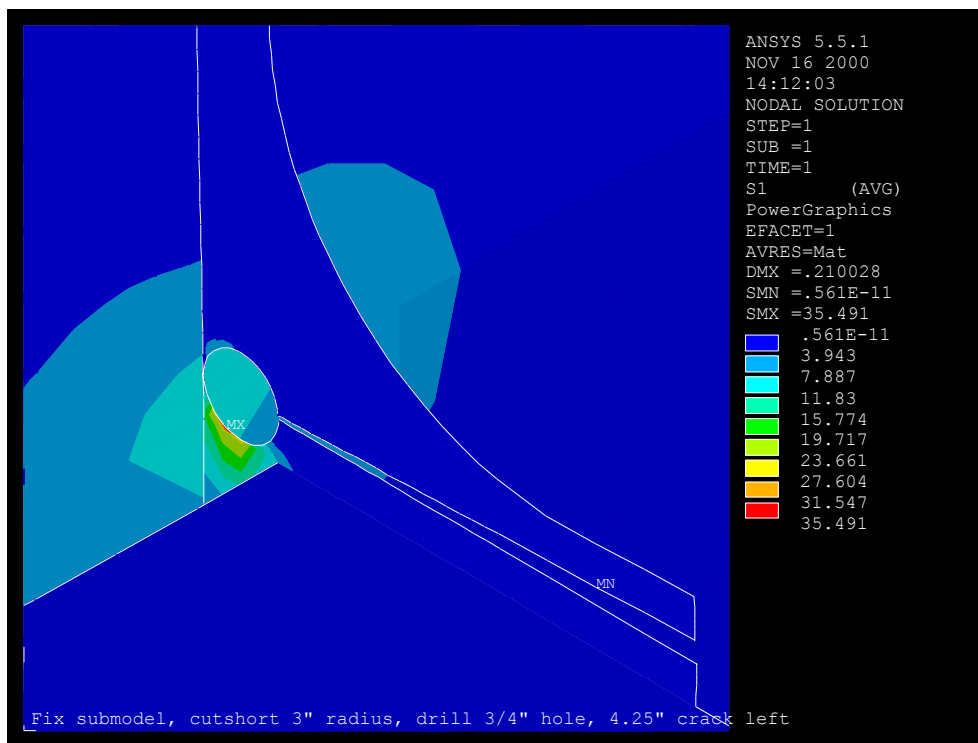
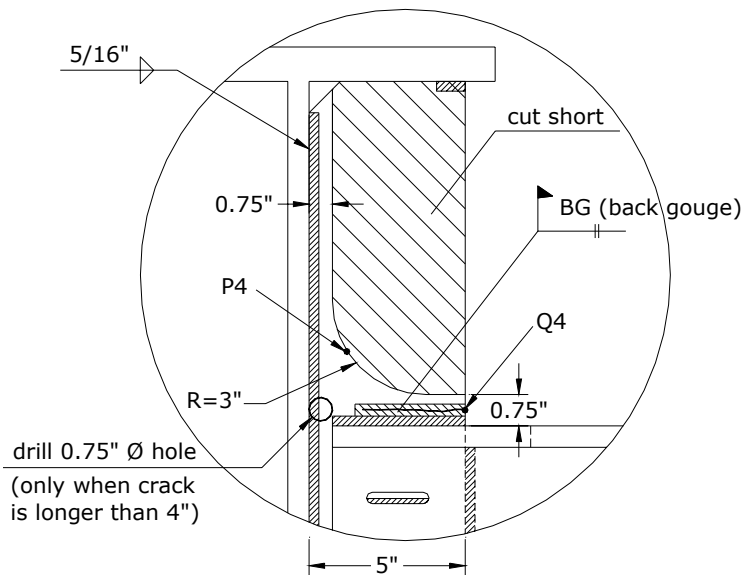


FIGURE 5-28: ANSYS Load Case 3, 1<sup>st</sup> Principal Stress Solution for Repair Plan 3



**FIGURE 5-29: Repair Plan 4: Cut Short Stiffener Partially and Re-weld the Crack**

The stress range is in the direction tangent to the curved surface at this point. If the cut edge is properly finished, a fatigue strength consistent with that of an AASHTO Category A detail can be obtained. Notice that the maximum stress range is lower than the constant amplitude fatigue threshold of detail Category A. However, an infinite life is not possible because the fatigue limit of  $\frac{1}{2}(\Delta F)_{TH}$  is exceeded. Table 5-14 shows the remaining service life calculated by using this repair method.

The Y direction crack opening stress at the original crack initiation point Q4 is decreased from 35.449 ksi to 2.23 ksi after rewelding, because the geometry constraints ahead of the concentration point has been significantly released due to the partial removal of the connection stiffener plate. If the rewelded coped floor-beam top flange to stiffener plate horizontal weld is still counted as a Category C detail, the stress range at point Q4 is now much lower than the fatigue limit  $\frac{1}{2}(\Delta F)_{TH}$  of 5 ksi. Thus no crack should ever reinitiate from this location.

**TABLE 5-14: Remaining Service Life using Repair Plan 4**

Location of maximum stress range: P4 (Figure 5-29)		
Category A detail, $A = 250 \times 10^8$ , $(\Delta F)_{TH} = 24$ ksi		
$\sigma_{max} = 22.515$ ksi (load case 3)		
$\sigma_{min} = -1.204$ ksi (load case 15)		
$\Delta\sigma = \sigma_{max} - \sigma_{min} = 23.719$ ksi $> 0.5(\Delta F)_{TH}$		
$N_Y = A / [(365) n (\Delta\sigma)^3 (ASTT)_{SL}]$		
Percentage of the 1996 truck traffic	Future ( $ADDT$ ) <sub>SL</sub>	Remaining service life $N_Y$ (year)
100%	344	15
50%	172	30
33%	115	45
25%	86	60

This repair method shifts the location of the maximum stress range from a high concentration point Q4 to a mild curved surface point P4. The magnitude of the stress fluctuation is reduced and a better fatigue category is obtained after the cut-short. Rewelding the cracked material eliminates the initial flaw site and restores the load carrying capacity of the connection plate. The crack opening stress at the original concentration point Q4 is now decreased to below the infinite life fatigue limit, so no crack should reinitiate from this point if the rewelding quality is good. The drawback is that this repair also requires a lot of field labor for cutting and rewelding. However the other repair options have equal or worse construction difficulties. Compared to the other three repair plans, the retrofit method proposed in this section exhibits obvious advantages in reducing the stress variation, increasing the fatigue strength, controlling the crack reinitiation, and extending the useful service life. Therefore, this repair method is recommended for use in the actual bridge rehabilitation.

### **5.5.3 Repair Recommendations**

The finite element studies carried out in section 5.5.2 for the different repair methods show that out-of-plane fatigue cracking is not easy to repair, both structurally and economically.

Often the stress range is lowered at one point, but is raised at another, and none of the repairs succeed in reducing the maximum stress range below the infinite life fatigue limit  $\frac{1}{2}(\Delta F)_{TH}$ .

The cut-short and rewelding method proposed by repair plan 4 softens the constraints at the floor-beam to exterior girder connection, so the detail can rotate more freely and act more like a pin. The out-of-plane bending moment locked into the connection can also be released after the cut-short, which in turn reduces the effect of stress concentration and postpones the crack initiation or propagation. The remaining service life provided by repair plan 4 is the longest and the geometry of the connection detail after the repair has the best fatigue resistance. Thus this repair method is recommended for the final retrofit.

To reach an AASHTO Category A detail for the horizontal, vertical, and curved cut lines, flame cutting can be used but the cut edges have to be ground to an ANSI/AASHTO/AWS D5.1 smoothness of 1,000  $\mu$ -in. or less [AASHTO LRFD, 1998]. To perform rewelding for the cracked stiffeners and horizontal fillet welds, the following repair procedures are suggested. First, the crack end needs to be located, preferably by dye penetrant, and marked approximately  $\frac{1}{4} \sim \frac{1}{2}$  in. beyond the crack tip. As illustrated in Figure 5-29, if the crack size is longer than 4 in., a  $\frac{3}{4}$  in. drilled hole is required at the end of the stiffener plate to check whether the crack has propagated into the girder web or not. For the uncracked condition, the assumed crack end can be located at half of the stiffener plate width along the weld toe. The crack should then be removed by gouging from the side of the stiffener with the longer crack. Make sure that all the cracked materials are removed from the stressed area back to the intact welds. After the gouge is filled with new weld, the welder should move to the other side of the stiffener plate, back gouge the crack, remove the weld slag, and reweld on this side. Finally, the newly welded surfaces on both sides of the stiffener plate should be ground smooth. If necessary, the dye penetrant test can

be applied again to check the repaired welds. Good quality welding process should be ensured so that crack will not initiate again at this location. For the connections with large crack sizes, if the crack is found to have entered the girder web, another drilled hole should be placed on the girder web to effectively arrest the crack propagation. The diameter of the hole should be large enough so that it can include all the extended cracks.

#### **5.5.4 Remaining Service Life**

It is believed that the traffic volume on the Arkansas River Bridge should be significantly decreased after the new Hutchinson Bypass is constructed. Thus the remaining service life is calculated by assuming future  $(ADTT)_{SL}$  value as a percentage of the 1996 truck traffic statistics, as shown in Table 5-14 for the recommended repair plan 4. However a conservative traffic prediction provided by KDOT in the year 2000 shows an overall trend of increase of the truck traffic during the next 20 years. Table 5-15 summarizes the major traffic information on the bridge for the years 2003~2023 based on the KDOT traffic forecast. For comparison purposes, the traffic data of the year 1996 is also included in the table. The construction of the new bypass has not started at that time. It is noticed that although the total percentage of the truck traffic decreases from the year 2003 to 2023, the average daily truck traffic increases, because the projected daily traffic on the bridge increases. However, only a small change is found in the truck traffic percentage, and the number of  $(ADTT)_{SL}$  also varies slightly, from 300 for the year 2003 to 360 for the year 2023. Since these numbers are close to the 1996  $(ADTT)_{SL}$  of 344, a remaining service life of 15 years should be an appropriate prediction for the subject bridge if repair plan 4 is used.

**TABLE 5-15: Traffic Prediction for the Arkansas River Bridge**

Year	Projected Daily Traffic	Percentage of Truck Traffic (%)			$(ADTT)_{SL}$	Predicted in Year
		Medium	Heavy	Total		
1996	12500 w/o bypass	3.0	8.0	11	344	1993
2003	12000 w/ bypass	2.1	7.9	10	300	2000
2013	14000 w/ bypass	2.1	7.9	10	350	2000
2023	16000 w/ bypass	1.9	7.1	9	360	2000

The actual remaining life of the repaired detail may exceed 15 years, because 1) the actual stress ranges experienced by the bridge members might be lower than calculated, and 2) the future truck traffic on the bridge could be less than predicted after the new bypass is put into use. As previously discussed in section 5.5.2.2 for the case of repair plan 2, the maximum stress range obtained from the finite element analysis is very high and the remaining life calculated based on this stress range is very short. However, in reality many Iowa DOT two-girder bridges have been repaired by the same method since 1980, and the repaired details all perform well according to recent inspections. It might be because the actual stress range occurring at the repaired detail is much lower than the theoretical value. The same situation may also be expected for repair plan 4. As long as the cut surface is well finished and the gouged crack is properly rewelded, a longer than 15 years life should be achieved. It is recommended that field testing be performed for the Arkansas River Bridge in order to assess the actual stress condition in the field, and a revised traffic count be provided after the Hutchinson Bypass is in normal service. Consequently a more reasonable estimate for the remaining life can be obtained. Before these efforts are carried out, the finite element based analysis conducted in this study presents a post-retrofit minimum service life of 15 years by using repair plan 4.

## 5.6 Summary

Type 3 out-of-plane fatigue cracks developed at the floor-beam to exterior girder connections have consisted of the worst cracking scenario in the Arkansas River Bridge. The finite element submodeling approach used in this case study successfully depicts the secondary stresses developed in the local concentration area, both quantitatively and qualitatively. A summary of the investigations conducted in this chapter is given as follows.

1. The maximum stress variation occurring at the crack initiation site is close to yielding. As the crack size increases, the stress field relaxes and the crack growth rate slows down. However, the propagation continues as the crack tip is still in high tension. Appropriate retrofit actions for the floor-beam to exterior girder connections thus should be carried out as soon as possible in order to eliminate the stress concentration and improve the fatigue resistance to the out-of-plane distortion.
2. Fatigue life experienced by the existing cracked details is calculated using both the traditional single edge crack  $K_I$  formula and the direct ANSYS  $K_I$  results. Both yield the number of stress cycles of about 6 million, which is consistent with the life estimate based on KDOT traffic count and is considered to be in good agreement with the actual condition.
3. Four different repair options are studied and repair plan 4, cutting the connection plate partially short and rewelding the crack, is recommended for the bridge retrofit. Though an infinite life is not achieved, a minimum remaining service life of 15 years can be obtained after the repair.
4. This case study is based entirely on the finite element analysis. Field testing is recommended as future work in order to obtain the actual stress ranges occurring in the bridge and to provide more accurate life prediction for the repair details.

## Chapter 6

### Case Study II: The Westgate Bridge

The Westgate Bridge developed fatigue cracks at small web gaps close to girder top flange. Repairs had been performed by welding the connection stiffener to the top flange in the girder positive moment regions and by adding a new stiffener plate opposite the existing connection stiffener in the girder negative moment regions. A two-level, stick frame to finite element analysis procedure is carried out in this chapter to investigate the web gap fatigue stresses around the crack details, to evaluate the existing repair methods used in the bridge, and to recommend new retrofit options when necessary.

#### 6.1 Bridge Structure and Crack Observation

The Westgate Bridge [KDOT Bridge No. 75-89-18.02(154)] was built in 1977 on US-75. It is a two-girder, no-skew bridge consisting of a girder/truss floor-beam/stringer system, as shown in Figure 6-1 and 6-2. This is a typical superstructure type used in the design of several KDOT welded plate girder bridges during that era. The two girders are 1758 ft long, consisting of 11 continuous spans with hinges only at Span No. 7. The roadway width is 40 ft, including two 12 ft traffic lanes, one 10 ft shoulder on the west, and another 6 ft shoulder on the east. The truss floor-beam depth varies from 5.5 ft to 12 ft. All steel plates are made of A36 material. The predicted annual average daily traffic (AADT) counts for the bridge are 27,300 for the year 1999 and 36,000 for the year 2019. Contributions due to medium and heavy trucks are 4.7% and 5.3%, respectively.

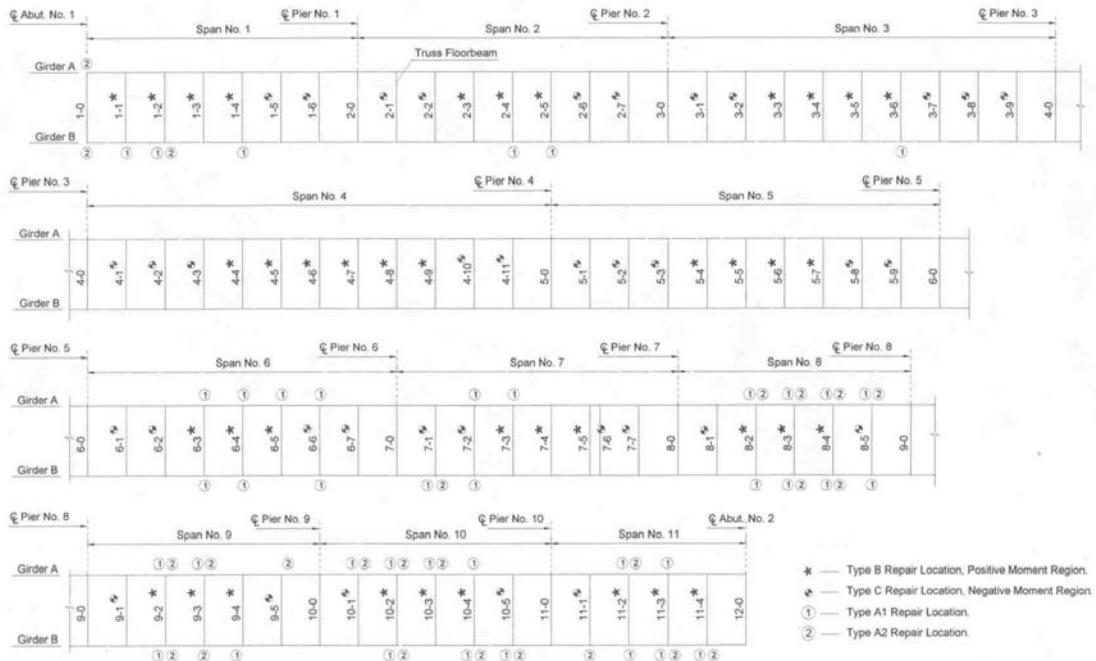


**FIGURE 6-1: Framing Plan and Retrofit Locations of the Westgate Bridge**

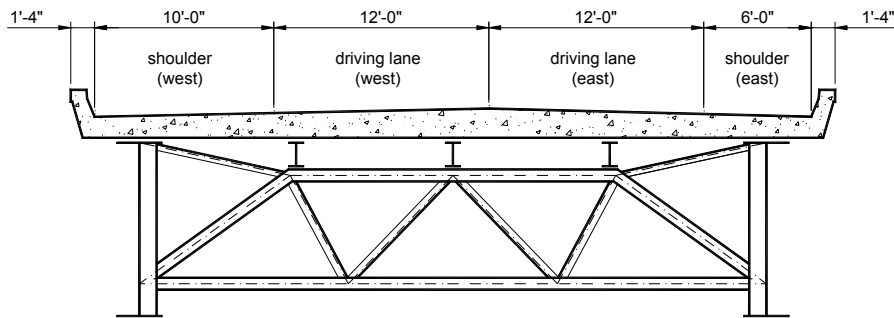


**FIGURE 6-2: Cross Section of the Westgate Bridge**

By the year 1994, 9 out of the 11 girder spans had developed horizontal or horseshoe cracks at the interior floor-beam to girder connections. All observed cracks occurred at the small web gaps close to girder top flange, in both the positive and negative moment regions. No cracks were found at the floor-beam connections at the bridge piers, where the stiffeners were designed to meet the bearing requirement and were used on both sides of the girder web. Figure 6-3 shows

the crack growth at the stiffener to web and top flange intersection. Although the connection stiffener was not designed to be welded to the flange, it was common practice at that time to attach a very short tack weld at the stiffener end for ease of fabrication. According to inspection records, the crack started when the tack weld was broken, which then left the web gap unstiffened and subject to out-of-plane distortion. This is reported as Phase I cracking. Phase II cracking occurred when the bottom of the web gap was pulled inward repeatedly by the floor-beam truss member, causing horseshoe cracks to initiate from the end of the stiffener-to-web welds. As the action of out-of-plane distortion continued, horizontal cracks then formed at the top of the web gap along the flange-to-web welds, introducing the Phase III cracking. Inspection pictures showing actual crack development on both sides of the girder web are presented in Figure 6-4. Although the girders are non-composite, the top flange is somewhat embedded into the concrete slab above, which prevents it from rotating with the web section beneath. The girder bottom flange is less constrained and more free to move laterally. Therefore cracks observed in this bridge were all located near the top flange. This is also the most frequently seen crack location in other KDOT bridges that have experienced fatigue cracking.

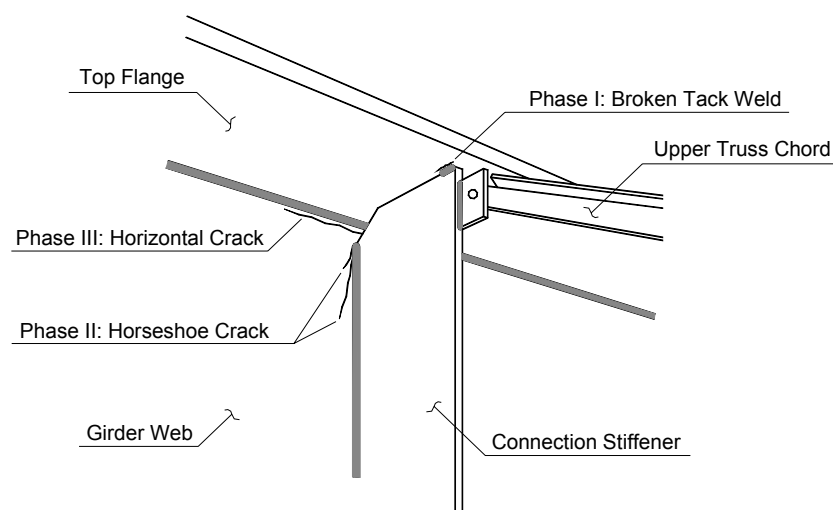


**FIGURE 6-3: Crack Growth Near the Girder Top Flange Connection**



(a) horizontal and horseshoe cracks on the interior girder web side



(b) horizontal crack on the exterior girder web side

**FIGURE 6-4: Inspection Pictures Showing Web Gap Cracks in the Westgate Bridge**

## 6.2 Repair Methods Used by KDOT

To prevent further crack growth while maintaining bridge use, an overall structural repair was carried out in 1998. All the interior floor-beam to girder connections were repaired, even though some of them had not developed fatigue cracks. The retrofit approaches used at different floor-beam locations are outlined in Figure 6-1. Figure 6-5 describes the detailed repair procedures as follows:

- a) At locations where horizontal or horseshoe cracks were identified, 1 in. diameter holes were drilled at the end of the cracks to stop the propagation [Figure 6-5(a) and (b)].
- b) At positive moment regions, the web gap areas were stiffened by connecting the stiffeners to the top flanges with  $\frac{5}{16}$  in. fillet welds [Figure 6-5(c)].
- c) At negative moment regions, new  $\frac{3}{4}$  in. stiffener plates were added on the other side of the girders to help resist out-of-plane distortion, and the existing stiffeners were welded to the girder bottom flanges [Figure 6-5(d)]. Repair welds were not made to the girder top flanges to avoid a detail susceptible to in-plane fatigue cracking. The new stiffener plates were fit tight to the tension flanges at the top, and cut short at the bottom if intersected with existing longitudinal stiffeners.

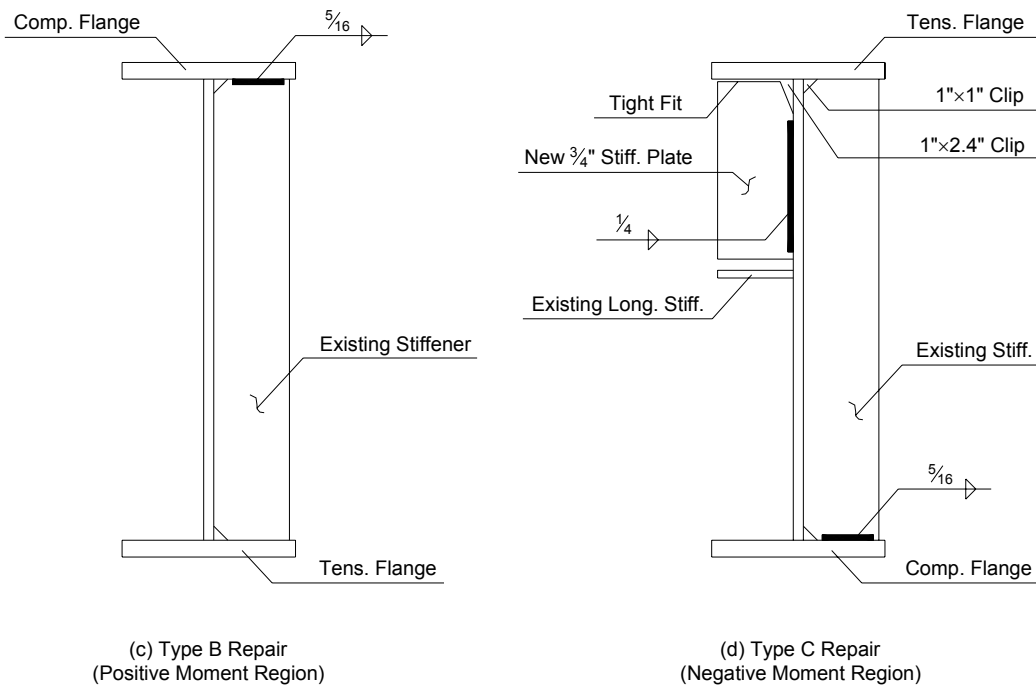
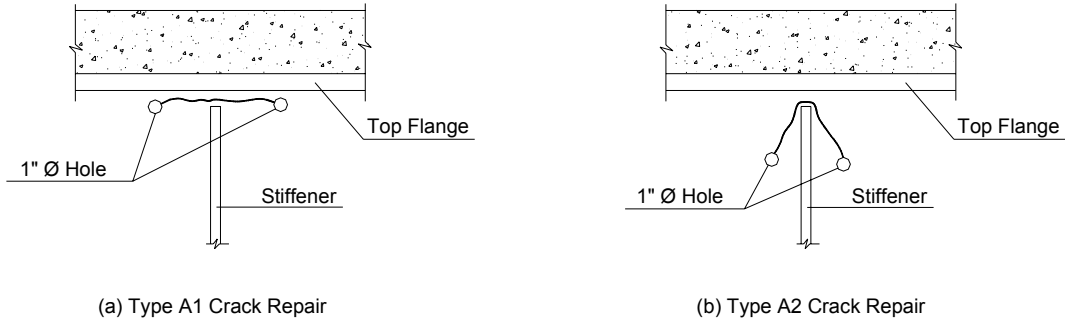


**FIGURE 6-5: Repair Approaches Used in the Westgate Bridge**

No new crack development has been reported since the bridge was repaired. However, the long-term effect of the applied retrofit is still a concern, as the direct cause of the out-of-plane distortion has not been eliminated. The web gap cracks developed in this bridge were actually caused by the upper truss chords pulling the connection stiffeners out-of-plane under traffic loading. The most effective method to eliminate the secondary stresses could be simply to

remove these members. However, although they were not designed as permanent load-carrying members, the upper chords can help stabilize the floor-beam trusses during deck replacement, and thus should be maintained wherever possible in each span. This case study investigates the effectiveness of both the existing repair methods used in the bridge and other proposed retrofit approaches that can decrease the fatigue stresses at the crack areas, including removal of the floor-beam upper truss chords. The goal is to reduce the stress magnitude to a level that no crack re-initiation or additional crack growth would occur at the web gap regions.

### **6.3 Modeling Procedures**

Span No. 10 represents the typical structural layout of the Westgate Bridge and is thus selected for detailed study. Its girder elevation is shown in Figure 6-6. A computational model capturing the relevant three-dimensional differential deflections and relative stiffnesses is constructed to study the structure's behavior. To simplify the analysis, only those components within the two rectangles are modeled using finite elements. Model FM1 represents the floor-beam to girder connections at the positive moment regions, and model FM3 represents those at the negative moment regions. The cut length for both models is equal to the floor-beam spacing (22 ft 8 in.), with half of the length (11 ft 4 in.) on each side of the connection stiffener. All the plates (flanges, webs, stiffeners) and welds are modeled by 8-node brick elements. The dimensions of these structural components are listed in Table 6-1. Figure 6-7 shows schematically the element mesh and the boundary conditions applied to the models. Since the top flange is restrained by the concrete roadway, all degrees of freedom are fixed for the flange upper surface nodes. The lateral diagonal bracings are connected to the web close to the bottom flange at mid floor-beam spacing, as illustrated in Figure 6-8, so the flange nodes on the girder cut edges are also assumed to be fixed.

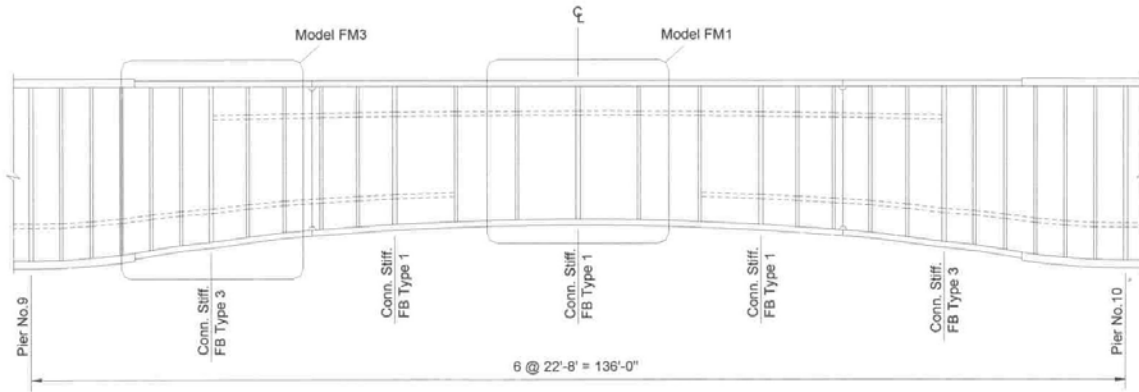


**FIGURE 6-6: Girder Elevation for Span No. 10**

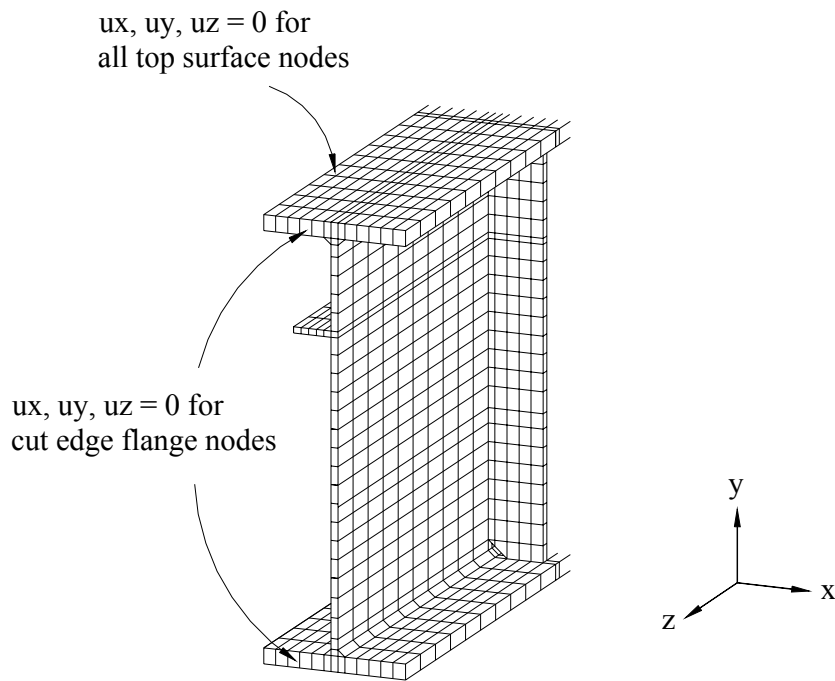


**FIGURE 6-7: Boundary Conditions for the Finite Element Model**

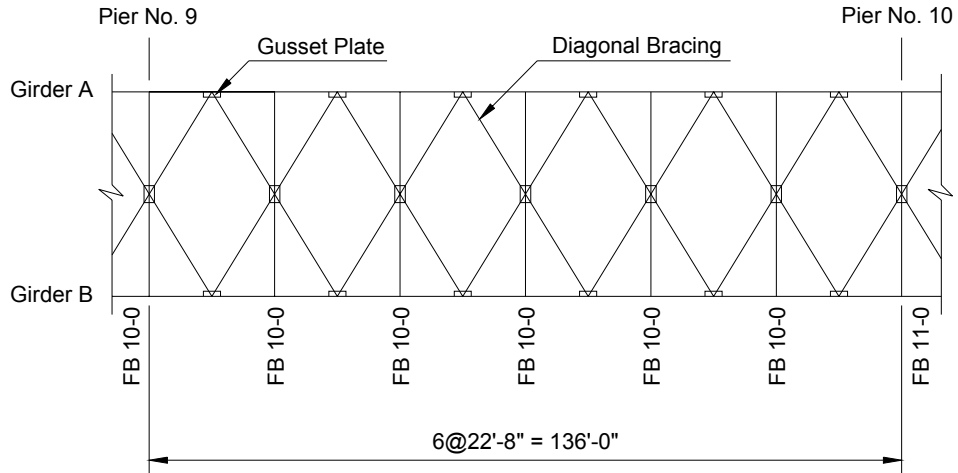


**FIGURE 6-8: Framing Plan for Diagonal Bracings in Span No. 10**

The load path of this structure that led to the out-of-plane distortion can be defined as:  
 truck loading  $\xrightarrow{(1)}$  deck slab  $\xrightarrow{(2)}$  stringer  $\xrightarrow{(3)}$  truss frame  $\xrightarrow{(4)}$  connection stiffener  
 $\xrightarrow{(5)}$  girder web. To derive the forces of those truss members that are directly attached to the connection stiffener, the bridge cross section shown in Figure 6-2 is disassembled into two independent stick frame models, as indicated in Figure 6-9.

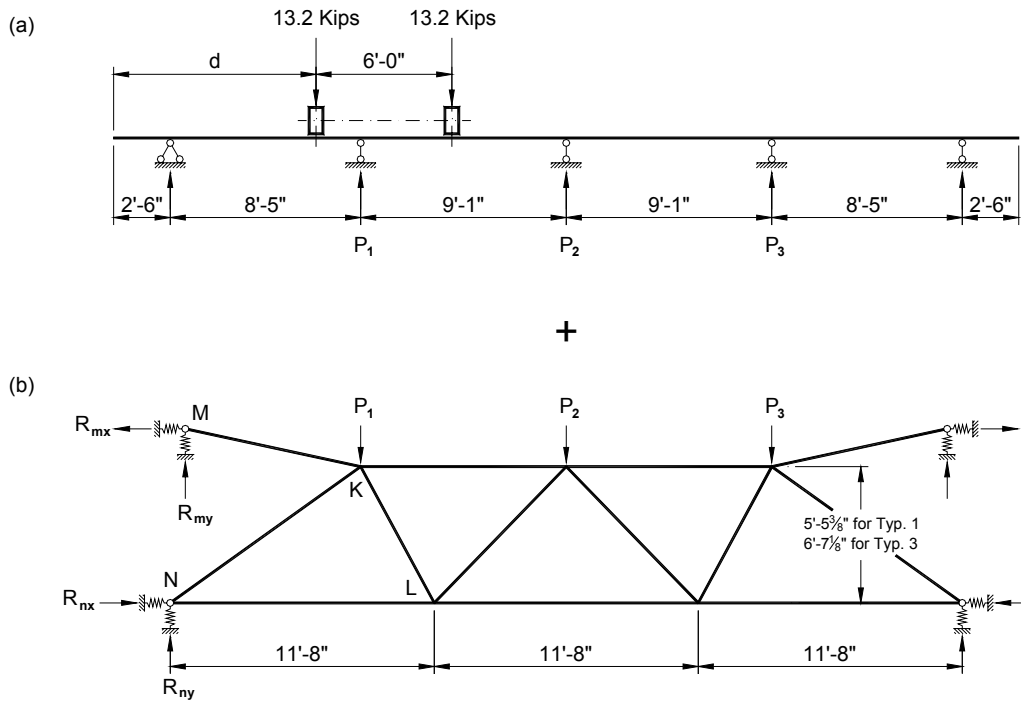


**FIGURE 6-9: Stick Frame Models for Load Path Calculation**

**TABLE 6-1: Plate and Weld Dimensions for Finite Element Modeling**

Item	Dimension (in.)	
	Model FM1	Model FM3
Flange	18 × 1-1/8	18 × 1-1/8
Web	3/8	3/8
Transverse intermediate stiffener	5 × 3/8	5 × 3/8, 6 × 7/16
Transverse connection stiffener	8 × 3/4	8 × 3/4
Longitudinal stiffener	3/8	3/8
Repair stiffener plate	—	3/4
Flange-to-web weld	5/16	5/16
Stiffener-to-web weld	1/4	1/4
Repair weld	5/16	5/16

The first two steps of the load path, from truck loading to stringers, are illustrated in Figure 6-9(a), where the deck slab is modeled as a rigid continuous beam, supported at the points where girders and stringers are located. The beam is loaded by the heaviest axle (either the drive axle or the rear trailer axle) of the HS15 fatigue truck. This loading pattern is similar to what was used by Ross et al. [1994] on the 2-D finite element analysis of a multi-girder/cross-frame bridge in New Mexico, as previously mentioned in Chapter 4. The truck is moved within the roadway width by 2 ft increments, from the utmost accessible position on the left, to the utmost accessible position on the right, for a total of 16 load cases. The edge distance  $d$  is 2 ft for Load Case No. 1 and 32 ft for Load Case No. 16. The reactions of the stringer supports,  $P_1 \sim P_3$ , for each load case are then applied to the model in Figure 6-9(b) for truss force calculation.

The third step of the load path from stringer to truss frame is modeled in Figure 6-9(b). The forces in members MK, NK, and NL are obtained through truss analysis and are then ready to be applied onto the connection stiffener. To facilitate the load transfer process, the equivalent support reactions,  $R_{mx}$ ,  $R_{my}$ ,  $R_{nx}$ , and  $R_{ny}$  are used as acting loads and are assigned to the nodes of the finite element model at corresponding locations, as shown schematically in Figure 6-10. The spring stiffnesses of the truss supports are obtained from the finite element model analyses, by finding reactions of the corresponding nodes due to imposed unit displacements along each axis. To clarify the load-imposing mechanism, the element mesh is not shown and only the girder geometry at the connection stiffener section is outlined in Figure 6-10.

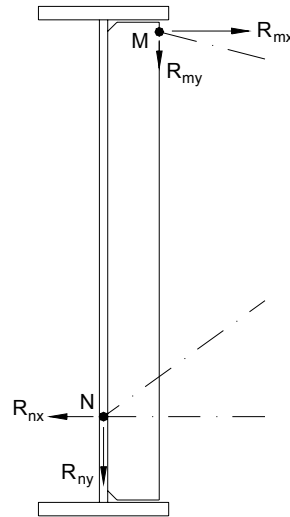


**FIGURE 6-10: Schematic of Loads Imposed on the Finite Element Model**

The discrete model described in Figure 6-9 includes the following two approximations.

1) In reality, the deck slab is not rigidly supported by the girders and stringers as shown by Figure 6-9(a). The stringer stiffness is less than the girder stiffness and thus the load carried by the stringers should be less than calculated. 2) Only the stringer reactions obtained from Figure 6-9(a) are carried over to Figure 6-9(b) for truss loading. The effect of girder reactions is not considered. Although these loads seemingly only relate to the girder in-plane bending, they contribute indirectly to the out-of-plane distortion through girder deflections. In fact, the girder section also deflects downward under traffic loading, so the relative vertical deflections between the girders and the stringers are less than implied by the Figure 6-9(b) model. The actual truss member forces, therefore, should also be less than calculated. Based on these two aspects, the preceding load path modeling approaches are conservative.

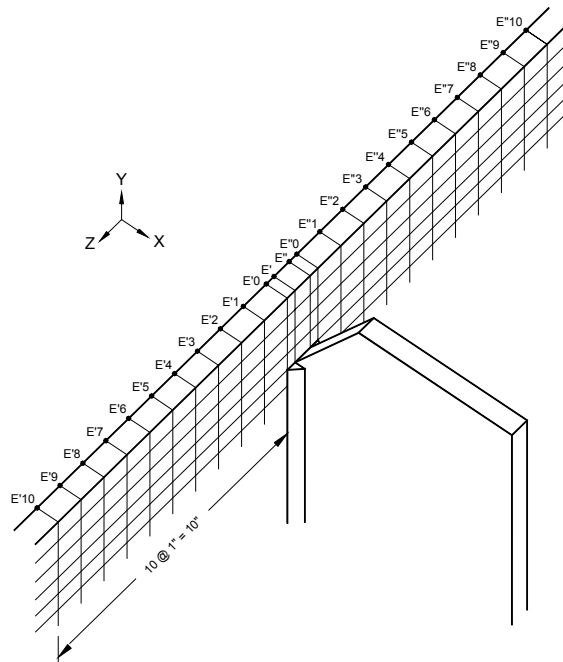
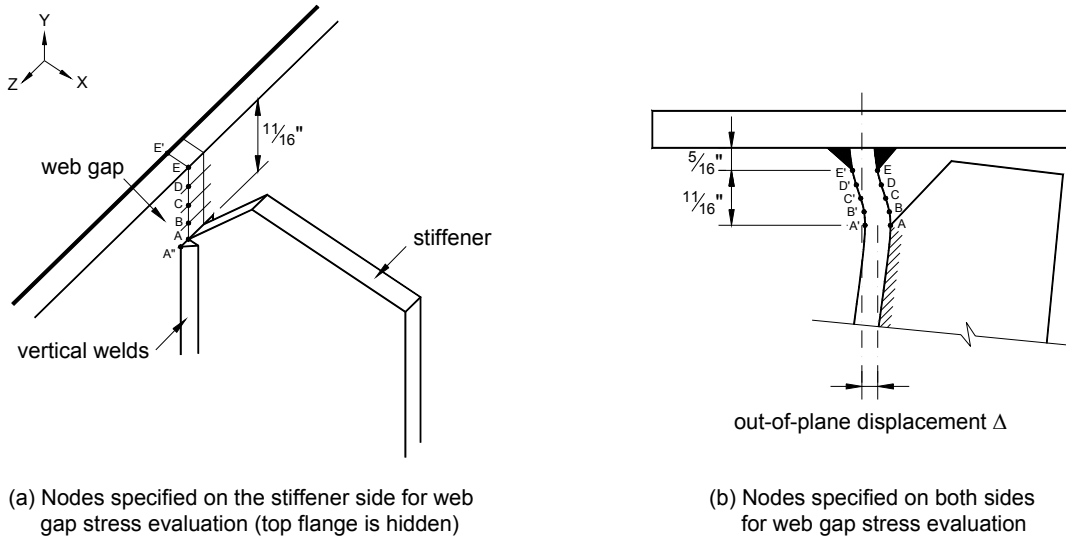
The above analytical procedures of this case study are carried out using STAAD/Pro 3.1 [1999] because the pre- and post-processors of this software are more user friendly for stick frame analysis. The investigation of the third to the fifth step of the load path, from truss frame

members to girder web gaps, is completed using finite element methods, and ANSYS 5.6 [2000] is used at this point for the next level analysis. Model FM1 has approximately 18,000 elements, 33,000 nodes, and 100,000 degrees of freedom. Model FM3 has about 26,000 elements, 46,000 nodes, and 138,000 degrees of freedom. The element mesh sizes for both models are controlled within 2 in. In particular, at the web gap areas, the mesh sizes are refined to  $1\frac{1}{64}$  in. in order to capture the effect of stress concentration.

## **6.4 Connections at the Positive Moment Regions**

### **6.4.1 Exploring Web Gap Stresses (Model FM1)**

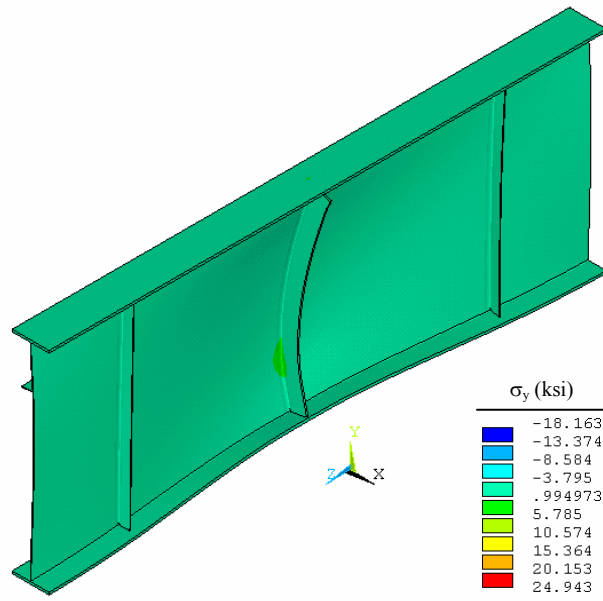
FM1 models the girder reaction subject to out-of-plane distortion at the mid span floor-beam connection. Finite element analyses for all 16 load cases are conducted and significant stress concentration effect is observed at the web gap region. Nodal stresses of those locations specified in Figure 6-11 are thus of the most interest to this study and will be used to explain the crack initiation. Nodes A and A' are evaluated for the stress concentration effect at the vertical stiffener-to-web weld end. The lateral deflection of Node A in the horizontal X-axis direction is used to define the out-of-plane displacement. Nodes A to E and A' to E' are evaluated for the stress gradient along the small web gap height. The distance between the adjacent nodes within the gap length is  $1\frac{1}{64}$  in. Nodes E', E'0 to E'10, E'', and E''0 to E''10 are evaluated for the stress distribution along the horizontal flange-to-web weld. The interval between nodes E'0, E'1, ..., E'10 and E''0, E''1, ..., E''10 is 1 in.



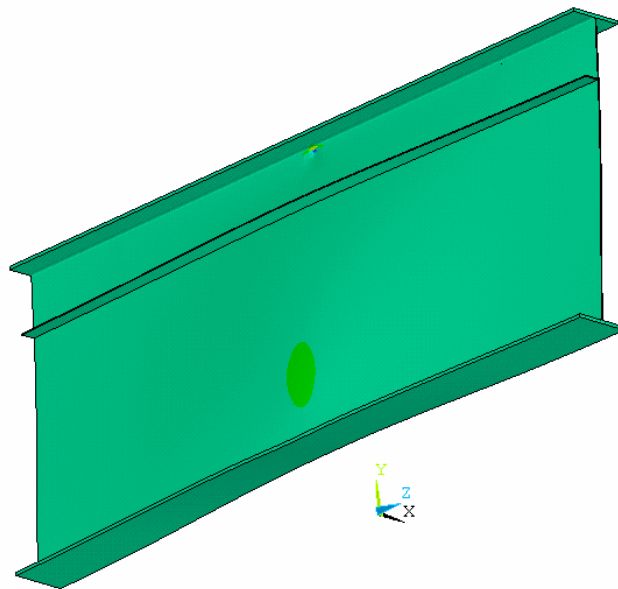
**FIGURE 6-11: Nodes in the Web Gap Specified for Stress Analysis**

Figure 6-12 shows the overall girder deformation and Y direction stress distribution of Load Case No. 7. Figure 6-13 exhibits zoomed-in views of web gap deformation and stress

contours of different axes on the connection stiffener side for the same load case. It is apparent that the stress concentration effect is confined to a very localized region. Node A at the weld root has the highest X and Y direction stresses, and Node A'' at the weld toe has the highest Z and 1<sup>st</sup> principle direction stresses. Node A'' is therefore the hottest spot on the model. The  $\sigma_x$  stress has high magnitude at the connection stiffener weld end, which could detach the stiffener from the girder web and cause cracks to form along the vertical welds [Figure 6-14(a)]. The  $\sigma_y$  contour indicates a radical stress variation within the short web gap, from high tensile stresses at the bottom end, to high compressive stresses at the top end. The high tensile  $\sigma_y$  at the web gap bottom is the direct cause of those short horizontal web cracks indicated in Figure 6-14(b). The maximum  $\sigma_z$  stress at the weld end is responsible for the initiation of vertical web cracks along the stiffener-to-web weld toes [Figure 6-14(c)]. Combination of the cracking conditions illustrated in Figure 6-14(a) and (b) can result in a “ $\pi$ ” shape crack on the exterior side of the girder web as shown in Figure 6-14(d). This is often seen during the bridge inspection when cracks have grown through the web thickness. Generally speaking, cracks occurring at the stiffener weld ends are all called horseshoe cracks.



(a) interior girder web side



(b) exterior girder web side

**FIGURE 6-12: Model FM1 Deformation and  $\sigma_y$  Contour at Load Case No. 7**

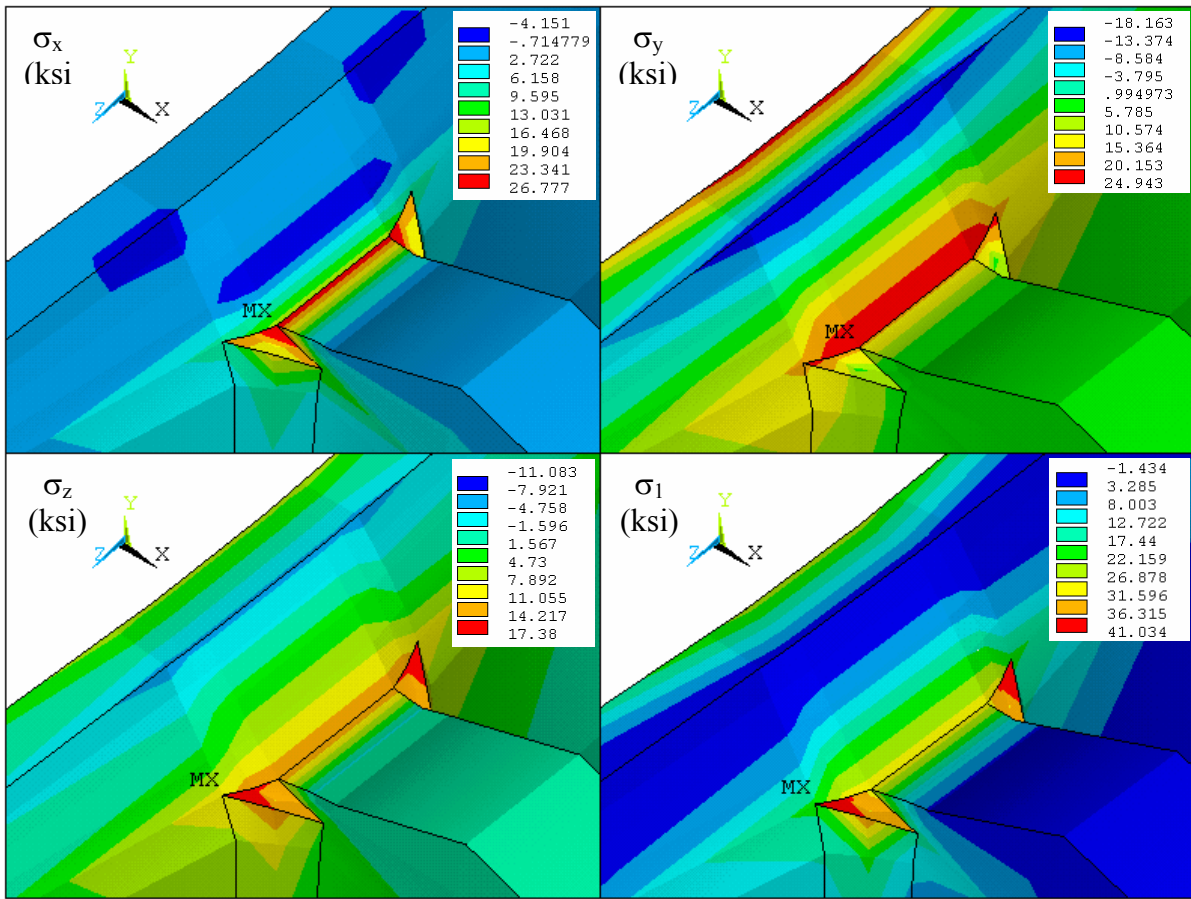


**FIGURE 6-13: Model FM1 Web Gap Stress Contours for Load Case No. 7**  
(flange elements are hidden)

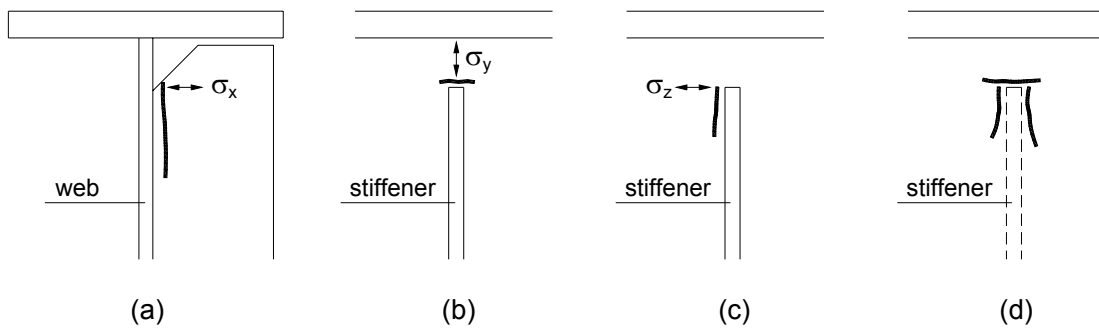


**FIGURE 6-14: Crack Formation Subject to Different Axial Stresses at the Stiffener End**

Figure 6-15 shows the web gap  $\sigma_y$  contour on the exterior girder face for Load Case No. 7. Contrary to what is seen on the interior side, the high tensile stresses are located at the top web gap end, and the high compressive stresses are located at the bottom web gap end. The highly stressed tension zone at the top end causes the occurrence of horizontal cracks along the flange-to-web fillet welds. Stress gradients on both sides of the web gap for Load Case No. 7 are plotted in Figure 6-16. The out-of-plane displacement at this load case is only  $1.6 \times 10^{-3}$  in. However, the stress variation within the web gap caused by this small displacement is significantly large, and it occurs over a short web gap of only  $1^{11}/_{16}$  in.

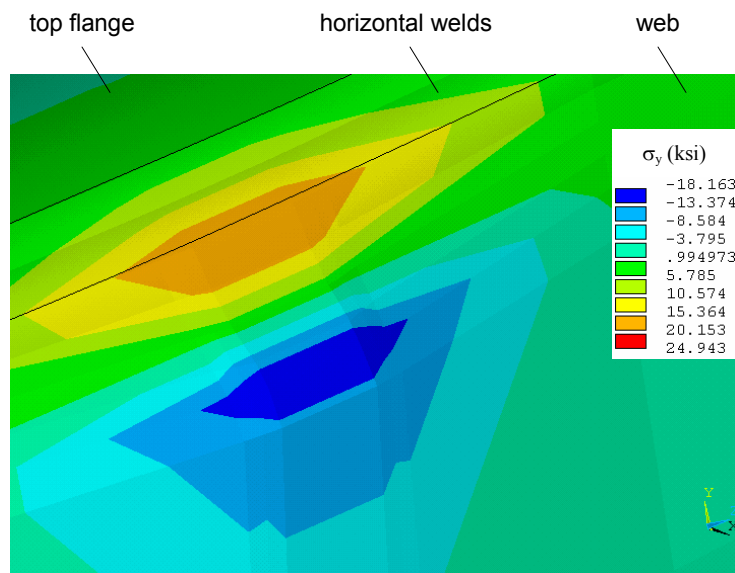


**FIGURE 6-15: Model FM1  $\sigma_y$  Contour of Load Case No. 7 on the Exterior Girder Face**

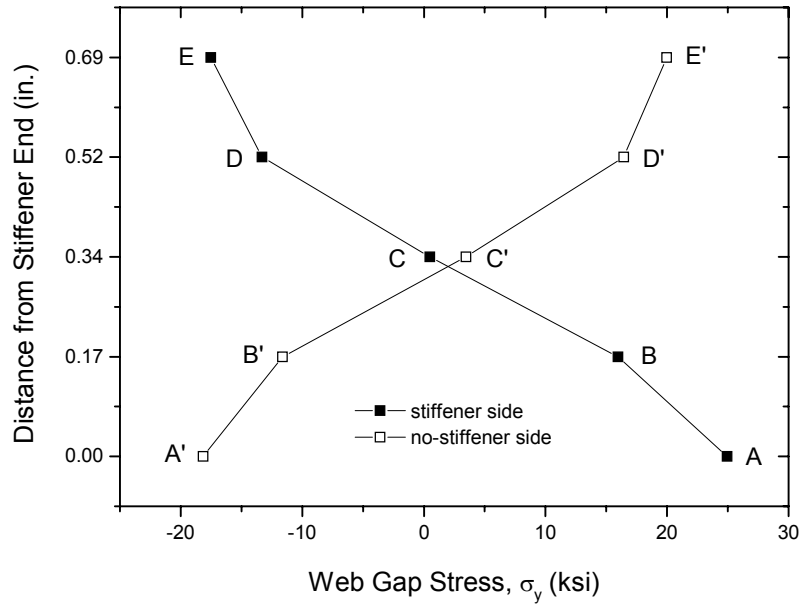


**FIGURE 6-16: Model FM1 Web Gap Stress Gradient at Load Case No.7**

Figure 6-17 shows the distribution of  $\sigma_y$  stresses normal to the horizontal flange-to-web weld along the weld toe on the exterior girder web side. Results plotted in the figure are for nodes close to the web gap region and those at 1 in. interval from each side of the stiffener-to-web welds for 10 in. The stress distribution is symmetric about the stiffener mid surface. High magnitude stresses occur near the web gap between E'0 and E''0, with a peak  $\sigma_y$  value of 20 ksi at Node E' and E''. Stress within the 2 in. area adjacent to this “hot” zone drops off rapidly and linearly to reach 2.9 ksi at E'2 and E''2. The next 2 in. area sees continuous stress reduction, but with a much less steep slope. Finally, at locations further from E'4 or E''4, a stable, close to zero stress field can be obtained. For this particular connection, it is safe to conclude from Figure 6-17 that the web area affected by out-of-plane distortion is within 5 in. length on each side of the connection stiffener. That is, within a 10 in. zone. The crack opening stresses outside this affected zone along the horizontal fillet weld toe are considered zero. This indicates that the adopted length for the FM1 model is long enough to accommodate the stress variation and

concentration effect at the web gap regions. The corresponding nodal stresses on the interior girder side are in a compression zone. The distribution pattern is the same but with negative stress magnitudes. Therefore, only the results on the exterior web side are discussed.

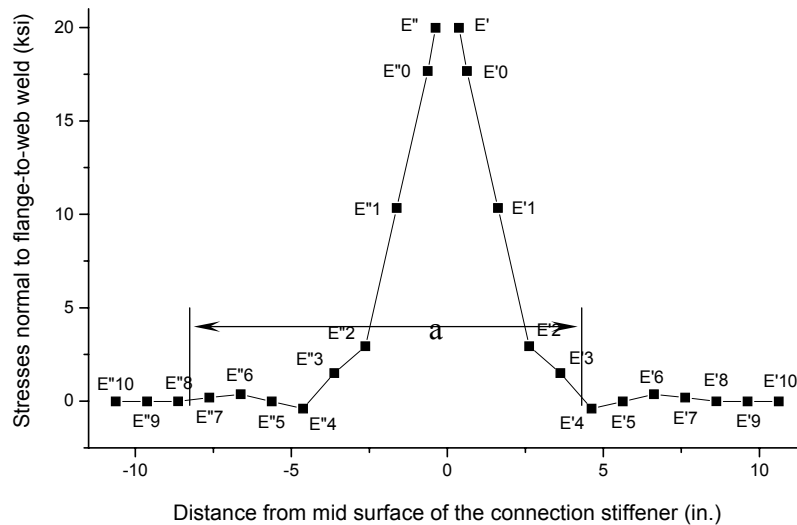


**FIGURE 6-17: Model FM1  $\sigma_y$  Distribution Along the Flange-to-Web Weld Toe at Load Case No.7**

The crack opening stress magnitude on the exterior web surface is less than that on the interior surface. For example,  $\sigma_y$  is 20 ksi at Node E' and 25 ksi at Node A. Recalling the crack occurring sequence observed in the bridge, since the tack weld is not included in the model, this result explains numerically why the Phase II horseshoe cracks initiated earlier than the Phase III horizontal cracks during the actual bridge service. The horizontal cracks presumably should initiate from the exterior web side first, since the  $\sigma_y$  stresses along the weld toes are in tension on the outside web surface and in compression on the inside web surface. However, in reality, bridge inspectors always see horizontal cracks occur earlier on the interior web side. This is caused by the residual stresses developed on the interior web side due to inadequate clearance between the vertical and horizontal fillet welds. As shown in Figure 6-18(a), bridges designed by KDOT and many other DOTs before the mid 1980s used a clip size of 1 in. by 1 in. at the

connection stiffener end, and the vertical welds were terminated at the end of the clip. This left only an  $1^{1}/_{16}$  in. gap in between the horizontal and vertical welds, which made it easy for the high welding residual stresses to occur in the web gap during the fabrication process. The current stiffener design detail requires a web gap length of four to six times of the web thickness at the intersection of horizontal and vertical welds. As shown in Figure 6-18(b), if the same detail is designed according to present design provisions, a clear distance between the vertical and horizontal welds of  $1^{1}/_{2} \sim 2^{1}/_{4}$  in. should be adopted. Compared to that of Figure 6-18(a), the dimension used in Figure 6-18(b) helps reduce the chances of developing residual stresses and at the same time soften the constraints at the web gap region as well. The condition of residual stress is usually complex and outside the range of this study, thus this effect is not considered during the finite element modeling.

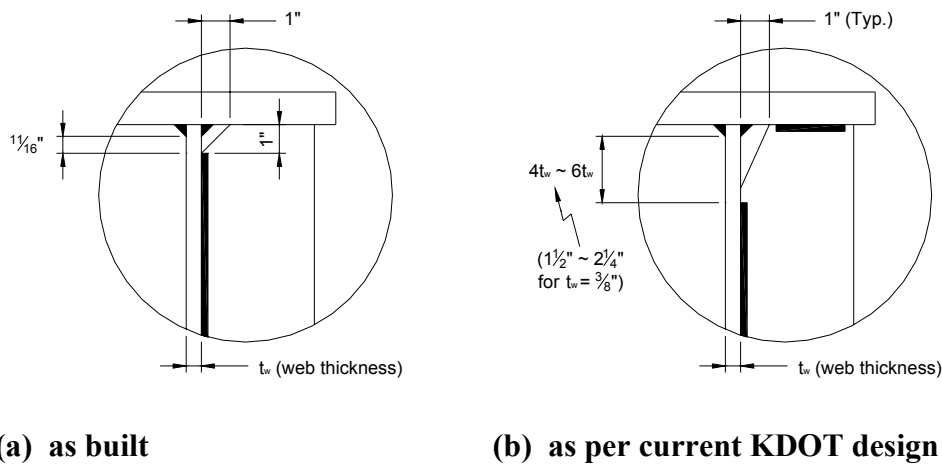


**FIGURE 6-18: Comparison of Web Gap Details Required by KDOT in the Earlier and Current Design**

The other 15 load cases have the same stress distribution pattern as Load Case No. 7, but the effect of stress concentration is less significant. The change of out-of-plane displacement for different truck locations is plotted in Figure 6-19. The web gap nodal  $\sigma_y$  stress variations are

shown in Figure 6-20 and 6-21. The maximum  $\sigma_x$  and  $\sigma_z$  stresses of the model at each load case are plotted in Figure 6-22. Stresses of Load Case No. 7 are always the highest for Model FM1 and are therefore assumed as stress ranges for fatigue evaluation. According to the AASHTO *LRFD Bridge Design Specifications* [1998], the fillet weld connections with welds normal to the direction of stress are classified as fatigue Category C' details at the toe of transverse stiffener-to-flange and stiffener-to-web welds, and are classified as Category C details in other conditions. The constant amplitude fatigue thresholds (CAFT) for Detail Category C and C' are 10 ksi and 12 ksi, respectively. The preceding stress analysis indicates that the flange-to-web welds are Category C details and the connection stiffener-to-web welds are Category C' details when subjected to out-of-plane distortion. The  $\sigma_y$  stress range at Node E' perpendicular to the flange-to-web welds is 20 ksi, which is almost two times of the CAFT of Detail Category C. The  $\sigma_x$  stress range at Node A is 27 ksi. The  $\sigma_z$  stress range at Node A'' is 17 ksi. Both of these stress ranges are normal to the stiffener-to-web welds and are higher than the CAFT of Detail Category C'. As a result, fatigue cracking could initiate from these hot spots whenever other conditions such as initial flaws coexist. The critical crack opening stresses and their respective locations are summarized in Table 6-2. The model analysis of FM1 thus successfully yields solutions for the distortion-induced stresses and effectively justifies the crack initiation rationale.

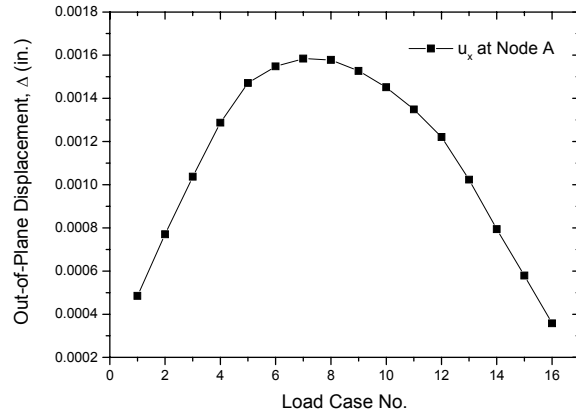


**Figure 6-19: Model FM1 Out-of-Plane Displacement**

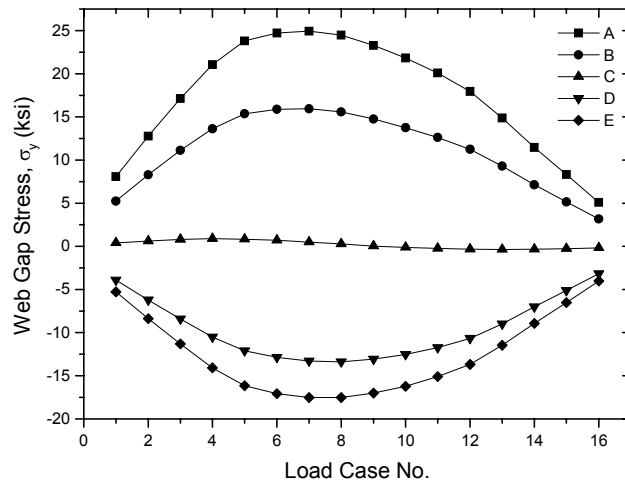


**FIGURE 6-20: Model FM1 Web Gap Stress Variation for Nodes on the Interior Web Side**

**TABLE 6-2: Critical Crack Opening Stresses in Model FM1 at Load Case No. 7**

	Stress (ksi)	Location (Node)	AASHTO Fatigue Detail Category	CAFT (ksi)
$\sigma_{x, \max}$	27	A	C'	12
$\sigma_{y, \max}$	25	A	—	—
	20	E'	C	10
$\sigma_{z, \max}$	17	A''	C'	12
$\sigma_{1, \max}$	41	A''	—	—

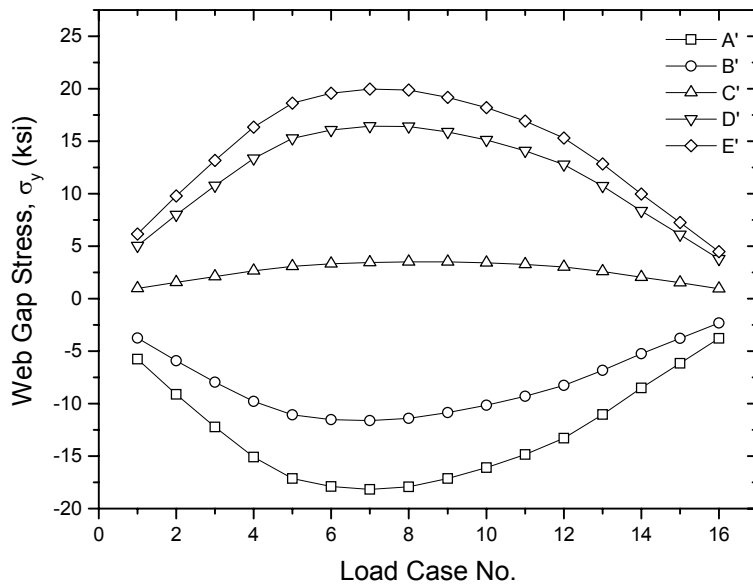


**FIGURE 6-21: Model FM1 Web Gap Stress Variation for Nodes on the Exterior Web Side**

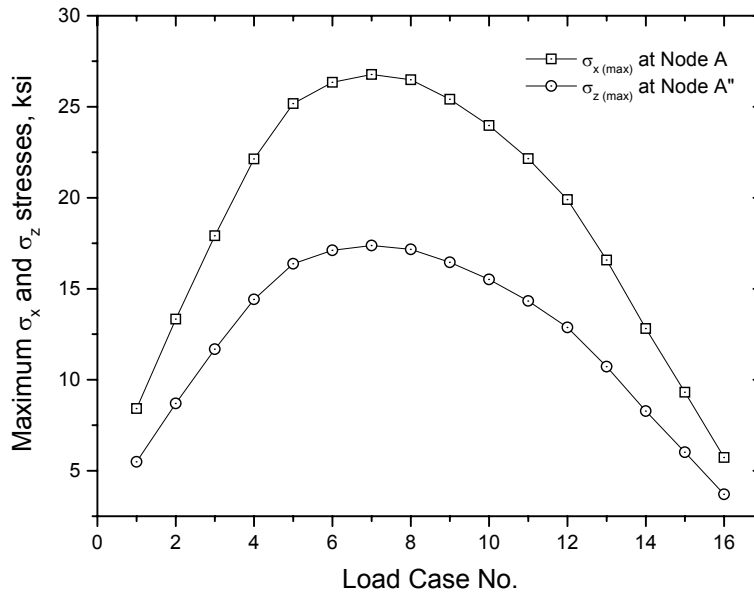


**FIGURE 6-22: Model FM1 Maximum  $\sigma_x$  and  $\sigma_z$  Stress Variation**

### 6.4.2 Repair Analysis

Additional finite element analyses are then conducted to see how effectively the secondary stresses in the web gap could be mitigated by using different repair methods. Three

retrofit approaches are considered: 1) to add connecting welds as actually implemented in the bridge repair; 2) to remove the upper truss chords; and 3) to remove the truss members in addition to the current welded repair. As shown schematically in Figure 6-23, either the local geometries or the loading conditions of FM1 are slightly changed for the repair models.

#### 6.4.2.1 Welding Connection Stiffener to Top Flange (Model FM1-w)

FM1-w [Figure 6-23(b)] models the actual retrofit applied to the connections at the positive moment regions. The repair welds are added to the finite element model and connect the stiffener to the top flange. The out-of-plane rotational stiffness of the girder section is thus changed, and the spring stiffness of the truss end supports and the loads on the finite element model have to be recalculated. Significant stress reduction is observed from this repair analysis. The stresses in the web gap indicate a mild, close to zero magnitude distribution. Compared to the stress values of those hot spots in Model FM1, the average percentage reductions of all 16 load cases for  $\sigma_x$ ,  $\sigma_y$ , and  $\sigma_z$  are 98%, 96%, and 98% for this model. The highest  $\sigma_x$ ,  $\sigma_y$ ,  $\sigma_z$  stresses in the web gap are 0.44 ksi, 0.87 ksi, and 0.39 ksi, respectively, which are much lower than the half of the CAFT of Detail Category C and C'. Therefore, an infinite fatigue life can be expected at the web gap details after the repair.

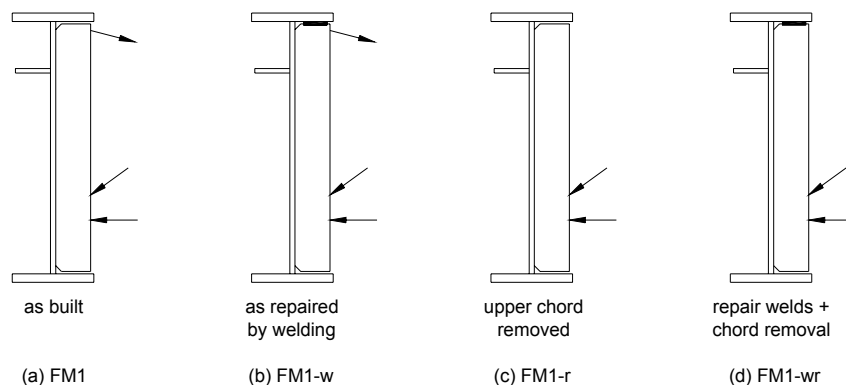


**FIGURE 6-23: FM1 Model Series**

The stress field ahead of the repair welds at the stiffener-to-flange connection is also a Category C' detail. It is important that the retrofit should not lead to a new concentration site at this area and introduce a new path for crack growth. Stresses normal to this newly welded connection are then examined for each load case and the maximum stress magnitude is observed at Load Case No. 6. The  $\sigma_y$  stress distribution along the repair weld toes for this load case is plotted as shown in Figure 6-24. The highest  $\sigma_y$  stress, 3.0 ksi, occurs at the point 7 in. away from the girder web. Although this stress is much higher than those at the web gap region, it is only one quarter of the CAFT of Detail Category C'. Figure 6-25 shows the ANSYS  $\sigma_y$  contour of Model FM1-w at the connection stiffener end for Load Case No. 6. The maximum stress occurs at the point where the truss member force is applied. The web gap and repair weld toes are in a zone of low stress magnitude. So the stiffener to web and flange connection detail is in a safe condition and fatigue cracking should not occur using the welded repair.

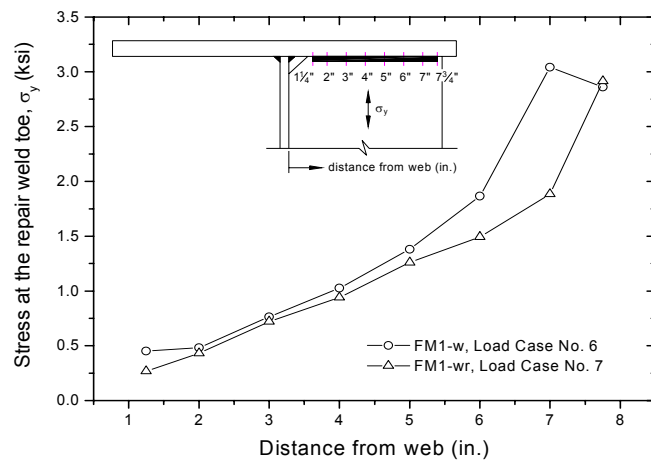


**FIGURE 6-24: Stress Distribution Along the Repair Welds**

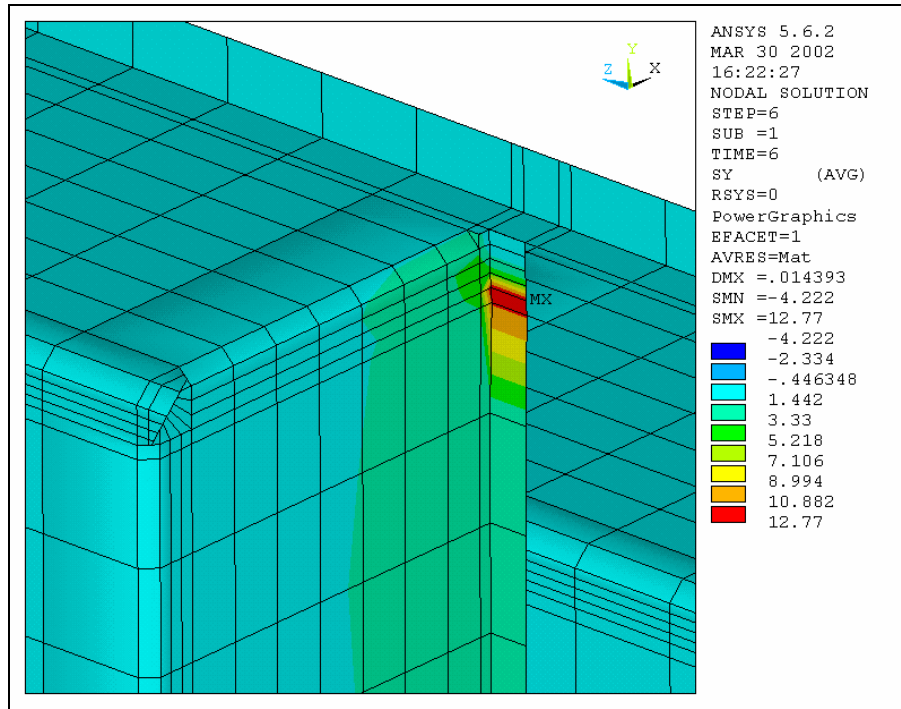


**Figure 6-25: ANSYS  $\sigma_y$  Stress Contour for Model FM1-w at Load Case No. 6**

#### **6.4.2.2 Removing Upper Truss Chord (Model FM1-r)**

FM1-r [Figure 6-23(c)] models the repair method by removing the upper truss chords. Both the truss model and the finite element model are reanalyzed, since the truck loading has to be redistributed into the truss members, changing the loading condition of the finite element model for each load case. The results show that the average percentage reductions for  $\sigma_x$ ,  $\sigma_y$ , and  $\sigma_z$  stresses at the web gap are 99%, 90%, and 96%, respectively, for 16 load cases. The maximum stress ranges occurring at the flange-to-web and stiffener-to-web connections are all much lower than half of the CAFT of Detail Category C or C'. The chord removal repair therefore can also effectively reduce the stress concentration and prevent the fatigue cracking driven by out-of-plane distortion.

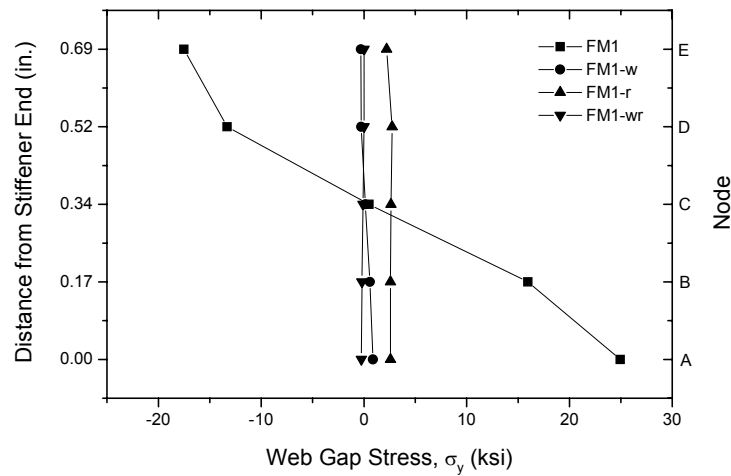
### ***6.4.2.3 Adding Connection Welds and Removing Truss Members (Model FM1-wr)***

Model FM1-wr [Figure 6-23(d)] combines the repair methods used in FM1-w and FM1-r. As can be predicted, stresses at the web gap region are greatly reduced, and are found in a zone of low compression (close to zero stress) in most load cases. The  $\sigma_x$ ,  $\sigma_y$ , and  $\sigma_z$  stresses at the locations corresponding to those hot spots of Model FM1 are decreased averagely by 100%, 101%, and 100%, respectively. More than 100% reduction is obtained because stresses have changed signs. The highest stress normal to the stiffener-to-flange weld toe is 2.9 ksi, occurring at a distance  $7\frac{3}{4}$  in. away from the web in Load Case No. 7. The  $\sigma_y$  stress distribution along the repair welds for this load case is also shown in Figure 6-24.

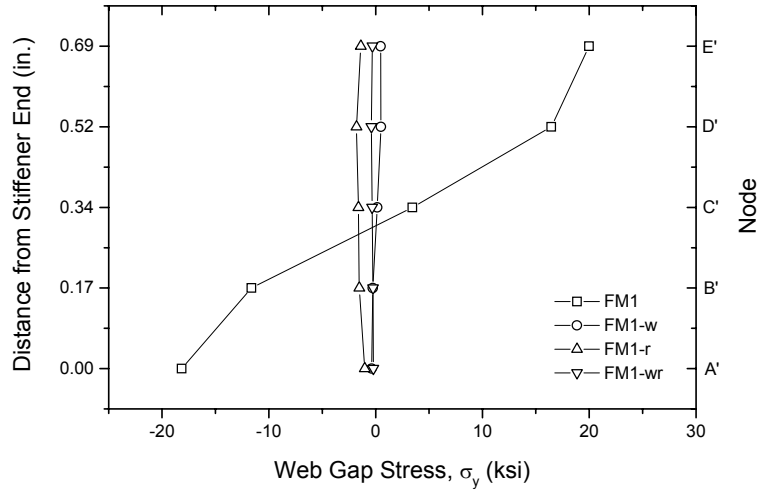
### **6.4.3 Evaluation of FM1 Model Series**

Table 6-3 summarizes the maximum web gap stresses for the FM1 model series. All the above three repair methods indicated stress reduction of at least 90 percent at the web gap region. Schematic comparison of stress gradient within the web gap is shown in Figure 6-26 and 6-27. The truss chord removal is the most appropriate retrofit method if the lateral support for floor-beam is sufficient. The floor-beam system in the Westgate Bridge is braced in the horizontal plane at the bottom through diagonal bracings and at the top by stringers and deck. Bracing in the vertical plane is provided by the girder web. As shown schematically by Figure 6-28, if the two upper chords are removed at all floor-beam to girder connections and the deck is completely removed for replacement, instability could occur. Retaining the connection of the two upper chords to the girders at the positive moment regions precludes this possible floor truss instability during full deck replacement. In addition, the combined welding and removing repair does not show much more advantage than the weld only repair in stress reduction, therefore additional chord removal will not be considered. The welding repair can satisfactorily reduce the out-of-

plane displacement and local stresses at the web gap, but the quality of the repair welds is a concern. If the area at the stiffener end and top flange connection is not properly cleaned and well prepared before welding, cracking may occur later along the repair welds, since the maximum stress in the connection now moves to the stiffener-to-flange weld toes. In addition, all the repair details in this bridge at the positive moment regions require field welding with overhead position. The repaired detail thus may not be able to achieve the quality of shop welds and may have fatigue resistance lower than Category C'. Of course in this bridge the stresses along the repair welds are very low and cracks are not likely to have the chance to develop, but attention should be paid to this detail during future bridge inspections.



**FIGURE 6-26: Load Case No. 7 Web Gap Stress Gradient of FM1 Model Series on Interior Web Side**



**FIGURE 6-27: Load Case No. 7 Web Gap Stress Gradient of FM1 Model Series on Exterior Web Side**

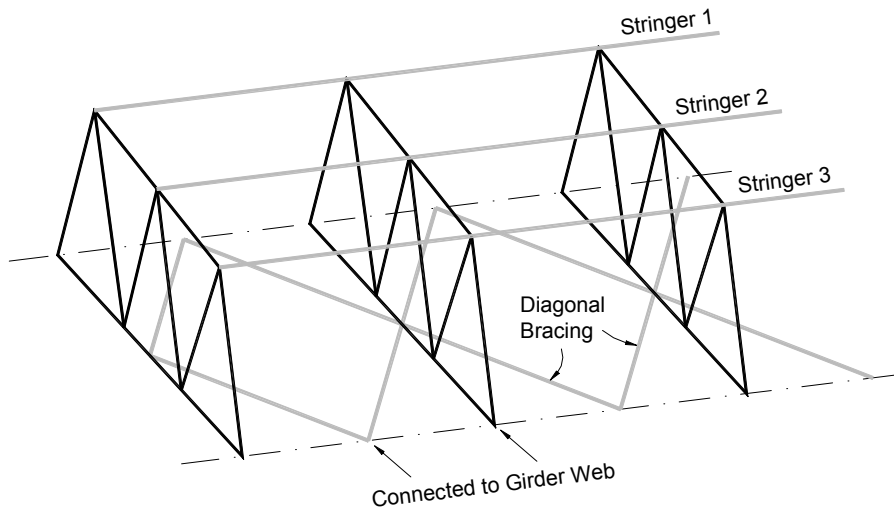


**FIGURE 6-28: Schematic of Floor-Beam Lateral Support without Upper Truss Chords**

**TABLE 6.3: Web Gap Stresses for FM1 Model Series**

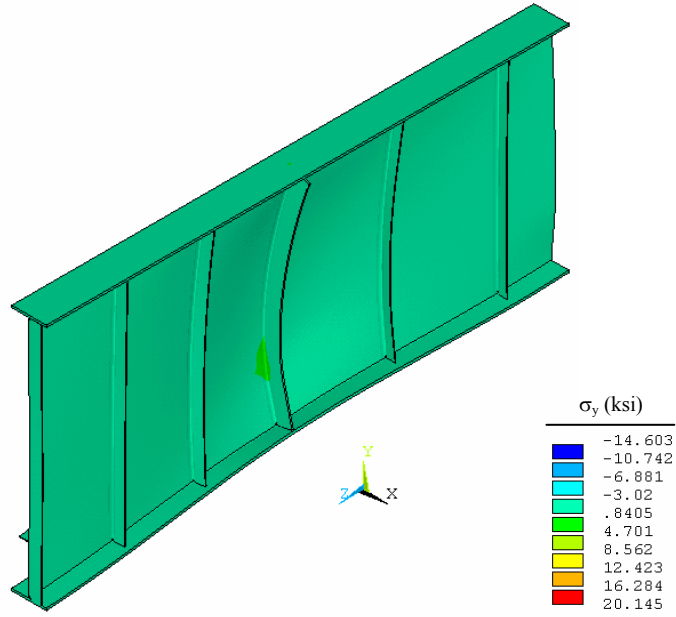
	FM1	FM1-w		FM1-r		FM1-wr	
	Maximum Stress (ksi)	Maximum Stress (ksi)	Average Percentage Reduction	Maximum Stress (ksi)	Average Percentage Reduction	Maximum Stress (ksi)	Average Percentage Reduction
$\sigma_x$ [L.C. No.]	27 [7]	0.44 [7]	98%	0.52 [5]	99%	0	100%
$\sigma_y$ [L.C. No.]	25 [7]	0.87 [6]	96%	2.8 [5]	90%	0	101%
$\sigma_z$ [L.C. No.]	17 [7]	0.39 [7]	98%	0.78 [5]	96%	0	100%

Note: extreme stresses occur mostly at Load Case No. 5, 6, and 7; percentage reductions are averages of all 16 load cases.

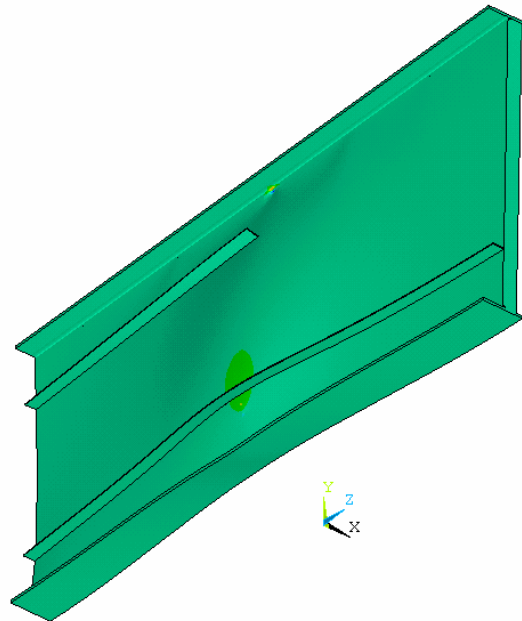
## 6.5 Connections at the Negative Moment Regions

### 6.5.1 Exploring Web Gap Stresses (Model FM3)

FM3 modeled the first interior floor-beam to girder connections next to the bridge piers. The stress distribution at the web gap region is similar to that of the FM1 model, so the same node designation shown in Figure 6-11 is also used for stress evaluation of this model. Load Case No. 7 is again found to have the most significant effect of stress concentration at the web gap, with the maximum out-of-plane displacement of  $1.3 \times 10^{-3}$  in. Figure 6-29 shows the overall model deflection and Y direction stress contour of Load Case No. 7. Figure 6-30 shows the stress distribution within the web gap at the same load case for X, Y, Z axes and the 1<sup>st</sup> principal stress direction. As summarized in Table 6-4, the maximum  $\sigma_x$  stress is 24 ksi, occurring at Node A; the maximum  $\sigma_y$  stresses on the interior and exterior web sides are 20 ksi and 16 ksi, occurring at Node A and E', respectively; and the maximum  $\sigma_z$  stress is 15 ksi, occurring at Node A". Node A" is the "hottest" spot in the model where the maximum 1<sup>st</sup> principal stress is located. All these crack opening stresses are higher than the CAFT of Detail Category C and C'.



(a) interior girder web side



(b) exterior girder web side

**FIGURE 6-29: Model FM3 Deformation and  $\sigma_y$  Contour at Load Case No. 7**

**TABLE 6-4: Critical Crack Opening Stresses in Model FM3 at Load Case No. 7**

	Stress (ksi)	Location (Node)	AASHTO Fatigue Detail Category	CAFT (ksi)
$\sigma_{x, \max}$	24	A	C'	12
$\sigma_{y, \max}$	20	A	–	–
	16	E'	C	10
$\sigma_{z, \max}$	15	A''	C'	12
$\sigma_{l, \max}$	35	A''	–	–

Figure 6-31 shows the  $\sigma_y$  stress gradient on both sides of the web gap at Load Case No. 7. The effect of out-of-plane bending is obvious. As observed from the FM1 model (Figure 6-16), a quasi-symmetric distribution pattern is formed within the small web gap. That is, corresponding nodal stresses on both web sides are almost symmetric about the web mid surface, and stresses on each side of the girder web are almost symmetric about the middle of the web gap, though with opposite signs. Figure 6-32 shows the  $\sigma_y$  stress distribution along the flange-to-web weld toe on the exterior girder web side. Unlike Model FM1, Model FM3 is not symmetric about the framed-in floor-beam plane, but the stresses at the horizontal weld toe still show symmetry about the mid surface of the connection stiffener. The maximum stress of 16 ksi occurs at Node E' and E''. As in the FM1 model, stresses outside the web gap soon decrease to low magnitudes. At Node E'2 and E''2,  $\sigma_y$  drops to 2.1 ksi. When passing over Node E'4 and E''4,  $\sigma_y$  remains close to zero. The web area affected by out-of-plane distortion is again found to be about 5 in. on each side of the connection stiffener. So the 10 in. affected zone can also be applied to the connections at the negative moment regions. The variations of web gap  $\sigma_x$ ,  $\sigma_y$ , and  $\sigma_z$  stresses for all 16 load cases are plotted in Figure 6-33 to 6-35.

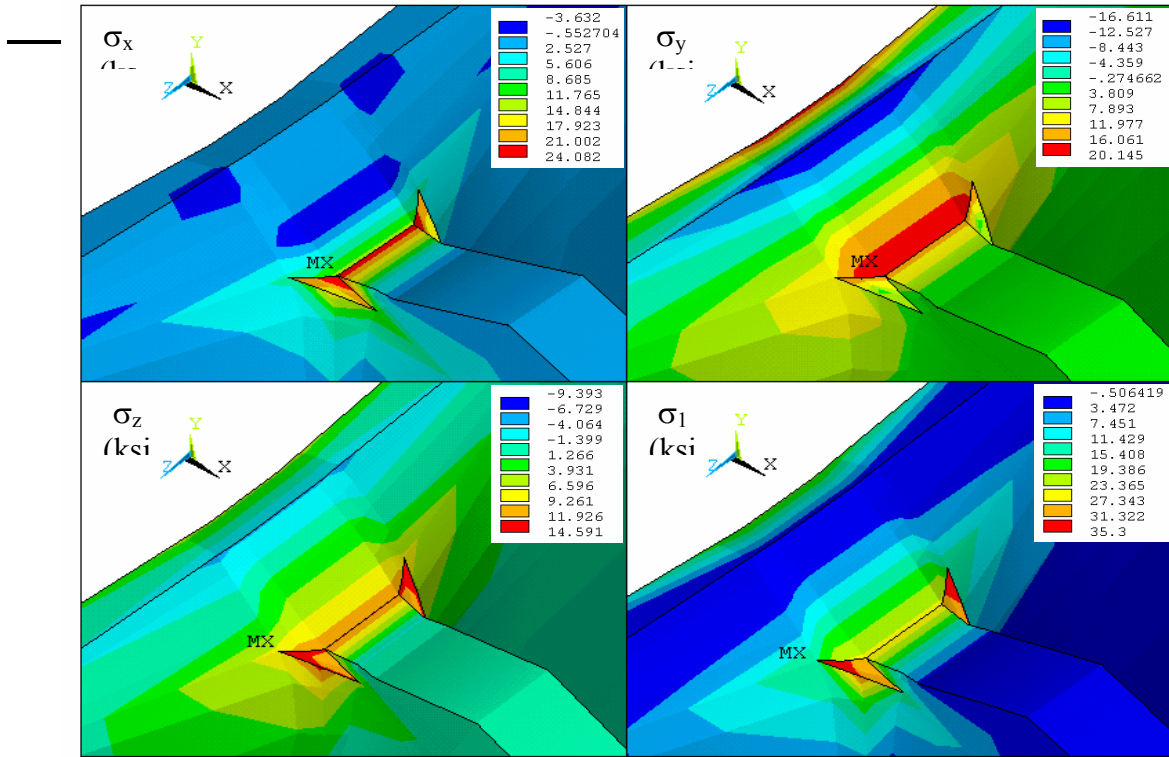


**FIGURE 6-30: Model FM3 Web Gap Stress Contours for Load Case No. 7**  
(flange elements are hidden)

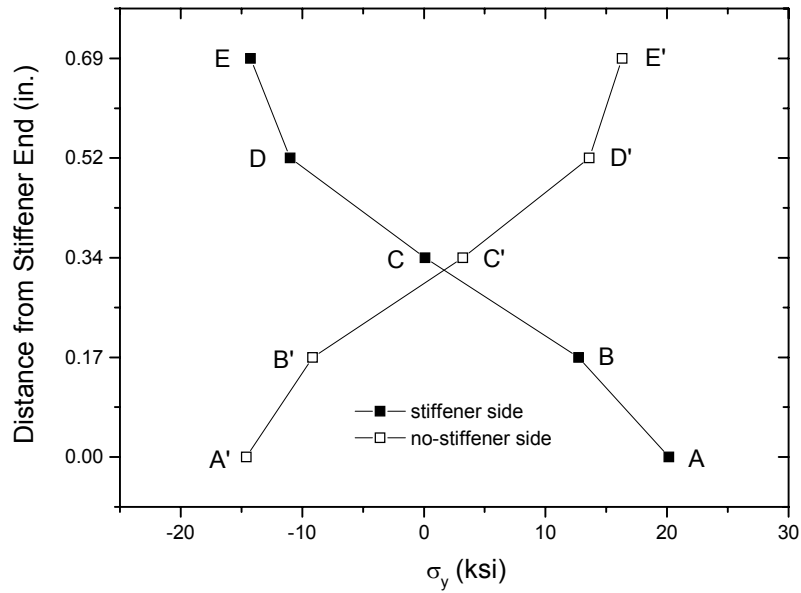


**FIGURE 6-31: Model FM3 Web Gap Stress Gradient at Load Case No.7**

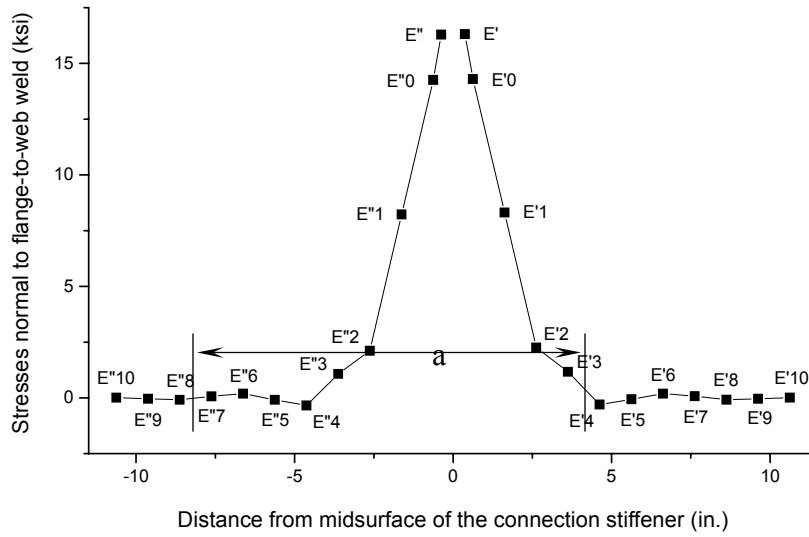


**FIGURE 6-32: Model FM3  $\sigma_y$  Distribution Along the Flange-to-Web Weld Toe at Load Case No.7**

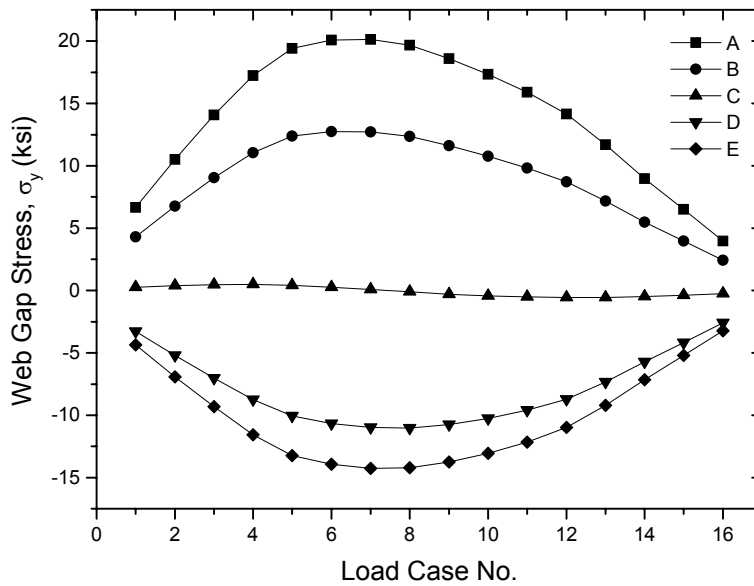


**FIGURE 6-33: Model FM3 Web Gap Stress Variation for Nodes on the Interior Web Side**

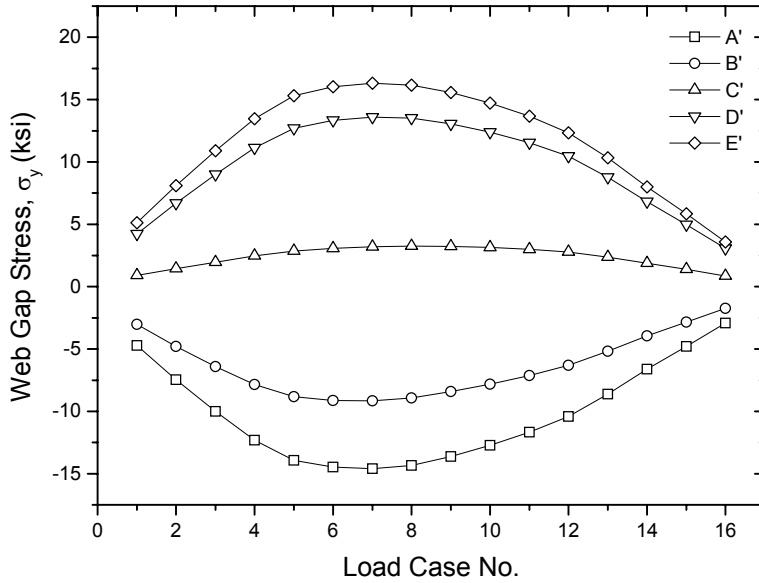


**FIGURE 6-34: Model FM3 Web Gap Stress Variation for Nodes on the Exterior Web Side**

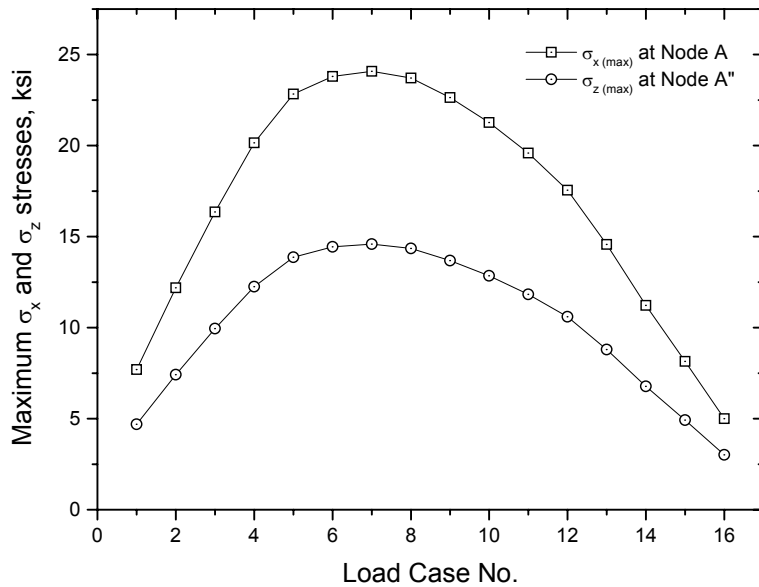


**FIGURE 6-35: Model FM3 Maximum  $\sigma_x$  and  $\sigma_z$  Stress Variation**

### 6.5.2 Repair Analysis

Three corresponding repair methods are then studied, as illustrated in Figure 6-36: 1) to add a new stiffener plate opposite the existing connection stiffener on the other side of the girder web, as actually used in the bridge repair [Figure 6-36(b)]; 2) to remove the upper truss chords

[Figure 6-36(c)]; and 3) to add new stiffener plate in addition to chord removal [Figure 6-36(d)]. Adding a new stiffener plate changes the rotational stiffness of the finite element model and the spring stiffnesses provided to the truss supports. Removing the upper truss chords changes the load flows into the truss members and consequently changes the load applied to the finite element model. Therefore, both the stick frame model and the finite element model have to be modified and reanalyzed for each repair condition.

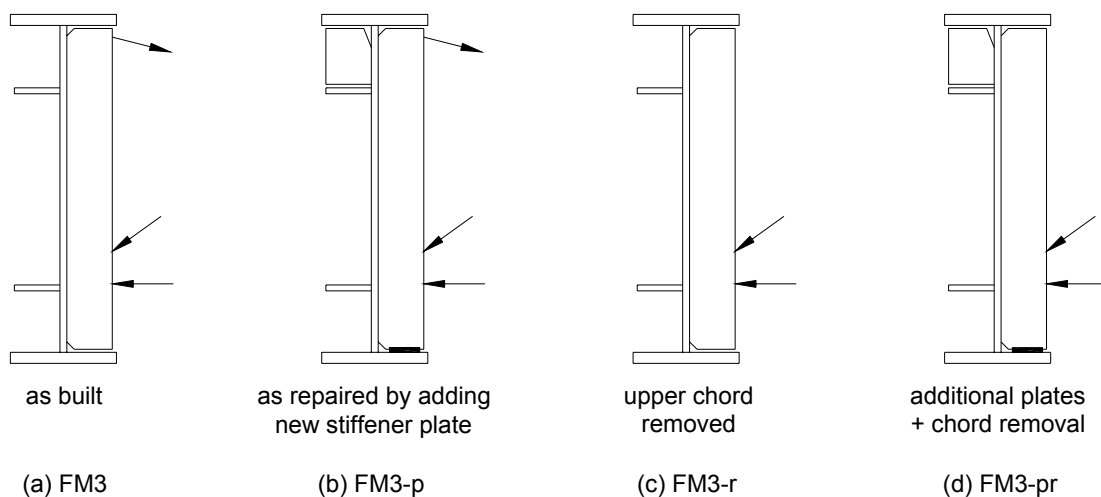


**FIGURE 6-36: FM3 Model Series**

**6.5.2.1 Adding New Stiffener Plate on the Other Side of the Girder Web (FM3-p)**

FM3-p [Figure 6-36(b)] models the current retrofit used in the bridge by welding a new stiffener plate on the other side of the girder web. However, both the existing and the new stiffener plates were fit tight to the top flange without positive attachments such as welding or bolting. The newly installed stiffener end presumably should be in bearing against the flange when subjected to out-of-plane distortion. This requires that contact analysis be carried out in order to model the bearing behavior, otherwise penetration would occur as shown schematically in Figure 6-37. As previously mentioned, finite element contact problems involve significant

amounts of non-linear calculation and require lengthy computing time. The actual contact region at the tight fit area is unpredictable; the friction between the contact surfaces is unknown; and if the convergence criteria are not specified appropriately, the two surfaces can go into or out of each other and penetration could still occur. To avoid dealing with these difficulties arising from contact analysis, coupling DOFs are used instead in this case study to simulate the bearing behavior. As illustrated by Figure 6-38, the tight fit surfaces on the side of the newly installed stiffener plate are meshed by six pairs of coincident nodes. An assumption is made that all DOFs of the coincident nodes are coupled if the stiffener node has a tendency to penetrate into the flange. From the outer edge of the stiffener, one pair of coincident nodes is added at a time. If penetration is observed from any of the remaining uncoupled nodes, then the adjacent pair of coincident nodes have to be coupled and the model needs to be reanalyzed. For each step of trial-and-error construction of the coupling model, the rotational stiffness of the finite element model and the spring stiffness of the truss supports are changed, and consequently the truss member forces and the loads applied to the finite element model are also changed, so both the stick frame and the finite element models have to be solved again to see if additional coupled sets are needed. It is not until the fourth pair of coincident nodes are coupled (Figure 6-38) that penetration stops occurring at the tight fit surfaces. Figure 6-39 shows the overall deflection and  $\sigma_y$  stress distribution of Mode FM3-p for Load Case No. 6. Figure 6-40 and 6-41 illustrate in detail the web gap deformation and  $\sigma_y$  stress contour for the interior and exterior web side, respectively, of the same load case. From Figure 6-41 it can be noticed that the fifth and sixth pairs of coincident nodes open apart and the uncoupled stiffener nodes deflect laterally under out-of-plane distortion. Those four pairs of coupled nodes are restrained from relative movement. In reality, however, the stiffener end in bearing with the flange can still move

laterally, which could then cause larger out-of-plane displacement and higher web gap stresses. So if the stress ranges obtained from this model are not lowered to a satisfactory level, then the actual repair detail could only yield a more serious stress condition and a shorter fatigue life.

Compared to the data obtained from Model FM3, the average web gap stress reductions after the repair at those mostly stressed nodes are 46%, 34%, and 43%, for  $\sigma_x$ ,  $\sigma_y$ , and  $\sigma_z$ , respectively. The maximum  $\sigma_x$  stress at Node A is decreased to 13 ksi, still a little higher than the CAFT of Category C'. The maximum  $\sigma_y$  stress, also occurring at Node A, is decreased to 14 ksi. The  $\sigma_y$  stress at Node E' is lowered to 10 ksi, which is close to the CAFT of Category C. The maximum  $\sigma_z$  stress at Node A'' is reduced to 8.8 ksi. It is lower than the CAFT, but still higher than half of the CAFT of Category C'. This repair approach thus does not provide sufficient resistance to the out-of-plane distortion. Infinite fatigue life is not achieved and fatigue cracking could still occur at the web gaps after a certain number of stress cycles. In order to reduce the stress ranges to a lower level, additional retrofit needs to be performed to help relieve the effect of stress concentration at the negative moment region connections.

#### ***6.5.2.2 Removing Upper Truss Chord (Model FM3-r)***

The repair method proposed by Model FM3-r [Figure 6-36(c)] is to remove the two diagonal upper truss chords. The maximum  $\sigma_x$ ,  $\sigma_y$ , and  $\sigma_z$  stresses in the web gap after repair are reduced by 98%, 89%, and 97%, respectively, averaged for 16 load cases. All the peak stress ranges were decreased to a level much lower than half of the CAFT of either Detail Category C or C'. This is apparently the most effective repair approach and would have been recommended instead of the actual bridge retrofit. From aesthetic point of view, another advantage of using this repair is that the exterior girder façade can be kept clean without having additional plates such as those already installed in the repaired connections.